Tunable Catalysts and Electrodes with High Material Utilization and Durability for Hydrogen Production

A Dissertation Presented for the

Doctor of Philosophy

Degree

The University of Tennessee, Knoxville

Lei Ding

May 2024

Copyright © 2024 by Lei Ding

All rights reserved.

ACKNOWLEDGEMENTS

I would like to express my most sincere appreciation to my advisor, Dr. Feng-Yuan Zhang, for his great support, patience and advice throughout my whole doctoral study. I would like to thank Dr. David A. Cullen, Dr. Peng Zhao and Dr. Zhiqiang Xie for being on my committees and providing me with significant guidance and suggestions for my research.

I would like to thank the NanoHELP group - Dr. Shule Yu, Dr. Gaoqiang Yang, Dr. Yifan Li, Dr. Kui Li, Weitian Wang, Jun Li, Yeshi Dohrmann - it has been my great honor to work with you.

I would also like to thank Dr. Matthew M. Mench, Dr. Douglas S. Aaron, Dr. Yu-Kai Weng, Anirban Roy, Frida Roenning, Dr. Bapi Bera, Dr. Manikandan Palanisamy, Dr. Wei Wang, Dr. Gerald Egeland, Dr. Neal D Evans, Dr. Gerd Duscher, Mohammad Alipanahrostami, Douglas Warnberg, Alexander Terekhov, Dr. Lu Liu, Dr. Lino Costa, Dr. Brian Canfield, Dr. Trevor M. Moeller, Dr. Reza Abedi, Dr. Lee Leonard, Gary Payne, Jack LeGeune for their countless help with my research.

I would like to express my appreciation to Dr. Adam Paxson, Dr. Monjid Hamdan, Dr. Adam Gage from Plug Power; Dr. Zili Wu, Dr. Haoran Yu, Harry M. Meyer III, Dr. Scott T. Retterer from Oak Ridge National Laboratory; Dr. Guido Bender, Dr. Scott Mauger, Dr. Sunilkumar Khandavalli, Dr. Zhiwen Ma, Dr. Jacob Wrubel from National Renewable Energy Laboratory; Dr. Pu-Xian Gao, Dr. Fangyuan Liu from University of Connecticut; Dr. Svitlana Pylypenko, Genevieve Stelmacovich, Lonneke van Eijk, Jayson Foster Colorado School of Mines; and Dr. Kathy Ayers, Chirstopher B. Capuano, Alex Keane from Nel Hydrogen for their great guidance, suggestion and help for my research.

Additionally, I would like to express my sincere appreciation to my family and friends. They have shown significant support throughout my whole doctoral life. Especially, I would like to express my great appreciation to my parents, Huohua Ding and Min Zeng for their unconditional belief and support towards me. I would like to also thank my sister Lu Ding and my brother Hao Ding. I also thank my friends Anqun Li and Zu Xu. They have provided me with the strong strength and confidence to overcome the issues and obstacles during my doctoral study.

I also greatly appreciate the support from U.S. Department of Energy's Office of Energy Efficiency and Renewable Energy (EERE) under the Hydrogen and Fuel Cell Technologies Office (HFTO) Award Number DE-EE0009236, DE-EE0008426 and DE-EE0008423, the Institute for Energy and Environment (IEE), Institute for a Secure and Sustainable Environment (ISSE) and Center for Materials Processing at UTK.

ABSTRACT

Hydrogen, the future energy carrier, has gained extensive attention due to its advantages of high energy density, low weight, and zero-carbon emission. So far, hydrogen has been widely used in various fields including transportation, oil upgrading, metal refining, etc. Most hydrogen is currently produced from fossil fuels, which can cause serious environmental problems. Water electrolysis was proposed to produce clean hydrogen with carbon-free emission and only byproduct of oxygen. Among various water electrolyzer devices, the proton exchange membrane electrolyzer cell (PEMEC) shows great potential to produce green hydrogen by integrating renewable sources (solar, wind, etc.) due to its advantages of high energy efficiency, high energy density, fast charging and discharging, compact system design and easily scale up/down. However, the high capital cost hinders the large-scale application and commercialization of the PEMEC, which is mainly due to platinum group metal (PGM)-based electrocatalysts/electrodes with scarcity and high price of PGMs. Hence, it is significant to develop novel and advanced electrocatalysts/electrodes with high material utilization and low cost to cut down the capital cost and then speed up the wide application of the PEMEC.

The main achievements of this dissertation are as follows: (a) Bifunctional NiFeW nanosheet fabrication via facile electrodeposition for alkaline water splitting. (b) Impacts of W-doping concentration on NiFe morphology and performance for water splitting. (c) High-performance Ir-integrated electrode for the PEMEC with high current operation capacity. (d) Highly porous Ir with fine honeycomb nanostructures and improved reaction kinetics for the PEMEC. (e) Nanoporous Ir nanosheets with abundant nanopores and edges

for the PEMEC, showing impressive performances and far exceeding the 2026 DOE targets. (f) Ultrathin Pt-NS with a thickness of about 4 nm as a cathode electrode for the PEMEC, achieving more than 99-fold catalyst savings and 237-fold higher catalyst utilization. This research provides guidance for the development of novel and advanced electrocatalysts/electrodes for water electrolyzers and other energy storage devices. Furthermore, the novel and advanced electrocatalyst/electrode designs with high material utilization and easy scalability could boost the commercialization and the industrial application of the PEMEC, and thus accelerate renewable energy evolution.

TABLE OF CONTENTS

CHAPTER ONE INTRODUCTION AND GENERAL INFORMATION 1

1.1 Overview 2

1.2 Background 3

1.3 Objectives 10

CHAPTER TWO CONSTRUCTING ULTRATHIN W-DOPED NIFE NANOSHEETS VIA FACILE ELECTROSYNTHESIS AS BIFUNCTIONAL ELECTROCATALYSTS FOR EFFICIENT WATER SPLITTING 11

2.1 Abstract 13

2.2 Introduction 14

2.3 Experimental Section 17

2.3.1 Materials and chemicals 17

2.3.2 Preparation of NiFe/CP and NiFeW/CP 17

2.3.3 Characterizations 18

2.3.4 Electrochemical measurements 18

2.4 Results and Discussions 20

2.4.1 Characterizations of NiFeW Nanosheets 20

2.5 Electrocatalytic performances 26

2.6 Conclusions 40

Appendix 42

CHAPTER THREE W-INDUCED MORPHOLOGICAL MODIFICATION OF NIFE LAYERED DOUBLE HYDROXIDES AS EFFICIENT ELECTROCATALYSTS FOR OVERALL WATER SPLITTING 63

3.1 Abstract 65

3.2 Introduction 66

3.3 Experimental 68

3.3.1 Chemicals and materials 68

3.3.2 Fabrication of NiFe hydroxides and NiFeW-LDHs 69

3.3.3 Characterizations 69

3.3.4 Electrochemical measurements 70

3.4 Results and Discussion 71

3.5 Conclusions 88

CHAPTER FOUR AN EFFICIENT INTEGRATED ELECTRODE ENABLES HIGH-CURRENT OPERATION AND EXCELLENT STABILITY FOR GREEN HYDROGEN PRODUCTION 92

4.1 Abstract 94

4.2 Introduction 95

4.3 Experimental Section 98

4.3.1 Electrode fabrication and characterization 98

4.3.2 The PEMEC assembly and test 98

4.4 Results and Discussions 99

4.5 Conclusions 121

Appendix 122

CHAPTER FIVE 126

HIGHLY POROUS IRIDIUM THIN ELECTRODES WITH LOW LOADING AND IMPROVED REACTION KINETICS FOR HYDROGEN GENERATION IN PEM ELECTROLYZER CELLS 126

5.1 Abstract 128

5.2 Introduction 128

5.3 Experimental Section 131

5.3.1 Preparation of CCLGDLs 131

5.3.2 Characterization 132

5.3.3 *Ex-situ* electrochemical measurements 132

5.3.4 The PEMEC assembly and test 133

5.4 Results and Discussions 134

5.4.1 Morphology and composition of the HC Ir CCLGDL 134

5.4.2 OER performance in a three-electrode system 139

5.4.3 Cell characterization in PEMECs 141

5.4.4 Post-analysis of the HC Ir CCLGDL after the cell test 154

5.5 Conclusion 156

Appendix 157

CHAPTER SIX IONOMER-FREE NANOPOROUS IRIDIUM NANOSHEET ELECTRODES WITH BOOSTED PERFORMANCE AND CATALYST UTILIZATION FOR HIGH-EFFICIENCY WATER ELECTROLYZERS 166

6.1 Abstract 168

6.2 Introduction 168

6.3 Experimental Section 172

6.3.1 Fabrication of ionomer-free IrNS integrated electrodes 172

6.3.2 Materials characterization 173

6.3.3 Electrochemical measurements 173

6.3.4 Cell assembly and performance evaluation of the PEMEC 173

6.4 Results and Discussions 175

6.4.1 Morphology and crystal structure of nanoporous IrNS electrode 175

6.4.2 Nanostructure of nanoporous IrNS catalysts 178

6.4.3 Full cell characterization of nanoporous IrNS in PEMECs with N117 membrane 179

6.4.4 Full cell characterization of nanoporous IrNS in PEMECs with N212 membrane 184

6.4.5 Post-analysis of IrNS catalysts after the electrolyzer test 187

6.5 Conclusions 189

Appendix 191

CHAPTER SEVEN ELECTROCHEMICALLY GROWN ULTRATHIN PLATINUM NANOSHEET ELECTRODES WITH ULTRALOW LOADINGS FOR ENERGY-SAVING AND INDUSTRIAL-LEVEL HYDROGEN EVOLUTION 197

7.1 Abstract 199

7.2 Introduction 200

7.3 Experimental Section 203

7.3.1 Platinum nanosheet integrated electrode fabrication 203

7.3.2 Material characterization 204

7.3.3 Ex-situ electrochemical measurements 204

7.3.4 Cell performance evaluation of the PEMEC 205

7.4 Results and Discussions 205

7.4.1 Morphology and composition of the Pt-NS electrode 205

7.4.2 Growth mechanisms of the Pt-NSs 208

7.4.3 Pt-NS characterization in PEMECs 217

7.4.4 Post-analysis of the Pt-NS electrode after the cell test 226

7.5 Conclusions 230

Appendix 231

CHAPTER EIGHT CONCLUSIONS AND SUGGESTIONS FOR FUTURE WORKS 237

LIST OF REFERENCES 245

VITA 270

LIST OF TABLES

Table 1. Elemental composition of NiFe/CP and NiFeW/CP based on EDS results. 47

Table 2. The literature survey of recently reported electrocatalysts for the OER catalytic activity (at 10 mA/cm^2)..... 49

Table 3. The OER electrochemical impedance parameters obtained by simulating the Nyquist plots in Figure 4E with an appropriate equivalent circuit model. 50

Table 4. The literature survey of various recently reported electrocatalysts for the HER catalytic activity (at -10 mA/cm^2)..... 52

Table 5. The HER electrochemical impedance parameters obtained by simulating the Nyquist plots in Figure 5D with an appropriate equivalent circuit model..... 53

Table 6. Elemental composition of electrocatalysts before and after stability tests characterized with EDS..... 58

Table 7. Comparison of recently reported bifunctional electrocatalysts for overall water electrolysis in alkaline media..... 62

Table 8. OER EIS fitting parameters derived from Nyquist plots in Figure 26A. 86

Table 9. HER EIS fitting parameters derived from Nyquist plots in Figure 26B..... 87

Table 10. OER overpotential comparison at 10 mA/cm^2. 90

Table 11. HER overpotential comparison at -10 mA/cm^2. 91

Table 12. Fitting results from EIS plots in Figure 31A. 110

Table 13. Details of different anodes and related cell performances..... 114

Table 14. Cell test results of different electrodes after the cell stability test. 120

Table 15. The PEMEC properties and operating conditions. 135

Table 16. Cell test results of the HC Ir and dense Ir CCLGDLs. 144

Table 17. The fitting data of the Nyquist plots at 200 mA/cm^2. 145

Table 18. Details of the bubble size distribution. 163

Table 19. Details of different electrode fabrications. 227

Table 20. EIS fitting parameters derived from the Nyquist plots in Figure 71C. 234

LIST OF FIGURES

Figure 1. One-step fabrication of the NiFeW/CP as a bifunctional electrocatalyst for efficient alkaline water splitting. For comparison, the NiFe/CP is also prepared. ... 23

Figure 2 (A, B) SEM (C, D) TEM, and (E) STEM-EDS images of morphology and elemental distribution of the NiFeW/CP..... 24

Figure 3 (A) The XPS full survey of the NiFeW/CP, the high-resolution XPS of (B) Ni, (C) Fe, and (E) O in the NiFe/CP and NiFeW/CP electrocatalysts. (D) The XPS spectra of W in the NiFeW/CP electrocatalyst. 25

Figure 4 (A) The OER polarization curves with *iR* correction of the NiFeW/CP, NiFe/CP, CP, and the commercial IrO_2/CP in 1 M KOH at 5.0 mV/s and (B) The related Tafel slopes. (C) OER overpotentials of different electrocatalysts at 1 mA/cm^2, 10 mA/cm^2, and 30 mA/cm^2. (D) Comparison overpotential at 10 mA/cm^2 with previous reported OER electrocatalysts in 1 M KOH. (E) Nyquist plots of the NiFeW/CP and NiFe/CP (recorded at 1.44 V (vs. RHE)) and the corresponding fitted Nyquist plots; Inset: the equivalent circuit model. (F) Chronopotentiometry measurements of the NiFeW/CP electrocatalyst at 10 mA/cm^2 and 100 mA/cm^2 in 1 M KOH at room temperature (Ar-saturated)..... 29

Figure 5 (A) The HER polarization curves with *iR* correction of the NiFeW/CP, NiFe/CP, CP, and the commercial IrO_2/CP in 1 M KOH at 5.0 mV/s. (B) The related Tafel slopes. (C) The HER overpotentials of different electrocatalysts at -1 mA/cm^2, -10 mA/cm^2, and -30 mA/cm^2. (D) Nyquist plots of the NiFeW/CP and NiFe/CP (recorded

at -0.15 V (vs. RHE)) and the corresponding fitted Nyquist plots. (E) Plots used to extract the double-layer capacitances. (F) Chronopotentiometry measurements of NiFeW/CP electrocatalyst at -10 mA/cm^2 and -100 mA/cm^2 in 1 M KOH at room temperature (Ar-saturated). 33

Figure 6. Schematic illustration of the OER (top part) and HER (bottom part) processes on the NiFeW/CP nanosheets, where * represents the reaction sites of the electrocatalysts. 36

Figure 7. (A) Schematic of the NiFeW/CP as a bifunctional electrocatalyst for overall water splitting in alkaline media. (B) Polarization curves with *iR* correction for overall water splitting using the NiFeW/CP counterparts and IrO_2/CP||Pt/CP. (C) Comparison of the cell voltage of recently reported bifunctional electrocatalysts. (D) Chronoamperometry tests of overall water splitting (10 mA/cm^2 and 100 mA/cm^2) at room temperature. The inset image is from the recorded video of overall water splitting. 39

Figure 8. Photographs of the CP substrate (a) and the NiFeW/CP electrode (b)..... 43

Figure 9. SEM images of bare carbon paper (A, B) and NiFeW/CP (C, D)..... 44

Figure 10. SEM images of the NiFe/CP. 45

Figure 11. XRD patterns of carbon paper (a), NiFe/CP (b), and NiFeW/CP (c)..... 46

Figure 12. CV curves of NiFeW/CP and NiFe/CP. 48

Figure 13. Comparison overpotential at -10 mA/cm^2 with previous reported HER electrocatalysts in 1 M KOH..... 51

Figure 14. CV curves for different electrocatalysts carried out in non-faradic regions at different scan rates in 1 M KOH. 54

Figure 15. SEM image and corresponding EDX mapping images of the NiFeW/CP after the OER stability test for 15 h. 55

Figure 16. SEM image and corresponding EDX mapping images of the NiFeW/CP after the HER stability test for 15 h. 56

Figure 17. XPS spectra comparison of fresh NiFeW/CP electrocatalyst and NiFeW/CP electrocatalysts after the OER and HER stability tests. Ni 2p (A), Fe 2p (B), and W 4F (C). 57

Figure 18. SEM images of NiFeW/CP after OER (A, B) and HER (C, D) stability tests (100 mA/cm^2) 59

Figure 19. SEM image and corresponding EDX mapping images of the NiFeW/CP as an anode after the stability test. 60

Figure 20. SEM image and corresponding EDX mapping images of the NiFeW/CP as a cathode after the stability test. 61

Figure 21. Schematic of electrocatalyst electrodeposition on CFPs to form bifunctional electrocatalysts. With W doping, the NiFe hydroxides with film structures are successfully engineered to the NiFeW-LDHs with nanosheet features. 72

Figure 22. SEM images with higher magnification and lower magnification (Insets) of carbon fiber papers (A) and electrocatalysts with different W precursor concentrations: 0 mM (B), 2.5 mM (C), 5 mM (D), 7.5 mM (E), and 10 mM (F)... 74

Figure 23. Effects of W doping concentration on NiFeW-LDH morphologies on carbon fiber papers..... 75

Figure 24. TEM images (A, B), SEM/EDS-mapping images (C), and EDS results of NiFeW-LDHs (5 mM W precursor) (D)..... 80

Figure 25. OER and HER performance evaluated in 1 M KOH with Ar-saturated at room temperature. The IR-corrected OER (A) and HER (D) polarization curves of different electrocatalysts. OER (B) and HER (E) overpotential comparisons at 1 mA/cm^2,10 mA/cm^2, -1 mA/cm^2 and -10 mA/cm^2. Corresponding OER (C) and HER (F) Tafel slopes..... 81

Figure 26. Nyquist plots at the overpotential of 210 mV for OERs (A) and 150 mV for HERs (B). Corresponding equivalent circuit models (Inset in A and B). The related OER (C) and HER (D) Bode plots: dots and solid lines: log(freq) vs. log(|Z|); dots: log(freq) vs. |phase|. Plots for deriving the double-layer capacitance (C_{dl}) (E). The electrochemically surface area (ECSA) comparison of different electrocatalysts (F). 85

Figure 27. Schematic of (A) Ir-integrated electrode fabrication. (B) Anode side membrane electrode assembly based on the Ir-integrated electrode for the PEMEC application. 102

Figure 28. (A-C) SEM images of the Ir/sintered Ti at different magnifications; (D-F) SEM images of the Ir/Pt sintered Ti at different magnifications and (G) SEM-EDS mapping images of the Ir/Pt sintered Ti..... 103

Figure 29. (A) Cell polarization and efficiency curves of different electrodes: 0.5-Ir/sintered Ti and 0.5-Ir/Pt sintered Ti. (B) Cell voltage comparison of different electrodes at 2, 4 and 6 A/cm^2, respectively. 104

Figure 30. (A) The HFR plots of the 0.5-Ir/sintered Ti and 0.5-Ir/Pt sintered Ti. (B) The related HFR-free cell polarization curves the 0.5-Ir/sintered Ti and 0.5-Ir/Pt sintered Ti. 107

Figure 31. EIS plots of the 0.5-Ir/sintered Ti and 0.5-Ir/Pt sintered Ti at (A) 0.2 A/cm^2. (B) The related equivalent electrical circuit for fitting. 108

Figure 32. (A) Cell polarization and efficiency curves of Ir/Pt sintered Ti electrodes with different Ir loadings: 0.3 mg/cm^2 and 0.5 mg/cm^2, respectively. (B) The related HFR-free cell polarization curves of the 0.3-Ir/Pt sintered Ti and 0.5-Ir/Pt sintered Ti. (C) EIS plots of the 0.3-Ir/Pt sintered Ti and 0.5-Ir/Pt sintered Ti at 0.2 A/cm^2. 111

Figure 33. (A) Cell voltage comparison at 2 A/cm^2 with previously reported anode electrodes: IrO_2@TiO_2; $IrRuO_x$ (TT); $IrOOH_x/TiO_2$; $W_{0.7}Ir_{0.3}O_y$; Sr_2CaIrO_6; Ir AC/NN; Ir-ND. (B) The related mass-specific current comparison at 1.7 V. 113

Figure 34. Cell stability tests at an ultrahigh current density of 5 A/cm^2 of the Ir/sintered Ti electrodes and Ir/Pt sintered Ti electrode. 116

Figure 35. (A) Polarization and efficiency curves of the Ir/Pt sintered Ti electrode before and after stability test, (B) HFR curves of the Ir/Pt sintered Ti electrode before and after stability test, (C) Cell polarization and efficiency curves of the Ir sintered Ti

electrode before and after stability test, (D) HFR curves of the Ir sintered Ti electrode before and after stability test. 119

Figure 36. SEM images of (A, B) the bare sintered Ti and (C, D) the Pt sintered Ti..... 122

Figure 37. Mapping images of the Ir/sintered Ti. 123

Figure 38. SEM images of the tested Ir/Pt sintered Ti electrode at different magnifications. (C) SEM-EDS mapping images of the tested Ir/Pt sintered Ti electrode. 124

Figure 39. SEM image of the tested Ir/sintered Ti electrode. 125

Figure 40. Schematic of (A) the PEMEC incorporated with the HC Ir CCLGDL; (B) The HC CCLGDL; (C) Advantages of improved multiphase transport and abundant active reaction sites of the HC Ir CCLGDL. 137

Figure 41. SEM images of (A, B) the Ir/PS/TTLGDL and (C, D) the HC Ir CCLGDL; (E) Cross-section SEM image of the honeycomb Ir catalyst layer; (F) the XRD pattern of the HC Ir CCLGDL. 138

Figure 42. (A) LSV curves with iR-correction; (B) The related Tafel slopes; (C) CV scan curves within 0 V ~ 1.5 V vs. RHE at 200 mV/s; (D) Outer charge comparison... 140

Figure 43. (A) Cell polarization curves of the HC Ir CCLGDL and dense Ir CCLGDL; (B) The HFR-free cell polarization curves and the corresponding HFR plots..... 142

Figure 44. (A) The Nyquist plots at 200 mA/cm^2 and the related fitting curves based on the circuit model; Inset: the related equivalent circuit; Bode plots of (B) the dense Ir CCLGDL and (C) the HC Ir CCLGDL: dots and solid lines: log(freq) vs. log(|Z|); dash lines: log(freq) vs. |phase|; (D) The Nyquist plots at 1000 mA/cm^2. 147

Figure 45. High-speed micro-scale visualization of oxygen bubble dynamics on electrode surfaces of (A) dense Ir CCLGDL and (B) HC Ir CCLGDL at 200 mA/cm^2 (Movies S1 and S2); (C) Bubble size distribution comparison of oxygen bubbles on the two CCLGDLs; (D) Bubble site number comparison of the two CCLGDLs at 1.85 V based on Movies S3 and S4. 149

Figure 46. (A) Cell voltage comparison at 1000 mA/cm^2 with previously reported anode catalysts; (B) The corresponding mass activity comparison at 1.7 V; (C) Cell stability test at 1800 mA/cm^2; (D) Cell performance comparison before and after the stability test. 151

Figure 47. (A) SEM image of the fresh HC Ir CCLGDL; (B) SEM image of the tested HC Ir CCLGDL; (C) EDS analysis of the fresh HC Ir CCLGDL; (D) EDS analysis of the tested HC Ir CCLGDL. 155

Figure 48. The top-view SEM image (A-C) of the TTLGDL with a pore size of 200 μm and a porosity of 40%, and (D) the related cross-section SEM image. 157

Figure 49. Schematic of the fabrication process of a honeycomb Ir CCLGDL. 158

Figure 50. SEM-EDS mapping images of the HC Ir CCLGDL cross-section. 159

Figure 51. (A) SEM image of the dense Ir CCLGDL; (B) EDS analysis of the dense Ir CCLGDL..... 160

Figure 52. The initial CV scan cycle (purple line) and the CV scan cycle after full activation (green line) of the HC Ir (A) and the dense Ir (B). 161

Figure 53. Overpotential comparison at different current densities. 162

Figure 54. (A) The comparison of HFR-free performance and HFR, (B) Nyquist plot comparison at 200 mA/cm^2..... 164

Figure 55. SEM-EDS mapping images of (A) the fresh HC Ir CCLGDL and (B) the tested HC Ir CCLGDL. 165

Figure 56. Schematic illustrating the design of the nanoporous IrNS integrated electrode composed of *in-situ* deposited ultrathin nanoporous iridium nanosheets on thin titanium LGDLs via a low-temperature chemical synthesis strategy. 177

Figure 57. Morphological and compositional characterizations. (a-b) Top-view and (c) cross-section SEM images of the employed TT-LGDL substrate. (d-f) SEM images of the nanoporous IrNS integrated electrode. (g-i) SEM-EDS elemental mapping of the electrode. (j) XRD pattern of the nanoporous IrNS catalysts. 180

Figure 58. (a-b) HAADF-STEM images of as-synthesized IrNS catalysts prior to cell test in PEMECs..... 181

Figure 59. (a) Polarization curves of an IrNS integrated electrode coupled with N117 membrane and conventional CCM/TT-LGDL in PEMECs at 80 ^{o}C. (b) The HFR comparison between 0 and 2000 mA/cm^2. (c) The HFR-free EIS plots of nanoporous IrNS and conventional CCM/TT-LGDL at 1000 mA/cm^2. (d) Cell stability test at 1000 mA/cm^2 for initial 20 hours and subsequent test at 1800 mA/cm^2 for over 120 h. (e) Mass-specific current comparison. (f) Cell performance comparison. 183

Figure 60. (a) Polarization curves of a nanoporous IrNS integrated electrode coupled with Nafion 212 membrane under high current densities of up to 6000 mA/cm^2. (b) Cell stability tests at 1800 mA/cm^2 for 90 h and 5000 mA/cm^2 for 130 h. 186

Figure 61. (a, b) HAADF-STEM images of IrNS catalysts after the cell stability test at 5000 mA/cm^2. 188

Figure 62. A schematic illustration of electrode assembly in a PEM water electrolyzer. 191

Figure 63. The SEM-EDS elemental mapping of the IrNS electrode at a higher magnification. 192

Figure 64. The polarization curve of nanoporous IrNS catalysts for the OER. (b) The corresponding Tafel plot. 193

Figure 65. The EIS plots of nanoporous IrNS coupled with Nation 117 membrane and conventional CCM/TT-LGDL baseline at 1000 mA/cm^2..... 194

Figure 66. The high-frequency resistance (HFR) plot of a nanoporous IrNS integrated electrode coupled with Nafion 212 membrane between 0 and 6000 mA/cm^2..... 195

Figure 67. High-resolution XPS spectra of Ir 4f for nanoporous IrNS catalysts before and after the stability test in a PEM water electrolyzer. 196

Figure 68. Schematic of the Pt-NS fabrication on the thin Ti substrate (with seeding and no seeding, respectively) *via* a highly efficient and facile electrochemical growth process at room temperature. 210

Figure 69. (A-C) Low magnification SEM images of Pt-NSs with different loadings: (A) 0.025 mg_{Pt}/cm^2 (without the seeding layer), (B) 0.025 mg_{Pt}/cm^2 (with the seeding layer), (C) 0.015 mg_{Pt}/cm^2 (with the seeding layer); (D-F) High magnification SEM images of Pt-NSs based on 0.025 mg_{Pt}/cm^2; (G) Top-view and (H) cross-section view SEM-EDS mapping images of the Pt-NS electrode based on 0.025 mg_{Pt}/cm^2; The related (I) EDS spectra; (J) XRD pattern of the Pt-NSs. 211

Figure 70. Pt-NS growth mechanisms without (top part) and with (bottom part) the seeding layer..... 215

Figure 71 Electrochemical characterizations of the Pt-NS/Ti *via* a three-electrode system in 0.5 M H_2SO_4. at room temperature. (A) IR-corrected HER polarization curves with a scan rate of 5.0 mV/s; (B) EIS plots recorded at −40 mV; (C) The fitting equivalent circuit model; (D) Double-layer capacitance comparison; High-speed visualization of hydrogen bubble dynamics on (E) the Pt-NS electrode and (F) the PtNP electrode, respectively, at 200 mA/cm^2 (Movies S1 and S2). 216

Figure 72. *In-situ* cell performance comparison of Pt-NS with and without the seeding layer in a PEMEC at 80 ℃. (A) Cell polarization curves of the Pt-NS electrodes with and without the seeding layer; (B) Enlarge cell polarization curves of the Pt-NS electrodes with and without the seeding layer within the current density range of 1.25 to 2 A/cm^2; (C) The related high-frequency resistance (HFR) plots; (D) The HFR-free cell polarization curves. 220

Figure 73. Cell performance comparison of the Pt-NS electrodes and the commercial CCM in a PEMEC at 80 ℃. (A) Cell polarization curves; (B) The related HFR plots; (C)

The corresponding Tafel plots; (D) Catalyst saving (Baseline: the CCM) and efficiency comparison at 1 A/cm^2 of the Pt-NS electrodes and the commercial CCM; (E) The related Pt mass-normalized cell polarization curves. 221

Figure 74. (A) Cell stability test at 1.8 A/cm^2; (B) Cell performance comparison before and after the stability test; (C) Cell voltage comparison at 2 A/cm^2 with previously reported cathode catalysts; (D) The corresponding mass-specific current comparison at 1.7 V; inset: enlarged area (the lower right) of the mass-specific current comparison at 1.7 V. 224

Figure 75. Morphology comparison before and after the *in-situ* cell stability test. SEM images of the (A, B) fresh and (C, D) tested Pt-NS electrode; (E) SEM-EDS mapping images of the tested Pt-NS electrode. 228

Figure 76. High-angle annular dark-field (HAADF) STEM images of (A, B) the fresh and (C, D) tested Pt-NS electrode..... 229

Figure 77. SEM image of Pt-NSs without the seeding layer: 0.07 mg$_{Pt}$/cm^2 Pt-NSs. 231

Figure 78. SEM image of Pt-NSs without the seeding layer: 0.14 mg$_{Pt}$/cm^2 Pt-NSs. 232

Figure 79. SEM images of Pt nanoparticle seeding layers (A and B); SEM images of Pt-NSs with the seeding layer, (C) 0.050 mg$_{Pt}$/cm^2 Pt-NSs, (D) 0.140 mg$_{Pt}$/cm^2 Pt-NSs. 233

Figure 80. The HFR-free cell polarization curves of commercial CCM and Pt-NS with seeding layer: 0.025 mg$_{Pt}$/cm^2 and 0.015 mg$_{Pt}$/cm^2. 235

Figure 81. EDS analysis of the tested Pt-NS CCLGDL (0.025 mg$_{Pt}$/cm^2). 236

LIST OF ATTACHMENTS

Movie S1. The bubble dynamics of the dense Ir CCLGDL at a current density of 200 mA/cm^2.

Movie S2. The bubble dynamics of the HC Ir CCLGDL at a current density of 200 mA/cm^2.

Movie S3. The bubble dynamics of the dense Ir CCLGDL at 1.85 V.

Movie S4. The bubble dynamics of the HC Ir CCLGDL at 1.85 V.

Movie S5. The bubble dynamics of the Pt-NS electrode at a current density of 200 mA/cm^2.

Movie S6. The bubble dynamics of the PtNP electrode at a current density of 200 mA/cm^2.

LIST OF ABBREVIATIONS

TTLGDL	Thin/Tunable Liquid/Gas Diffusion Layer
CCLGDL	Catalyst-Coated Liquid/Gas Diffusion Layer
CCM	Catalyst-Coated Membrane
CV	Cyclic Voltammetry
SCE	Saturated Calomel Electro
RHE	Reversible Hydrogen Electrode
CFP	Carbon Fiber Paper
CL	Catalyst Layer
ESCA	The Electrochemically Surface Area
CPE	Constant Phase Element
EDS	Energy-Dispersive X-Ray Spectroscopy
EIS	Electrochemical Impedance Spectroscopy
GDE	Gas Diffusion Electrode
HAADF	High-Angle Annular Dark-Field
HER	Hydrogen Evolution Reaction
HFR	High Frequency Resistance
MPL	Microporous layer
LGDL	Liquid/Gas Diffusion Layer
LSV	Linear Sweep Voltammetry
MEA	Membrane Electrode Assembly
OA	Oxalic Acid

OER	Oxygen Evolution Reaction
PEM	Proton Exchange Membrane
PEMEC	Proton Exchange Membrane Electrolyzer Cell
PGM	Platinum Group Metal
GDL	Gas Diffusion Layer
PTL	Porous Transport Layer
HHV	High Heat Value
SEM	Scanning Electron Microscopy
SPE	Solid Polymer Electrolyte
AEM	Anion Exchange Membrane
STEM	Scanning Transmission Electron Microscopy
TEM	Transmission Electron Microscopy
XRD	X-ray diffraction
TPB	Triple-Phase Boundary
XPS	X-ray Photoelectron Spectroscopy
FFT	Fourier Transform
SGEIS	Staircase Galvano Electrochemical Impedance Spectroscopy

CHAPTER ONE

INTRODUCTION AND GENERAL INFORMATION

1.1 Overview

Hydrogen, as the efficient energy carrier in the future society, has gained increasing interest from researchers and can be applied in various applications such as transportation, agriculture, and metal refining.[1] [2] [3] However, so far, most hydrogen is produced from non-electrochemical strategies such as natural gas reforming, refinery gas reforming, and coal gasification, which can cause serious environmental issues. Developing energy conversion and storage technologies with high efficiency is a promising strategy to solve the global energy crisis and environmental pollution. Notably, a water electrolyzer, one of the most ideal alternative energy storage technologies to conventional strategies, is a device driven by electricity from regenerative and clean energy sources.[4] [5] Among various water electrolyzer devices, solid polymer electrolyte (SPE) electrolyzer cells, including proton exchange membrane (PEM) and anion exchange membrane (AEM) electrolyzer cells, have attracted extensive attention and efforts due to low-temperature operation, high current operation capacity, quick response, high energy efficiency, and high energy density, especially for the PEM electrolyzer cells (PEMECs). [6] [7] Extensive research resources and efforts have been devoted to the development of clean hydrogen since the U.S. Department of Energy (DOE) issued the first Energy Earth short, Hydrogen Shot, to reduce the cost of clean hydrogen to $1 per 1 kilogram in 1 decade ("1 1 1"). Nevertheless, the large-scale application and commercialization of water electrolyzers are impeded by high capital costs and the scarcity of platinum group metals (PGM), especially for the anode side, which involves sluggish reaction kinetics. [8] [9] [10] Hence, developing highly active and stable electrocatalysts/electrodes for water electrolyzers with high efficiency and low cost is

desired. Herein, in this dissertation, the development of tunable, advanced, and high-performance electrocatalysts/electrodes with ultrahigh material utilization and stability will be introduced in the following chapters. These studies would provide guidance for future electrocatalyst/electrode designs in practical water electrolyzers for green hydrogen production, accelerating the commercialization of low-cost and high-efficiency water electrolyzers.

1.2 Background

A solid polymer electrolyte electrolyzer cell can be separated into two parts: the anode part and the cathode part. Based on the polymer electrolyte types, the SPE electrolyzer cell can be classified into anion exchange membrane electrolyzer cells (AEMECs) and proton exchange membrane electrolyzer cells (PEMECs), respectively. [11] [12] For the AEMEC, non-precious metal-based materials can be used as electrocatalysts, which could save the catalyst cost. However, the efficiency of the AEMEC to produce hydrogen is low and the durability of the cell still does not have a proven study, and membrane degradation usually happens during cell operation. [13] [14] [15] Hence, it is still in the research and development stage. For the PEMEC, the application is wider and shows great potential to be commercialized due to its high cell efficiency, high energy density, rapid response, and easily scale-up and down. [16] [17] [18] [19] In this dissertation, more studies and efforts were performed on the PEMEC. In the middle of an SPE electrolyzer cell, the solid polymer electrolyte (membrane) is normally coated with anode and cathode catalyst layers (CLs) and then sandwiched by anode and cathode liquid/gas diffusion layers (LGDLs), forming membrane electrode assembly (MEA), which is significant to the performance and

efficiency of the cell. Notably, to develop high-performance MEAs for high-efficiency PEMECs, it is crucial to understand the working principle of the PEMEC. The related working principle is elaborated as follows: water, as the reactant, is pumped and transported through the LGDL to the interphase of the anode CL and membrane of the PEMEC. Afterward, with the electricity power as the driving force, the water would be split into protons, and electrons and then generate oxygen simultaneously. The formed oxygen would diffuse back into the channels through the anode LGDL. The protons transport through the membrane and reach the interphase of the cathode CL and membrane. Meanwhile, the electrons would go through the electric circuit and also reach the cathode reaction interphase and combine with the protons to generate hydrogen. Similarly, the formed hydrogen would diffuse back into the channels through the cathode LGDL. Hence, the middle membrane not only serves as the electrolyte but also can separate the generated oxygen and hydrogen well to avoid crossover and ensure safety.

Two types of MEAs have been reported currently, one is the conventional catalyst-coated membrane (CCM) with anode and cathode LGDLs; the other is the gas diffusion electrode combined with membrane. For the conventional CCM design, there are some limitations.[19 20 21 22] First, multiple and complex fabrication processes are needed for the CCM design. Specifically, fabricated or purchased catalyst powders are needed, which might involve harsh, expensive, and complex procedures for the fabricated ones. Subsequently, materials of catalyst powders, solvent, and ionomer are mixed together by stirring and ultrasonic to form homogenous catalyst ink. Afterward, the catalyst ink can be deposited on the membrane via spray, decal, blade, etc., which may need expensive equipment such as

ultrasonic spray. Second, the resultant CCM shows thick catalyst layers of up to dozens of micrometers, which can increase the proton and electron pathways. Third, the electrical conductivity of the CL is low due to the ionomer use. Fourth, high PGM loadings are needed to ensure performance and stability for the PEMEC, which is normally of up to 3 mg/cm^2 and increase the high capital cost. Fifth, the involved ionomer tends to degrade during the long-term operation, easily leading to the CL collapse. Furthermore, Mo et al. [23] discovered the true reaction of electrochemical water splitting and verified the importance of the triple-phase boundary (TPB). With the specially designed LGDL and the in-situ high-speed visualization, Mo et al. demonstrated that most catalysts in the CCM are underutilized due to the low electronic conductivity in the CL. The ionomer involved in the CL hinders the TPB in the CCM and thus leads to significant waste of a large portion of catalysts. Typically, the TPB should satisfy the presence of catalysts, electron/proton, and reactant/gas diffusion simultaneously. The presence of ionomer hinders the electron pathways. To improve the catalyst utilization and cut down the capital cost of the PEMEC, it is necessary to optimize the TPB. Three strategies could be used for the TPB optimization: 1. Improving the electron/proton conductivity; 2. Maximizing accessible active sites; 3. Enhancing mass transport properties. A novel, advanced, and ionomer-free gas diffusion electrode (GDE) design, directly depositing the catalysts on gas diffusion layers rather than the membrane, could improve the TPB. The properties of the ionomer-free CL in the GDE design could be engineered by tuning the fabrication strategies, including nanostructure, morphology, phase, and composition. Hence, the GDE design could efficiently optimize TPB to improve the catalyst utilization and significantly decrease the PGM catalyst loading simultaneously.

Based on the Overview and above discussed, it is significant to improve the efficiency and cut down the capital cost of PEMECs to accelerate its large-scale application and commercialization. The novel GDE design is one of the efficient strategies to decrease capital cost and improve efficiency with higher catalyst utilization and superior performances. Hence, this research mainly focuses on novel GDE designs with facile and efficient fabrication processes and tunable CLs of nanostructure, morphology, and composition control.

Firstly, some efforts were made to develop high-performance Ir-integrated electrodes with significantly simplified fabrication processes. Efficient electrode fabrication processes with low cost and sustainability play crucial roles in boosting the commercialization of the PEMEC. As mentioned above, complex electrode fabrication processes with low efficiency and expensive equipment are needed for the conventional CCM. To avoid these disadvantages, facile fabrication processes with high efficiency and easy scalability are desired for electrode development. In this research, instead of using the complicated electrode fabrication procedures involved in the CCM, simplified electrode fabrication strategies such as facile electrodeposition, and low-temperature wet chemical method were developed to fabricate integrated electrodes with high activity and stability. So far, several studies have been reported to develop electrodes with simplified fabrication processes, including electrodeposition, sputtering and other strategies. For example, Choe *et al.* [24] electrodeposited IrO_2 catalysts on the Ti mesh substrate with a loading of 0.4 mg/cm^2 to an ionomer-free GDE design, showing improved performance and stability compared to an ionomer-containing IrO_2 GDE. With a fast and facile electrodeposition process, Yu *et al.*

[25] fabricated various anode electrodes of Ir catalyst-coated TTLGLDs with different loadings for the PEMEC, achieving significantly improved catalyst utilization and reaction kinetics. Jeong *et al.* [26] combined a Ni electrodeposition process with a galvanic replacement to prepare Ir-based GDEs to serve as anode electrodes for the PEMEC. Apart from the electrodeposition method, physical vapor deposition (e.g. sputtering) is another efficient strategy to prepare electrodes with simplified fabrication processes. For example, Slavcheva *et al.* [27] deposited iridium oxide films on the carbon paper substrate via magnetron sputtering to serve as anode for the PEMEC, which not only shows a simplified fabrication process but also significantly decreased the catalyst loading. Liu *et al.* [28] also sputtered iridium on the Ti felt with different loadings to form porous transport electrodes as anodes for the PEMEC. Apart from the anode fabrication, the sputtering technique was also used to prepare cathode electrodes in the PEM water electrolyzer. For example, Mo *et al.* [23] and Kang *et al.* [29] also adopted the one-step sputtering method to deposit platinum nanoparticles on TTLGDLs to achieve enhanced electronic conductivity, significantly reduced catalyst loading, and improved catalyst utilization. Notably, compared to the physical vapor deposition such as sputtering, the electrodeposition method is preferred due to the easier scalability of the electrode fabrication and more tunable parameters to control the properties of the catalysts such as nanostructures, phases, and compositions.

Secondly, efforts and studies were carried out to prepare some nanostructured catalyst layers. Compared to nanoparticle-like or film-like CLs with dense structures, nanostructured CLs could optimize the TPB to achieve improved performance. Specifically, the nanostructured CL could improve the catalytic activity by exposing

abundant active sites for the electrochemical reaction. Additionally, multiphase transport properties of favorable water diffusion and gas detachment could be achieved with the nanostructured CL. Currently, abundant studies verified that micro/nano structures with rough surfaces achieve favorable bubble detachment due to reduced bubble contact area and weaker bubble adhesive force on the micro/nanostructures. As a result, smaller bubbles are removed from the nanostructured electrode surface quickly. For example, Li *et al.* [30] demonstrated that pine-shaped Pt nanoarray with an electrodeposition process presented an underwater superaerophobicity, revealing smaller bubble adhesive forces and higher bubble contact angles compared to those of electrodes with nanosphere and flat structures. Additionally, with the fabricated honeycomb-based films, Kamei *et al.* [31] discovered faster bubble removal due to larger bubble contact angles and lower adhesion forces compared to those of flat surfaces. Lu *et al.* [32] reported that underwater superaerophobic surfaces are achieved on the nanostructured MoS_2 electrode, contributing to fast bubble detachment with smaller bubble sizes. Under a current density of 100 mA/cm^2, Xie *et al.* [33] compared the bubble dynamic of the Pt nanowire-structured electrode and Pt nanoparticle-based electrode and verified a smaller bubble detachment range achieved for the nanostructured Pt electrode. Additionally, superior performance is also demonstrated by the Pt nanowire-structured electrode due to the high surface area exposing rich active sites.

Due to the advantages of the nanostructures, so far, some works have been reported to design and develop nanostructured CL-based GDEs for the PEMEC. For example, Lim *et al.* [34] electrodeposited IrO_2 on hemispherical Pt particles to form Pt@IrO_2 core-shell structured anodes with a total PGM loading of 0.43 mg/cm^2 on the Ti felt substrate,

showing improved cell performances than electrodeposited IrO_2 anode without Pt support. Kim et al. [35] prepared dendritic Au-supported Ir by choosing dendritic Au as the support and following by a pulse deposition to deposit Ir, which tuned the Ir electronic structure to improve intrinsic OER activity and enhance catalyst utilization, conductivity and mass transfer. Yasutake *et al.* [36] used NaOH etching to achieve nanostructured porous transport layer (PTL) and then deposited Ru and Ir, with arc plasma deposition, respectively to prepare Ru-core Ir-shell catalyst nanostructures. However, these studies focus on the substrate modification to achieve the nanostructured CLs, which are complex, and the nanostructures of the CLs are highly dependent on the substrate morphology. Moreover, some of them involved noble metal use such as Pt and Au, which increase the capital cost of the PEMEC. It is desired to fabricate nanostructured CLs directly without substrate morphology assistance, which could be more efficient and tunable. Currently, there are only a few related studies reported. For example, Xie *et al.* [33] prepared well-aligned Pt nanowires with a thin thickness of about 5 nm on TTLGDL *via* a room-temperature wet chemical method for HER in the PEMEC, demonstrating significantly improved performance compared to the sputtered Pt nanoparticles. However, almost no nanostructured anode GDEs have been reported in the PEMEC so far, which needs more attention and effort due to the multiple electrons involved reaction and sluggish kinetics. Studies and investigations were conducted in this research to achieve nanostructured CLs with high material utilization and stability for the PEMEC.

1.3 Objectives

The objective of this research is to develop novel, advanced, and high-performance electrodes with tunable nanostructures, morphologies, and compositions in water electrolyzer cells for hydrogen production with high efficiency and low cost. The following shows the main studies: (a) Developing bifunctional NiFeW electrocatalysts via facile electrodeposition for alkaline water electrolysis. (b) Developing W-induced fine NiFeW nanosheets with different W doping concentrations for highly efficient water splitting. (c) Developing Ir-integrated electrodes for high-efficiency PEM water electrolyzers with high current operation capacity. (d) Developing highly porous Ir with fine honeycomb catalyst layers for low-cost and high-efficiency water electrolyzer. (e) Developing nanoporous Ir nanosheets with impressive performance for green hydrogen production via PEM water electrolyzers. (f) Developing ultrathin Pt nanosheets with ultralow loadings via efficient and scalable electrodeposition process as PEM water electrolyzer cathodes.

CHAPTER TWO

CONSTRUCTING ULTRATHIN W-DOPED NIFE NANOSHEETS VIA FACILE ELECTROSYNTHESIS AS BIFUNCTIONAL ELECTROCATALYSTS FOR EFFICIENT WATER SPLITTING

A version of this chapter was originally published as:

Ding, L., Li K., Xie Z., Yang G., Yu S., Wang W., Yu H., Baxter J., Meyer III H. M., Cullen D.A., Zhang, F-Y.,

Constructing Ultrathin W-doped NiFe Nanosheets via Facile Electrosynthesis as Bifunctional Electrocatalysts for Efficient Water Splitting, ACS Applied Materials & Interfaces 13, no. 17 (2021): 20070-20080.

CRediT authorship contribution statement

Lei Ding: Electrocatalyst Fabrication, Electrochemical Measurements, Data Analysis, SEM, EDS, and XRD Characterizations, Original Draft Writing, Writing-Reviewing and Editing. Kui Li: SEM Characterization, Electrochemical Measurements, Data Analysis, Writing-Reviewing and Editing. Zhiqiang Xie: SEM and EDS Characterizations, Data Analysis, Writing-Reviewing and Editing. Gaoqiang Yang: Electrochemical Measurements, Data Analysis, Writing-Reviewing and Editing. Shule Yu: SEM and EDS Characterizations, Writing-Reviewing and Editing. Weitian Wang: Measurements, Data Analysis, Visualizations, Writing-Reviewing and Editing. Haoran Yu: STEM, EDS, and TEM Characterizations, Writing-Reviewing and Editing. Jefferey Baxter: STEM and EDS Characterizations, Writing-Reviewing and Editing. Harry M. Meyer III: X-ray Photoelectron Spectroscopy (XPS) Measurements, Writing-Reviewing and Editing. David A. Cullen: Study Design, Writing- Reviewing and Editing, Supervision. Feng-Yuan Zhang: Idea Conception, Writing-Reviewing and Editing, Supervision.

I am fully responsible for the work submitted in the publication.

2.1 Abstract

Exploring cost-effective and efficient bifunctional electrocatalysts via simple fabrication strategies is strongly desired for practical water splitting. Herein, an easy and fast one-step electrodeposition process is developed to fabricate W-doped NiFe (NiFeW) layered double hydroxides with ultrathin nanosheet features at room temperature and ambient pressure as bifunctional catalysts for water splitting. Notably, the NiFeW nanosheets require overpotentials of only 239 mV and 115 mV for the oxygen evolution reaction (OER) and hydrogen evolution reaction (HER), respectively, to reach a current density of 10 mA/cm^2 in alkaline media. Their exceptional performance is further demonstrated in a full electrolyzer configuration with the NiFeW as both anode and cathode catalysts, which achieves a low cell voltage of 1.59 V at 10 mA/cm^2, 110 mV lower than that of the commercial IrO_2 (anode) and Pt (cathode) catalysts. Moreover, the NiFeW nanosheets are superior to various recently reported bifunctional electrocatalysts. Such remarkable performances are mainly ascribed to W doping, which not only effectively modulates the electrocatalyst morphology but also engineers the electronic structure of NiFe hydroxides to boost charge transfer kinetics for both the OER and HER. Hence, the ultrathin NiFeW nanosheets with an efficient fabrication strategy are promising as bifunctional electrodes for alkaline water electrolyzers.

2.2 Introduction

Water splitting utilizing clean and renewable energy sources is one of the most effective approaches to generate high purity hydrogen. [37] [38] [39] [40] [41] It is known that the anodic oxygen evolution reaction (OER) and cathodic hydrogen evolution reaction (HER) are involved in water splitting. [42] [23] [43] [44] Notably, the OER is kinetically slow and has been identified as the main challenge for large-scale commercial water splitting since a multistep proton-coupled electron transfer is involved and a high kinetic barrier has to be overcome. [45] [46] Currently, platinum group metals (PGMs) are recognized as state-of-the-art electrocatalysts for water splitting, e.g. Pt-based composites toward the HER and Ir-/Ru-based composites for the OER. [47] [48] Unfortunately, single function, high cost, and reserve scarcity of these precious metals hamper widespread practical application of water splitting. Therefore, cost-effective non-precious metal catalysts with high catalytic activity are highly desired to decrease the energy barrier and boost the energy conversion efficiency for water splitting, especially for alkaline water splitting, for which some of the non-precious metal catalysts even surpass the state-of-the-art catalysts. [37] [49]

Performing the HER and OER processes in the same solution and applying bifunctional electrocatalysts is significant, which could not only simplify fabrication procedure but also reduce total cost. [50] [51] To date, transition metal-based materials have been largely investigated as valid bifunctional electrocatalysts for alkaline water splitting, such as Ni, Fe, and Co, because of low cost, sustainability, and easy availability. [52] [53] Moreover, in alkaline conditions, they exhibit high catalytic performance and outstanding stability. Practically, NiFe catalysts exhibit great potential as bifunctional electrocatalysts in alkaline

solutions. Because they show remarkable OER activity and moderate HER performance in alkaline media. [54] Furthermore, recent reports have demonstrated that foreign element doping can modulate the morphological and/or electronic structures of the NiFe catalysts, which exhibit the potential to provide multiple electrocatalytically active sites and thus enhance the electrocatalytic activity of the pristine catalysts. By now, various dopants (V, Cr, Co, etc.) in NiFe catalysts have been reported to form ternary layered double hydroxides (LDH) electrocatalysts to achieve enhanced HER and/or OER performances compared to the binary NiFe LDH. However, the above ternary LDH electrocatalysts are difficult to be extended to practical industrial application because of high-cost and complicated fabrication process (high pressure, high temperature, or long synthesis time), and thus low efficiency for large-scale water splitting application. Hence, it is urgent to explore cost-effective and simple strategies to synthesize electrocatalysts with high activity for commercial water splitting. Notably, as an earth-abundant transition metal, tungsten has been verified to show optimum adsorption energy for hydrogen intermediates (*H) and thus can boost the combination of *H to form H_2 in the HER. [55] [56] Also, some tungsten-based OER electrocatalysts have been reported, demonstrating that tungsten with high valance exhibits strong electron capture affinity and thus could reduce kinetic barriers in the OER. [57] [58] Hence, tungsten doping is expected to considerably enhance the OER and HER performances of NiFe catalysts, which would contribute to bifunctional electrocatalysts with high activity for alkaline water splitting.

To explore the expression of high catalytic performance, *in-situ* growth of electrocatalysts on a conductive substrate is an efficient fabrication way. Electrocatalysts fabricated *via* this

strategy generally exhibit enhanced structural stability and better conductivity compared to other methods. [59] Besides high catalytic activity, a cost-effective synthesis approach is also a crucial factor for large-scale practical application of electrocatalysts. Compared to other methods, electrodeposition exhibits several merits including room-temperature and ambient-condition fabrication, short deposition time, and controllable deposition of electrocatalysts. [60] Hence, electrodeposition shows great potential to be scaled up in industry to prepare catalysts for practical water splitting, boosting wide commercialization of water splitting. On the other hand, carbon paper (CP), a commonly used conductive substrate, shows a high conductivity and excellent corrosion resistance in alkaline media. [61] Additionally, carbon paper exhibits good mass transport and outstanding mechanical properties, which has been widely used as a gas diffusion layer in water electrolyzers. [62] *In-situ* growth of electrocatalysts on CP offers the fabricated electrodes with two main advantages. One is dramatically increasing the electrocatalysts' surface area to expose more reaction active sites, benefiting the electrolyte penetration and boosting the formation and overflow of the gas bubbles, the other one is effectively reducing charge transfer resistance due to CP's long-range conducting networks. [63]

Based on the above idea and consideration, for the first time, we fabricate W-doped NiFe layered double hydroxide nanosheets on carbon paper (NiFeW/CP) *via* a simple and fast electrodeposition process at room temperature, which could be used as a high-efficiency bifunctional electrocatalyst for overall water splitting in alkaline media. Due to the well-aligned ultrathin nanosheets and engineered electronic structures from W doping, the as-formed NiFeW electrocatalyst exhibits superior electrochemical performances. As a result,

only 239 mV overpotential for the OER and 115 mV overpotential for the HER is required at 10 mA/cm^2 in 1 M KOH. Moreover, the ultrathin NiFeW nanosheets show a low cell voltage of 1.59 V (j=10 mA/cm^2) with outstanding electrochemical stability when used as a bifunctional electrocatalyst for overall water splitting.

2.3 Experimental section

2.3.1 Materials and chemicals

Nickel sulfate hexahydrate ($NiSO_4 \cdot 6H_2O$), ferrous sulfate heptahydrate ($FeSO_4 \cdot 7H_2O$), sodium tungstate dihydrate ($Na_2WO_4 \cdot 2H_2O$), and saccharin were purchased from Sigma-Aldrich. Boric acid (H_3BO_3) was purchased from Showa. The above chemical reagents were used as electrolyte components for electrodeposition of tungsten doped nickel-iron layered double hydroxides. Potassium hydroxide and potassium chloride were purchased from Riedel. Iridium dioxide (IrO_2) and Pt were purchased from Alfa-Aesar. Deionized (DI) water was used throughout the experimental processes.

2.3.2 Preparation of NiFe/CP and NiFeW/CP

NiFeW/CP (loading amount: ~0.8 mg/cm^2, W precursor dosage: 5 mM) was fabricated via an electrodeposition process in a three-electrode system. The carbon paper, graphite rod, and Ag/AgCl electrode (1 M KCl) were used as the working electrode, counter electrode, and reference electrode, respectively. Before the electrodeposition, carbon paper was cut into 2.5 × 0.5 cm in size and cleaned in nitric acid for 30 min, followed by sonication in methanol and deionized water for 15 min, respectively. Typically, 45 mM $NiSO_4 \cdot 6H_2O$, 7.5 mM $FeSO_4 \cdot 7H_2O$, and 5 mM $Na_2WO_4 \cdot 2H_2O$ were dissolved in 20 mL DI water as

electrolyte, which also contained 40 g L^{-1} boric acid and 1g L^{-1} saccharin. The electrodeposition was performed under an applied potential of -1.0 V (vs. Ag/AgCl) for 1 hour. Afterward, the resultant sample was carefully withdrawn from the electrolyte, rinsed with DI water, and dried in air.

2.3.3 Characterizations

The morphologies and compositions of the electrocatalysts were characterized by a field emission JEOL JSM-6320F SEM and Hitachi HF3300 TEM/ STEM with energy-dispersive X-ray spectroscopy (EDS). X-ray photoelectron spectroscopy (XPS) experiments were conducted using a Thermo Scientific K-Alpha XPS instrument equipped with a hemispherical electron energy analyzer and a monochromatic Al Ka x-ray source.

2.3.4 Electrochemical measurements

All electrochemical measurements were conducted on a potentiostat VSP/VMP3B-100 (Bio-Logic) at room temperature in 1 M KOH electrolyte. The OER and HER tests were performed in a conventional three-electrode system in which the as-fabricated NiFeW/CP (working area: ~ 1 cm^2) as the working electrode, a graphite rod as the counter electrode, and a saturated calomel electrode as the reference electrode, respectively.

Before the measurements, the calibration of the saturated calomel electrode was carried out in a three-electrode system with Pt wire used as the working electrode, Pt foil used as the counter electrode, and the saturated calomel electrode used as the reference electrode with H_2-saturated. When testing, 10 times of cyclic voltammetry (CV) were performed at a scan rate of 100 mV/s to condition the system and reach a stable current density. After the

conditioning, the linear sweep voltammetry (LSV) polarization curves were recorded at a scan rate of 5 mV/s from high to low potentials for the OER to avoid possible interferences of the oxidation peak with the OER onset. Also, the HER LSV curves were recorded from low to high potentials to avoid the reduction peak with the HER onset.

The electrochemical impedance measurements for the OER and HER were performed at the potential of 1.44 V (vs. RHE) and -0.15 V (vs. RHE), respectively from 200 kHz to 50 mHz with an amplitude of 10 mV. And then, Z-view software was used to fit the equivalent circuit with experimental EIS data. The polarization curves were iR-corrected to exclude the ohmic resistance of the solution. The recorded potentials were calibrated to reversible hydrogen electrode (RHE) via Nernst equation: $E_{RHE} = E_{SCE} + 0.243\ V + 0.0591 \times pH$. The overpotentials for the OER and HER can be evaluated with equation $\eta = E_{RHE} - 1.23\ V$ and $\eta = E_{RHE} - 0$, respectively.

Tafel slopes can be obtained via plotting overpotential η vs. logarithm of current density based on polarization curves. Moreover, a galvanostatic measurement at a fixed current density of 10 mA/cm^2 or -10 mA/cm^2 was carried out at room temperature to study the stability of NiFeW/CP for the OER and HER tests.

The electrochemically surface area (ESCA) was studied based on the double-layer capacitance (C_{dl}). Briefly, static CVs are recorded at non-faradaic regions at different sweep rates of 10, 20, 40, 60, 80, and 100 mV/s from -0.15 to -0.05 V (vs. SCE). By plotting capacitive current ($j_{anodic} - j_{cathodic}$) at -0.1 V (vs. RHE) against the scan rate, a linear trend was obtained, and the slope is the double-layer capacitance (C_{dl}).

Overall water splitting tests were conducted in a homemade two-electrode system with the NiFeW/CP as both the cathode and anode. The mass loading was calculated to be 0.8 mg/cm^2. For the benchmark precious-metal-based catalysts, IrO_2/CP||Pt/CP was fabricated with the same mass loading as NiFeW/CP. To specify, for the cathode, 0.802 mg of IrO_2 was dispersed in 250 µL isopropanol and 25 µL 5% Nafion; then, 35 µL of the suspension was coated on carbon paper (1 cm × 0.5 cm). Notably, the preparation of the IrO_2 electrode was via depositing IrO_2 ink on a CP support and then was protected by a polymer binder (Nafion). The process to prepare the anode is similar except for the use of Pt (0.796 mg/cm^2) instead of IrO_2. The LSV curves were conducted in 1 M KOH at a scan rate of 5 mV/s within 1.0-1.9 V (vs. RHE). The long-term durability was investigated in chronopotentiometry test at a current density of 10 mA/cm^2.

2.4 Results and Discussions

2.4.1 Characterizations of NiFeW Nanosheets

As schematically shown in **Figure 1**, W-doped NiFe vertically aligned nanosheets are *in-situ* grown on carbon paper (NiFeW/CP) substrate using a simple and fast one-step electrodeposition process at room temperature (experimental details in the Supporting Information (SI)). Briefly, cathodic electrodeposition is conducted at -1.0 V vs. Ag/AgCl (1 M KCl) in an electrolyte containing Ni^{2+}, Fe^{3+}, and W^{6+} ions for 1 h, forming grey colored NiFeW layered double hydroxide nanosheets on carbon paper (CP) substrate (**Figure 8**). As a result, the well-aligned W-doped NiFe nanosheets can be served as bifunctional electrocatalysts for efficient alkaline water splitting. From **Figure 9A, B**, we can observe that bare CP shows a quite smooth surface with a diameter of around 10 µm.

After the electrodeposition process, abundant vertically well-defined nanosheets with an average thickness of about 5.2 nm are grown on the surface of CP (**Figure 2A, B**), which could offer a large surface area and expose numerous electrochemically active sites. Moreover, as shown in the SEM image with lower magnification (**Figure 9 C**), the good uniformity of NiFeW nanosheets on the CP can be observed. For comparison, an electrocatalyst of NiFe/CP is also prepared in the absence of W, showing film-like features (**Figure 10**). To further investigate the morphology of the electrocatalysts, the well-defined NiFeW nanosheets are peeled off from the CP substrate by sonicating in isopropanol and characterized with TEM. The well-defined nanosheet features of the NiFeW/CP electrocatalyst are further confirmed in the TEM image (**Figure 2C**), in which we could observe that the nanosheets are nearly transparent owing to their ultrathin thickness (~5.2 nm), and this can effectively promote charge transfer. [63] The TEM image with higher resolution (**Figure 2D**) exhibits that the nanosheets compose of crystalline phases with good lattice fringes (separated by green-dotted lines) and amorphous-looking phases (separated by yellow-dotted lines). Notably, the amorphous-looking phases show the potential to expose more active sites owing to abundant randomly oriented bonds and more dense unsaturated sites, which could boost the adsorption of reactants.[50] Additionally, the XRD results of NiFeW/CP, NiFe/CP, and carbon paper are shown in **Figure 11**, and strong characteristic peaks of carbon paper are detected in all three electrocatalysts. However, because of the low contents of NiFe hydroxides and NiFeW nanosheets compared to that of carbon paper and the strong carbon paper peaks, the NiFe and NiFeW crystalline phases cannot be observed in the XRD patterns. To further demonstrate the successful W doping and elemental distribution in the NiFeW nanosheets, scanning TEM (STEM) equipped

with energy dispersive X-ray spectrometer (EDS) is applied to gain more structural information. As shown in **Figure 2E**, apart from elements of Ni, Fe, and O are detected in the nanosheet structures, W element with an atomic ratio of 3.74 is also homogeneously distributed in the structures (**Table 1**). Hence, the above results demonstrate the successful uniform doping of W species into NiFe hydroxides.

To investigate the elemental composition and valence states of the NiFeW/CP nanosheets, XPS characterization is performed. As revealed with XPS full survey in **Figure 3A**, elements of Ni, Fe, W, O, and C are detected in the NiFeW/CP nanosheets, which is in good agreement with the STEM-EDS results (**Figure 2E**). Also, the NiFe/CP electrocatalyst is used as a reference and related high-resolution XPS results are shown in **Figure 3**. For Ni2p spectra (**Figure 3B**), two peaks at 855.6 eV and 873.3 eV ascribed to the Ni $2p_{3/2}$ and Ni $2p_{1/2}$ are observed, along with two satellite peaks. As reported in previous work, these peaks correspond to Ni^{2+} in $Ni(OH)_2$. [64] [65] In the Fe 2p XPS spectra, two binding energies of Fe $2p_{1/2}$ and Fe $2p_{3/2}$ are detected, which are attributed to Fe^{3+} in $Fe(OH)_3$ (**Figure 3C**). [66] Even though there is no difference detected for the Ni 2p spectra when comparing the valence states of Ni between the NiFe/CP and NiFeW/CP, Fe binding energies show a negative shift about 0.3 eV after W doping, demonstrating that the electronic environment of Fe sites is well modulated. For the high-resolution W4f spectra (**Figure 3D**), two typical peaks at 34.9 eV and 37.1 eV are observed, assigned to W $4f_{7/2}$ and W $4f_{5/2}$, respectively, implying the doped W species is in the W^{6+} state. [55]

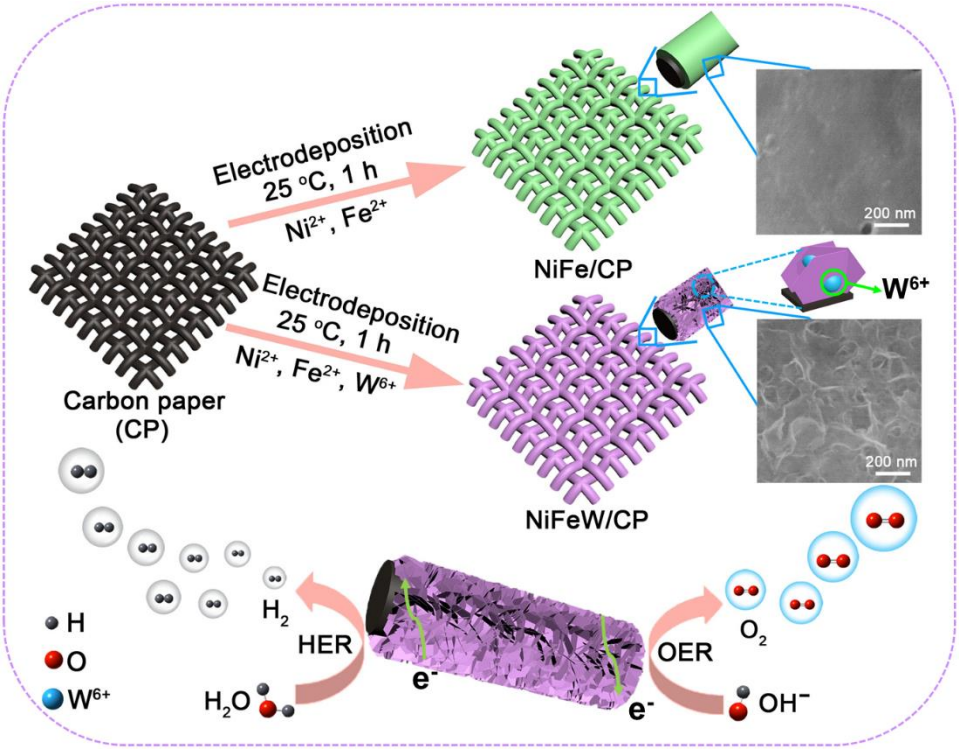


Figure 1. One-step fabrication of the NiFeW/CP as a bifunctional electrocatalyst for efficient alkaline water splitting. For comparison, the NiFe/CP is also prepared.

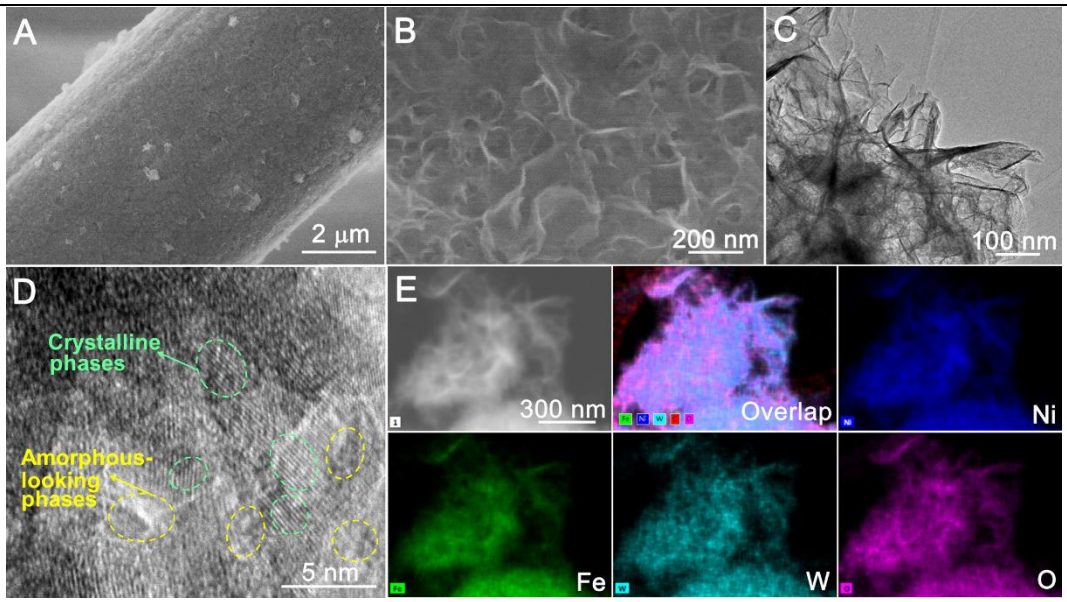


Figure 2 (A, B) SEM (C, D) TEM, and (E) STEM-EDS images of morphology and elemental distribution of the NiFeW/CP.

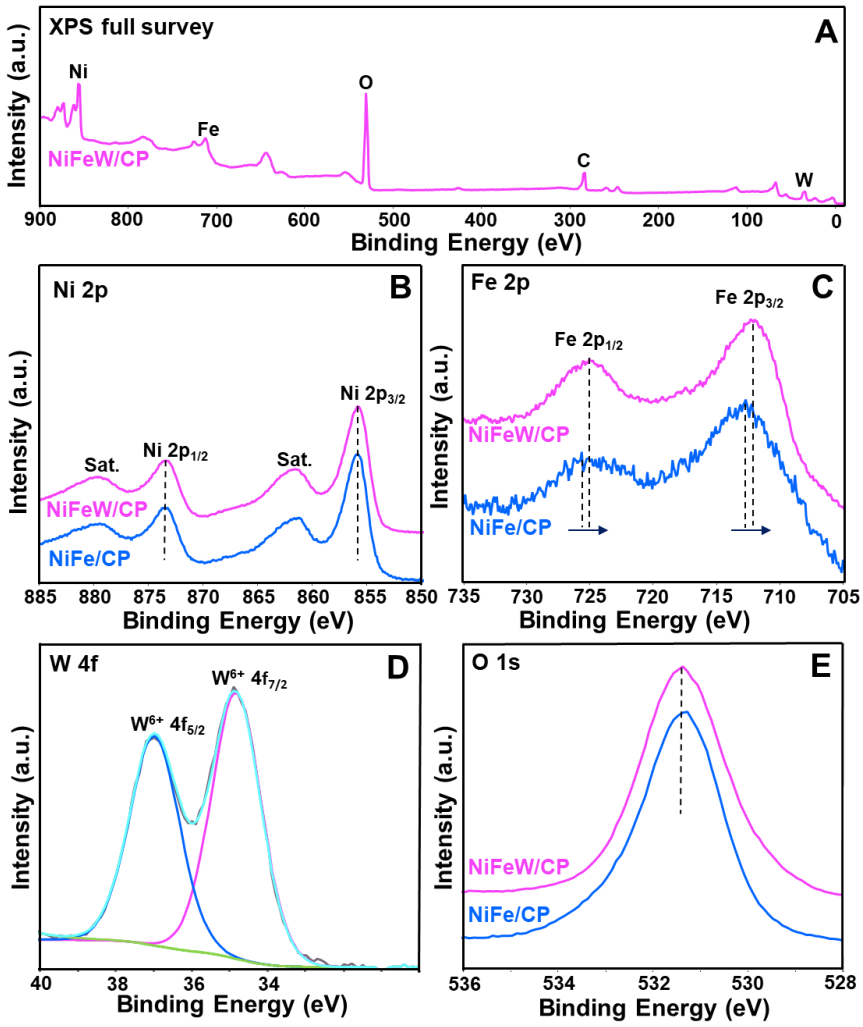


Figure 3 (A) The XPS full survey of the NiFeW/CP, the high-resolution XPS of (B) Ni, (C) Fe, and (E) O in the NiFe/CP and NiFeW/CP electrocatalysts. (D) The XPS spectra of W in the NiFeW/CP electrocatalyst.

The O spectra for both NiFe/CP and NiFeW/CP electrocatalysts show a peak at 531.2 eV, which is assigned to Ni-OH and Fe-OH (**Figure 3E**). [66] This further demonstrates that the fabricated electrodes are composed of NiFe based hydroxides, which have been extensively explored as efficient electrocatalysts for alkaline OER. [67]

2.5 Electrocatalytic performances

The OER and HER activities of the as-fabricated electrocatalysts are first explored in a three-electrode configuration with Ar-saturated 1 M KOH (experimental details in the SI). For comparison, the commercial IrO_2 and Pt are deposited on the CP substrate to form IrO_2/CP and Pt/CP, respectively, along with the pristine CP substrate, the three samples are also tested under the same conditions. Notably, an oxidation peak and a reduction peak of Ni species can be detected when performing a CV scan (**Figure 12**), which have also been reported in some related publications. [48] [49] For example, Batchellor et al. [49] investigated geometric and intrinsic OER activities of Ni(Fe)OOH films based on different mass loadings. They verified that the Ni^{2+} is oxidized to a Ni^{3+} or Ni^{4+} with an oxidation peak observed when the electrode is swept anodically. While with a cathodic sweep, the Ni^{3+} or Ni^{4+} is reduced to the Ni^{2+}, and a reduction peak is detected. Hence, to avoid the interferences of the oxidation peak with the OER onset, the OER LSV curves from high to low potentials are used in this study to evaluate the OER performance. Likewise, the HER LSV curves are recorded from low to high potentials to avoid the reduction peak with the HER onset. As shown in the OER polarization curves (**Figure 4A**), the NiFeW/CP electrocatalyst requires a low onset overpotential of 207 mV, which is much less than that of NiFe/CP (233 mV) and IrO_2/CP (306 mV). To better understand the electrocatalytic

kinetics of the catalysts, corresponding Tafel slopes are evaluated based on the polarization curves (Figure 4B). The Tafel slope of the NiFeW/CP electrocatalyst is 36 mV/dec, lower than that of NiFe/CP (41 mV/dec) and IrO_2/CP (80 mV/dec), indicating superior activity and fast kinetic property of the NiFeW/CP electrocatalyst during the OER process. Notably, the Tafel slope of the NiFeW/CP electrocatalyst is between 30 mV/dec and 40 mV/dec, which implies the second step in the OER process ($*HO \rightarrow *O + H^+ + e^-$) that determines the reaction rate. [49] Furthermore, overpotential to operate at a current density of 10 mA/cm^2 is also a critical parameter for electrochemical water splitting, because solar-light-coupled water splitting configuration usually works at 10 mA/cm^2 under a standard condition of 1 Sun illumination, AM 1.5.[37, 68] Among different electrocatalysts, the NiFeW/CP nanosheets exhibit the best OER activity and demand only a low overpotential of 239 mV to operate 10 mA/cm^2. In contrast, the NiFe/CP and IrO_2/CP show an inferior OER performance with 270 mV and 379 mV overpotentials, respectively (**Figure 4C**). Meanwhile, overpotentials at 30 mA/cm^2 for these electrocatalysts display a similar tendency. Moreover, to compare the OER performance of the as-formed NiFeW/CP electrocatalyst with recently reported electrocatalysts, an OER activity comparison summary has been collected, as shown in **Figure 4D and Table 2**. We can conclude that the NiFeW/CP electrocatalyst surpasses most of the recently reported electrocatalysts in alkaline media.

Meanwhile, electrochemical impedance spectroscopy (EIS) measurements are conducted to explore kinetics on the surface of the electrodes. As shown in **Figure 4E**, the Nyquist plots are presented and fitted with an appropriate equivalent circuit model, which contains

three resistors (R_s, R_1, and R_{ct}) along with two constant phase elements (Q_1, Q_{ct}), where R_s reveals the solution resistance, R_1 and Q_1 are ascribed to the interfacial transport impedance, R_{ct} and Q_{ct} reflect the charge transfer resistance at the interface between the electrodes and the electrolyte. [69] As summarized in **Table 3**, with W doping, the value of charge-transfer resistance (R_{ct}) of the NiFe/CP significantly drops from 9.4 $\Omega \cdot cm^2$ to 1.3 $\Omega \cdot cm^2$, highlighting that the accelerated faradaic possess and superior OER kinetics of the NiFeW/CP electrocatalyst. Apart from the electrochemical performance, stability is also a vital criterion to evaluate the activity of electrocatalysts. In the present work, the NiFeW/CP nanosheets are evaluated in 1 M KOH by chronopotentiometry measurements at two current densities of 10 mA/cm^2 and 100 mA/cm^2 at room temperature to examine the OER stability. As presented in **Figure 4F**, the potential of NiFeW/CP is very stable and maintains at 1.47 V with neglected loss (~0.4 %) at 10 mA/cm^2 after 15 h durability testing, while an acceptable degradation occurs for the one tested at 100 mA/cm^2, indicating remarkable stability of the NiFeW/CP nanosheets during the OER process.

With a scan rate of 5 mV/s, HER polarization curves of different electrocatalysts are recorded in 1 M KOH. As shown in **Figure 5A**, the NiFeW/CP electrocatalyst exhibits a low onset overpotential of 30 mV to reach -1 mA/cm^2, which is much lower than that of NiFe/CP (105 mV) and close to that of Pt/CP (26 mV). Calculated Tafel slopes also show a similar trend (**Figure 5B**), the NiFeW/CP electrocatalyst exhibits superior HER kinetics with a Tafel slope of 113 mV/dec, clearly better than that of NiFe/CP (130 mV/dec). The modest Tafel slope of the NiFe/CP implies the Volmer-Heyrovsky step of the HER process, where the Volmer process ($H_2O + e^- \rightarrow H^* + HO^-$) is the rate-determining step.

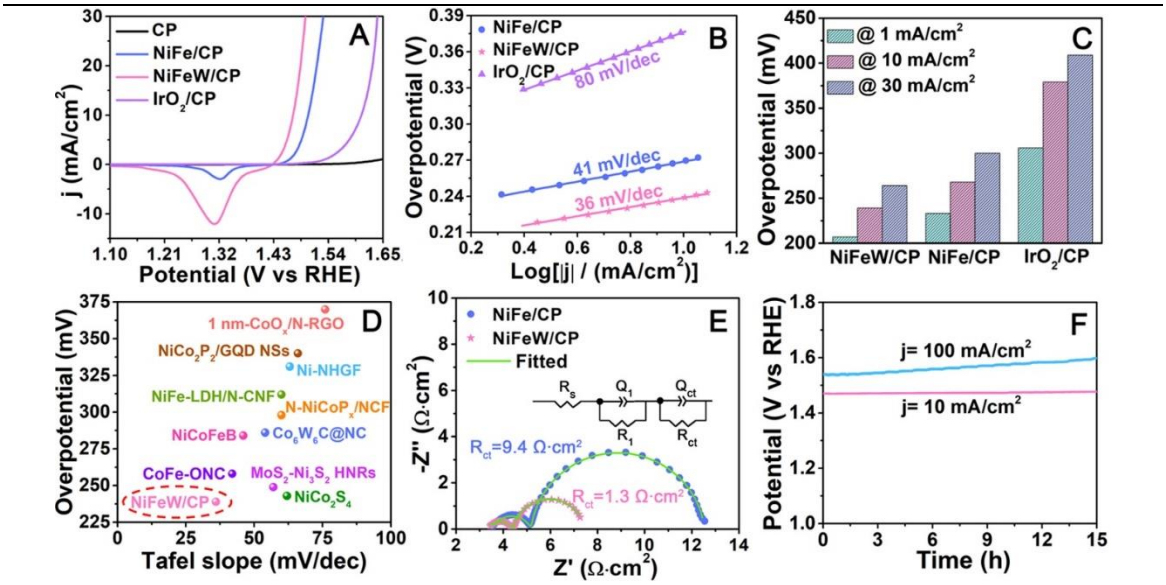


Figure 4 (A) The OER polarization curves with *iR* correction of the NiFeW/CP, NiFe/CP, CP, and the commercial IrO_2/CP in 1 M KOH at 5.0 mV/s and (B) The related Tafel slopes. (C) OER overpotentials of different electrocatalysts at 1 mA/cm^2, 10 mA/cm^2, and 30 mA/cm^2. (D) Comparison overpotential at 10 mA/cm^2 with previous reported OER electrocatalysts in 1 M KOH. (E) Nyquist plots of the NiFeW/CP and NiFe/CP (recorded at 1.44 V (vs. RHE)) and the corresponding fitted Nyquist plots; Inset: the equivalent circuit model. (F) Chronopotentiometry measurements of the NiFeW/CP electrocatalyst at 10 mA/cm^2 and 100 mA/cm^2 in 1 M KOH at room temperature (Ar-saturated).

Likewise, based on the HER polarization curves, the overpotentials of these electrocatalysts to drive -1, -10, and -30 mA/cm^2 are summarized in **Figure 5C**. A small overpotential of 115 mV is required for the NiFeW/CP electrocatalyst to drive -10 mA/cm^2, much less than that of NiFe/CP (228 mV). These results indicate that the W doping greatly enhances the HER activity, and the fabricated NiFeW/CP is a promising cathode electrode for alkaline water electrolyzers. Such superior performance outperforms most of the recently reported non-precious HER electrocatalysts (**Figure 13 and Table 4**). [80-88] Also, overpotentials of the NiFe/CP and NiFeW/CP at -30 mA/cm^2 show a similar tendency compared to those at -1 mA/cm^2 and -10 mA/cm^2, and a modest overpotential of 166 mV is needed to deliver -30 mA/cm^2 for the NiFeW/CP electrocatalyst.

With a scan rate of 5 mV/s, HER polarization curves of different electrocatalysts are recorded in 1 M KOH. As shown in **Figure 5A**, the NiFeW/CP electrocatalyst exhibits a low onset overpotential of 30 mV to reach -1 mA/cm^2, which is much lower than that of NiFe/CP (105 mV) and close to that of Pt/CP (26 mV). Calculated Tafel slopes also show a similar trend (**Figure 5B**), the NiFeW/CP electrocatalyst exhibits superior HER kinetics with a Tafel slope of 113 mV/dec, clearly better than that of NiFe/CP (130 mV/dec). The modest Tafel slope of the NiFe/CP implies the Volmer-Heyrovsky step of the HER process, where the Volmer process ($H_2O + e^- \rightarrow H^* + HO^-$) is the rate-determining step. Likewise, based on the HER polarization curves, the overpotentials of these electrocatalysts to drive -1, -10, and -30 mA/cm^2 are summarized in **Figure 5C**. A small overpotential of 115 mV is required for the NiFeW/CP electrocatalyst to drive -10 mA/cm^2, much less than that of NiFe/CP (228 mV). These results indicate that the W doping greatly enhances the HER

activity, and the fabricated NiFeW/CP is a promising cathode electrode for alkaline water electrolyzers. Such superior performance outperforms most of the recently reported non-precious HER electrocatalysts (**Figure 13 and Table 4**). [80-88] Also, overpotentials of the NiFe/CP and NiFeW/CP at -30 mA/cm^2 show a similar tendency compared to those at -1 mA/cm^2 and -10 mA/cm^2, and a modest overpotential of 166 mV is needed to deliver -30 mA/cm^2 for the NiFeW/CP electrocatalyst.

Furthermore, EIS measurements are performed to further examine the catalytic kinetics of the HER process on NiFeW/CP (**Figure 5D**). The fitted Nyquist plots reveal that NiFeW/CP shows the smallest semicircular diameter with a low R_{ct} value of only 5.9 Ω·cm^2, which is greatly smaller than that of NiFe/CP (64.6 Ω·cm^2) (**Table 5**). This verifies that the NiFeW/CP electrocatalyst possesses the best charge-transfer ability in the HER process, which is consistent with the HER activity evaluation above. Meanwhile, the electrochemical active surface areas (ECSA) of different electrocatalysts are evaluated by testing the cyclic voltammetry (CV) curves in the non-faradaic region at different scan rates (**Figure 14A-C**) to gain electrochemical double-layer capacitance (C_{dl}), which is in proportion to the ECSA. [69] As displayed in **Figure 5E**, the NiFeW/CP electrocatalyst shows the highest C_{dl} of 11 mF/cm$^2_{electrode}$ which is remarkably higher than that of the NiFe/CP (2.9 mF/cm$^2_{electrode}$). The large ECSA of the NiFeW/CP indicates abundant electrochemically active sites of the electrocatalyst, which could be expected by the vertically well-aligned ultrathin nanosheets (**Figure 2**). Furthermore, the HER stability of the NiFeW/CP electrocatalyst is evaluated by performing chronopotentiometry measurements at current densities of -10 mA/cm^2 and -100 mA/cm^2 at room temperature.

As displayed in **Figure 5F**, the NiFeW/CP electrocatalyst could maintain at -10 mA/cm^2 for 15 h without obvious decay and a reasonable decay is observed for that tested at -100 mA/cm^2, demonstrating the good HER stability of NiFeW/CP.

To further investigate the activity of the prepared electrocatalysts, ECSA-normalized specific activity, a parameter to reveal the activity per active site is studied to reveal the intrinsic activity of the electrocatalysts. [51] The ECSA of the prepared electrocatalysts can be evaluated with the equation of $ECSA = C_{dl}/C_s$. Where C_s is the specific capacitance, and its value is 0.04 mF/cm$^2_{ECSA}$ on metal electrodes in 1 M KOH as previously described. [69] According to the equation, the ECSA value for the NiFeW/CP is calculated to be 275 cm$^2_{ECSA}$/ cm$^2_{electrode}$, and the ECSA value for the NiFe/CP is 72.5 cm$^2_{ECSA}$/ cm$^2_{electrode}$. With the ECSA, the OER specific activity of the NiFeW/CP at 1.48 V vs. RHE is evaluated to be 62.3 μA/cm$^2_{ECSA}$, which is higher than that of the NiFe/CP (49.6 μA/cm$^2_{ECSA}$). Additionally, the HER specific activities of the NiFeW/CP and NiFe/CP at 0.1 V vs. RHE are also studied, and the specific activity value (31 μA/cm$^2_{ECSA}$) of the NiFeW/CP is about 3-fold higher than that of the NiFe/CP (13 μA/cm$^2_{ECSA}$). These results further demonstrate that the W doping efficiently boosts the intrinsic activity of the pristine NiFe/CP, and thus contributes to the outstanding performances in water splitting. Based on the publications, the co-existence of Ni and Fe is essential for high activities for OER and HER, but the identification of active sites in NiFe-based electrocatalysts is still controversial.[41, 48, 50 67 69] For OER, most research studies experimentally and theoretically demonstrated that NiOOH is the active center for the OER in NiFe-based (oxy)hydroxide. [41 48]

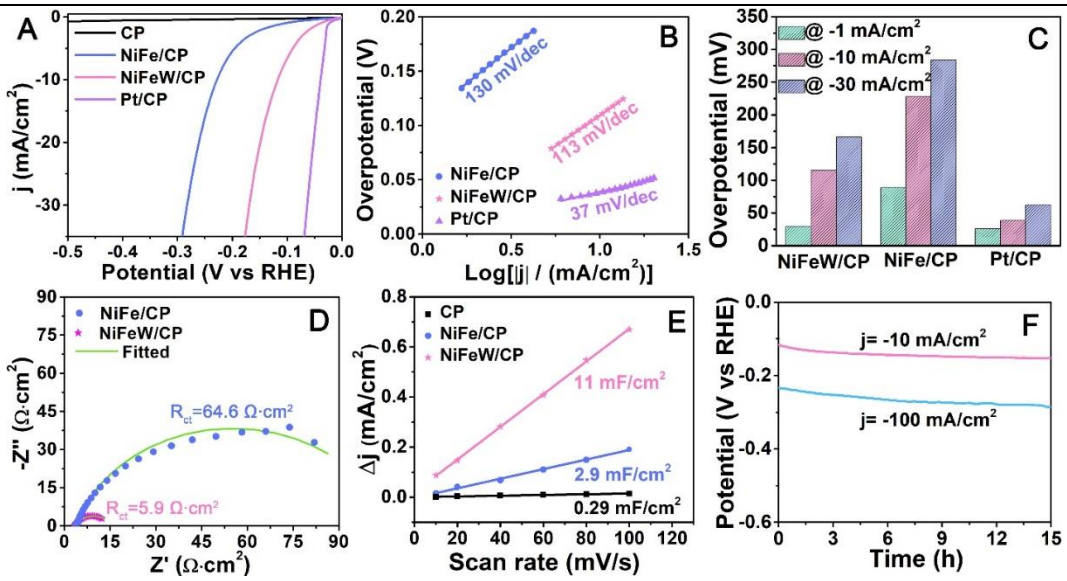


Figure 5 (A) The HER polarization curves with *iR* correction of the NiFeW/CP, NiFe/CP, CP, and the commercial IrO_2/CP in 1 M KOH at 5.0 mV/s. (B) The related Tafel slopes. (C) The HER overpotentials of different electrocatalysts at -1 mA/cm^2, -10 mA/cm^2, and -30 mA/cm^2. (D) Nyquist plots of the NiFeW/CP and NiFe/CP (recorded at -0.15 V (vs. RHE)) and the corresponding fitted Nyquist plots. (E) Plots used to extract the double-layer capacitances. (F) Chronopotentiometry measurements of NiFeW/CP electrocatalyst at -10 mA/cm^2 and -100 mA/cm^2 in 1 M KOH at room temperature (Ar-saturated).

For HER, publications reported that the Ni-Fe synergistic effect optimizes the HER reaction path, decreases the kinetic barrier of the HER, thus contributing to low HER overpotential. [41] [50]

The focus of this work is to investigate the effects of W doping on OER/HER activities. Sor far, the research of the OER/HER activity improvement ascribed to W doping has been studied experimentally and theoretically. [55] [56] [60] [70] Based on their DFT modeling results, we propose the OER and HER catalytic processes on the NiFeW/CP nanosheets is illustrated in **Figure 6**. As shown in the top part in **Figure 6**, the OER process involves the following steps. Firstly, HO^- adsorbs on the surface of the nanosheets and proceeds 1-electron oxidation to generate *HO group. As Tao *et al.* reported, NiFe-based electrocatalysts show rich surface reactivity towards OER, which means that *HO can more easily form on the surface of these electrocatalysts. [45] The high coverage of *HO can contribute to lower overpotential and Tafel slope, verifying the outstanding OER performance of the NiFeW/CP in our work. Then, the *HO group loses one couple of proton and electron to form *O radical, which can occur on the W^{6+} doping site. [70] Thereafter, the *O radical experiences two different pathways to produce O_2. One is two *O radicals combine to form O_2 (orange route). The other is a hydroxyl anion absorbs on *O radical and then participates in O-O coupling to form *OOH. Notably, this step varies from that of NiFe-LDH, in which the O-O coupling does not prefer to form at the high spin d^4 Fe^{4+} but at the low spin d^6 Ni^{4+} [69]. While with the W doping, the W^{6+} with low spin d^0 can stabilize the unpaired electron of the O radical and then boost the O-O coupling formation. After that, the *OOH intermediate absorbed on the W^{6+} sites proceeds

deprotonation to produce O_2 (blue route). [70] Hence, due to the low spin d^0 characteristic, both the O radical and O-O coupling prefer to form at the W^{6+} doping sites. For the HER schematic, two steps are involved (bottom part in **Figure 6**). In the first step, one water molecule is absorbed on NiFeW/CP and dissociated into hydrogen intermediates (*H) by combing an electron. Subsequently, because the doped W exhibits moderate association to H atoms, the W doping sites serve as the binding sites of the *H and effectively convert the *H to H_2.[80] The synergistic effect of Ni-Fe sites and W sites decreases the kinetic barrier for the HER process and thus accelerates the HER rate. Hence, with the W doping, the NiFeW/CP electrocatalyst exhibits remarkably enhanced kinetic property and dramatically lower OER and HER overpotentials compared to those of the pristine NiFe/CP electrocatalyst.

After the OER and HER stability tests, EDS-mapping, XPS, and SEM characterization are performed to examine the chemical composition changes in the structures and the morphology variation. As illustrated in **Figure 15, Figure 16, and Table 6**, the elemental compositions of the tested NiFeW/CP electrocatalysts show small variations compared to that of the fresh NiFeW/CP electrocatalyst, demonstrating outstanding stability of the electrocatalyst during the electrochemical test. Moreover, there are no major shifts observed in the XPS spectra for both the OER and HER tested electrocatalysts when compared to the fresh electrocatalyst (**Figure 17**). This further demonstrates the excellent stability of the NiFeW nanosheets in alkaline media.

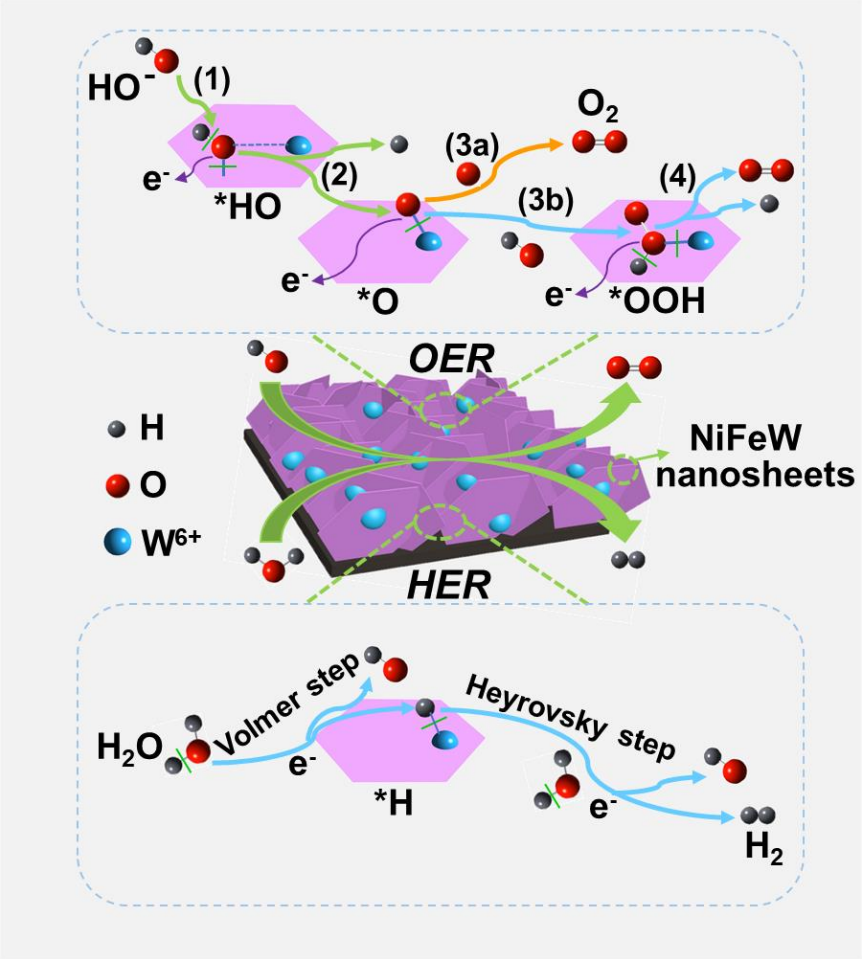


Figure 6. Schematic illustration of the OER (top part) and HER (bottom part) processes on the NiFeW/CP nanosheets, where * represents the reaction sites of the electrocatalysts.

Additionally, the morphology variation of the electrocatalysts tested at 100 mA/cm^2 are also investigated by SEM, As shown in **Figure 18**, relatively good nanosheet structures are observed even though tested at 100 mA/cm^2 for 15 h. While the observation of K in OER tested electrocatalyst is due to the adsorption of the KOH electrolyte during the tests and peaks for W metal in the HER tested electrocatalyst is ascribed to the reduction reaction during the HER process.

Overall, based on the thorough investigation of the OER and HER performances of the prepared electrocatalyst, it is known that the NiFeW/CP nanosheets exhibit remarkably improved OER and HER electrocatalytic performances than those of the NiFe/CP electrocatalyst. With various characterization strategies including SEM, TEM, STEM, and XPS, several reasons can be concluded. Notably, W doping plays a significant role in the enhanced performances. Firstly, the W doping modulates the electronic environment of the NiFe hydroxides based on the XPS results. Secondly, the doped-W well assists the vertically aligned ultrathin nanosheets formation of the NiFeW electrocatalyst according to the SEM and TEM images. The as-formed NiFeW nanosheets exhibit a much larger surface area than that of NiFe/CP, which could expose more electrochemically active sites and effectively boost electrolyte penetration and gas evolution. Hence, the large surface area is one of the obvious reasons for the notably enhanced electrochemical performance. Moreover, the introduced W^{6+} with high valence behaves strong electron capture affinity and could promote charge transfer. Also, the generation of O radical and O-O binding both occur at the W^{6+} sites, involving the rate-determining step of the OER process. Furthermore, W shows moderate adsorption ability to *H and could effectively facilitate

the conversion of *H to H_2. Due to the above reasons, the NiFeW/CP electrocatalyst possesses considerably enhanced electrocatalytic activity compared to that of the pristine NiFe/CP electrocatalyst.

Due to the outstanding activities toward the OER and HER processes in alkaline media, the NiFeW/CP electrocatalyst is applied as a bifunctional catalyst in a two-electrode electrolyzer, demonstrated in the schematic (**Figure 7A**). As displayed in **Figure 7B**, only 1.59 V cell voltage is needed at 10 mA/cm^2. This cell performance is not only 110 mV lower than that of the commercial IrO_2/CP||Pt/CP but also superior to those of most recently reported non-precious bifunctional electrocatalysts in 1 M KOH (**Figure 7C and Table 7**). For the stability test (**Figure 7D**) at room temperature, the NiFeW/CP counterparts maintain a stable overpotential of 360 mV with a neglected decay of only 1.2 % at 10 mA/cm^2 after 15 h testing, and this overpotential is very close to that in the three-electrode configuration (354 mV, combining the OER and HER processes). The potential variance of 6 mV is mainly due to the different measurement systems.[89] For comparison, the long-term measurement of IrO_2/CP||Pt/CP is also performed and shows insufficient stability with the potential decay of 3.9 % after the 15 h running, and thus implying the favorable stability of the NiFeW electrocatalyst for alkaline water splitting. To further demonstrate the excellent stability of the prepared electrocatalyst, the tested NiFeW/CP counterparts are characterized by EDS-mapping to investigate the element composition change. As revealed in **Figure 19 and Figure 20**, elements of Ni, Fe, W, and O are still uniformly distributed in the structures after the long-term testing.

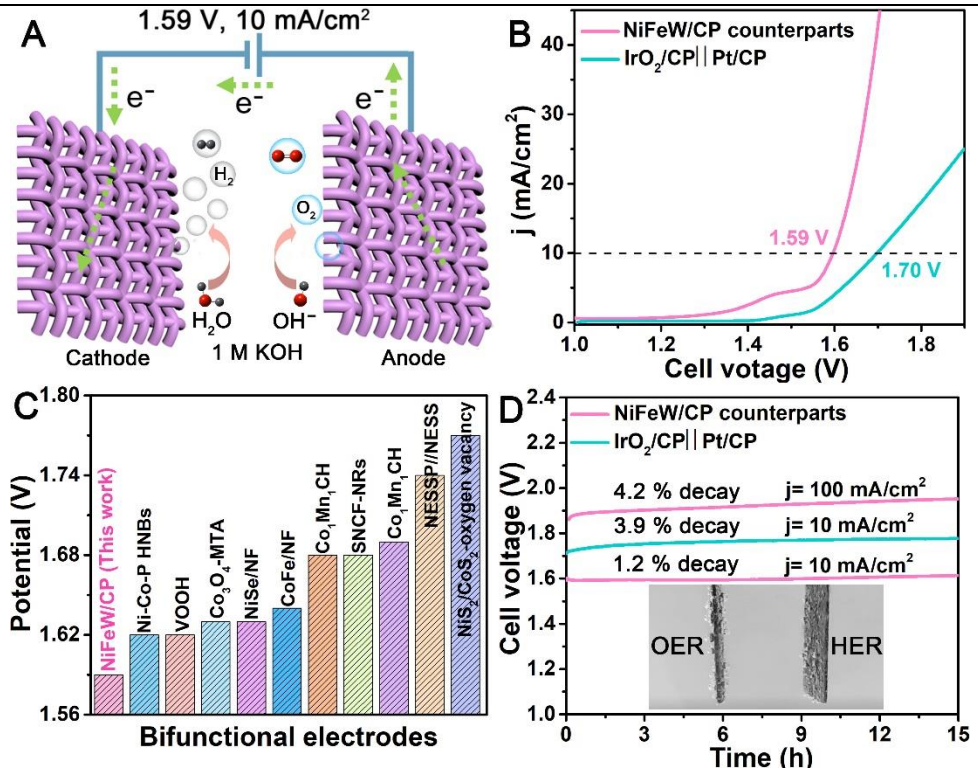


Figure 7. (A) Schematic of the NiFeW/CP as a bifunctional electrocatalyst for overall water splitting in alkaline media. (B) Polarization curves with *iR* correction for overall water splitting using the NiFeW/CP counterparts and IrO_2/CP||Pt/CP. (C) Comparison of the cell voltage of recently reported bifunctional electrocatalysts. (D) Chronoamperometry tests of overall water splitting (10 mA/cm^2 and 100 mA/cm^2) at room temperature. The inset image is from the recorded video of overall water splitting.

Moreover, to further evaluate the stability of the NiFeW/CP counterparts, a stability test at 100 mA/cm^2 is conducted for 15 h. As shown in **Figure 7D**, a reasonable degradation rate of 4.2 % is demonstrated after the test. Overall, the above results indicate the remarkable activity and stability of the NiFeW/CP counterparts in alkaline conditions, which is critical for the large-scale application of electrocatalysts. Hence, the NiFeW/CP nanosheets are promising bifunctional electrodes for high-efficient alkaline water electrolyzers.

2.6 Conclusions

In summary, with a high-efficiency and simple one-step electrodeposition process, we develop *in-situ* growth of W-doped NiFe bifunctional electrocatalysts with ultrathin nanosheet features on carbon paper (NiFeW/CP) at room temperature and ambient pressure for highly efficient water splitting. The electrodeposition strategy significantly promotes large-scale electrocatalyst fabrication for commercial water splitting. Consequently, the as-formed NiFeW nanosheets show high performance toward alkaline water splitting with low overpotentials of 239 mV for the OER and 115 mV for the HER, respectively, at 10 mA/cm^2. Moreover, only 1.59 V cell voltage is needed at 10 mA/cm^2 in 1 M KOH when applying NiFeW/CP as both an anode and cathode in a full electrolyzer configuration. Notably, the doped-W could not only effectively boost the formation of vertically well-aligned NiFeW ultrathin nanosheets but also successfully engineer the electronic structure of the NiFe hydroxides to achieve enhanced kinetic properties. Furthermore, the doped-W significantly decreases the kinetic barriers for both the OER and HER processes. Therefore, the bifunctional NiFeW nanosheets with an efficient fabrication strategy and remarkable

electrochemical performances in alkaline media exhibit great potential as bifunctional electrodes for alkaline water electrolyzers.

Appendix

Electrochemical oxygen evolution and hydrogen evolution mechanism:

The OER in alkaline solution:

$HO^- + * \rightarrow *HO + e^-$ (1)

$*HO \rightarrow *O + H^+ + e^-$ (2)

$2*O \rightarrow O_2$ (3a)

$HO^- + *O \rightarrow *OOH + e^-$ (3b)

$*OOH \rightarrow O_2 + * + H^+ + e^-$ (4)

The HER in alkaline solution:

$H_2O + e^- \rightarrow *H + HO^-$ Volmer step

$2*H \rightarrow H_2$ Tafel step

$*H + H_2O + e^- \rightarrow HO^- + H_2$ Heyrovsky step

where * represents the reaction sites of the electrocatalysts.

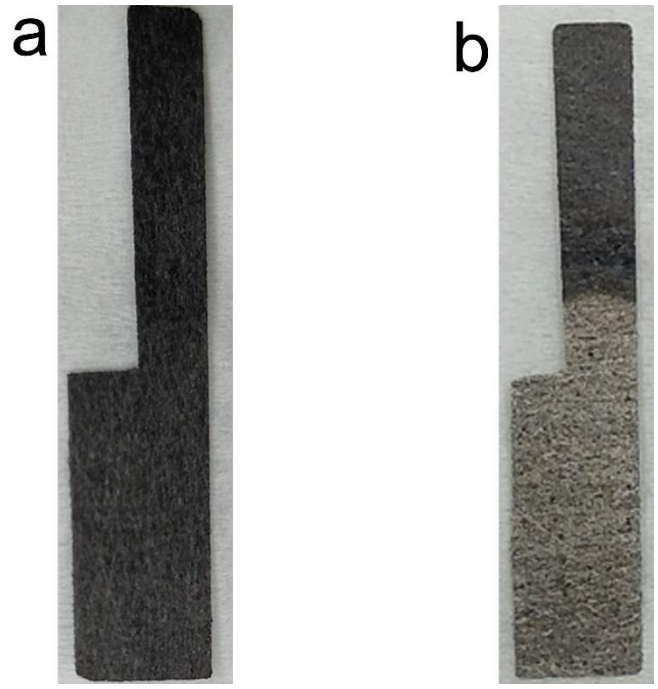


Figure 8. Photographs of the CP substrate (a) and the NiFeW/CP electrode (b).

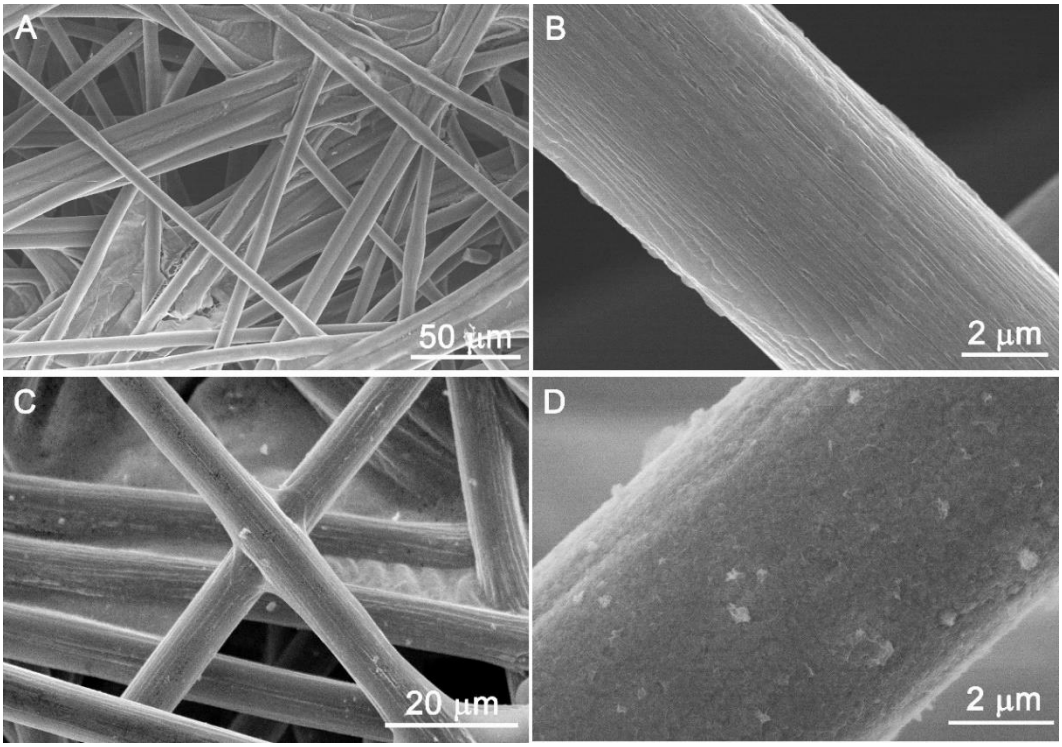


Figure 9. SEM images of bare carbon paper (A, B) and NiFeW/CP (C, D).

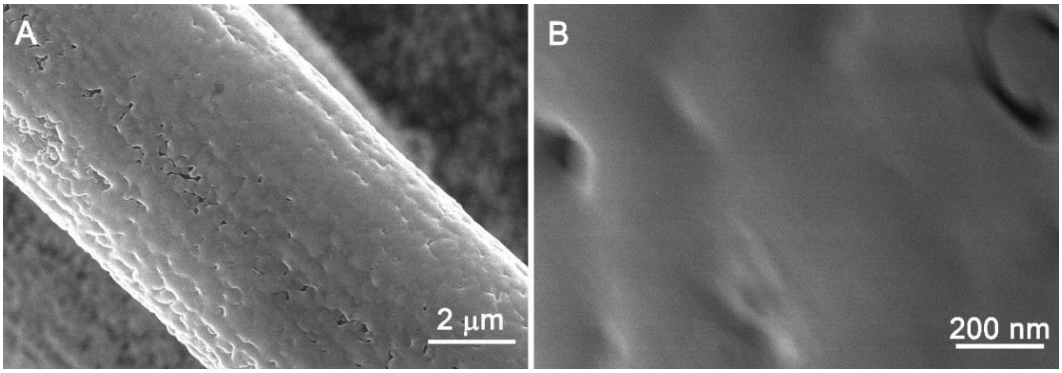


Figure 10. SEM images of the NiFe/CP.

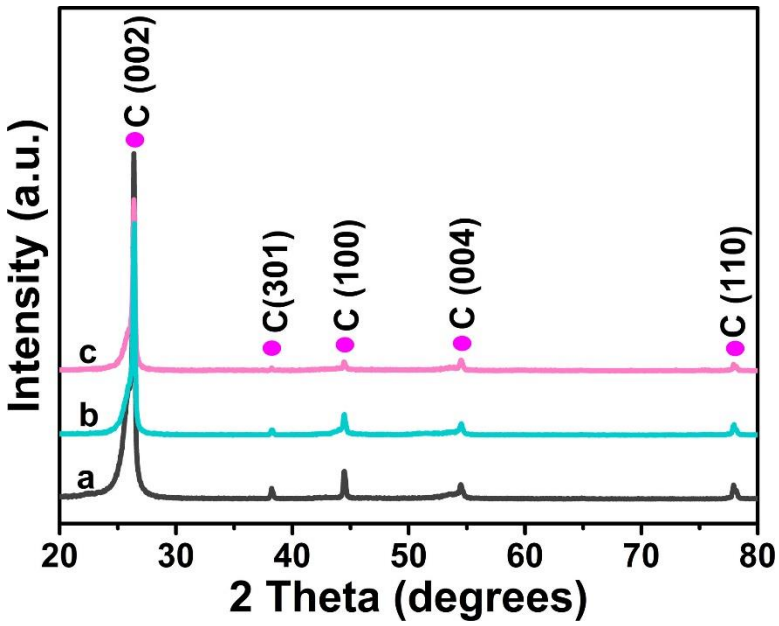


Figure 11. XRD patterns of carbon paper (a), NiFe/CP (b), and NiFeW/CP (c).

Table 1. Elemental composition of NiFe/CP and NiFeW/CP based on EDS results.

Electrocatalysts	Ni (At%)	Fe (At%)	W (At%)
NiFe/CP	76.49	23.51	/
NiFeW/CP	70.32	25.94	3.74

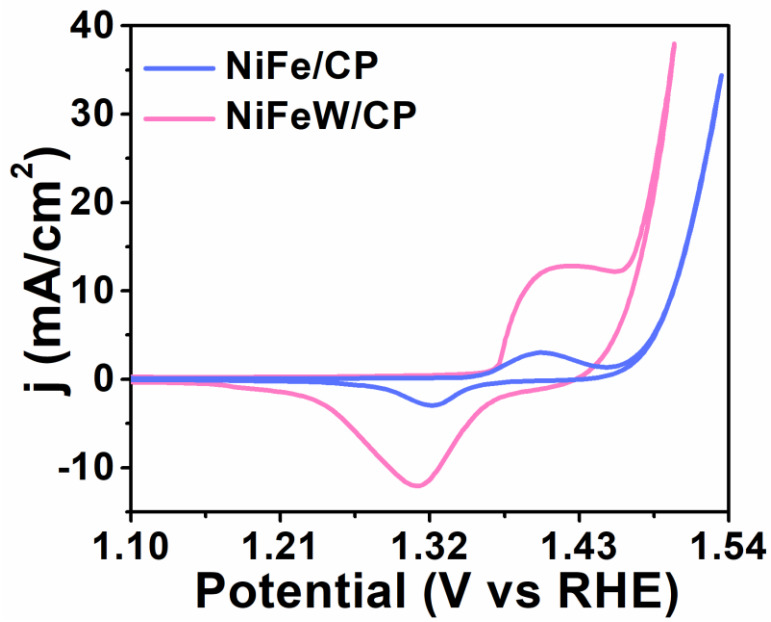


Figure 12. CV curves of NiFeW/CP and NiFe/CP.

Table 2. The literature survey of recently reported electrocatalysts for the OER catalytic activity (at 10 mA/cm^2).

Electrocatalysts	Tafel slope (mV/dec)	Overpotential (at 10 mA/cm^2)	Reference
NiFeW/CP	36	239	This work
Co_6W_6C@NC	54	286	[70]
MoS_2-Ni_3S_2 HNRs	57	249	[71]
$NiCo_2S_4$	62	243	[72]
CoFe-ONC	42	258	[73]
$NiCo_2P_2$/GQD NSs	66	340	[74]
N-$NiCoP_x$/NCF	60	298	[75]
Ni-NHGF	63	331	[76]
NiFe-LDH/N-CNF	60	312	[77]
1 nm-CoO_x/N-RGO	76	370	[78]
NiCoFeB	46	284	[79]

Table 3. The OER electrochemical impedance parameters obtained by simulating the Nyquist plots in Figure 4E with an appropriate equivalent circuit model.

Electrocatalysts	R_s ($\Omega \cdot cm^2$)	Q_1 (F)	R_1 ($\Omega \cdot cm^2$)	Q_{ct} (F)	R_{ct} ($\Omega \cdot cm^2$)	Error
NiFe/CP	3.4928	0.0006613	7.37028	0.04538	9.44236	0.5416
NiFeW/CP	3.22371	0.244	2.79756	0.0008713	1.2768	0.02974

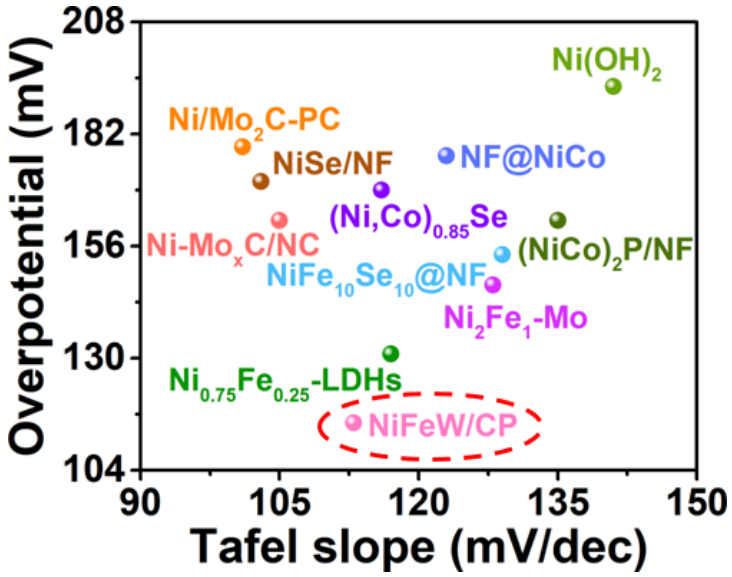


Figure 13. Comparison overpotential at -10 mA/cm^2 with previous reported HER electrocatalysts in 1 M KOH.

Table 4. The literature survey of various recently reported electrocatalysts for the HER catalytic activity (at -10 mA/cm^2).

Electrocatalysts	Tafel slope (mV/dec)	Overpotential (at 10 mA/cm^2)	Reference
NiFeW/CP	113	115	This work
Ni/Mo_2C-PC	101	179	80
$Ni(OH)_2$	141	193	81
$Ni_{0.75}Fe_{0.25}$-LDHs	117	131	81
NF@NiCo	123	177	82
NiSe/NF	103	171	83
$(Ni,Co)_{0.85}Se$	116	169	84
$NiFe_{10}Se_{10}$@NF	129	154	85
Ni_2Fe_1-Mo	128	147	86
Ni-Mo_xC/NC	105	162	87
$(NiCo)_2P$/NF	135	162	88

Table 5. The HER electrochemical impedance parameters obtained by simulating the Nyquist plots in Figure 5D with an appropriate equivalent circuit model.

Electrocatalysts	R_s ($\Omega \cdot cm^2$)	Q_1 (F)	R_1 ($\Omega \cdot cm^2$)	Q_{ct} (F)	R_{ct} ($\Omega \cdot cm^2$)	Error
NiFe/CP	3.77468	0.04395	33.1226	0.0147	64.5696	0.07932
NiFeW/CP	3.46448	0.02359	4.14652	0.01161	5.8528	0.1094

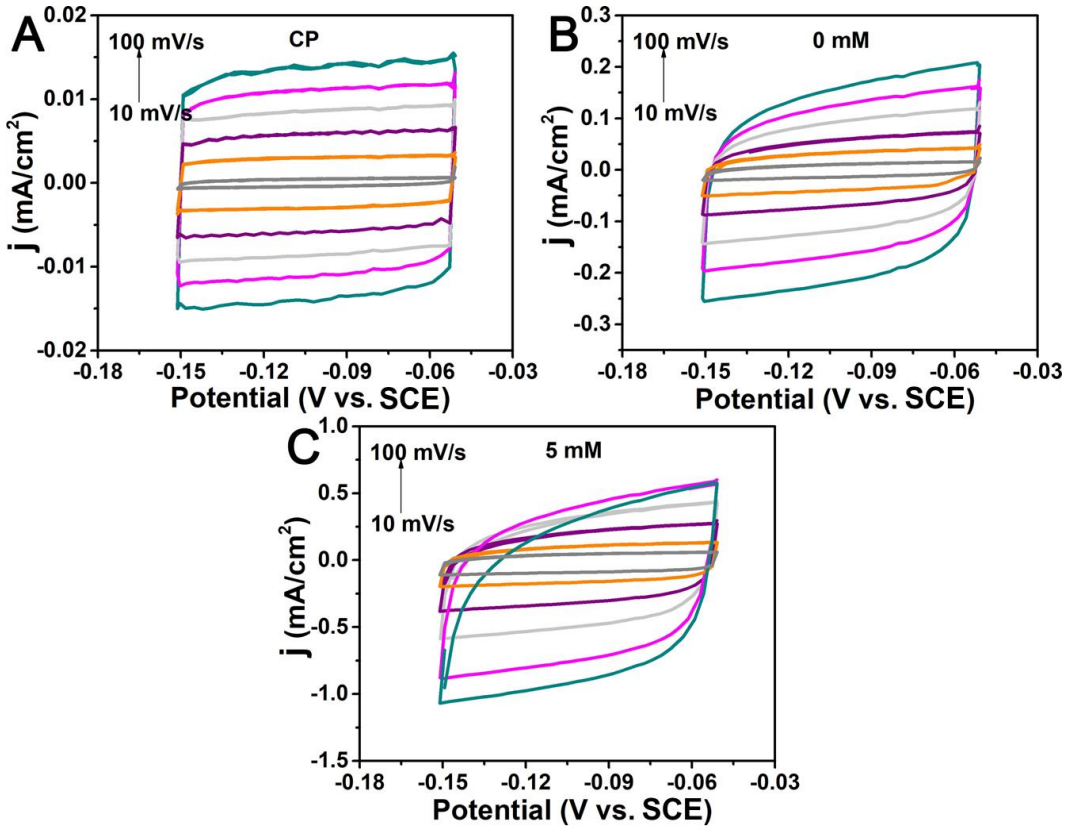


Figure 14. CV curves for different electrocatalysts carried out in non-faradic regions at different scan rates in 1 M KOH.

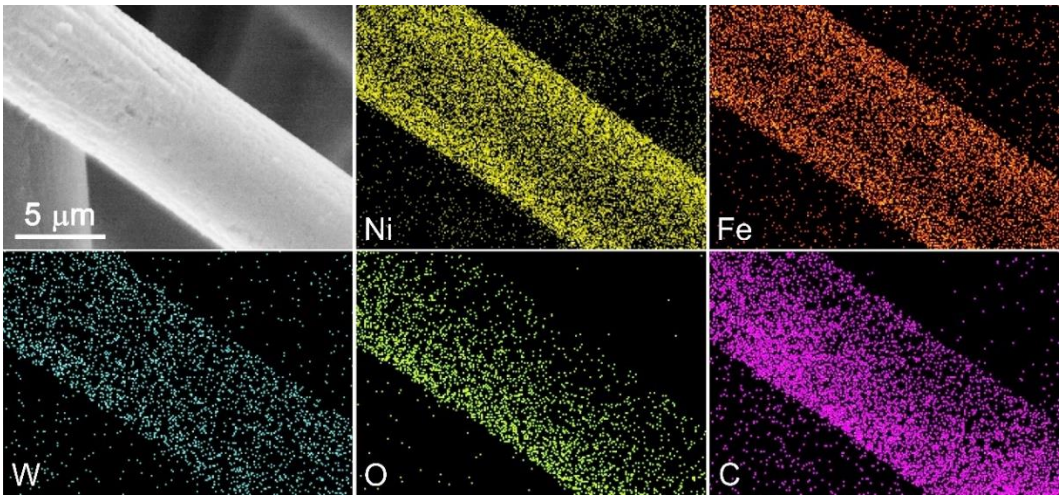


Figure 15. SEM image and corresponding EDX mapping images of the NiFeW/CP after the OER stability test for 15 h.

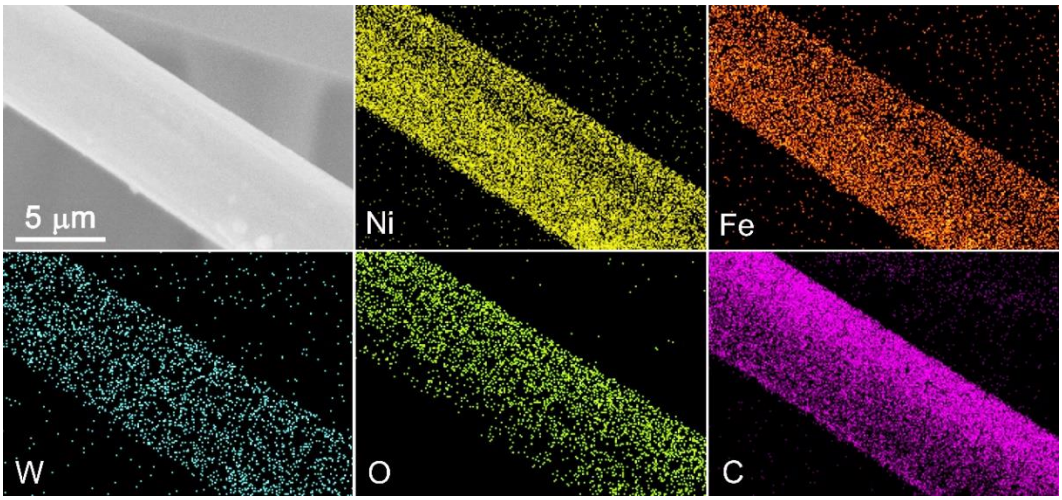


Figure 16. SEM image and corresponding EDX mapping images of the NiFeW/CP after the HER stability test for 15 h.

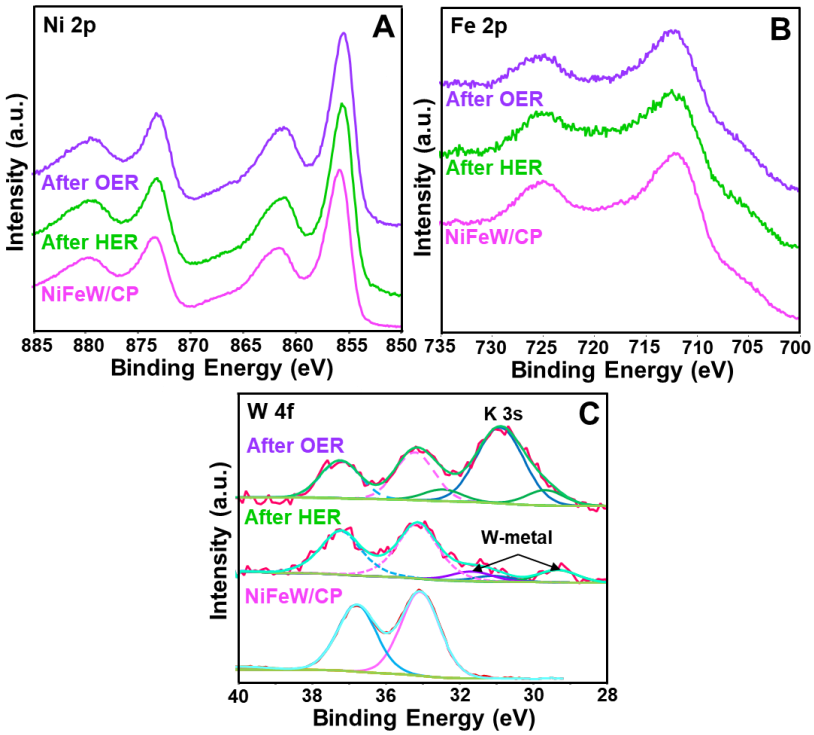


Figure 17. XPS spectra comparison of fresh NiFeW/CP electrocatalyst and NiFeW/CP electrocatalysts after the OER and HER stability tests. Ni 2p (A), Fe 2p (B), and W 4F (C).

Table 6. Elemental composition of electrocatalysts before and after stability tests characterized with EDS.

Electrocatalysts	Ni (At%)	Fe (At%)	W (At%)
Fresh NiFeW/CP	70.32	25.94	3.74
NiFeW/CP after OER (10 mA/cm^2)	71.78	25.47	2.75
NiFeW/CP after HER (10 mA/cm^2)	69.96	27.43	2.61
NiFeW/CP after OER (100 mA/cm^2)	71.13	25.64	3.23
NiFeW/CP after HER (100 mA/cm^2)	69.81	26.28	3.91

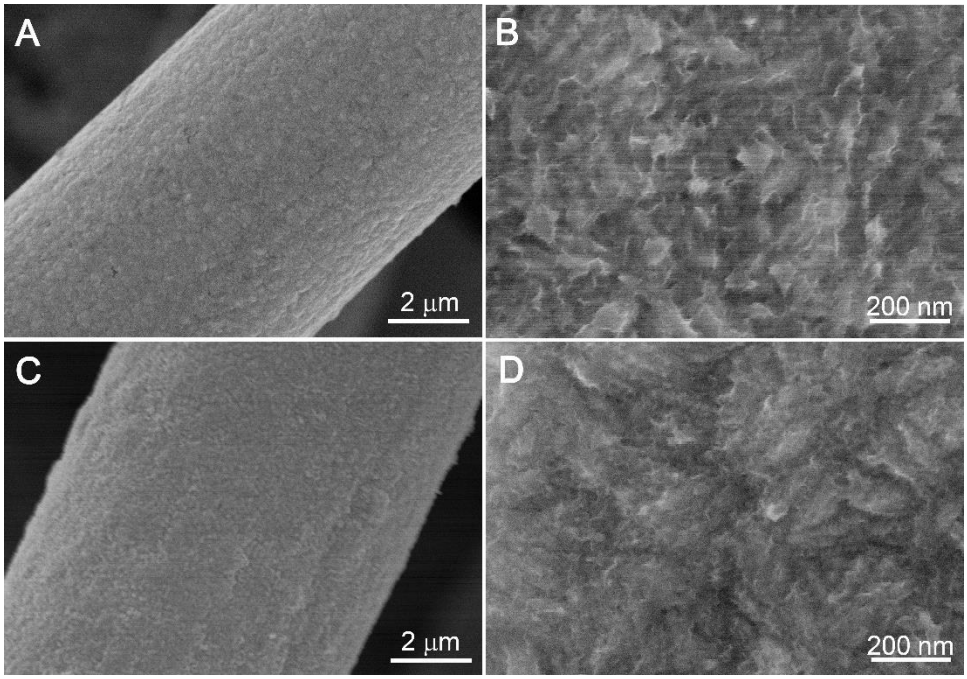


Figure 18. SEM images of NiFeW/CP after OER (A, B) and HER (C, D) stability tests (100 mA/cm^2).

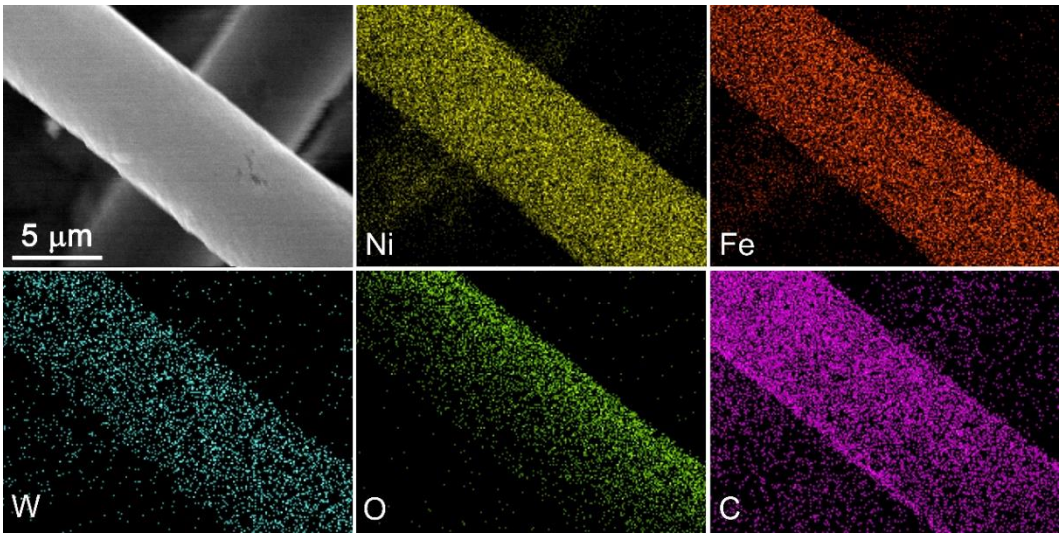


Figure 19. SEM image and corresponding EDX mapping images of the NiFeW/CP as an anode after the stability test.

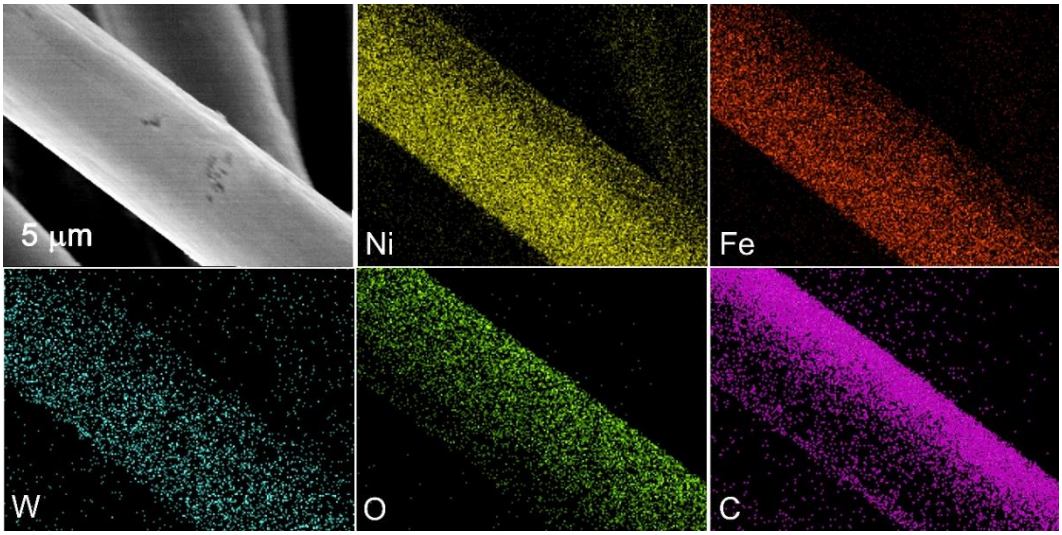


Figure 20. SEM image and corresponding EDX mapping images of the NiFeW/CP as a cathode after the stability test.

Table 7. Comparison of recently reported bifunctional electrocatalysts for overall water electrolysis in alkaline media.

Electrocatalysts	Cell Voltage / V	Electrolyte (KOH)	Ref.
NiFeW/CP	1.59	1 M	This work
IrO_2/CP || Pt/CP	1.70	1 M	This work
Ni-Co-P HNBs	1.62	1 M	90
CoFe/NF	1.64	1 M	91
Co_3O_4-MTA	1.63	1 M	92
VOOH	1.62	1 M	93
Co_1Mn_1CH	1.68	1 M	94
NiSe/NF	1.63	1 M	95
SNCF-NRs	1.68	1 M	96
NiS_2/CoS_2-oxygen vacancy	1.77	1 M	97
NESSP//NESS	1.74	1 M	98
NF@MoCo	1.69	1 M	82

CHAPTER THREE

W-INDUCED MORPHOLOGICAL MODIFICATION OF NIFE LAYERED DOUBLE HYDROXIDES AS EFFICIENT ELECTROCATALYSTS FOR OVERALL WATER SPLITTING

A version of this chapter was originally published as:

Ding, L., Li, K., Xie, Z., Yang, G., Yu, S., Wang, W., Cullen, D.A., Yu, H. and Zhang, F-Y., W-induced morphological modification of NiFe layered double hydroxides as efficient electrocatalysts for overall water splitting. Electrochimica Acta 395 (2021): 139199.

CRediT authorship contribution statement

Lei Ding: electrocatalyst preparation, electrochemical tests, data analysis, SEM and XRD characterizations, original draft writing, writing, reviewing, and editing. Kui Li: SEM and EDS characterizations, electrochemical tests, data analysis, original draft writing, writing, reviewing, and editing. Zhiqiang Xie: SEM characterization, data analysis, writing, reviewing, and editing. Gaoqiang Yang: electrochemical tests, data analysis, writing, reviewing, and editing. Shule Yu: SEM and XRD characterizations, writing, reviewing, and editing. Weitian Wang: electrochemical tests, data analysis, writing, reviewing, and editing. Haoran Yu: TEM characterization, writing, reviewing, and editing. David A. Cullen: TEM characterization, writing, reviewing, and editing. Feng-Yuan Zhang: study design and idea conception, writing, reviewing, and editing, supervision. All authors commented on and edited the manuscript.

I am fully responsible for the work submitted in these publications.

3.1 Abstract

Layered double hydroxides (LDHs) are one of the most efficient electrocatalysts for water splitting due to their nanosheet features and compositional flexibilities. This work explored the impact of W precursor concentration (0 ~ 10 mM) on LDH morphologies and performance in hydrogen production. Using an electrodeposition W-doping process, W-induced NiFe LDHs (NiFeW-LDHs) were *in-situ* grown on carbon fiber papers for water splitting. A performance peak was found at a W doping of 5 mM with well-aligned nanosheets, which not only boosted the charge transfer ability and gas evolution but also offered more than a four-fold electrochemical surface area increase compared to film-like NiFe hydroxides. The NiFeW-LDHs exhibited remarkable performance compared to NiFe hydroxides, showing decreased overpotentials of 31 mV and 114 mV for the oxygen evolution reactions (OERs) and hydrogen evolution reactions (HERs) at 10 mA/cm^2 and -10 mA/cm^2, respectively, in alkaline media. The performance enhancement at 5 mM W-doping was linked to the well-aligned NiFeW-LDH nanosheets; smaller, less-textured nanosheets were observed with lower or higher W precursor concentrations (2.5 mM or >7.5 mM), leading to inferior OER and HER performances. Hence, an appropriate W doping is crucial to generating the morphologies that contribute to the higher performance of NiFeW-LDHs.

3.2 Introduction

Electrochemical water splitting, one of hydrogen generation technologies, has become a research hotspot currently since it can not only achieve the green production of clean energy hydrogen from electric energy but also provide the potential to utilize intermittent-renewable energy sources such as wind and solar. [23, 42, 43 8 99 100] To enhance water splitting efficiency, it is crucial to explore valid electrocatalysts to reduce key conversion barriers of two half-reactions in the splitting, namely, the hydrogen evolution reactions (HERs) involved two electrons at the cathode and the oxygen evolution reactions (OERs) with four involved electrons at the anode, respectively [40 101 33 102 103 104]. So far, water splitting mainly depends on noble catalysts (e.g., Pt, RuO_2, IrO_2.), which severely hamper the wide commercialization of practical water splitting owing to their low abundance, high cost, and mono functionality [29, 39, 47, 105-107]. Hence, exploring efficient strategies to reduce noble catalysts utilization meanwhile maintaining or even enhancing catalytic activity is a vitally significant challenge.

So far, abundant non-noble-based materials such as transition metal-based alloys [108-111], hydroxides [112-115], phosphides [116], selenides [117], and nitrides [118] have been explored as alternatives. Among them, NiFe-based catalysts in alloys, hydroxides, and other derived composites have gained particular interest because of their high catalytic activity, low cost, and high earth's abundance [52, 53, 66]. Particularly, NiFe-based layered double hydroxides (LDHs) have gained widespread research attention due to their nanosheet features and compositional flexibilities. Meanwhile, *in-situ* growth of electrocatalysts on conductive substrates (e.g., carbon fiber paper, nickel foam.) have gained widespread research

attention because it offers the electrocatalysts with three-dimensional (3D) structures, which could effectively boost electron transfer, facilitate electrolyte penetration, and promote gas evolution [119, 120]. To date, common strategies of *in-situ* LDH growth mainly include the hydrothermal and electrodeposition method. Compared to the hydrothermal process, electrodeposition exhibits great potential to be scaled up in the industrial field to prepare electrocatalysts for practical water splitting, since ambient conditions (room temperature and pressure) and short fabrication time are available for this strategy, which is simpler, more timesaving, and more convenient. Hence, the electrodeposition technique has been acknowledged as an effective strategy to construct 3D LDH nanosheets on substrates, boosting the realization of electrocatalyst large-area preparation for industrial fields. Through the fast and effective electrodeposition technique, various kinds of NiFe-based LDH nanosheets are reported. For example, a series of LDHs (MFe-LDHs, M: Ni, Co, and Li) with an ultrafast one-step electrodeposition process at room temperature were reported [60]. Yang, *et al.* [121] reported novel hierarchical CoFe@NiFe-200/NF electrocatalysts with core-shell architecture for water splitting in alkaline solution with a fast electrodeposition process. Additionally, NiFe-based LDHs have been demonstrated to show the potential to be bifunctional electrocatalysts for water splitting with excellent electrochemical performance for the OERs but moderate HER activity in alkaline media [118]. To improve the moderate HER activity, foreign element doping technology has been currently widely used, which could not only modulate morphology and electronic configuration but also induce synergetic effects between host layers and the dopants, showing significant potential to increase the active surface area and create amorphous phases to bring new properties toward the HERs and also boost the inherent performance

for the OERs [112]. Currently, many works have been proposed to introduce foreign elements to the pristine NiFe LDHs to improve their electrochemical performance, such as Co [112, 122], Cr [123], Se [85].

In this work, for the first time, the introduction of W into film-like NiFe hydroxides and its influence on the morphological structure and the electrocatalytic activity are comprehensively studied. With an electrodeposition process at room temperature, we investigate the structure engineering pathway of the film-like NiFe hydroxides *via* various proportions of W-doping on carbon fiber paper (CFP) substrate, a commonly used conductive substrate that offers good mass transport and excellent mechanical properties for the fabricated electrocatalysts. As a result, compared to high overpotentials of 272 mV for the OERs and 231 mV for the HERs of NiFe hydroxides, the as-modulated W-doped NiFe LDHs (5 mM W precursor) with vertically well-aligned nanosheet features exhibit significantly enhanced water splitting performances with a low OER overpotential of 241 mV and a moderate HER overpotential of 117 mV at 10 mA/cm^2 and -10 mA/cm^2, respectively, in 1 M KOH.

3.3 Experimental

3.3.1 Chemicals and materials

Nickel sulfate hexahydrate (98%), ferrous sulfate heptahydrate (99%), sodium tungstate dihydrate (99-101.0%), saccharin (99%), and boric acid (98%) are the compositions of the electrolyte for electrodeposition, and the former four chemicals were purchased from Sigma-Aldrich while the boric acid was purchased from Showa. Potassium hydroxide (85%) and potassium chloride (99%) were purchased from Riedel. Deionized water (18.2

MΩ·cm) was used throughout the experimental processes. Additionally, ultra-high purity Ar (99.999%) and nitric acid (68-70%) were purchased from Airgas and Alfa Aesar, respectively. Carbon fiber papers (Toray 090, 280 μm) and carbon rods were supplied from Full Cell Store and Gamry Instruments, respectively.

3.3.2 Fabrication of NiFe hydroxides and NiFeW-LDHs

Through an electrodeposition process in a three-electrode system, NiFe hydroxides and a series of NiFeW-LDHs electrocatalysts were fabricated. The carbon fiber paper, carbon rod, and Ag/AgCl electrode (1 M KCl) were used as the working electrode, counter electrode, and reference electrode, respectively. Carbon fiber paper with a size of 2.5 × 0.5 cm was cleaned in nitric acid for 30 min, followed by sonication in methanol and deionized water for 15 min, respectively. For the electrodeposition, a 20 mL electrolyte containing 45 mM $NiSO_4 \cdot 6H_2O$, 7.5 mM $FeSO_4 \cdot 7H_2O$, x mM $Na_2WO_4 \cdot 2H_2O$ (x= 0, 2.5, 5, 7.5, and 10), 40 g/L boric acid, and 1g/L saccharin was used. After the electrodeposition process at -1.0 V (vs. Ag/AgCl) at room temperature (25 ℃) for 1 hour, the resultant sample was carefully withdrawn from the electrolyte, rinsed with DI water, and dried in air.

3.3.3 Characterizations

The morphologies and compositions of the electrocatalysts were characterized by a field emission JEOL JSM-6320F scanning electron microscope (SEM) with energy-dispersive X-ray spectroscopy (EDS) and Hitachi HF3300 transmission electron microscopy (TEM).

3.3.4 Electrochemical measurements

A conventional three-electrode system with the as-fabricated electrodes (working area: ~ 1 cm^2) as the working electrode, a carbon rod as the counter electrode, and a saturated calomel electrode (SCE) as the reference electrode, respectively was used for the OER and HER tests. All electrochemical tests were performed on a potentiostat VSP/VMP3B-100 (Bio-Logic) at room temperature in 1 M KOH. Before electrochemical tests, to condition the system and reach a stable current density, three cycles of cyclic voltammetry (CV) were conducted at a scan rate of 100 mV/s. Subsequently, the linear sweep voltammetry (LSV) polarization curves were recorded at a scan rate of 5 mV/s from high to low potentials for the OER to avoid possible interferences of the oxidation peak with the OER onset, and the HER LSV curves were recorded from low to high potentials to avoid the reduction peak with the HER onset. Within a frequency range of 200 kHz~ 50 mHz with an amplitude of 10 mV, the electrochemical impedance measurements for the OERs and HERs were performed at overpotentials of 210 mV and 150 mV, respectively. Subsequently, with an appropriate equivalent circuit model, the experimental (electrochemical impedance spectroscopy) EIS data was fitted by Z-view software. Moreover, *iR*-correction was performed for the polarization curves to exclude the ohmic resistance of the solution. Through the Nernst equation: $E_{RHE} = E_{SCE} + 0.243\ V + 0.0591 \times pH$, recorded potentials were calibrated to reversible hydrogen electrode (RHE). OER and HER overpotentials can be evaluated with equations $\eta = E_{RHE} - 1.23\ V$ and $\eta = E_{RHE} - 0$, respectively.

3.4 Results and Discussion

As illustrated in **Figure 21**, through a one-step reductive electrodeposition process, electrocatalysts are *in-situ* deposited on CFPs to form bifunctional electrodes in a three-electrode configuration with an electrolyte containing Ni-Fe or Ni-Fe-W precursors. Notably, with W doping, the NiFe hydroxides with film-like morphology can be well modulated to vertically well-aligned NiFeW layered double hydroxides (LDHs), showing ultrafine nanosheet features. For the electrolyte, apart from the Ni, Fe, and W precursors, 40 g/L boric acid is also added to act as a buffering agent, hindering the increase of pH in the electrolyte. [124] While saccharin with a concentration of 1 g/L serves as a structure-controlling agent, which can reduce the internal stresses and prevent the crack generation of the electrodeposits. [125] The electrodeposition process is performed under a negative potential of -1.0 V (*vs.* Ag/AgCl) at room temperature to induce a cathodic current because of the reduction of water molecules ($2H_2O + 2e^- \rightarrow H_2 + OH^-$). Subsequently, the generated OH^- contributes to the rapid deposition of precipitation of the NiFe-based hydroxides on the surface of the CFP substrate.

To develop highly efficient electrocatalysts for water splitting *via* controlling the morphology and composition. A series of NiFeW-LDHs with different W precursor concentrations (0 mM, 2.5 mM, 5 mM, 7.5 mM, and 10 mM) are fabricated, and their electrocatalytic performances are subsequently investigated. As shown in **Figure 22A** along with its Inset, the bare CFP substrate displays a quite smooth surface. However, after the electrodeposition process, different electrocatalysts with varied morphologies can be observed on the surface of the CFPs (Insets in **Figure 22B-F**).

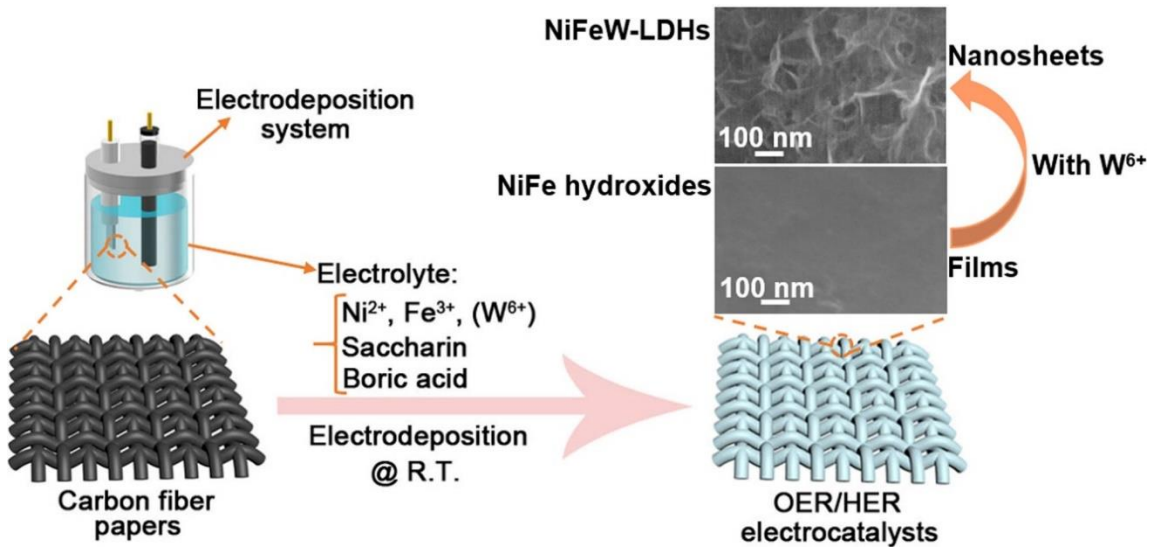


Figure 21. Schematic of electrocatalyst electrodeposition on CFPs to form bifunctional electrocatalysts. With W doping, the NiFe hydroxides with film structures are successfully engineered to the NiFeW-LDHs with nanosheet features.

In the absence of W, the NiFe hydroxides present a smooth film-like structure, and no obvious features are observed (**Figure 22B**). With a low-level addition of W precursor (2.5 mM), electrocatalyst morphology becomes very coarse, and some nanosheet-like grains exhibit in the structure (**Figure 22C**). When increasing the W precursor concentration to 5 mM, abundant vertically well-defined nanosheets with flexibility and an average thickness of about 5 nm are grown on CFPs (**Figure 22D**), which could offer a larger surface area. However, with higher W precursor doping concentrations (7.5 mM and 10 mM), the formed nanosheets become dense and smaller (**Figure 22E, F**), which results in smaller surface area and could decrease active sites of the electrocatalysts and eventually increase the conversion barriers for electrochemical reaction. Hence, excessive W doping levels could damage the finely aligned nanosheet morphology and lead to dense and smaller nanosheets. Overall, the W doping concentration exhibits a powerful influence on the morphological structures of the NiFeW-LDHs.

Based on the SEM characterization, possible mechanisms are proposed to figure out the reason behind the morphology formation and transition of the NiFe-hydroxide films to the NiFeW-LDH nanosheets, where W doping plays a crucial role to induce heterogeneous seeds in the homogeneous formation of the nanosheets (**Figure 23**). Unlike most reported NiFe composites prepared by electrodeposition with intrinsic nanosheet features [60, 126]. In our work, the electrodeposited NiFe hydroxides present smooth and film-like structures, which could be ascribed to different electrolytes and an appropriate addition of saccharin in our electrolyte.

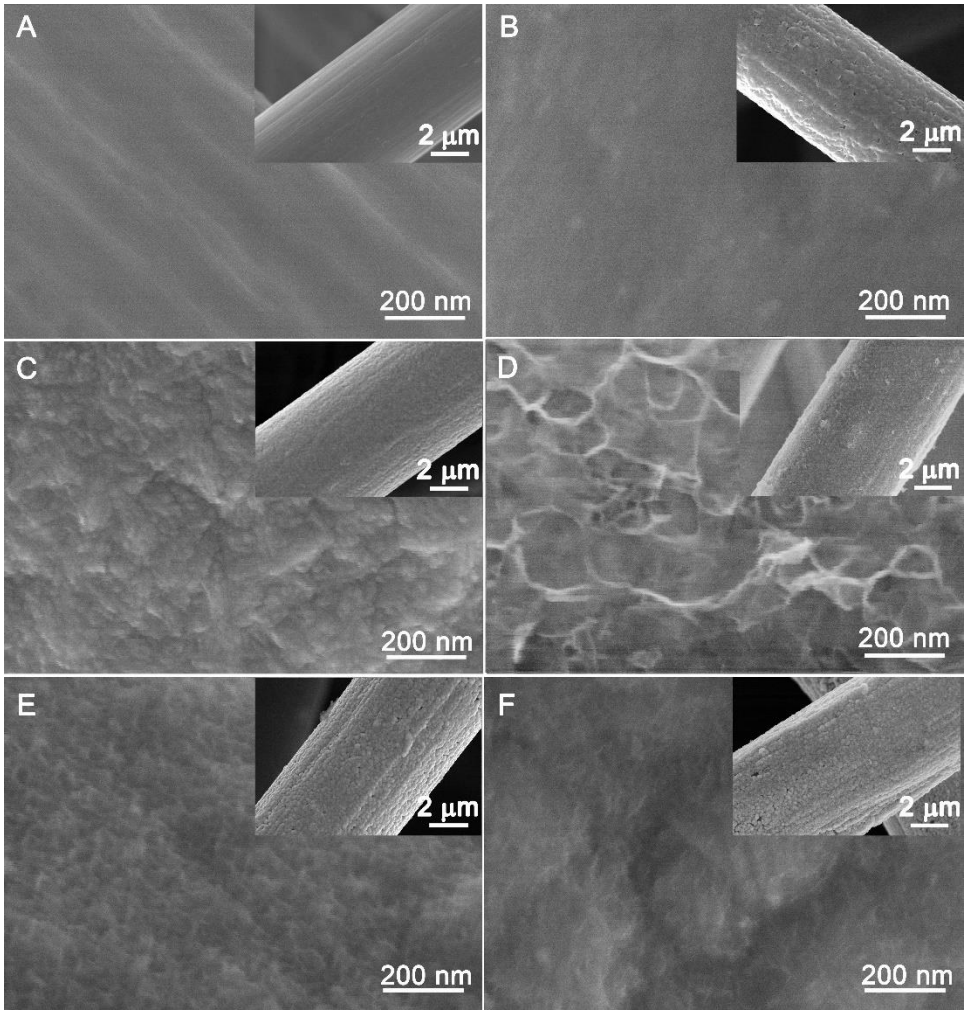


Figure 22. SEM images with higher magnification and lower magnification (Insets) of carbon fiber papers (A) and electrocatalysts with different W precursor concentrations: 0 mM (B), 2.5 mM (C), 5 mM (D), 7.5 mM (E), and 10 mM (F).

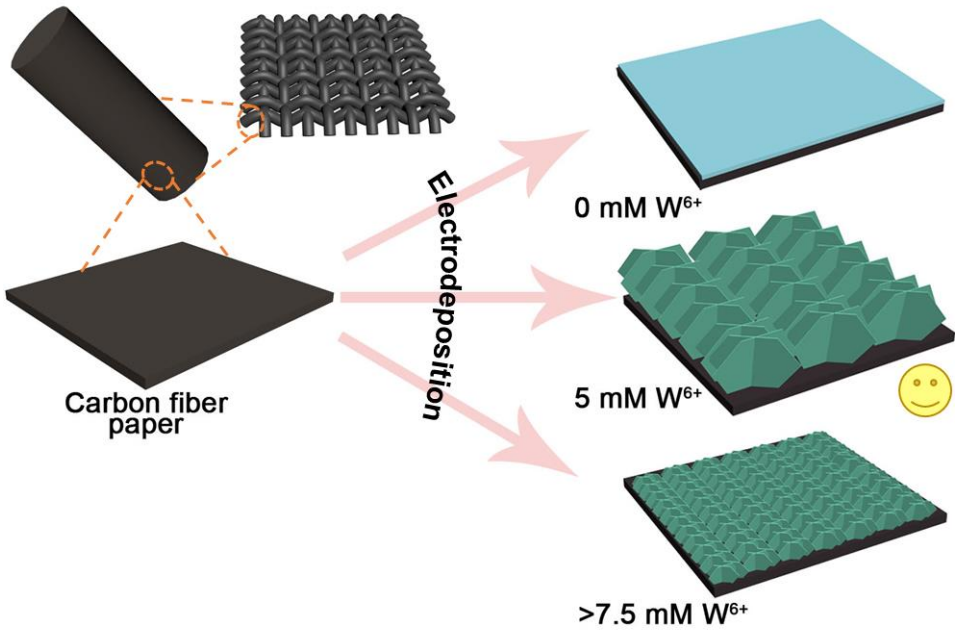


Figure 23. Effects of W doping concentration on NiFeW-LDH morphologies on carbon fiber papers.

As previous work studied, organic addictive saccharin containing aromatic sulfones can effectively modify the microstructure and smooth the surface of the electrodeposits [127-130]. With a suitable addition of saccharin in the electrolyte, electrodeposits with smooth surfaces without cracks can be achieved due to decreased internal stresses [131-133]. For example, Kim *et al.* [134] demonstrated that with a saccharin concentration less than 3.0 g/L in the electrolyte, the electrodeposit exhibited smooth surfaces. While burnt and torn deposits or faceted islands can be observed if there is no saccharin, or the saccharin concentration is higher than 3.0 g/L. The mechanism of saccharin promotes the formation of smooth surfaces involves the adsorption of the saccharin on the active sites of the cathode and subsequent nucleation rate change on various crystal faces [127]. Specifically, the adsorbed saccharin can form a chemical barrier layer for adions and adatoms on the cathode surface and then generate nucleation points. Subsequently, the generated nucleation points could accelerate the electrodeposit growth rate, contributing to grain refinement and reduced internal stresses.

With the same saccharin concentration (1 g/L), the smooth NiFe hydroxide films can be successfully transformed into vertically aligned NiFeW-LDH nanosheets *via* W doping. Hence, it can be inferred that the doped W could induce heterogeneous seeds for the nanosheet evolution in NiFe hydroxides, promoting the formation of homogeneous NiFeW-LDHs with nanosheet features. We speculate that the W doping effectively tunes the competitive micro-environment of the NiFe hydroxides, thereby influencing the growth of crystal structure and then modulating the morphological structures of the electrocatalysts. With an appropriate W precursor level of 5 mM, vertically well-aligned

nanosheets can be developed on the surface of CFPs, which could boost the electrolyte diffusion and the gas evolution [23, 110, 135, 136]. However, the formed nanosheets become dense and smaller with higher W doping levels (> 7.5 mM W precursor). The dense nanosheets with smaller sizes may ascribe to limit growth space caused by higher W doping levels in the structures, which could hinder the nanosheets to further grow with a larger size and then result in a higher density of nanosheets with a smaller size in the same growing space. It could be demonstrated by similar morphological transformations induced by ion doping. Recently, Huang *et al.* [137] demonstrated that Zr-regulated 3D CoFeZr nanosheets were successfully fabricated *via* introducing Zr into CoFe oxides, which not only tune the morphology but also modify the electronic environment around the Co and Fe sites for optimizing adsorption energies. More recently, Chu *et al.* [138] reported that Fe-doping could induce the crystalline nanoparticles of CeO_2 to transform to partially amorphous Fe-CeO_2 nanosheets, showing rich oxygen vacancies.

Moreover, the modulated NiFeW-LDHs with an appropriate W precursor concentration of 5 mM and well-aligned nanosheets are sonicated in isopropanol and then loaded on a copper grid for TEM characterization to gain a more insightful structure and composition distribution of the electrocatalyst. As shown in **Figure 24A**, the TEM images further validate the thin and flexible nanosheet features of the NiFeW-LDHs, which are almost transparent with an average thickness of about 5 nm (**Figure 22D**). Moreover, the nanosheets are composed of crystalline phases and partially amorphous-like phases according to **Figure 24B**, which well matches the results reported in our previous study. [139] Notably, the electronic structure of the NiFeW-LDHs is successfully engineered

because of the W doping, which would contribute to enhanced performances for water splitting. [139] Compared to crystalline phases, the amorphous-like phases in the structures possess rich unsaturated sites and randomly oriented bonds, showing great potential to expose more active sites for electrochemical reaction and therefore could considerably enhance the performance for water splitting. [138] Furthermore, the elemental composition is investigated by SEM-mapping and EDS characterization (**Figure 24C, D**). Based on the results, we could observe that the W element with an atomic ratio of about 2.79 is successfully doped in the structures and homogeneously distributed throughout the surface of CFPs.

Electrocatalytic performances of different electrocatalysts for OERs and HERs are evaluated in a conventional three-electrode cell in 1 M KOH at room temperature (Ar-saturated). As illustrated in **Figure 25A and D**, iR-corrected OER and HER polarization curves of different electrocatalysts are recorded at a scan rate of 5 mV/s for evaluation. To compare the performance of the prepared electrocatalysts, firstly, according to previous studies, the onset potential at about 1 mA/cm^2 or -1 mA/cm^2 are compared [81, 108, 109, 112, 115]. Meanwhile, to determine the exact onset potential, some measurement methods are performed in the previous study. For example, Nia, et al. [140] determined the HER onset potential (-0.4 V_{RHE}) *via* online differential electrochemical mass spectrometry measurements. From the OER LSV curves, we can observe that with the W doping, the OER activity of the NiFeW-LDHs is dramatically enhanced compared with that of NiFe hydroxides. The OER polarization curves show that the modulated NiFeW-LDHs electrocatalyst with well-aligned nanosheets (5 mM W precursor) exhibit the lowest onset

potential with a value of 211 mV, which is superior to the electrocatalysts prepared with 0 mM (235 mV), 2.5 mM (226 mV), 7.5 mM (211 mV), and 10 mM (220 mV) W precursor (**Figure 25A**). To deliver the current density of 10 mA/ cm^2, the well-aligned NiFeW-LDHs electrocatalyst affords an overpotential of 241 mV, lower than those of most other NiFeW-LDHs and much lower than that of NiFe hydroxides (272 mV) (**Figure 25B**). Based on the polarization curves, Tafel slopes of different electrocatalysts are calculated ($\eta = b \log |j| + a$, where j is the current density, and b is the Tafel slope)) to investigate the electrocatalytic kinetic of different electrocatalysts. As shown in **Figure 25C**, the well-aligned NiFeW-LDHs electrocatalyst exhibits a low Tafel slope of 37 mV/dec, a value between 30 mV/dec and 40 mV/dec, implying a rate-determining step in the OER process and contributing to the outstanding OER performance. [81] This Tafel slope is close to those of the NiFeW-LDHs based on 7.5 mM W precursor (36 mV/dec) and 10 mM W precursor (38 mV/dec) and is lower than those of the NiFeW-LDHs based on 2.5 mM W precursor (42 mV/dec) and the NiFe hydroxides (46 mV/dec), indicating the faster OER kinetics of the well-aligned NiFeW-LDHs.

For the HER performances of the series of electrocatalysts, a similar performance trend is presented in comparison to the OER performances. After introducing the W element, the HER activity of the NiFe hydroxides enhances remarkably, resulting in significant decreases of its onset potential and overpotential (**Figure 25D, E**). Among the series of W-doped LHDs, the well-aligned NiFeW-LDHs electrocatalyst shows the smallest onset potential of only 33 mV.

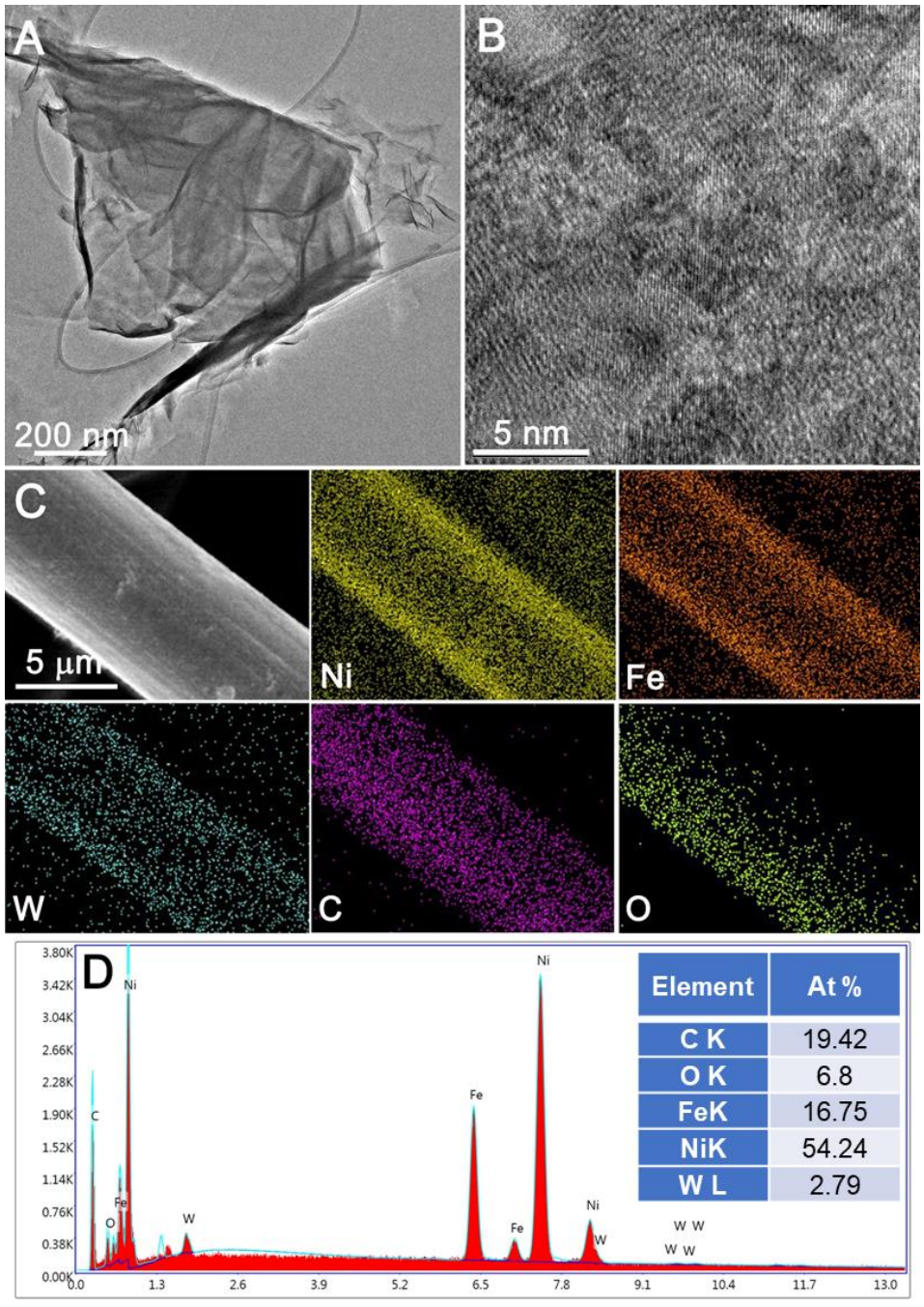


Figure 24. TEM images (A, B), SEM/EDS-mapping images (C), and EDS results of NiFeW-LDHs (5 mM W precursor) (D).

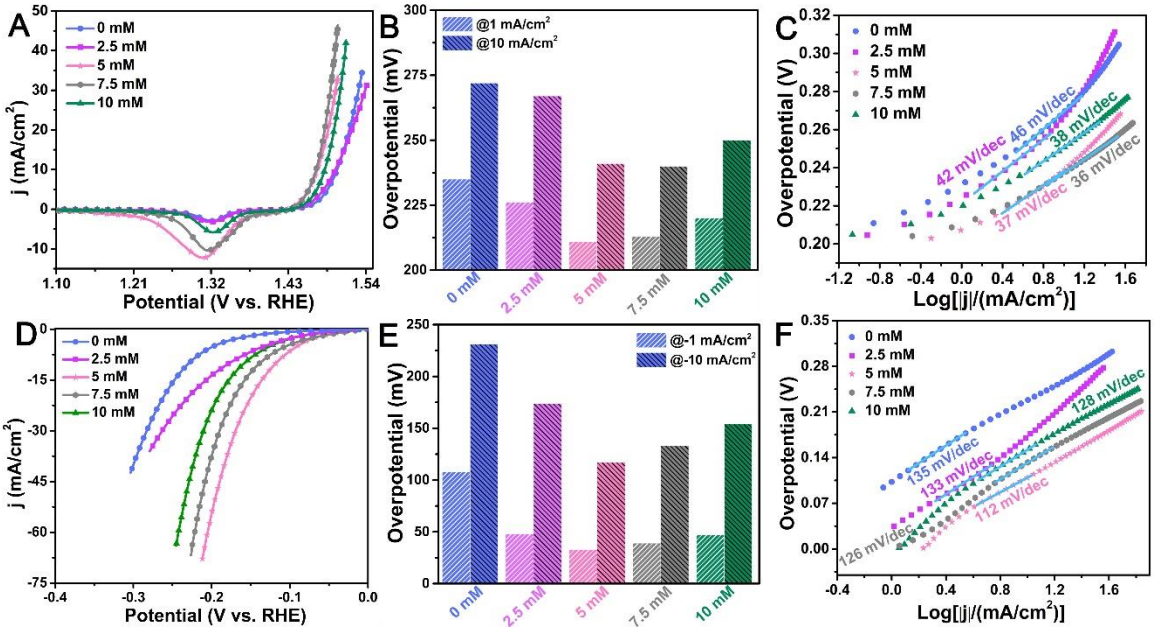


Figure 25. OER and HER performance evaluated in 1 M KOH with Ar-saturated at room temperature. The IR-corrected OER (A) and HER (D) polarization curves of different electrocatalysts. OER (B) and HER (E) overpotential comparisons at 1 mA/cm^2,10 mA/cm^2, -1 mA/cm^2 and -10 mA/cm^2. Corresponding OER (C) and HER (F) Tafel slopes.

Additionally, the lowest overpotential of 117 mV is also achieved by the well-aligned NiFeW-LDHs electrocatalyst, further verifying that 5 mM W precursor is an appropriate level for fabricating the nanosheet electrocatalyst. While the overpotentials of other electrocatalysts show a sequence of 7.5 mM (133 mV) < 10 mM (154 mV) < 2.5 mM (174 mV) < 0 mM (231 mV). Meanwhile, the intrinsic HER performance of different electrocatalysts is accessed by the Tafel plots. The derived Tafel slopes in **Figure 25F** reveal that the well-aligned NiFeW-LDHs electrocatalyst exhibit a moderate Tafel slope of 112 mV/dec, lower than those of electrocatalysts with other W precursor concentrations (0 mM: 135 mV/dec, 2.5 mM: 133 mV/dec, 7.5 mM: 126 mV/dec, and 10 mM: 128 mV/dec), indicating a faster HER kinetic. Moreover, the EIS tests are performed to further investigate the intrinsic reaction kinetics of the electrocatalysts. As presented in **Figure 26**, the OER and HER Nyquist plots recorded at the overpotentials of 210 mV and 150 mV, respectively, are fitted with reasonable equivalent circuits. For the OER EIS curves, the equivalent circuit composed of R_s (electrolyte resistance), R_1 (may ascribe to interfacial resistance), R_{ct} (charge transfer resistance), and CPE_1/CPE_2 (constant phase elements) is chosen as the fitting modeling because there are two arcs in the high- and low-frequency ranges, respectively, which could ascribe to the multistep and complex OER pathways [141-143]. For the HER EIS curves, the equivalent circuit without R_1 is used for the fitting since almost only one arc is observed. [117] Based on the equivalent circuit, EIS fitting is carried out and all derived parameters are summarized in **Table 8 and Table 9**. Compared to the case of the pristine NiFe hydroxides, electrocatalysts with W doping show remarkably decreased R_{ct} for both OERs and HERs. For the OER Nyquist plots (**Figure 26A**), the as-modulated NiFeW-LDHs with ultrafine nanosheet features exhibit a small R_{ct} of 1.276

$\Omega \cdot cm^2$, significantly lower than that of the NiFe hydroxides (~9.442 $\Omega \cdot cm^2$). The small R_{ct} of the well-aligned NiFeW-LDHs electrocatalyst is similar to that of NiFeW-LDHs with 7.5 mM W precursor (1.255 $\Omega \cdot cm^2$) and followed by those of 2.5 mM (~5.20 $\Omega \cdot cm^2$) and 10 mM-based (~3.938 $\Omega \cdot cm^2$) LDHs. Hence, the well-aligned NiFeW-LDHs electrocatalyst presents a faster faradaic process in OERs. Meanwhile, the values of interfacial resistance R_1 vary along with the W doping amounts (**Table 8**) and lower R1 may indicate more electrochemical reaction sites of the electrocatalysts. [16] As shown in **Table 8**, a low R_1 value (2.797 $\Omega \cdot cm^2$) is achieved for the well-aligned NiFeW-LDHs (5 mM), which is much smaller than those of electrocatalysts based on 0 mM, 2.5 mM, and 10 mM W precursor and similar to that of 7.5 mM-based electrocatalyst. For the HER Nyquist plots (**Figure 26B**), the smallest semicircle is observed for the well-aligned NiFeW-LDHs, contributing to the lowest R_{ct} (~9.235 $\Omega \cdot cm^2$), which is more than 9 folds lower than that of the pristine NiFe hydroxides. This indicates the fastest charge transfer of the well-aligned NiFeW-LDHs for the HER process. Additionally, the Bode plots of OERs and HERs reveal that the well-aligned NiFeW-LDHs show low resistance and phase angle among various electrocatalysts. This further demonstrates the outstanding charge transfer ability in both OER and HER processes, [144] which well matches the results in **Tables 8 and 9**. Moreover, similar electrolyte resistances are observed for all electrocatalysts, which is expected, since all measurements are performed in 1 M KOH. Furthermore, the ECSAs of different electrocatalysts are investigated *via* double-layer capacitance (C_{dl}), which is in proportion to ECSA and can be derived from the cyclic voltammetry tests. [132] As shown in **Figure 26C**, the well-aligned NiFeW-LDHs exhibit the largest C_{dl} value of 9.5 mF/cm^2, which is much higher than other electrocatalysts (0 mM:

2.3 mF/cm^2, 2.5 mM: 2.8 mF/cm^2, 7.5 mM: 6.0 mF/cm^2, and 10 mM:3.9 mF/cm^2). Based on the C_{dl} results, ECSA values of different electrocatalysts are evaluated *via* the equation of $ECSA = C_{dl}/C_s$, where C_s is the specific capacitance of 40 μF/cm$^2_{ECSA}$ for metal electrodes in 1 M KOH. [139] As a result, the calculated ECSA value for the 5 mM-based NiFeW-LDHs is 235.5 cm$^2_{ECSA}$/ cm^2, which is more than 4 times larger than that of the pristine NiFe hydroxides (57.5 cm$^2_{ECSA}$/ cm^2) and much higher than those of other electrocatalysts (2.5 mM: 70 cm$^2_{ECSA}$/cm^2, 7.5 mM: 150 cm$^2_{ECSA}$/cm^2, and 10 mM: 97.5 cm$^2_{ECSA}$/cm^2) (**Figure 26D**). The largest ECSA of the efficiently modulated NiFeW-LDHs well matches their low interfacial resistance from the EIS results, which could be expected through the vertically well-aligned nanosheet features. Notably, the large ECSA could expose more electrocatalytic active sites of the electrocatalyst and thus effectively decrease the conversion barriers for water splitting.

Overall, by tuning W doping amounts, electrocatalysts with different morphologies and various ECSAs are successfully obtained. Meanwhile, their different interfacial resistances are demonstrated according to the EIS fitting results. Furthermore, the electronic structure of the LDHs is also well-modulated due to the W doping. As a result, the NiFeW-LDHs based on 5 mM W precursor with the modulated electronic structure show ultrafine nanosheet features, the largest ECSA, low charge transfer resistance and interfacial resistance. Due to these factors, the electrolyte diffusion and the gas evolution are boosted, more electrochemical active sites are exposed, and faster charge transfer is achieved, which contributes to the excellent performances of the well-aligned NiFeW-LDHs for water splitting.

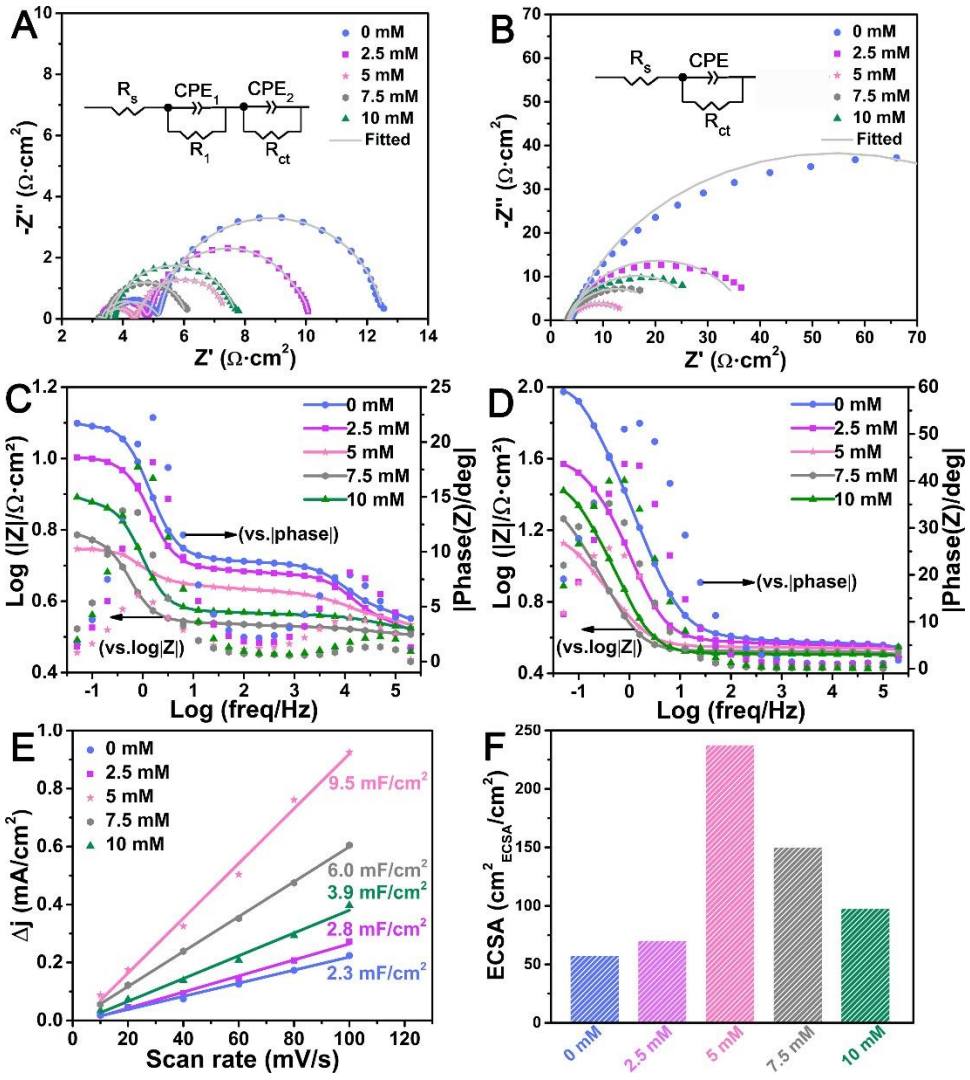


Figure 26. Nyquist plots at the overpotential of 210 mV for OERs (A) and 150 mV for HERs (B). Corresponding equivalent circuit models (Inset in A and B). The related OER (C) and HER (D) Bode plots: dots and solid lines: log(freq) vs. log(|Z|); dots: log(freq) vs. |phase|. Plots for deriving the double-layer capacitance (C_{dl}) (E). The electrochemically surface area (ECSA) comparison of different electrocatalysts (F).

Table 8. OER EIS fitting parameters derived from Nyquist plots in Figure 26A.

W concentration	R_s ($\Omega \cdot cm^2$)	CPE_1 (mF)	R_1 ($\Omega \cdot cm^2$)	CPE_2 (mF)	R_{ct} ($\Omega \cdot cm^2$)
0 mM	4.371	0.6613	7.370	45.38	9.442
2.5 mM	3.263	0.1346	5.075	42.71	5.204
5 mM	3.223	244	2.797	0.8713	1.276
7.5 mM	3.366	175.6	2.754	0.6057	1.255
10 mM	3.203	1.849	3.824	78.33	3.938

Table 9. HER EIS fitting parameters derived from Nyquist plots in Figure 26B.

W concentration	R_s ($\Omega \cdot cm^2$)	*CPE* (mF)	R_{ct} ($\Omega \cdot cm^2$)
0 mM	3.177	11.79	87.27
2.5 mM	3.014	23.98	28.24
5 mM	2.931	103.1	9.235
7.5 mM	2.903	95.39	16.33
10 mM	2.743	51.33	21.47

To further demonstrate the outstanding performances of the as-fabricated NiFeW-LDHs, overpotential comparisons at 10 mA/cm^2 in 1 M KOH with various electrocatalysts are performed. As a result, the NiFeW-LDHs electrocatalyst exhibits remarkably enhanced performances with low overpotentials for both the OERs (241 mV) and HERs (117 mV), which suppresses than those of NiFe hydroxides (the OERs: 272 mV, the HERs: 231 mV). Moreover, the electrochemical performance of the NiFeW-LDHs electrocatalyst is also superior to most of the recently reported electrocatalysts. For the OER performance, the OER overpotential of the NiFeW-LDHs electrocatalyst is smaller than most of recently reported OER electrocatalysts [85, 122, 123, 145-151] (**Table 10**). Moreover, the HER performance of the NiFeW-LDHs electrocatalyst is also better than most of the recent HER electrocatalysts [123, 81, 85, 88, 124, 137, 140, 145] (**Table 11**). Hence, the well-aligned NiFeW-LDHs electrocatalyst with a fast electrodeposition method shows excellent electrochemical performance toward both the HERs and OERs, which could remarkably enhance the commercialization of water splitting.

3.5 Conclusions

In this work, NiFeW-LDH nanosheets with controllable morphologies are successfully *in-situ* grown on carbon fiber papers *via* a one-step W-doping process with tunable W precursor concentrations. Notably, the doped W plays a crucial role in triggering heterogeneous seeds for the formation of the homogeneous nanosheet. With an appropriate W precursor concentration (5 mM), film-like NiFe hydroxides are efficiently modulated to NiFeW-LDHs with abundant vertically well-aligned nanosheets, showing a more than 4-time increased ECSA. As a result, the effectively modulated NiFeW-LDHs electrocatalyst

demonstrates considerably improved performances compared to pristine NiFe hydroxides, exhibiting decreased OER overpotential of 31 mV and HER overpotential of 114 mV at 10 mA/cm^2 and -10 mA/cm^2 respectively, in 1 M KOH. However, inferior OER and HER performances are demonstrated with lower or higher W precursor concentrations because of smaller and less structured nanosheets, leading to lower ECSA. Due to the significantly enhanced performances and a fast electrodeposition method, the well-aligned NiFeW-LDHs exhibit a great potential to boost the large-scale application of practical water splitting.

Table 10. OER overpotential comparison at 10 mA/cm^2.

Electrocatalysts	Electrolyte	Overpotential (at 10 mA/cm^2)	Reference
NiFeW-LDHs	1 M KOH	241	This work
Co-NiFe LDH	1 M KOH	278	123
$Ni_{0.6}Fe_{0.3}Cr_{0.1}O_x$/CC	1 M KOH	251	85
FeCoNi	1 M KOH	288	145
ZIF@LDH	1 M KOH	318	146
(Ni, Fe)S_2@MoS_2	1 M KOH	270	1470
MoP/NF	1 M KOH	265	148
Ni@CoO@CoNC	1 M KOH	309	149
FeB_2	1 M KOH	296	150
NiFe-NS	1 M KOH	300	151

Table 11. HER overpotential comparison at -10 mA/cm^2.

Electrocatalysts	Electrolyte	Overpotential (at -10 mA/cm^2)	Reference
NiFeW-LDHs	1 M KOH	117	This work
NiFeSe	1 M KOH	154	124
$Ni_{0.75}Fe_{0.125}V_{0.125}$-LDHs/NF	1 M KOH	125	140
FeCoNi	1 M KOH	149	85
Ni_2P/rGO	1 M KOH	142	88
NiFe NTAs-NF	1 M KOH	181	145
Ni-Fe-P nanocubes	1 M KOH	182	123
Co/(NiCo)Se_2	1 M KOH	190	81

CHAPTER FOUR

AN EFFICIENT INTEGRATED ELECTRODE ENABLES HIGH-CURRENT OPERATION AND EXCELLENT STABILITY FOR GREEN HYDROGEN PRODUCTION

A version of this chapter was originally published as:

Ding, L.,[1] Wang, W.,[1] Xie, Z., Aaron, D.S., Paxson, A., Hamdan, M., Mench, M.M. and Zhang, F.Y., Efficient Integrated Electrode Enables High-Current Operation and Excellent Stability for Green Hydrogen Production. ACS Sustainable Chemistry & Engineering 11, no. 30 (2023): 11219-11228.

[1] These authors contribute equally to this work.

CRediT authorship contribution statement

L.D.: Conceptualization, Methodology (electrode fabrication, SEM, SEM-EDS mapping, XRD characterizations, performance evaluation), Data curation, Writing - original draft, review & editing, Investigation, Validation. W.W.: Conceptualization, Methodology (electrode fabrication, performance evaluation), Data curation, Writing - review & editing, Investigation, Validation. Z.X.: Validation, Methodology, Writing - review & editing. D.S.A.: Validation, Writing - review & editing. A.P.: Methodology (CCM fabrication), Validation, Writing - review & editing. M.H.: Validation, Writing - review & editing. M.M.M.: Validation, Writing - review & editing. F.-Y. Z: Conceptualization, Supervision, Validation, Writing - review & editing.

I am fully responsible for the work submitted in these publications.

4.1 Abstract

Generating green hydrogen through proton exchange membrane electrolyzer cells (PEMECs) is promising to build future sustainable energy systems. Operating PEMECs at high current densities with high efficiency is a realistic strategy to reduce the capital costs of PEMECs and increase their sustainability. Herein, an Ir-integrated electrode was developed *via* facile electrodeposition as an efficient anode for PEMECs, successfully achieving high-current operation of up to 6 A/cm^2. More importantly, the electrode shows excellent stability under an ultrahigh current density of 5 A/cm^2, showing almost no performance loss after the stability test. Further studies indicate that a platinum protection layer on Ti substrates plays a crucial role in superior performance and stability, which not only provides electrodes with improved electrical conductivity resulting in improved catalyst activity but also enhances crack-free catalyst layer achieving catalysts' adhesion improvement to the substrate and prevents the substrate oxidation. With platinum, the cell voltage can be improved by 33, 59, and 87 mV at current densities of 2, 4, and 6 A/cm^2, respectively. Overall, considering efficient high-current operation capability, remarkable stability and significantly simplified and low-cost fabrication process with easy scalability, the developed integrated electrodes are believed to have great potential in future sustainable energy systems.

4.2 Introduction

The development of sustainable energy systems attracts great interest in human society. Hydrogen is offered by many as a potential candidate to act as an energy storage media in future sustainable energy systems.[152-160]; The integration of sustainable energy sources and electrolysis devices is a widely recognized technical route to produce sustainable hydrogen. In the present electrolysis markets, alkaline electrolysis is the earliest and most mature technique to produce "green hydrogen". While disadvantages of alkaline electrolysis, including low partial load range, limited current density, and low operating pressure, urge people to develop advanced electrolysis devices to ensure compatibility with fluctuated sustainable energy sources. [3, 161-166] In the 1960s, General Electric first developed water electrolyzers based on solid polymer electrolytes.[3, 161, 167] The developed proton exchange membrane (PEM) has the advantages of high proton conductivity, low gas crossover, high-pressure operation, and compact system design.[40, 168-171] Nowadays, PEM electrolyzer cells (PEMECs) have been considered as one of the most promising candidates for commercial sustainable hydrogen production. Advantages of the PEMEC include high current density (above 2 A/cm^2), high hydrogen pressure, high hydrogen purity, long durability, *etc.* However, before the large-scale application in sustainable systems, the cost barriers of the PEMEC must be overcome.

The high costs of the PEMECs including capital costs, operation costs and maintenance costs hinder the large-scale applications of the PEMEC. One realistic method to reduce the high costs is to produce more hydrogen with a given PEMEC system, which means that a relatively high operating current density is desired.[172] In the academic community, various

PEMECs operated at a current density higher than 4 A/cm^2 are reported.[172-175] Another strategy to reduce the costs is to simplify and optimize the fabrication procedure of membrane electrode assembly (MEA). For conventional MEAs, catalyst-coated membranes (CCMs) are normally used, in which catalysts need to be mixed with ionomer to form inks first, and then coated on each side of the membrane. The conventional MEA preparation method usually involves complex procedures including Adams fusion reactions, drying, mixing, ultrasonic stirring, ultrasonic spraying, decal transfer, *etc*. The complex fabrication process causes high energy and material costs, which decreases sustainability. Moreover, the preparation parameters usually significantly impact the PEMEC performance.[176-179] So far, various studies about the conventional MEA have been reported. For example, Xie *et al.*, [180] carefully tuned the ionomer content in the anode catalyst layer to achieve the best cell performance. Mo *et al.*, [181] discovered that the electronic conductivity and wettability of the catalyst layer need to be carefully optimized to achieve a uniform reaction distribution in the catalyst layer and higher catalyst utilization. These tuning processes are usually costly and time-consuming, which normally require relatively high facility costs, labor costs, and time costs. To simplify the MEA fabrication and increase the sustainability of fabrication, IrO_2 catalysts were directly sputtered on carbon papers or electrodeposited on porous Ti meshes to be anodes for the PEMEC.[24, 27] Moreover, Pt-coated gas diffusion electrodes were developed by Kang *et al.*, [29] for hydrogen evolution reactions (HERs), achieving a 58-fold higher mass activity compared to the conventional CCM. In addition, Yu *et al.*, [25] adopted a facile electrodeposition process to prepare a series of catalyst-coated liquid/gas diffusion layers (CCLGDLs), delivering high hydrogen production efficiency. Based on different thin/tunable liquid/gas

diffusion layer (TTLGDL) substrates, they unveiled that the substrate patterns have great impacts on the activation and utilization of catalysts. With a similar porosity, the substrate with a smaller pore size could achieve better performance. However, electrodes with high current-operation feasibility and excellent stability are critical for PEMEC commercialization. The superior performance of CCLGDLs has been validated in the current density range of 0 ~ 3 A/cm^2, but their performances and stabilities at ultra-high current density have not been demonstrated.

Herein, integrated electrodes achieving high-current operation up to 6 A/cm^2 were developed by depositing Ir catalysts on sintered Ti powder substrates *via* a facile and efficient electrodeposition process as high-performance anodes for the PEMEC. As discovered, with a Pt protection layer, cell voltages at 2, 4 and 6 A/cm^2 can be improved 33, 59 and 87 mV, respectively. In addition, excellent stability at an ultrahigh current density of 5 A/cm^2 is demonstrated, showing almost no performance loss after the stability test. The improved performance and remarkable stability are due to the Pt layer on the Ti substrate, which not only provides the electrode excellent electrical conductivity to achieve improved catalyst activity but also enables a crack-free catalyst layer without peel-off achieving enhanced catalyst adhesion to the substrate and avoids the Ti substrate oxidizing under harsh conditions. Hence, due to the significantly simplified fabrication with low-cost and easy scalability, efficient high-current operation capability, and outstanding stability, the developed integrated electrode shows great potential to decrease hydrogen costs and ensure sustainability in future sustainable energy systems.

4.3 Experimental Section

4.3.1 Electrode fabrication and characterization

Ir catalysts were electrodeposited on two kinds of substrates: the Pt-coated sintered Ti powder (Pt sintered Ti) and bare sintered Ti powder (sintered Ti), which are provided by Plug Power (Latham, NY). Before the Ir electrodeposition, the substrates were immersed in acetone for 10 min to remove organic chemicals and impurities. Afterward, deionized (DI) water was used to rinse the substrates several times to remove inorganic chemicals and impurities. Subsequently, the rinsed substrates were pre-treated in 0.05 mol/L oxalic acid solution at 90 ℃ for 14 min to remove the surface oxides. At a constant voltage of 1.5 V and under 85 ℃, about 0.5 mg/cm^2 Ir catalysts were electrodeposited on the two substrates to obtain samples of 0.5-Ir/Pt sintered Ti and 0.5-Ir/sintered Ti, respectively. Meanwhile, a lower Ir loading of 0.3 mg/cm^2 was also electrodeposited on the Pt-coated substrate to form 0.3-Ir/Pt sintered Ti for further comparison. The Ir loadings on substrates were calculated by the mass differences before and after electrodeposition. In addition, the morphologies and element distributions of all samples were characterized by a field emission JSM-IT700HR scanning electron microscope (SEM) with energy-dispersive X-ray spectroscopy (EDS).

4.3.2 The PEMEC assembly and test

For cell tests, cathode-only catalyst-coated membranes (CCMs) from Plug Power with a thickness of 50 μm (Nafion 212) were used, showing a Pt black catalyst loading of 0.4 mg$_{PtB}$/cm^2 for the cathode catalyst layer and an active area of 5 cm^2. Microporous layer-

coated carbon papers (MPL/CP) were adopted as cathode gas diffusion layers (GDLs). The prepared electrodes of Ir/Pt sintered Ti and Ir/sintered Ti were used as anodes. Au-coated Ti plate and graphite plate showing parallel flow channels were used as anode and cathode bipolar plates, respectively. The CCM was sandwiched by the prepared electrode and MPL/CP to form the membrane electrode assembly (MEA). The assembled MEA, gaskets, copper plates and bipolar plates were sandwiched by two stainless steel endplates to form a PEMEC. The copper plates were inserted between the bipolar plate and the endplate to apply current to the PEMEC. Subsequently, the whole PEMEC was uniformly tightened to 40 in·lb of torque by eight evenly distributed bolts. A potentiostat with a booster (VSP/VMP-100, Bio-Logic) was used to record all the tested data. With a water flow rate of 60 mL/min at the anode, the cell test was carried out at 80 °C and 1 atm. The cell temperature was maintained by a pre-heat water bath (WB10, Poly science) and a PID temperature controller. Cell polarization curves were measured within a current density range of 0~6 A/cm^2. High-frequency resistance (HFR) plots were recorded at a frequency of 5 kHz. Electrochemical impedance spectroscopies (EIS) measurements were recorded at a current density of 0.2 A/cm^2 within 10 kHz ~ 100 mHz.

4.4 Results and Discussions

As illustrated in **Figure 27**, Ir-integrated electrodes can be easily obtained by directly electrodepositing Ir catalysts on sintered Ti substrates, serving as efficient anodes for the PEMEC. SEM images of the two used sintered Ti substrates are shown in **Figure 36**: the bare sintered Ti shows smooth surfaces (**Figure 36A and B**) while the Pt-coated sintered Ti has rough surfaces (**Figure 36C and D**). As seen in **Figure 28**, without or with the Pt

coating, different catalyst layer morphologies are observed after the Ir deposition. For the bare sintered Ti substrate, with the Ir deposition, the obtained Ir/sintered Ti surface shows some cracks and peel-off and also some bare Ti surfaces, and nanoparticles are observed at higher magnification (**Figure 28A-C**). In addition, SEM-EDS mapping images were performed and the Ir element is relatively homogeneously distributed on the Ti substrate (**Figure 37**). For the Pt-coated substrate, rough surfaces are maintained after the Ir electrodeposition. Notably, there are no catalyst cracks and peel-off and bare Ti substrates observed on the Ir/Pt sintered Ti surface (**Figure 28D and E**), which could offer more active sites for the electrochemical reaction. Meanwhile, the resultant catalysts also show nanoparticle morphologies with rough surfaces on the Pt-coated Ti substrates (**Figure 28F**), which are crack-free and could protect the substrate well. With the SEM-mapping characterization (**Figure 28G**), we could find that the Ir element is homogeneously covered on the Pt-coated Ti substrate. Hence, the Pt coating on the Ti substrate enables crack-free Ir catalyst layer formation, which is expected to improve the catalyst activity and electrode stability under aggressive operation conditions or long-term operations.

With a similar Ir loading of about 0.5 mg/cm^2, the two electrodes of 0.5-Ir/Pt sintered Ti and 0.5-Ir/sintered Ti were combined with cathode-only CCMs for cell tests. As shown in **Figure 29A**, the electrode of 0.5-Ir/Pt sintered Ti exhibits better cell performance and higher efficiency than those of the 0.5-Ir/sintered Ti within the test range of 0 ~ 6 A/cm^2. Cell voltages at 2, 4 and 6 A/cm^2 of the two electrodes are collected and compared. As presented in **Figure 29B,** the 0.5-Ir/Pt sintered Ti shows low cell voltages of 1.682, 1.814 and 1.930 V at 2, 4 and 6 A/cm^2, respectively, which are 33, 59 and 87 mV lower than those of the 0.5-Ir/sintered Ti (1.715 V, 1.873 V, and 2.017 V at 2 A/cm^2, 4 A/cm^2, and 6

A/cm^2, respectively). Meanwhile, energy conversion efficiency is an important indicator of sustainable energy utilization. A higher efficiency usually means more energy storage with the same energy inputs, which indicates superior sustainability. In this study, the efficiency is calculated based on high heat value (HHV), which is the ratio between thermal neutral voltage (1.48 V at 80 ℃) and cell voltage at different current densities (Efficiency=$V_{thermal\ neutral}/V_{cell}$ (1)). [182] As shown in **Figure 29A**, the efficiency curve of the 0.5-Ir/Pt sintered Ti is above that of the 0.5-Ir/sintered Ti, which indicates higher efficiency is achieved. Specifically, higher cell efficiency values of about 89%, 82%, 77% are achieved at 2 A/cm^2, 4 A/cm^2, and 6 A/cm^2, respectively for the 0.5-Ir/Pt sintered Ti. While lower efficiency values of about 86%, 79%, 73% are obtained at 2 A/cm^2, 4 A/cm^2, and 6 A/cm^2, respectively, for the 0.5-Ir/sintered Ti. Meanwhile, mass-specific currents at 1.7 V of the two electrodes were collected and compared. And the 0.5-Ir/Pt sintered Ti shows a higher mass-specific current value of 4.5 A/mg_{Ir} than that of the 0.5-Ir/sintered Ti (3.7 A/mg_{Ir}). The superior performance of the 0.5-Ir/Pt sintered Ti should be because of the Pt coating layer on the Ti substrate surface, which serves as a protecting layer to avoid the Ti substrate to be oxidized under the high current operation and ensures a good conductivity of the electrode. Hence, lower HFR values are expected for the 0.5-Ir/Pt sintered Ti. Meanwhile, the better conductivity of the substrate could boost the catalyst utilization and thus result in superior performance.

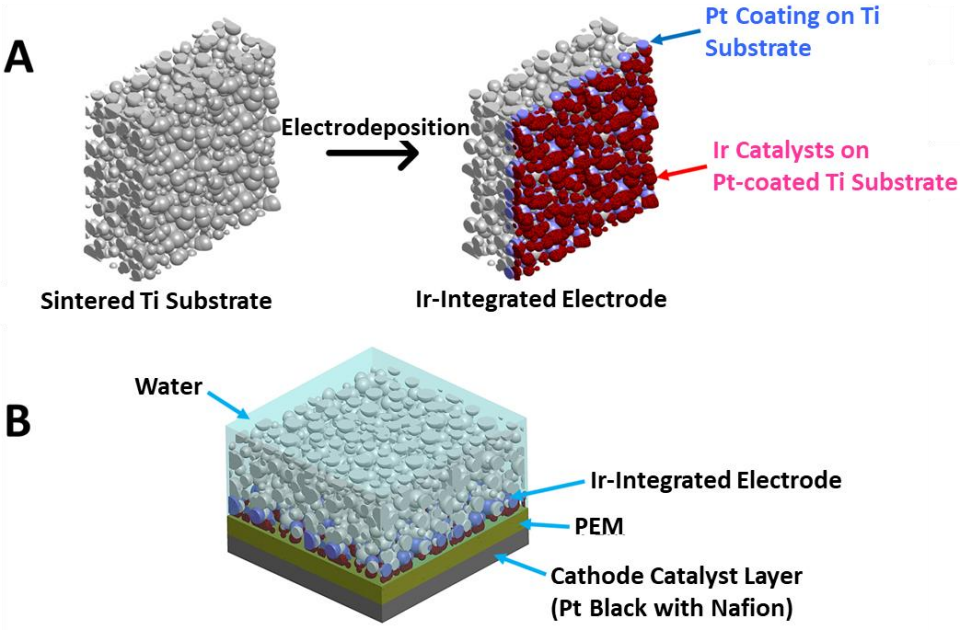


Figure 27. Schematic of (A) Ir-integrated electrode fabrication. (B) Anode side membrane electrode assembly based on the Ir-integrated electrode for the PEMEC application.

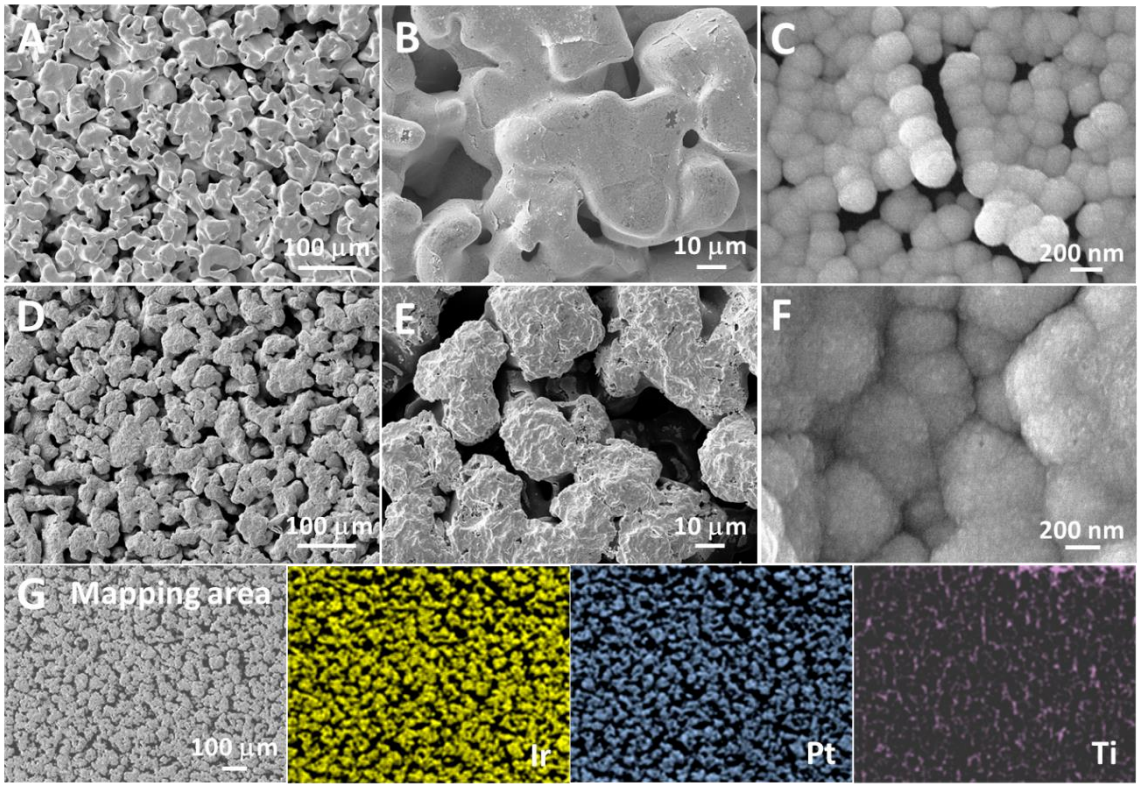


Figure 28. (A-C) SEM images of the Ir/sintered Ti at different magnifications; (D-F) SEM images of the Ir/Pt sintered Ti at different magnifications and (G) SEM-EDS mapping images of the Ir/Pt sintered Ti.

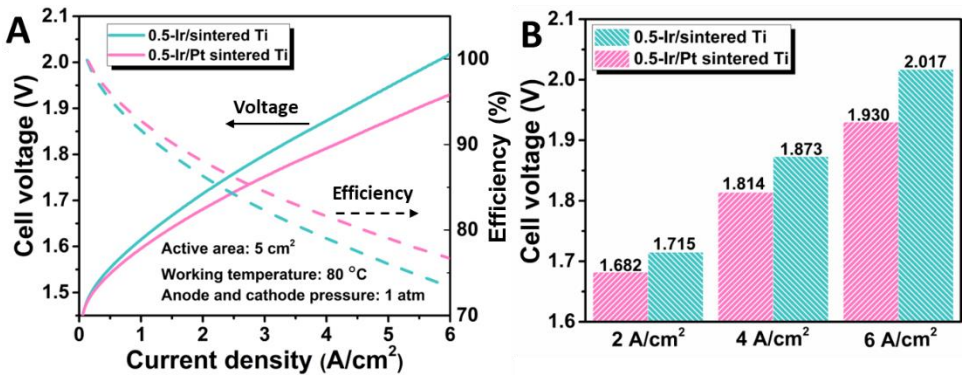


Figure 29. (A) Cell polarization and efficiency curves of different electrodes: 0.5-Ir/sintered Ti and 0.5-Ir/Pt sintered Ti. (B) Cell voltage comparison of different electrodes at 2, 4 and 6 A/cm^2, respectively.

HFR plots are recorded within 0 ~ 2 A/cm^2 and presented in **Figure 30A**. As expected, the 0.5-Ir/Pt sintered Ti shows a low HFR value of 47 mΩ·cm^2 at 2 A/cm^2, which is 12 mΩ·cm^2 smaller than that of the 0.5-Ir/sintered Ti with an HFR value of 59 mΩ·cm^2. The decreased HFR value of 12 mΩ·cm^2 for the 0.5-Ir/Pt sintered Ti contributes to 24 mV cell voltage improvement at 2 A/cm^2. Hence, part of the 33-mV voltage difference at 2 A/cm^2 is ascribed to the HFR improvement, and the rest 9-mV voltage difference should be from the catalyst activity difference. Both electrodes are coated with metallic Ir catalysts, the difference is the substrate, one is a bare Ti substrate, and the other is a Pt-coated substrate. Hence, the catalyst activity difference should be from the Pt coating. As reported by previous studies,[34, 183, 184] the Pt coating or support offers sufficient electrical conductivity and electrochemical stability of catalysts and thus shows enhanced performance. For example, Ioroi *et al.* [183] adopted Pt black as the support of the IrO_2 catalysts and achieved improved performance for both fuel cell and water electrolyzer. Lim *et al.* [34] fabricated nanostructured Pt on Ti felt substrates first and then deposited IrO_2 on the surface of the Pt-coated Ti felt for the unitized regenerative fuel cell (URFC) application. Based on the HFR plots, HFR-free cell polarization curves are derived. As shown in **Figure 30B**, the 0.5-Ir/Pt sintered Ti shows a low HFR-free voltage of 1.587 V at 2 A/cm^2. While a higher HFR-free voltage of 1.595 V is presented for the 0.5-Ir/sintered Ti. The voltage difference of 8 mV almost matches well with the activation loss mentioned above.

To quantitatively analyze different losses in the cell performance of the two electrodes, EIS measurements were performed at 0.2 A/cm^2 and fitted. As shown in **Figure 31A**, one arc is presented for the two electrodes, showing two intersections with the X-axis. The left intersection at the high-frequency range represents the ohmic resistance and the right one

at the low-frequency range is the resistance sum of the whole cell.[100, 185, 186] Since the recorded current density of 0.2 A/cm^2 is low, the arc should be assigned to charge transfer rather than diffusion since mass transport should not be a problem within low current density ranges.[187] To get more insight into the ohmic loss and activation loss, an appropriate equivalent electrical circuit is used to fit the EIS plots.[188] As shown in **Figure 31B**, components of an inductor *L*, a resistor R_Ω related to ohmic loss, a resistor assigned to the charge transfer and a constant phase element *Q* are involved in the circuit. The fitting results are collected and presented in **Table 12**. Small errors of 0.2606% and 0.2536% are found for the Ir/Pt sintered Ti and Ir/sintered Ti, respectively, indicating that a well-matched fitting is achieved with the chosen circuit. As shown in the table, a lower ohmic resistance of about 44 mΩ·cm^2 is found for the Ir/Pt sintered Ti while the Ir/sintered Ti shows a higher value of about 51 mΩ·cm^2, indicating a lower ohmic loss. This is in good accordance with the HFR results shown in **Figure 31A**. Moreover, the Ir/Pt sintered Ti shows a lower charge transfer resistance of about 131 mΩ·cm^2 while a higher value of 137 mΩ·cm^2 is observed for the Ir/sintered Ti powder, which means that a lower activation loss is achieved for the Ir/Pt sintered Ti.

Meanwhile, capacity between the electrode and membrane, double layer capacitance (C_{dl}) is also derived based on the Nyquist plots, which is closely related to the number of active sites. [139, 189-193] The higher value of the C_{dl}, the more active sites are achieved for the electrode. As shown in **Table 12**, a higher C_{dl} value of 10.27 mF/cm^2 is observed for the Ir/Pt sintered Ti, and a lower one is presented for Ir/sintered Ti with a value of 8.250 mF/cm^2. The higher C_{dl} value indicates more active sites are achieved for Ir/Pt sintered Ti.

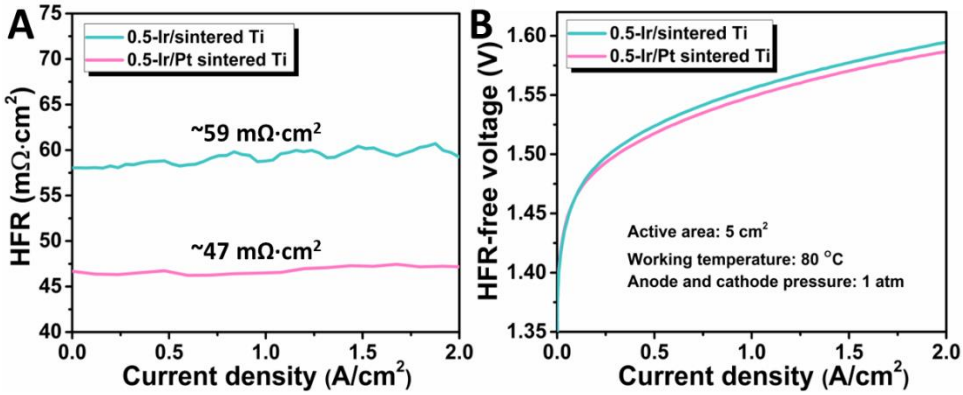


Figure 30. (A) The HFR plots of the 0.5-Ir/sintered Ti and 0.5-Ir/Pt sintered Ti. (B) The related HFR-free cell polarization curves the 0.5-Ir/sintered Ti and 0.5-Ir/Pt sintered Ti.

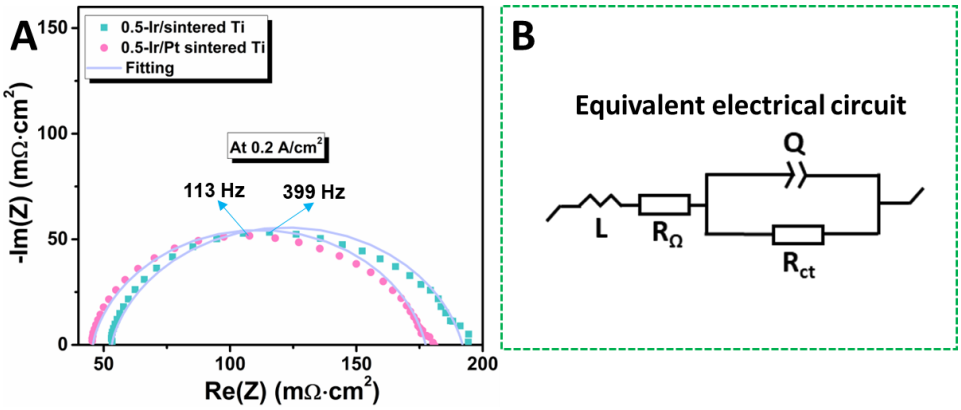


Figure 31. EIS plots of the 0.5-Ir/sintered Ti and 0.5-Ir/Pt sintered Ti at (A) 0.2 A/cm^2. (B) The related equivalent electrical circuit for fitting.

Overall, due to the smaller ohmic loss and activation loss and more active sites, improved cell performance is demonstrated for the Ir/Pt sintered Ti. In addition, as shown in **Figure 31A**, a lower peak frequency of 126 Hz is observed for the Ir/Pt sintered Ti (the Ir/sintered Ti: 399 Hz). Based on the EIS theory, [194] the peak frequency of the EIS plot is decreased as the increase along with the multiplying charge transfer resistance and double layer capacitance, as shown in the equation: $\omega=1/(R_{ct}*C_{dl})$ (2). Hence, considering the lower R_{ct} of the Ir/Pt sintered Ti cell, the lower peak frequency of the Ir/Pt sintered Ti also implies more active sites exposed to the electrochemical reaction.

Based on the optimized 0.5-Ir/Pt sintered Ti electrode, a lower catalyst loading of 0.3 mg/cm^2 was electrodeposited on the Pt-coated substrate to obtain an electrode of 0.3-Ir/Pt sintered Ti for further performance comparison. As shown in **Figures 32A and B**, even though with a lower Ir loading, the 0.3-Ir/Pt sintered Ti sample shows a similar performance to that of the 0.5-Ir/Pt sintered Ti (0.3-Ir/Pt sintered Ti: 1.671 V, 1.800 V, 1.911 V at 2 A/cm^2, 4 A/cm^2, 6 A/cm^2, respectively). In addition, a similar HFR-free cell voltage at 2 A/cm^2 of 1.583 V is achieved with the lower Ir loading compared to that of the 0.5-Ir/Pt sintered Ti (1.587 V). Meanwhile, the efficiency curve of the 0.3-Ir/Pt sintered Ti is also derived for comparison, showing similar efficiency values (89%, 82%, 77% at 2 A/cm^2, 4 A/cm^2, 6 A/cm^2, respectively,) to those of the 0.5-Ir/Pt sintered Ti (**Figures 32A**). Notably, with a lower catalyst loading of 0.3 mg/cm^2 and similar cell performance, a higher mass-specific current of 8.1 A/mg$_{Ir}$ at 1.7 V is achieved for the 0.3-Ir/Pt sintered Ti. As presented in **Figure 32C**, similar EIS plots with the same characteristic frequencies are observed, indicating similar activation loss for the two samples to some extent.

Table 12. Fitting results from EIS plots in Figure 31A.

Electrode	R_{Ω} [mΩ·cm^2]	R_{ct} [mΩ·cm^2]	Q [mF·s^{n-1}/cm^2]	n	C_{dl} [mF/cm^2]	Error [%]
Ir/Pt sintered Ti	43.96	131.0	24.38	0.8693	10.27	0.2606
Ir/sintered Ti	51.40	136.5	21.30	0.8603	8.25	0.2536

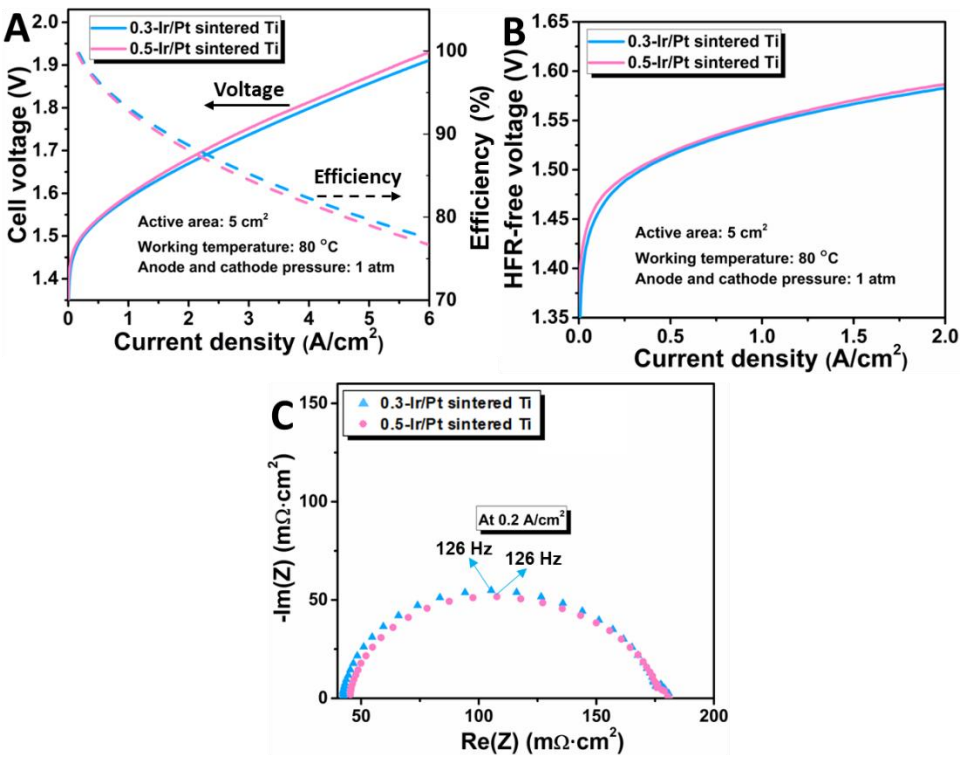


Figure 32. (A) Cell polarization and efficiency curves of Ir/Pt sintered Ti electrodes with different Ir loadings: 0.3 mg/cm^2 and 0.5 mg/cm^2, respectively. (B) The related HFR-free cell polarization curves of the 0.3-Ir/Pt sintered Ti and 0.5-Ir/Pt sintered Ti. (C) EIS plots of the 0.3-Ir/Pt sintered Ti and 0.5-Ir/Pt sintered Ti at 0.2 A/cm^2.

Hence, compared to 0.5 mg/cm^2, a lower catalyst loading of 0.3 mg/cm^2 is enough for the electrochemical reaction while with higher catalyst utilization, which can decrease the PEMEC capital cost and accelerate its commercialization.

To demonstrate the sustainability and advantages of the developed Ir-integrated electrode, performance and fabrication comparisons with different anodes for the PEMEC were performed and shown in **Figure 33** and **Table 13**. As presented in **Figure 33A**, the developed 0.5-Ir/Pt sintered Ti exhibits better performance than most of the previously reported anodes with a low voltage of 1.682 V at 2 A/cm^2.[194-201] Meanwhile, the 0.5-Ir/Pt sintered Ti shows higher catalyst utilization with a high mass-specific current of 4.5 A/mg$_{Ir}$ at 1.7 V (**Figure 33B**). Moreover, the 0.3-Ir/Pt sintered Ti achieves a higher catalyst utilization with a higher mass-specific current of 8.1 A/mg$_{Ir}$ at 1.7 V due to the lower catalyst loading. Moreover, as shown in **Table 13**, most of the previously reported anodes show complex fabrication methods, which are typical traditional CCM fabrication methods with multiple steps and elaborate equipment. Generally, these studies need to prepare catalyst powders first with different methods of molten salt oxidation route, solvothermal method, sol-gel method, etc., and then mix the obtained catalyst powders with ionomer and solvent to form catalyst ink. Afterward, the prepared catalyst ink was sprayed or bladed on the membrane to form CCM, which normally involves elaborate or additional equipment such as a spray coater, Mayer-rod coating machine and tube furnace. [46-52] While the developed Ir-integrated of this study shows a facile and easily scalable electrodeposition process, which is significantly simplified, low cost, energy-saving and without elaborate equipment involved. Hence, the developed Ir-integrated with the facile electrodeposition method shows significant low cost and sustainability for renewable energy production.

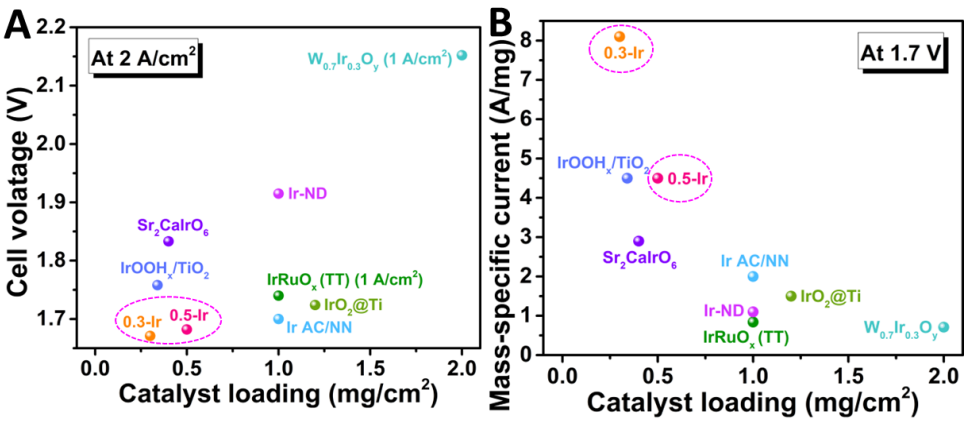


Figure 33. (A) Cell voltage comparison at 2 A/cm^2 with previously reported anode electrodes: IrO_2@TiO_2; $IrRuO_x$ (TT); $IrOOH_x/TiO_2$; $W_{0.7}Ir_{0.3}O_y$; Sr_2CaIrO_6; Ir AC/NN; Ir-ND. (B) The related mass-specific current comparison at 1.7 V.

Table 13. Details of different anodes and related cell performances.

Anode catalyst	Anode fabrication	Catalyst loading	Voltage (V) at 2 A/cm^2	Mass-specific current at 1.7 V (A/mg)	Elaborate /Additional equipment	Ref.
0.5-Ir	**Electrodeposition**	**0.5**	**1.682**	**4.5**	**/**	**This work**
0.3-Ir	**Electrodeposition**	**0.3**	**1.671**	**8.1**	**/**	**This work**
IrO_2@TiO_2	Wet chemical method/spray	1.2	1.724	1.5	Spray coater.	195
$Ir_{0.7}Ru_{0.3}O_X$ (TT)	Wet chemical method/spray	1	1.740*	0.84	Spray coater	196
$IrOOH_x/TiO_2$	Molten salt oxidation route/blade	0.34	1.758	4.5	Mayer-rod coating machine	197
$W_{0.7}Ir_{0.3}O_y$	Solvothermal method/ replacement reaction method/spray	2	2.152*	0.71	Tube furnace /spray coater	198
Sr_2CaIrO_6	Sol-gel method/spray	0.4	1.833	2.9	Tube furnace /spray coater	199
Ir AC/NN	Modified molten salt synthesis method/polyol method/spray	1	1.700	2	Tube furnace /spray coater	200
Ir-ND	Sol-gel and hydrothermal method/wet chemical/spray	1	1.915	1.1	Freeze dryer/spray coater	201

*Voltage at 1 A/cm^2.

Apart from the cell voltage investigation, electrode stability is also a critical parameter for the long-term operation of the PEMEC. As shown in **Figure 34**, the stability of the two electrodes was evaluated at an ultrahigh current density of 5 A/cm^2. The result presents that the Ir/Pt sintered Ti shows better stability compared to that of the Ir/sintered Ti. For the Ir/Pt sintered Ti, three pumps at about the 5th hour, 27th hour, and 47th hour are observed, which are due to the water refilling at the anode side water supply tank. However, the cell became stabilized soon after the water refilling. After the first 5-h cell stabilization, the PEMEC based on the Ir/sintered Ti operated stably for 80 h at the ultrahigh current density of 5 A/cm^2 with a small cell voltage increase from 1.933 V to 1.953 V. As a result, the Ir/Pt sintered Ti shows a low degradation rate of about 0.223 mV/h after an 80-h stability test at the ultrahigh current density of 5 A/cm^2. While the Ir/sintered Ti shows inferior stability with a much shorter operation of about 18 h at 5 A/cm^2. Evaluated from the 5th h, the cell voltage obviously increased from 2.006 V to 2.066 V, showing a high degradation rate of 3.35 mV/h. This might be due to the severe Ti substrate oxidation and the formation of some possible cracks and peel-off in the catalyst layer. As shown in SEM images in **Figures 28B and C**, when the Ir catalysts were directly electrodeposited on the sintered Ti without the Pt coating, some cracks and peel-off are observed. Due to the cracks and peel-off, the Ti substrate cannot be well protected and then is oxidized under the aggressive operation condition, thus resulting in inferior stability. While for the Ir/Pt sintered Ti, the rougher Pt-coated Ti substrate contributes to a crack-free catalyst layer, as shown in the SEM images in **Figures 28E and F**. This should be the main reason why the Ir/Pt sintered Ti shows good stability at the ultrahigh current density.

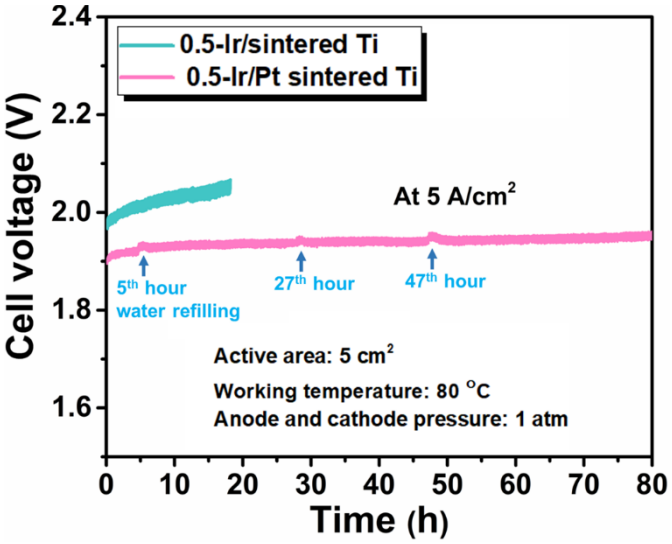


Figure 34. Cell stability tests at an ultrahigh current density of 5 A/cm^2 of the Ir/sintered Ti electrodes and Ir/Pt sintered Ti electrode.

Cell performance and efficiency after the stability test were also recorded for comparison. As shown in **Figure 35A,** for the 0.5-Ir/Pt sintered Ti, the degradation from the stability test is recoverable, and the cell performance is well-maintained after the 80-h stability test at the ultrahigh current density of 5 A/cm^2, showing similar cell voltages of 1.671, 1.819 and 1.954 V at 2, 4 and 6 A/cm^2, respectively, as collected in **Table 14**. Hence, similar efficiency is maintained after the stability test, showing values of 89%, 81%, 76% at 2, 4 and 6 A/cm^2, respectively. In addition, similar average HFR values are observed: 47 mΩ·cm^2 before the stability test and 51 mΩ·cm^2 after the stability test (**Figure 35B**). The above results demonstrate the remarkable stability of the 0.5-Ir/Pt sintered Ti even under such a harsh operation condition. Notably, the reversible performance loss could be due to the gas stagnation within the catalyst layer and the slightly increased voltage can be recovered by interrupting the cell current.[202 203] While for the 0.5-Ir/sintered Ti, obviously increased cell voltages of 1.738, 1.960 and 2.134 V at 2, 4 and 6 A/cm^2 are observed (**Figure 35C**) after the stability test. Meanwhile, inferior efficiency is observed, showing decreased efficiency value of from 73% to 69% at 6 A/cm^2. This could be mainly due to the non-Pt-coated substrate and some cracks and peel-off in the catalyst layer. After the aggressive operation condition of running 80 h at an ultrahigh current density of 5 A/cm^2, the non-Pt-coated substrate cannot be well protected and thus is oxidized. As a result, the average HFR value of the 0.5-Ir/sintered Ti significantly increased from 59 to 83 mΩ·cm^2 (**Figure 35D**), which leads to obviously degraded cell performance. Hence, the Pt protecting layer plays a significant role for the sample during the constant high-current operation. Meanwhile, some post-analysis characterizations of the Ir/Pt sintered Ti and the Ir/sintered Ti electrodes were performed to investigate the morphology and catalyst surface

coverage change. As shown in **Figure 38A and B**, for the Ir/Pt sintered Ti, the Ir catalysts maintaining good nanoparticle morphology are still uniformly distributed on the Ti substrate after the stability test and separation with the membrane. Moreover, according to the SEM-EDS mapping images (**Figure 38C**), the elements of Ir and Pt are still uniformly distributed on the Ti substrate surface after the stability test. However, for the Ir/sintered Ti electrode, significant catalyst peel-off is observed and large portion areas of bare Ti substrate are presented after the separation with the membrane (**Figure 39**). Hence, with the Pt coating on the Ti substrate surface, the adhesion of the Ir catalyst layer to the substrate can be enhanced, which could improve the stability of the Ir/sintered Ti electrode to some extent.

Overall, through operating the PEMEC at a constant ultrahigh current density of 5 A/cm^2 for 80 h, the stability of the 0.5-Ir/Pt sintered Ti was evaluated, showing remarkable stability with almost no performance loss observed. While most of the reported anodes evaluate the stability under much lower current densities such as 500 mA/cm^2, or 1 A/cm^2, or 2 A/cm^2 [196] [198] [199] [204] [205], or no stability evaluation in the PEMEC [195] [197, 201]. Hence, compared to most of the recently reported anodes, the 0.5-Ir/Pt sintered Ti shows a significantly simplified fabrication method of a facile, fast and easily scalable electrodeposition process and outstanding stability at an ultrahigh current density of 5 A/cm^2, which exhibits a great potential in the future sustainable energy system.

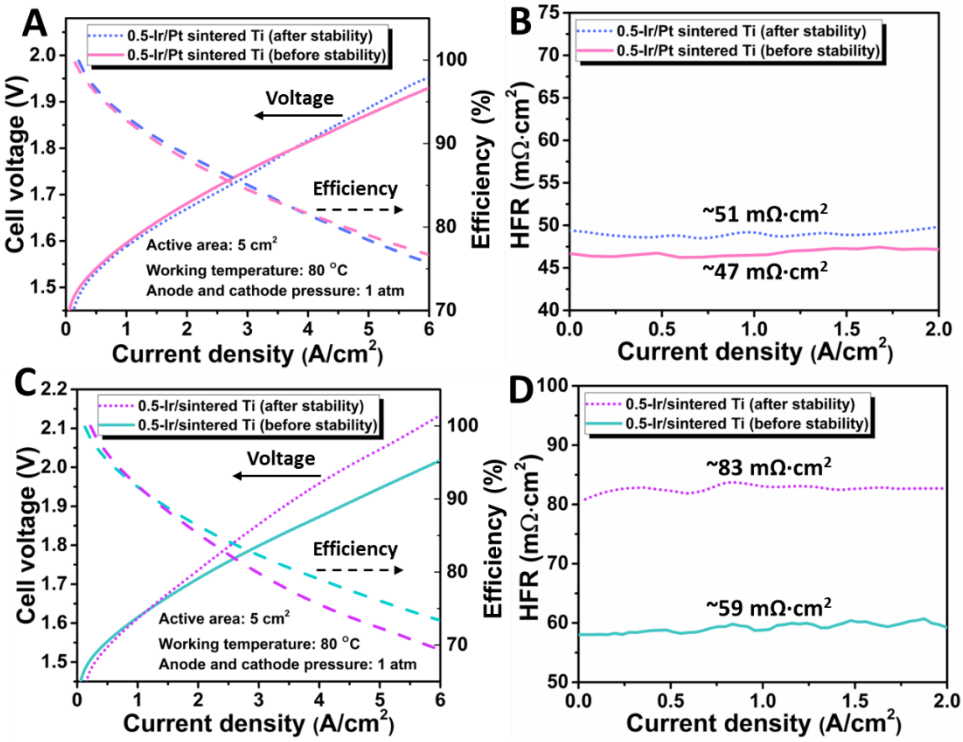


Figure 35. (A) Polarization and efficiency curves of the Ir/Pt sintered Ti electrode before and after stability test, (B) HFR curves of the Ir/Pt sintered Ti electrode before and after stability test, (C) Cell polarization and efficiency curves of the Ir sintered Ti electrode before and after stability test, (D) HFR curves of the Ir sintered Ti electrode before and after stability test.

Table 14. Cell test results of different electrodes after the cell stability test.

Electrode	Cell voltage at 2 A/cm^2 (V)	Cell voltage at 4 A/cm^2 (V)	Cell voltage at 6 A/cm^2 (V)	Average HFR (mΩ·cm^2)
Ir/Pt sintered Ti before stability	1.682	1.814	1.930	47
Ir/Pt sintered Ti after stability	1.671	1.819	1.954	51
Ir/sintered Ti before stability	1.715	1.873	2.017	59
Ir/sintered Ti after stability	1.738	1.960	2.134	83

4.5 Conclusions

In this study, Ir-integrated electrodes were developed *via* a facile electrodeposition method as high-performance anode electrodes for the PEMEC, which show high current capacities of up to 6 A/cm^2. Moreover, there is almost no performance loss observed after a stability test at ultrahigh current stability of 5 A/cm^2. And studies found that a Pt protection layer on the substrate plays a critical role in superior performance and stability, which not only provides the electrode excellent electrical conductivity achieving improved catalyst activity but also enables a crack-free catalyst layer to enhance the catalyst adhesion to the substrate and protects the Ti substrate from being oxidized under aggressive operations. As a result, with the Pt layer, cell voltages can be improved by 33, 59, and 87 mV at current densities of 2, 4 and 6 A/cm^2, respectively, which is mainly attributed to the decreased ohmic loss and activation loss. Overall, due to the significantly simplified fabrication with low-cost and easy scalability, high-current operation capability with high efficiency, and excellent stability, the developed integrated electrode shows superior sustainability in the renewable energy system and could efficiently accelerate sustainable energy evolution.

.

Appendix

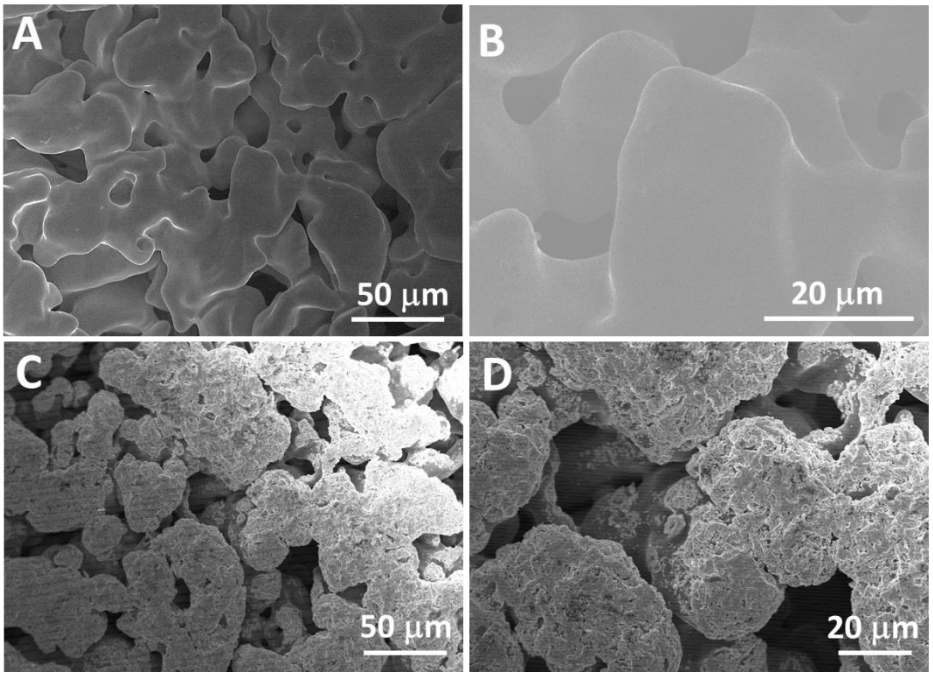


Figure 36. SEM images of (A, B) the bare sintered Ti and (C, D) the Pt sintered Ti.

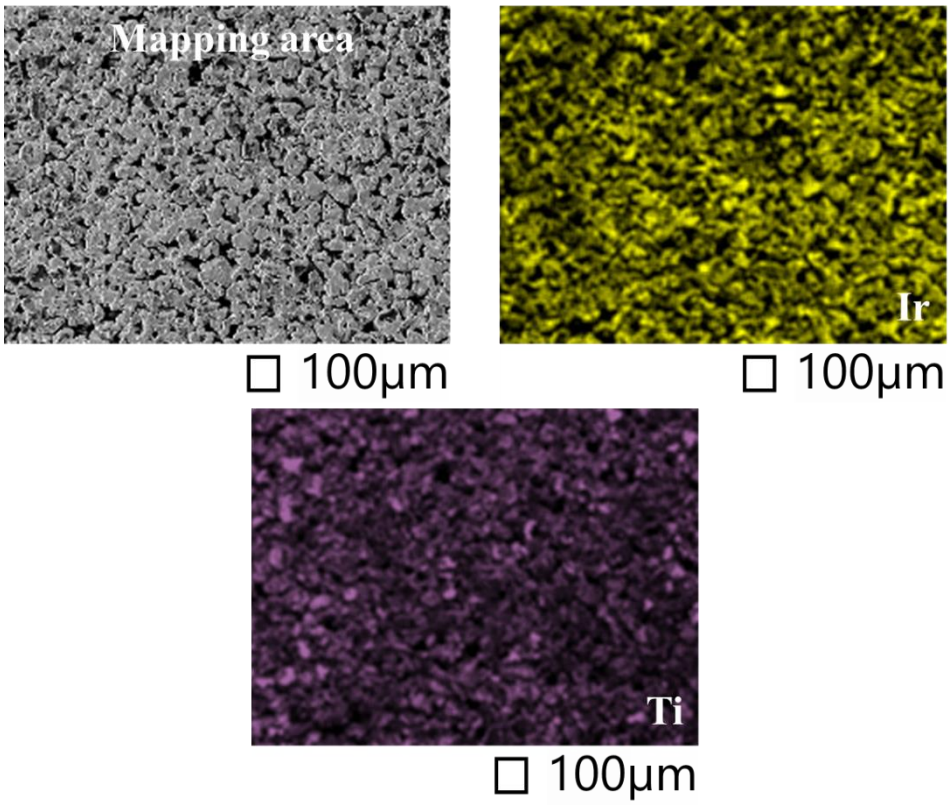


Figure 37. Mapping images of the Ir/sintered Ti.

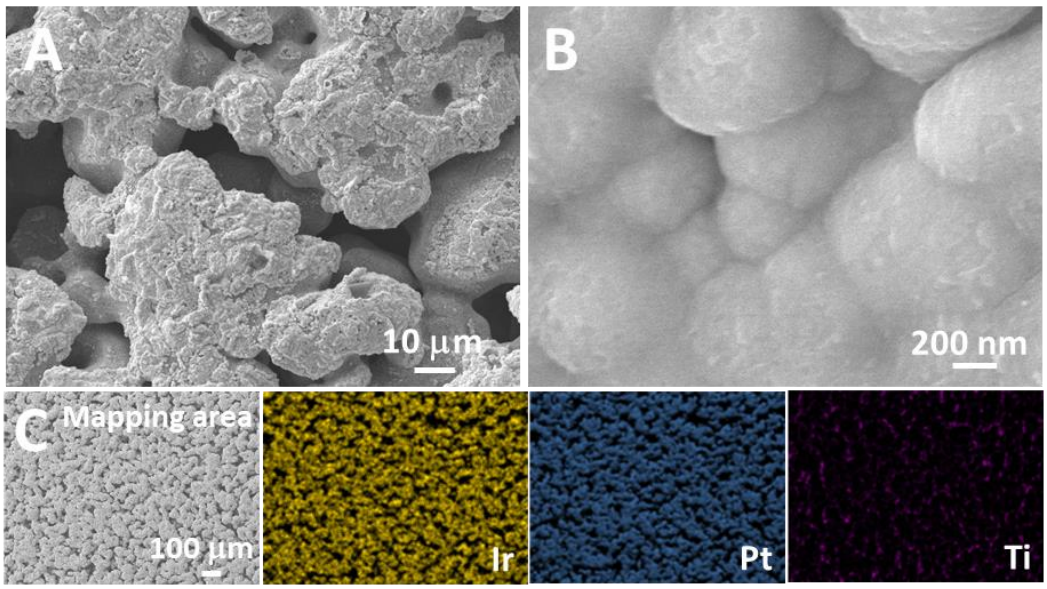


Figure 38. SEM images of the tested Ir/Pt sintered Ti electrode at different magnifications. (C) SEM-EDS mapping images of the tested Ir/Pt sintered Ti electrode.

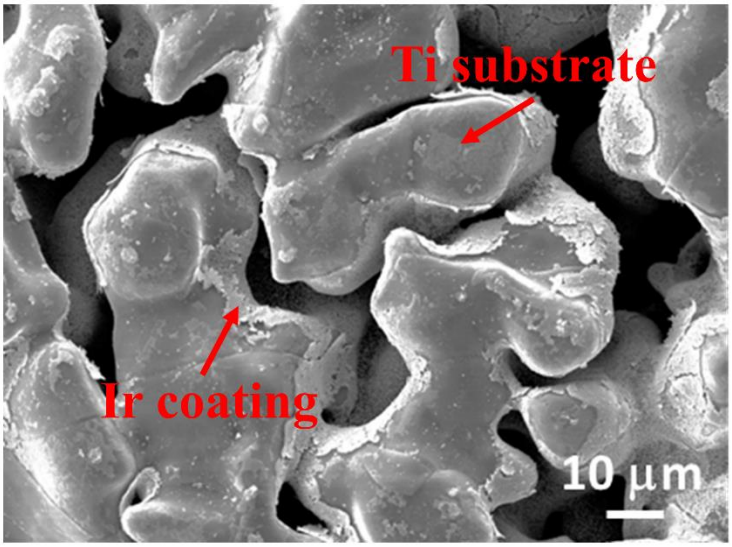


Figure 39. SEM image of the tested Ir/sintered Ti electrode.

CHAPTER FIVE

HIGHLY POROUS IRIDIUM THIN ELECTRODES WITH LOW LOADING AND IMPROVED REACTION KINETICS FOR HYDROGEN GENERATION IN PEM ELECTROLYZER CELLS

A version of this chapter was originally published as:

Ding, L., Wang, W., Xie, Z., Li, K., Yu, S., Capuano, C.B., Keane, A., Ayers, K. and Zhang, F.Y., Highly Porous Iridium Thin Electrodes with Low Loading and Improved Reaction Kinetics for Hydrogen Generation in PEM Electrolyzer Cells. ACS Applied Materials & Interfaces 2023, 15, 20, 24284–24295

CRediT authorship contribution statement

L.D.: Conceptualization, Methodology (electrode fabrication, SEM, SEM-EDS mapping, XRD characterizations, performance evaluation), Data curation, Writing - original draft, review & editing, Investigation, Validation. W.W.: Methodology, Investigation, Validation, Writing - review & editing. Z.X.: Validation, Methodology (material characterization), Writing - review & editing. K.L.: Validation, Writing - review & editing. S.Y.: Methodology, Investigation, Validation, Writing - review & editing. C.B.C.: Validation, Writing - review & editing. A.K.: Methodology (CCM fabrication), Validation, Writing - review & editing. K.A.: Validation, Writing - review & editing. F.-Y. Z: Conceptualization, Supervision, Validation, Writing - review & editing.

I am fully responsible for the work submitted in these publications.

5.1 Abstract

Highly efficient electrodes with simplified fabrication and low cost are highly desired for the commercialization of proton exchange membrane electrolyzer cells (PEMECs). Herein, highly porous Ir-coated thin/tunable liquid/gas diffusion layers with honeycomb-structured catalyst layers were fabricated as anode electrodes for PEMECs *via* integrating a facile and fast electroplating process with an efficient template removal. Combined with a Nafion 117 membrane, a low cell voltage of 1.842 V at 2000 mA/cm^2 and high mass activity of 4.16 A/mg_{Ir} at 1.7 V were achieved with a low Ir loading of 0.27 mg/cm^2, outperforming most of the recently reported anode catalysts. Moreover, the thin electrode shows outstanding stability at a high current density of 1800 mA/cm^2 in the practical PEMEC. Moreover, with *in-situ* high-speed visualizations in PEMECs, the catalyst layer structure impact on real-time electrochemical reactions and mass transport phenomena was investigated for the first time. Increased active sites and improved multiphase transport properties with favorable bubble detachment and water diffusion for the honeycomb-structured electrode are revealed. Overall, the significantly simplified ionomer-free honeycomb thin electrode with low catalyst loading and remarkable performance could efficiently accelerate the industrial application of PEMECs.

5.2 Introduction

Serious environmental problems have been impacted by the extensive use of nonrenewable fossil fuels. [163, 190, 204, 206-209] Hence, renewable energy sources such as solar, wind, and tide, have emerged to be excellent alternatives to traditional fossil fuels to generate power in more sustainable methods. [39, 187, 189, 210-212] Nevertheless, providing stable power is an issue

for these renewable energy technologies since they are intermittent during the application process, which could prevent consistent electricity large-scale delivery in the current electrical grid. [205, 213-215] Therefore, it is of great significance to develop efficient energy storage and conversion system to store the excess generated power for further use.

Due to its high efficiency, quick startup, compact design, and low maintenance cost, the proton exchange membrane electrolyzer cell (PEMEC) has been considered as a promising energy storage device to combine with renewable energy sources to accelerate renewable energy evolution.[28, 43, 171, 216-218] However, the low-cost and high-efficiency electrode fabrication is still challenging for the wide commercialization of the PEMEC, especially since the anode side with more sluggish. To date, Ir, IrO_x, and IrO_2 are the state-of-the-art catalysts for anode electrodes, which are scarce and high cost. However, conventional catalyst-coated membranes (CCMs) involving low conductivity ionomer normally require high catalyst loadings of up to 3 mg/cm^2 to ensure the high efficiency and long durability of the PEMEC. Additionally, the CCM with a gas diffusion layer (GDL) is most widely used for a membrane electrode assembly design, which is complex, time-consuming, and expensive. [219, 220] More importantly, Mo *et al.* [23] demonstrated that the CCM shows low catalyst utilization, discovering that a large portion of the catalysts is underutilized because of the limited conductivity of the ionomer mixed catalyst layer. Therefore, an efficient strategy of directly depositing catalysts on the GDL to form gas diffusion electrodes (GDEs) is proposed to decrease the catalyst loading and simplify the electrode fabrication, showing the possibility of avoiding ionomer use and enhancing the catalyst utilization. For example, Slavcheva *et al.* [27] sputtered IrO_2 on the carbon paper substrate *via* magnetron

sputtering to decrease the anode catalyst loading for the PEMEC. And a cell performance of 300 mA/cm^2 was achieved at 1.6 V with the resultant anode electrode. Choe *et al.* [24] electrodeposited an IrO_2 layer onto a porous Ti mesh with a loading of about 0.4 mg/cm^2, showing a current density of 970 mA/cm^2 at 1.6 V at an operating temperature of 120 °C. Recently, Yu *et al.* [25] developed a series of anode electrodes of Ir catalyst-coated Ti thin/tunable substrates for the PEMEC to investigate the impacts of the Ti thin/tunable substrates on the catalyst utilization and reaction kinetics. And they also *in-situ* visualized the reaction interface of the electrode/PEM with a novel two-side transparent cell. Notably, instead of using conventional porous transport layers with thick thicknesses and 3D random structures, novel thin-tunable liquid/gas diffusion layers (TTLGDLs) were employed to prepare the electrodes, showing reduced resistance and improved catalyst utilization because of the significantly reduced thickness, well-controlled morphology, and planar surfaces. However, in these studies, the prepared electrodes all show flat catalyst layers with dense structures, and some also exhibit thick thicknesses, leading to limited multiphase transport, scant active reaction sites, large ohmic resistance, and material waste. Therefore, it is significant to develop high-efficient and low-cost electrodes with nano-structured catalyst layers and simplified fabrication to accelerate the industrial application of PEMECs.

Herein, we firstly developed a highly efficient honeycomb Ir catalyst-coated TTLGDL (HC Ir CCLGDL) with a low Ir loading of 0.27 mg/cm^2 as a thin anode electrode for the PEMEC *via* combining an efficient template use with a facile and fast Ir electroplating process. The resultant HC Ir CCLGDL shows a fine interconnected honeycomb-structured catalyst layer

exposing abundant active sites. When integrated with a cathode-only Nafion 117 CCM (N117), a low cell voltage of only 1.842 V was achieved at 2000 mA/cm^2, which outperforms most of the recently reported anode catalysts. And a high mass activity of 4.16 A/mg_{Ir} is demonstrated at 1.7 V for the HC Ir CCLGDL. Moreover, *in-situ* high-speed visualizations in PEMECs revealed that increased active sites and improved multiphase transport properties are achieved for the HC Ir CCLGDL, which are the main reasons for the remarkable performances. The outstanding stability of the HC Ir CCLGDL is demonstrated at a high current density of 1800 mA/cm^2 with a 100-h running in a practical cell.

5.3 Experimental Section

5.3.1 Preparation of CCLGDLs

Before the Ir electroplating, the TTLGDLs (manufactured *via* lithographically mask-patterned wet chemical etching of thin foils) [23] were sonicated in acetone, ethanol, and deionized (DI) water for 15 min, respectively, and then treated in 0.05 M oxalic acid (OA) at 90 ℃ for 20 minutes. Afterward, polystyrene (PS) suspension (10 wt%, Alfa Aesar) with a sphere diameter of 1 μm was dispersed in 4 mL ethanol (0.5 wt%) and assembled on the OA-treated TTLGDL *via* solvent self-assembly at the gas/liquid interface method at 50 ℃ for about 2 h. And then, under a constant current density of 3 mA/cm^2, Ir catalysts were electroplated on the PS-assembled TTLGDL at 85 °C with an electroplating solution of IRIDEX 300 B, 15 g_{Ir}/L from Electroplating Engineers of Japan Ltd. The resultant sample shows a geometric Ir loading of about 0.27 mg/cm^2. After immersing the prepared sample in the

tetrahydrofuran (THF), the PS templates were removed to obtain a honeycomb Ir catalyst layer on the TTLGDL. For comparison, dense Ir with a geometric loading of about 0.27 mg/cm^2 was also prepared by directly electroplating on the TTLGDL without the PS templates.

5.3.2 Characterization

The morphology and composition of the sample were characterized by a field emission JSM-IT700HR scanning electron microscope (SEM) with energy-dispersive X-ray spectroscopy (EDS). And the crystalline structure of the sample was analyzed by a Rigaku SmartLab X-ray diffraction (XRD) system.

5.3.3 *Ex-situ* electrochemical measurements

The *ex-situ* electrochemical measurements of the prepared electrodes were evaluated in a typical three-electrode system at room temperature with a saturated calomel electrode (SCE) as the reference electrode and a carbon rod as the counter electrode, respectively. All electrochemical measurements were conducted on a potentiostat VSP/VMP3B-100 (Bio-Logic) in 0.5 M H_2SO_4 and the recorded potentials were calibrated to a reversible hydrogen electrode (RHE) *via* Nernst equation: $E_{RHE} = E_{SCE} + 0.26$ V. Before the electrochemical tests, the electrolyte was deoxygenated by saturating with Ar for 30 min. Afterward, cyclic voltammetry (CV) scans were performed within a potential window of 0 V ~ 1.5 V vs. RHE at a scan rate of 200 mV/s to fully activate the catalysts. Meanwhile, the outer charge (Q) was evaluated from the voltammogram with the equation:

$$Q = \int_{E1}^{E2} \frac{|j|}{v} dE \quad (1)$$

where *j* is the current density obtained from the CV curve, *v* is the scan rate of 200 mV/s, and *E* is the scanning potential within 0.7 V ~ 1.4 V vs. RHE. By integrating the voltammogram at the scan rate of 200 mV/s, the outer charge *Q* was obtained. Afterward, linear sweep voltammetry (LSV) curves were recorded within a potential window of 1 V ~ 1.5 V vs. RHE at a scan rate of 5 mV/s. To eliminate the electrolyte ohmic resistance, the recorded LSV curves were *iR*-corrected (*R*: the electrolyte resistance). In addition, the mass activity was investigated *via* the equation of

$$i_{Mass\ activity} = \frac{i_{Measured}}{m_{Ir}} \quad (2)$$

where m_{Ir} is Ir mass loading.

5.3.4 The PEMEC assembly and test

A cathode-only Nafion 117 CCM (3.0 mg_{PtB}/cm^2, 175 μm in thickness, Nel Hydrogen) with an active area of 5 cm^2 was used for the cell test. Toray 090 carbon papers (thickness: 280 μm, porosity: 78%) were employed as the cathode LGDLs. With the TTLGDLs (thickness: 50 μm, porosity: 40%) as the anode LGDLs, the prepared Ir with a loading of 0.27 mg/cm^2 on the TTLGDLs (Ir CCLGDLs) were used as anode electrodes. The graphite plate and sputtering Au-coated titanium plate with parallel flow channels were employed as the cathode and anode bipolar plates (BPPs), respectively, and parallel flow channels were used to introduce the reactants and products in and out of the PEMEC. Along with the cathode and anode BPPs, the Ir CCLGDL, CCM, carbon paper and gaskets, were sandwiched by two stainless steel endplates to obtain a whole PEMEC. To apply current to the whole PEMEC, a copper plate was inserted between the BPP and the endplate at both

the anode and cathode sides, respectively. Afterward, with eight evenly distributed bolts, the cell was tightened (40 in·lb of torque) and assembled. Subsequently, the assembled PEMEC was connected to a potentiostat with a booster (VSP/VMP-100, Bio-Logic) to record the data. The test was operated at 80 °C and under atmospheric pressure with a water flow rate of 20 mL/min at the anode side. And detailed properties and operating conditions of the PEMEC are shown in **Table 15**. After an optimized conditioning process, polarization curves within 0 mA/cm^2 ~ 2000 mA/cm^2 were recorded, and high-frequency resistance (HFR) curves were recorded at a frequency of 5 kHz. Meanwhile, the electrochemical impedance spectroscopies (EIS) at current densities of 200 mA/cm^2 and 1000 mA/cm^2 were measured within a frequency range of 10 kHz ~ 100 mHz, respectively. In addition, the setup of the visualization system, including camera, lens, lighting, and transparent PEMEC can be found in our previous publications [187, 221-223].

5.4 Results and Discussions

5.4.1 Morphology and composition of the HC Ir CCLGDL

Some drawbacks such as thick thickness, random structures, and large ohmic resistance of the conventional GDLs are difficult to avoid in the PEMEC. To avoid the above drawbacks, herein, novel TTLGDLs were employed as substrates to fabricate catalyst-coated TTLGDLs (CCLGDLs) for the PEMEC (**Figure 40A**). As shown in **Figure 48**, the novel TTLGDL shows planar surfaces, well-controlled pore structure and size (~ 200 μm), and a thin thickness of only 50 μm, which could reduce the resistance and improve the catalyst utilization in the PEMEC. [29]

Table 15. The PEMEC properties and operating conditions.

Properties and conditions	Details
Membrane type	Nafion 117 (thickness: 175 mm)
Anode catalyst loading	0.27 mg/cm^2 (Ir)
Cathode catalyst loading	3 mg/cm^2 (PtB)
Anode LGDL	TTLGDL
Cathode LGDL	Toray 090 carbon papers
Testing temperature	80 °C
Testing pressure	1 atm
Anode water flow rate	20 mL/min
Torque	40 in·lb
Active reaction area	5 cm^2

Without the PS template assembly, the bare TTLGDL exhibits smooth surfaces. After the PS assembly and Ir electroplating, Ir-coated well-ordered spheres are observed and maintained well on the surface of the TTLGDL (Ir/PS/TTLGDL) (**Figures 41A-B and Figure 49**). Afterward, with an efficient template removal in THF, a fine honeycomb structured Ir catalyst layer was successfully obtained, as illustrated in **Figure 49** and **Figure 40B**. As shown in **Figures 41C-D**, a fine honeycomb Ir catalyst layer is observed, which could offer a large surface area, and thus expose rich active reaction sites for the electrochemical reaction. Meanwhile, the catalyst layer cross-section image (**Figure 28E**) demonstrates the interconnected honeycomb structures of the catalyst layer, which play significant roles in multiphase transport. With the honeycomb structures, improved multiphase transport of favorable gas detachment [33] and water diffusion and abundant active reaction sites could be achieved (**Figure 40C**). The cross-section SEM-EDS mapping images of the whole HC Ir CCLGDL (**Figure 50**) exhibit that the Ir catalyst is uniformly covered on the thin Ti substrate. Moreover, the XRD pattern (**Figure 41F**) indicates that apart from the peaks assigned to the Ti substrate, only diffraction peaks ascribed to metallic Ir are detected and no other iridium oxide or impurities are observed. For comparison, a dense Ir catalyst layer was also prepared *via* direct electroplating on the surface of the TTLGDL without the template use. As shown in **Figure 51**, the resultant Ir catalyst layer exhibits dense film structures with an Ir atomic ratio of 35.94%, and no special features are observed.

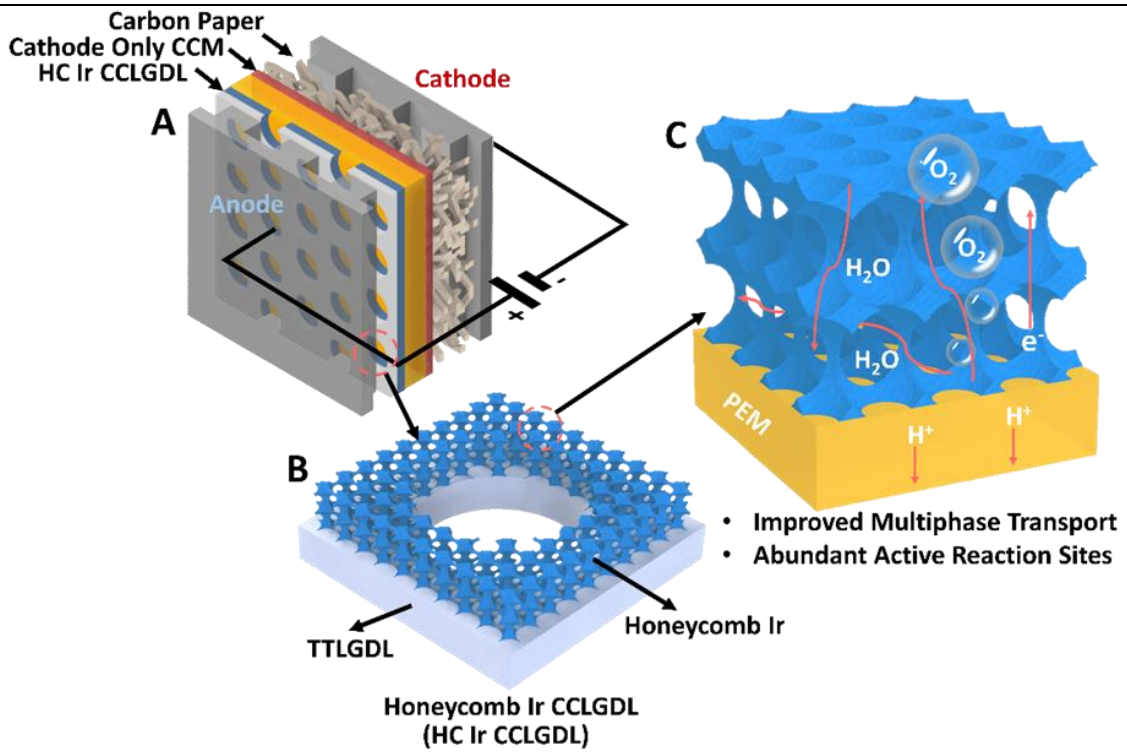


Figure 40. Schematic of (A) the PEMEC incorporated with the HC Ir CCLGDL; (B) The HC CCLGDL; (C) Advantages of improved multiphase transport and abundant active reaction sites of the HC Ir CCLGDL.

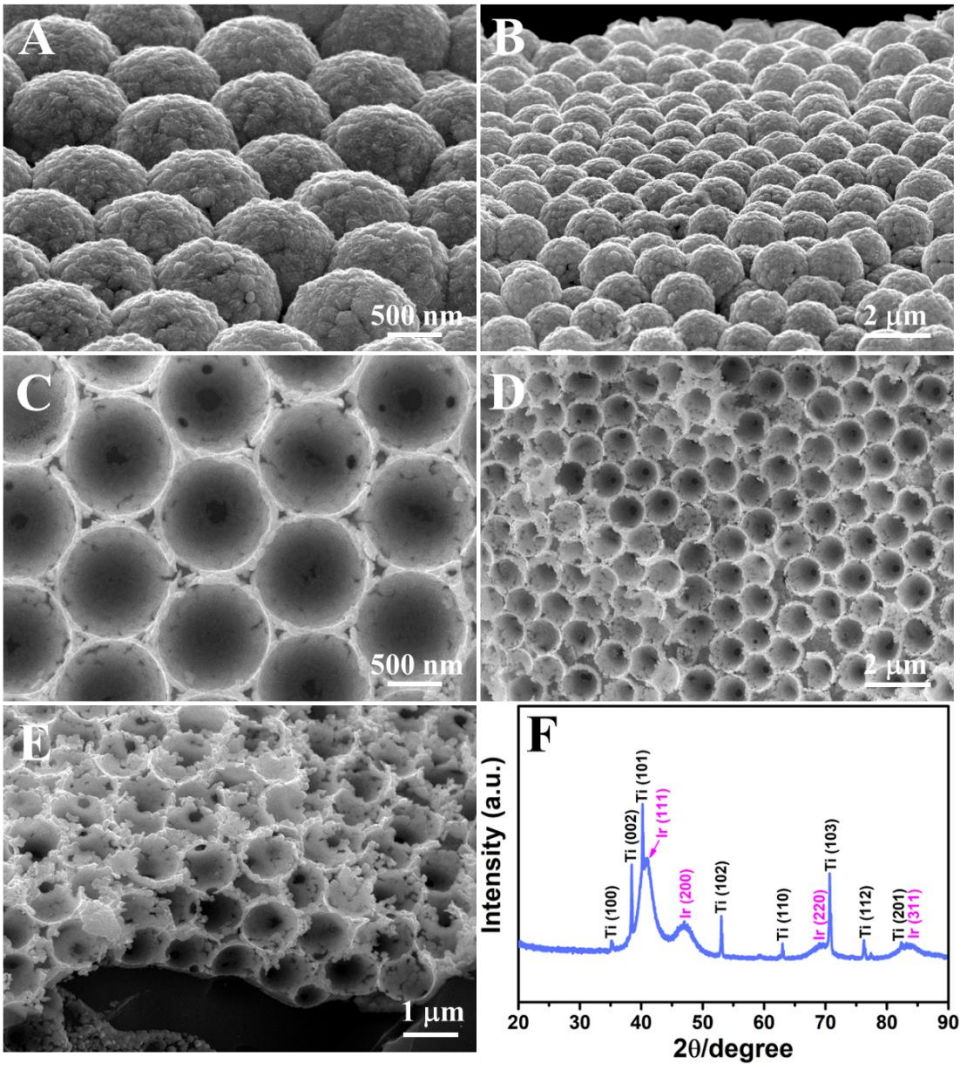


Figure 41. SEM images of (A, B) the Ir/PS/TTLGDL and (C, D) the HC Ir CCLGDL; (E) Cross-section SEM image of the honeycomb Ir catalyst layer; (F) the XRD pattern of the HC Ir CCLGDL.

5.4.2 OER performance in a three-electrode system

Firstly, the OER performance of the prepared electrodes was evaluated in a three-electrode system. Before the linear sweep voltammetry (LSV) curve recording, cyclic voltammetry (CV) scans were performed to activate the catalysts. Comparing the initial CV scan and the last CV scan (**Figure 52**), the hydrogen underpotential deposition (H_{upd}) peak between 0 V and 0.4 V assigned to metallic Ir disappeared after the full activation, implying that catalyst surface composition changed from metallic states to oxidic states.[224, 225] Afterward, LSV polarization curves were recorded. As presented in **Figure 42A**, the HC Ir catalyst exhibits significantly enhanced OER performance compared to that of the directly electroplated Ir with dense structures. And different overpotentials at different current densities of 10 mA/cm^2, 30 mA/cm^2, and 50 mA/cm^2 are summarized and displayed in **Figure 53**. Overall, the HC Ir shows lower overpotentials (10 mA/cm^2: 284 mV, 30 mA/cm^2: 307 mV, 50 mA/cm^2: 322 mV) than those of the dense Ir catalyst (10 mA/cm^2: 307 mV, 30 mA/cm^2: 355 mV, 50 mA/cm^2: 388 mV), and the overpotential difference increases with the increase of the current density. According to the LSV curves, Tafel slopes are evaluated *via* the equation of $\eta = b \cdot log|j| + a$, where b is the Tafel slope and j is the current density. As displayed in **Figure 42B**, the HC Ir catalyst exhibits a similar Tafel slope of 54.7 mV/dec to that of the dense Ir catalyst (56.5 mV/dec), showing similar kinetics in the three-electrode system.[226-229] Meanwhile, the outer charge (Q) was also studied based on CV scans (**Figure 42C**) at a high scan rate of 200 mV/s *via* a voltammogram integration method, which generally indicates the outer active sites and accessible active surfaces and can be directly related to the OER activity. [224]

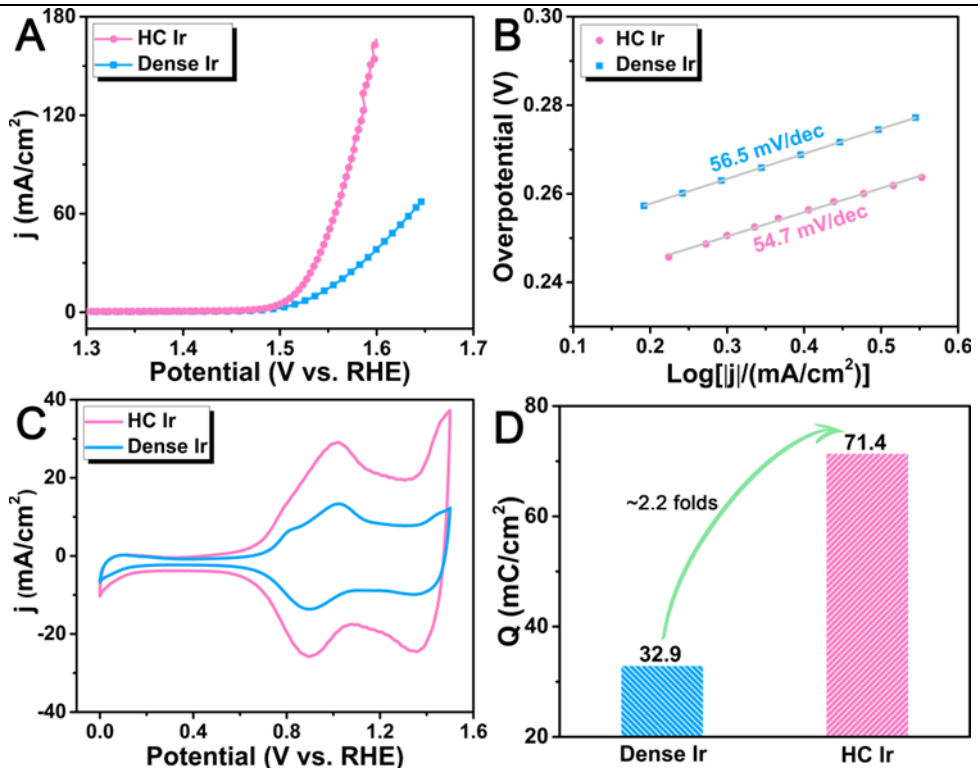


Figure 42. (A) LSV curves with iR-correction; (B) The related Tafel slopes; (C) CV scan curves within 0 V ~ 1.5 V vs. RHE at 200 mV/s; (D) Outer charge comparison.

And a higher Q value indicates a higher OER activity achieved for the catalysts. Based on the CV scans, the Q values of the two catalysts are calculated and compared. As presented in **Figure 42D**, the HC Ir shows a high Q value of 71.4 mC/cm^2, more than 2 folds higher than that of the dense Ir (32.9 mC/cm^2), verifying the more accessible active surface area for the HC Ir catalyst.

5.4.3 Cell characterization in PEMECs

Moreover, the OER performance of the two electrodes in a practical PEM electrolyzer cell was also evaluated by coupling with a cathode-only Nafion 117 CCM (N117). Polarization curves in **Figure 43A** exhibit that low cell voltages of 1.690 V and 1.842 V at 1000 mA/cm^2 and 2000 mA/cm^2 are demonstrated, respectively, for the HC Ir. While for the dense Ir CCLGDL, higher cell voltages of 1.710 V and 1.883 V are observed. For the HFR plots, as seen in **Figure 43B**, less HFR variance is observed along with the current density increase for the HC Ir CCLGDL compared to that of the dense Ir CCLGDL. This could be because the fine interconnected honeycomb structures could achieve faster bubble release and water diffusion, minimizing the bubble accumulation at the interface of the electrode and the PEM. As a result, a more stable HFR plot is achieved under high current densities for the HC Ir CCLGDL. In addition, a lower average HFR value of 105 mΩ·cm^2 is observed for the HC Ir CCLGDL (the dense Ir CCLGDL: 111 mΩ·cm^2). And a lower HFR value of 107 mΩ·cm^2 is also demonstrated at 2000 mA/cm^2 (the dense Ir CCLGDL: 116 mΩ·cm^2). The lower HFR indicates that decreased ohmic loss is achieved for the HC Ir CCLGDL. Based on the initial polarization curves and HFR results, the HFR-free polarization curves are plotted.

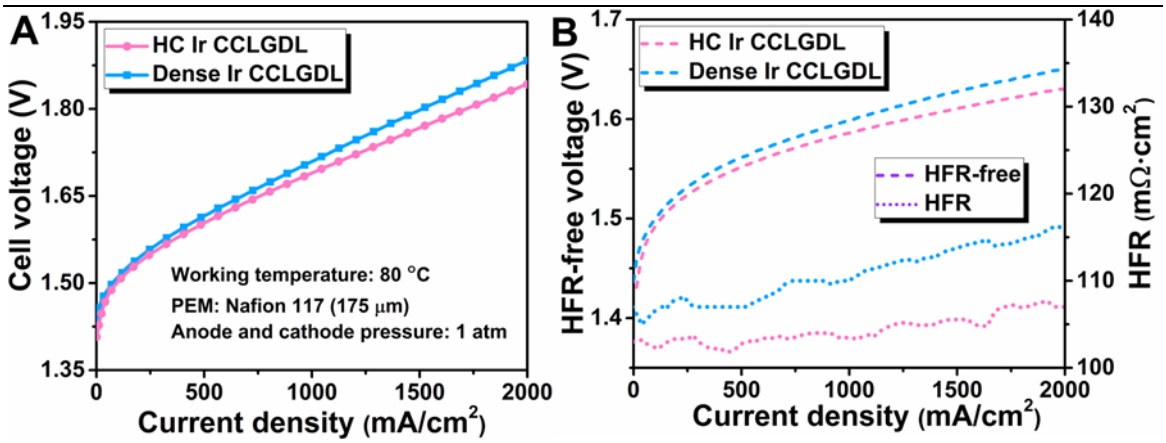


Figure 43. (A) Cell polarization curves of the HC Ir CCLGDL and dense Ir CCLGDL; (B) The HFR-free cell polarization curves and the corresponding HFR plots.

As presented in **Figure 43B**, lower HFR-free voltages of 1.586 V and 1.630 V are achieved for the HC Ir CCLGDL at 1000 mA/cm^2 and 2000 mA/cm^2 compared to those of the dense Ir CCLGDL (1.599 V, 1.650 V). Overall, 41 mV and 20 mV voltage differences are achieved for the pristine cell performance and the HFR-free performance, respectively, at 2000 mA/cm^2 for the two electrodes. About 10 mΩ·cm^2 HFR difference is observed at 2000 mA/cm^2. Related data is summarized and presented in **Table 16**. With the above results and the data in **Table 16**, we could conclude that for the pristine cell voltage difference of 41 mV, about 20 mV voltage difference is from the ohmic resistance assigned to the HFR difference, and the rest voltage difference should be ascribed to the decreased activation loss and diffusion loss.

Based on the equation of $C = Q^{\frac{1}{n}} \cdot R^{\frac{1-n}{n}}$, where R is the sum of R_{hf} and R_{lf}, [232] the values of the double-layer capacitances (C_{dl}) can be calculated, which represent the capacitance between the interface of the electrode and the electrolyte and closely correspond to the active reaction sites, a higher C_{dl} value indicates more active reaction sites exposed. [233] As shown in **Table 17**, the HC Ir CCLGDL exhibits a high $C_{dl,\,hf}$ value of 0.05116 mF/cm^2, which is around 2.6 folds higher than that of the dense Ir CCLGDL (0.0194 mF/cm^2). The higher $C_{dl,\,hf}$ value of the HC Ir CCLGDL indicates increased active reaction sites ascribed to the fine honeycomb-structured catalyst layer. As discussed above, the Nyquist plots involve two processes with two different time constants. The $C_{dl,\,lf}$ at the low frequency is a "slow process" since the reaction sites need a larger time constant. [168] The lower $C_{dl,\,lf}$ value for the HC Ir CCLGDL means that the reaction sites assigned to the "slow process" are less than those of the dense Ir CCLGDL.

Table 16. Cell test results of the HC Ir and dense Ir CCLGDLs.

CCLGDL	Cell voltage at 2000 mA/cm^2 [V]	Average HFR [mΩ·cm^2]	HFR at 2000 mA/cm^2 [mΩ·cm^2]	HFR-free voltage at 2000 mA/cm^2 [V]
HC Ir	1.842	105	107	1.630
Dense Ir	1.883	111	116	1.650

Table 17. The fitting data of the Nyquist plots at 200 mA/cm^2.

CCLGDL	R_{Ω} [mΩ·cm^2]	R_{hf} [mΩ·cm^2]	Q_{hf} [F·s^{a-1}/cm^2]	n_{hf}	R_{lf} [mΩ·cm^2]	Q_{lf} [F·s^{a-1}/cm^2]	n_{lf}	$C_{dl,hf}$ [F/cm^2]	$C_{dl,lf}$ [F/cm^2]	Error
HC Ir	101.45	59.1	0.05172	0.9995	120.7	0.4572	0.6528	0.0516	0.1628	0.0187
Dense Ir	108.55	75.3	0.01941	0.9999	122.65	0.741	0.7525	0.0194	0.3941	0.0218

Namely, more accessible active reaction sites are achieved for the HC Ir CCLGDL with a higher $C_{dl,\ hf}$ value and a lower $C_{dl,\ lf}$ value, resulting in decreased activation loss and enhanced performance in the PEMEC. As shown in **Figure 44D**, as the current density increased to 1000 mA/cm^2, a third arc assigned to mass diffusion occurred for both electrodes. And we could observe that a smaller diffusion arc is presented for the HC Ir CCLGDL, indicating less diffusion loss is achieved. This demonstrates the multiphase transport issues of gas and water transport are efficiently mitigated for the HC Ir CCLGDL because of the fine interconnected honeycomb-structured catalyst layer. Compared to the dense Ir CCLGDL, bubbles can more easily and quickly detach from the HC Ir CCLGDL, and meanwhile, the water can be more easily accessed at the reaction sites, enabling more exposed active sites for the electrochemical reaction.

To investigate the honeycomb-structured catalyst layer impact on the mass transport phenomena (oxygen bubble detachment, water transport, etc.) and real-time electrochemical reactions, *in-situ* visualizations in a transparent PEMEC were performed. With a high-speed and microscale visualization system, the bubble detachment process and electrochemical reactions on the dense Ir CCLGDL and HC Ir CCLGDL were both investigated. As shown in **Figure 45A and Movie S1**, under a small current density of 200 mA/cm^2, large detachment bubbles are observed for the dense Ir CCLGDL, which could block some active sites for the electrochemical reaction. While for the HC Ir CCLGDL, faster bubble nucleation and detachment rates are presented (**Movie S2 and Figure 45B**), resulting in more dynamic bubbles with smaller bubble sizes. As a result, improved bubble evolution properties are achieved with the fine honeycomb-structured catalyst layer.

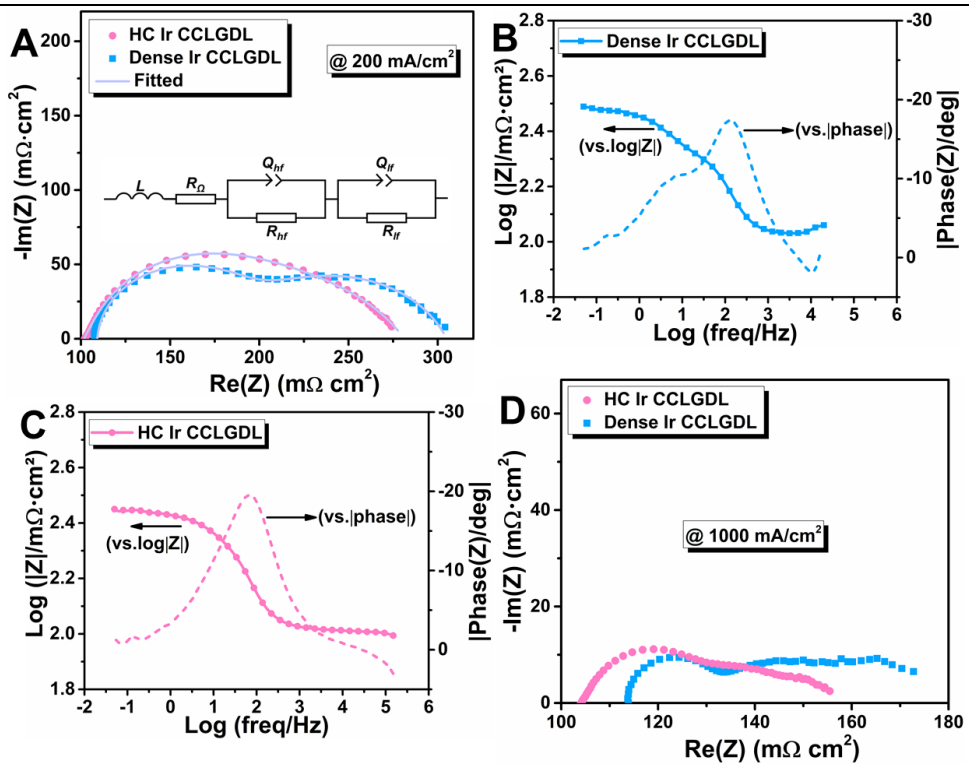


Figure 44. (A) The Nyquist plots at 200 mA/cm^2 and the related fitting curves based on the circuit model; Inset: the related equivalent circuit; Bode plots of (B) the dense Ir CCLGDL and (C) the HC Ir CCLGDL: dots and solid lines: log(freq) vs. log(|Z|); dash lines: log(freq) vs. |phase|; (D) The Nyquist plots at 1000 mA/cm^2.

Based on the movies, bubble detachment sizes of the two CCLGDLs are statistically analyzed. By measuring and collecting the bubble detachment diameters, we obtain the bubble size distributions of dense Ir and HC Ir, respectively. As shown in **Figure 45C and Table 18**, all bubbles on the HC Ir CCLGDL detached below 50 μm. Specifically, 81.50 % of bubbles detached within a small size range of 10 ~ 20 μm, only 18.5 % of the bubbles detached within 20 ~ 50 μm, and no larger bubble than 50 μm was observed. While for the dense Ir CCLGDL, 53.15 % of bubbles detached within 10 ~ 20 μm, 39.64 % of the bubbles detached within 20 ~ 50 μm, and 7.21 % of bubbles detached with large sizes above 50 μm. Moreover, *in-situ* visualizations at a voltage of 1.85 V were also recorded (**Movies S3 and S4**) to provide more insights into the bubble dynamics and the electrochemical reaction. As shown in **Figure 45D**, due to the fine honeycomb-structured catalyst layer, the average bubble site number increased from 10 to 13 per pore, indicating that more active sites are exposed on the HC Ir CCLGDL. Therefore, compared to the dense catalyst layer, the honeycomb-structured catalyst layer demonstrates improved multiphase transport properties and increased reaction sites, resulting in enhanced performance in the PEMEC.

To further demonstrate the excellent performance of the HC Ir CCLGDL, a cell performance comparison with various anode catalysts is performed. As shown in **Figure 46A**, the HC Ir CCLGDL with a low catalyst loading of 0.27 mg/cm^2 exhibits a better cell performance than most of the recently reported anode catalysts in the PEMEC so far. [180] [196, 201, 234-241] Meanwhile, mass activities at 1.7 V are also summarized.

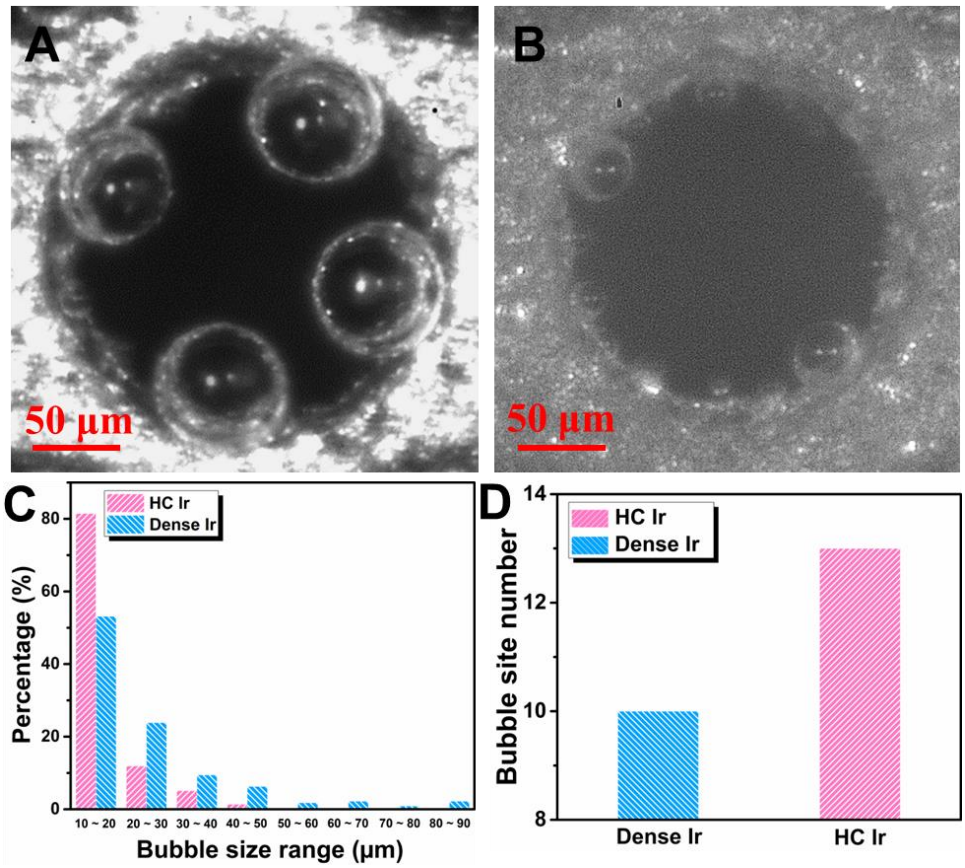


Figure 45. High-speed micro-scale visualization of oxygen bubble dynamics on electrode surfaces of (A) dense Ir CCLGDL and (B) HC Ir CCLGDL at 200 mA/cm^2 (Movies S1 and S2); (C) Bubble size distribution comparison of oxygen bubbles on the two CCLGDLs; (D) Bubble site number comparison of the two CCLGDLs at 1.85 V based on Movies S3 and S4.

As presented in **Figure 46B**, the HC Ir CCLGDL exhibits the highest mass activity of 4.16 A/mg_{Ir}, which is higher than that of the dense Ir CCLGDL (3.58 A/mg_{Ir}) and also higher than most of the reported anode catalysts.

The high mass activity demonstrates the improved catalyst utilization of the HC Ir CCLGDL, which could be ascribed to the fine honeycomb-structured catalyst layer exposing abundant active sites. Moreover, the stability of the HC Ir CCLGDL was evaluated in the PEMEC at a high current density of 1800 mA/cm^2. The result shows that the HC Ir CCLGDL exhibits excellent stability at the high current density of 1800 mA/cm^2 after 100-h running (**Figure 46C**). Since the cell needs some time to get stabilized when starting at the stability test, we exclude the first 5 hours (including the stop-restart plot) and use a linear fitting method to compute the degradation rate of the HC Ir CCLGDL, and a degradation rate of about 220 μV/h is derived. The good stability could be due to the interconnected honeycomb-structured catalyst layer with favorable bubble detachment and water diffusion. With the fine honeycomb interconnected structure, gas accumulation and blockage at the electrode and PEM interface could be efficiently mitigated. Hence, after the 100-h stability test, the performance of the HC Ir CCLGDL can almost maintain the same as the initial test. As shown in **Figure 46D**, the cell polarization curves of the HC Ir CCLGDL before and after the stability test almost overlap with each other. Moreover, HFR-free polarization curves, HFR plots, and Nyquist plots before and after the stability test are also compared, and all of them also almost overlap (**Figure 54**).

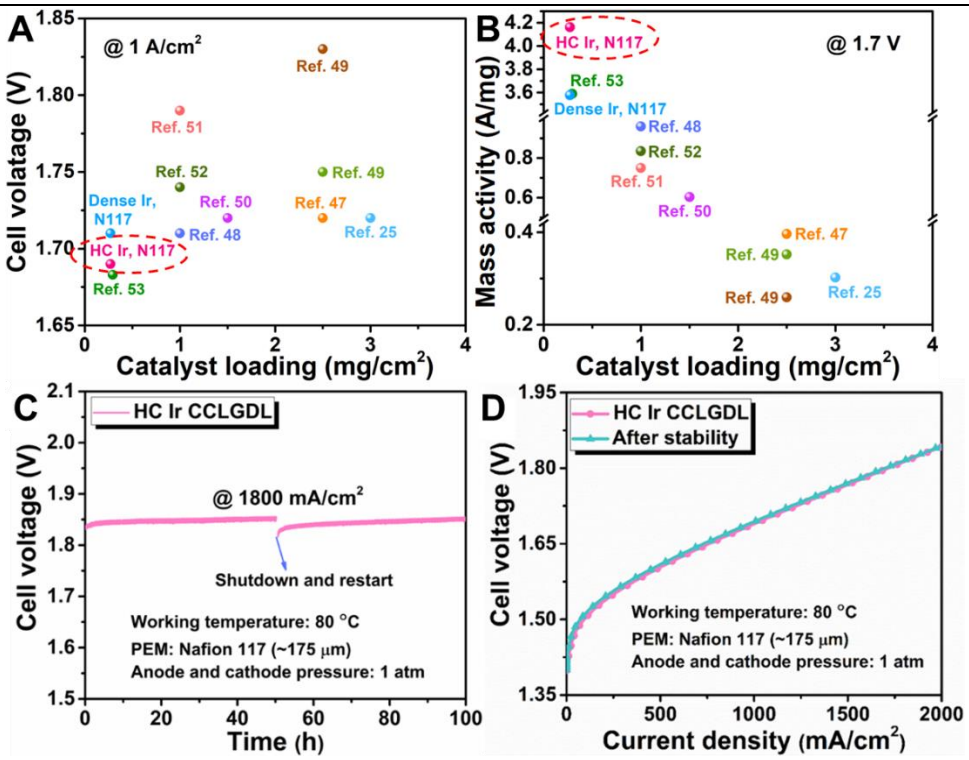


Figure 46. (A) Cell voltage comparison at 1000 mA/cm^2 with previously reported anode catalysts; (B) The corresponding mass activity comparison at 1.7 V; (C) Cell stability test at 1800 mA/cm^2; (D) Cell performance comparison before and after the stability test.

Notably, most of the recently reported anode electrodes in the PEMEC so far are in conventional ionomer mixed CCM design with a thick membrane electrode assembly and large catalyst layer thickness normally up to dozens of micrometers, which shows limited electron conductivity and complex fabrication methods involving multiple steps and expensive equipment. [205,27,234,235,196, 238, 242] For example, Li et al., [238] fabricated $Ir_{0.6}Sn_{0.4}O_2$-based anode CCM *via* combining a surfactant-assisted wet chemical method and spray coating, which consists of multiple fabrication processes and additional or elaborate equipment. Specifically, with $H_2IrCl_6{\cdot}5H_2O$ and $SnCl_4{\cdot}5H_2O$ as reaction precursors and $NaBH_4$ as the reducing agent, a hydrophilic triblock polymer such as Pluronic®F108 surfactant was also introduced during the wet chemical process to stable the solid-solution structure formation. After stirring and aging for 12 h, respectively, the resultant powder was annealed at 400 °C for 2 h to remove residual surfactant and boost $Ir_{0.6}Sn_{0.4}O_2$ alloy formation. Afterward, catalyst ink was prepared by mixing the $Ir_{0.6}Sn_{0.4}O_2$ catalyst powders, Nafion ionomer and isopropanol and then sprayed on the membrane via a spray coater. In addition, before the catalyst spray, 0.6 mg/cm^2 ionomers were sprayed on both sides of the membrane on a hot plate at 80 °C. The whole fabrication process is complicated, time-consuming and expensive. However, with a simple combination of facile and fast (< 10 min) electrodeposition and efficient template removal, the developed HC Ir CCLGDL in our study shows a novel nanostructured ionomer-free integrated electrode design with a thin electrode thickness of about 50 μm and thin catalyst layer of less than 3 μm, exhibiting improved conductivity and material/weight/volume/cost saving. Furthermore, the developed novel HC Ir CCLGDL shows excellent stability at a high

current density of 1.8 A/cm^2 with almost no performance loss after a 100-h operation. While most of the recently reported anode electrodes running the stability at a lower current density such as 1 A/cm^2; [204, 205, 27, 234, 235, 196, 238] or operating the stability test in a three-electrode system, which is different from the PEMEC conditions; [24, 237] or no stability evaluation. [243, 180, 242] Hence, compared to most of the recently reported anode electrodes, the HC Ir CCLGDL shows an ionomer-free nanostructure engineered catalyst layer with fine honeycomb structures exposing abundant active sites and improving mass transport properties, significantly simplified fabrication, and excellent stability at a high current density, which not only provides new insights into designing and fabricating nanostructured catalyst layer but also shows great potential to accelerate PEMEC commercialization.

Overall, several advantages of the honeycomb-structured catalyst layer are as follows. Firstly, the fine honeycomb-structured catalyst layer could mitigate multiphase transport issues, as evidenced by the *in-situ* high-speed visualization and EIS analysis. Many studies also demonstrated that compared to flat surfaces, micro/nano structures with rough surfaces could decrease the bubble contact area on the electrode surface, successfully achieving weaker bubble adhesive force and quick bubble removal with smaller sizes. [31, 33, 244] For example, Kamei *et al.* [31] prepared ultra-bubble-repellent honeycomb-based films for various potential artificial device applications and demonstrated that the honeycomb-based films show larger bubble contact angles and lower adhesion forces than flat surfaces. Lu *et al.* [30] found that the nanostructured MoS_2 electrode with underwater superaerophobic surfaces achieved quick bubble removal with smaller detachment bubble sizes. Xie *et al.*

[33] compared the bubble detachment behavior of the PtNW-structured electrode and Pt-sputtered electrode under 100 mA/cm^2. They verified that a smaller bubble detachment range was achieved for the PtNW-structured electrode (50 ~ 100 μm) compared to that of the Pt-sputtered electrode. Secondly, because of the favorable bubble detachment on the honeycomb structures, the gas accumulation at the interface of the electrode and the PEM could be mitigated, which could avoid the active site blockage from bubbles and the triple-phase-boundary active site loss. Therefore, decreased ohmic resistance and a more stable HFR plot are obtained. Thirdly, the honeycomb-structured catalyst layer offers a large surface area to expose rich active reaction sites, thus achieving higher activity and lower activation loss for the cell test.

5.4.4 Post-analysis of the HC Ir CCLGDL after the cell test

To investigate the morphology and composition changes of the honeycomb Ir catalyst layer, SEM, SEM-EDS mapping and EDS characterizations of the HC Ir CCLGDL after the cell test were performed. As shown in the SEM images in **Figures 47A and B**, compared to the fresh HC Ir CCLGDL, the honeycomb structures of the Ir catalyst layer are maintained well after the cell test. According to the SEM-EDS mapping results (**Figures 55A and B**), the Ir element is still uniformly and fully distributed on the Ti substrate. Moreover, similar Ir contents are observed based on the EDS analysis. As shown in the inset tables in **Figures 47C and D**, the Ir atomic ratio after the cell test is 35.81 %, which is similar to that of the fresh CCLGDL (37.40 %). The similar Ir contents indicate no significant catalyst detachment from the substrate. Overall, the above results demonstrate the good stability of the prepared HC Ir CCLGDL in a practical PEMEC.

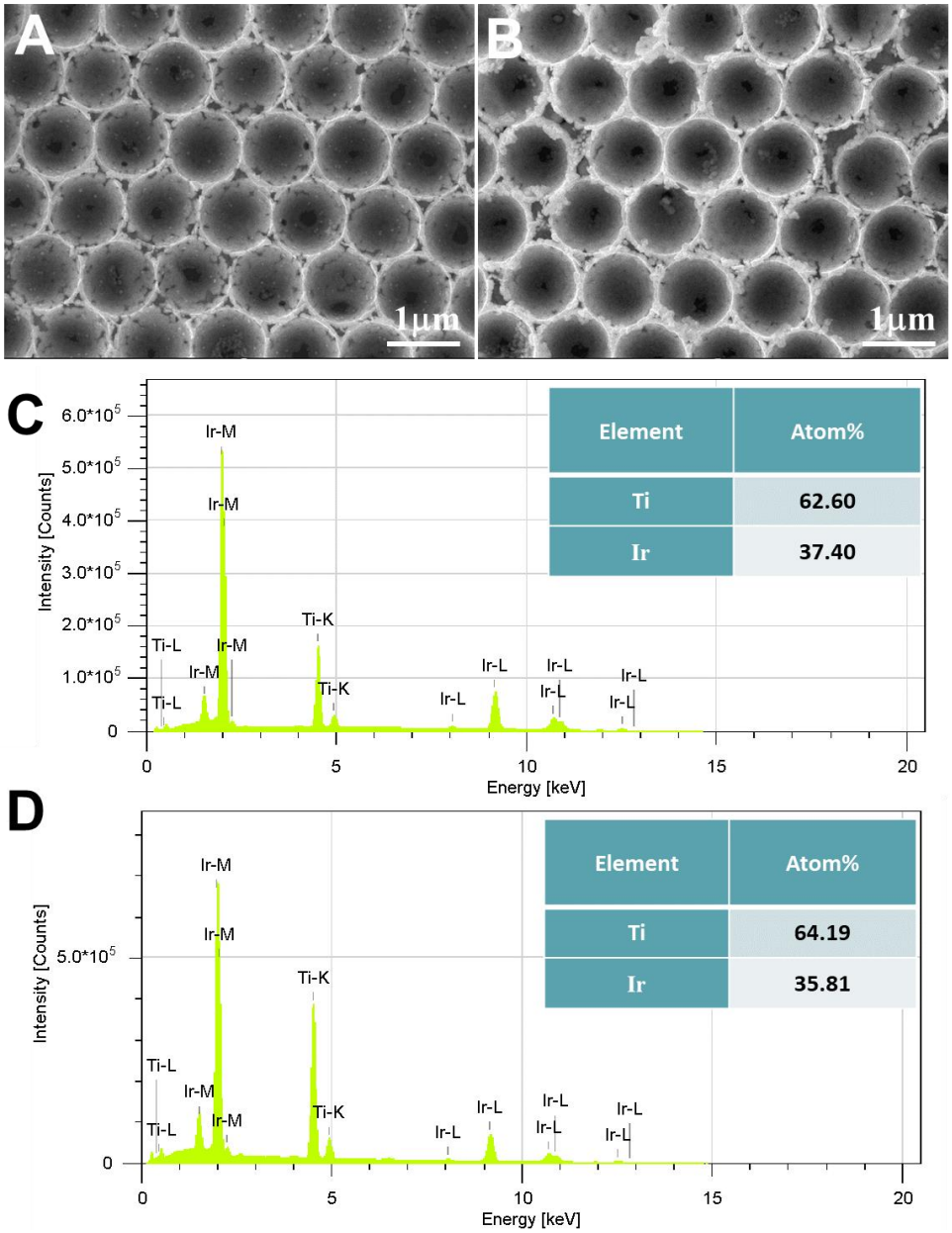


Figure 47. (A) SEM image of the fresh HC Ir CCLGDL; (B) SEM image of the tested HC Ir CCLGDL; (C) EDS analysis of the fresh HC Ir CCLGDL; (D) EDS analysis of the tested HC Ir CCLGDL.

5.5 Conclusion

In summary, a fine interconnected honeycomb Ir catalyst layer was *in-situ* deposited on the TTLGDL (HC Ir CCLGDL) to be a highly efficient anode thin electrode for the PEMEC by combining an efficient template use with a facile and fast electroplating process. The as-fabricated HC Ir CCLGDL with a low Ir loading of 0.27 mg/cm^2 achieves a low cell voltage of 1.842 V at 2000 mA/cm^2 and high mass activity of 4.16 A/mg$_{Ir}$ at 1.7 V when combined with a cathode-only Nafion 117 CCM. The outstanding cell performance is superior to most of the recently reported anode catalysts. In addition, the HC Ir CCLGDL shows outstanding stability after testing for 100 hours at a high current density of 1800 mA/cm^2. *In-situ* high-speed visualizations demonstrate the improved multiphase transport properties of bubble and water transport and increased active sites of the HC Ir CCLGDL, resulting in remarkable performances. Overall, the developed high-efficiency and ionomer-free HC Ir CCLGDL with simplified electrode fabrication, decreased catalyst loading, and excellent performance could boost the commercialization of the PEMEC and thus accelerate renewable energy evolution.

Appendix

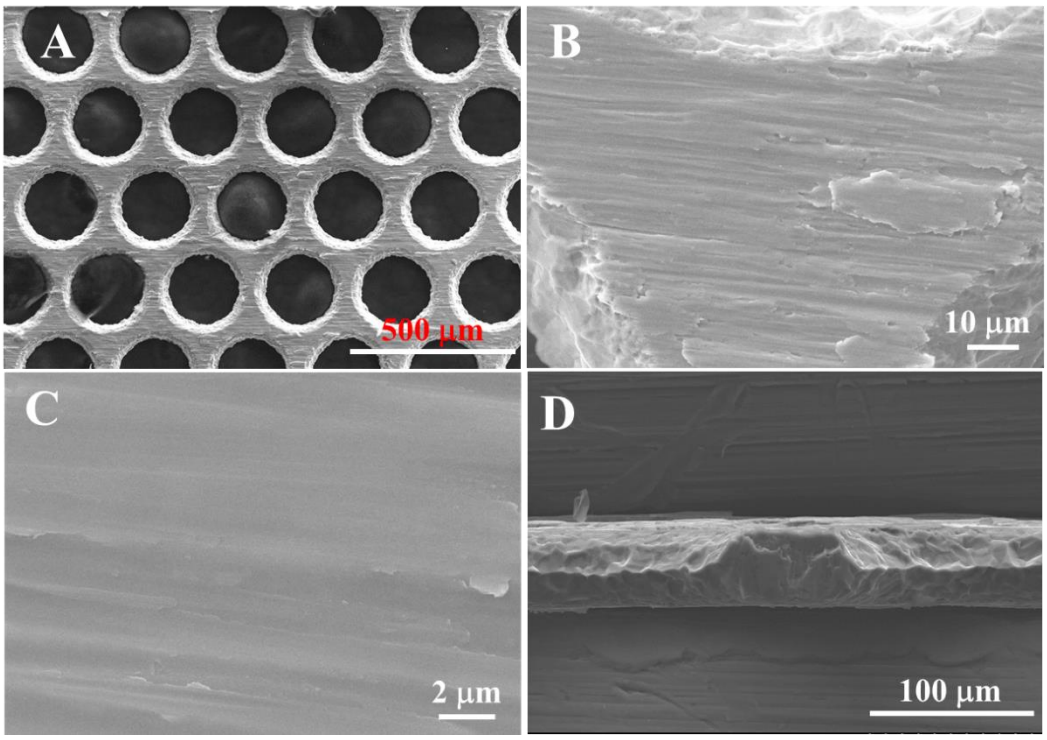


Figure 48. The top-view SEM image (A-C) of the TTLGDL with a pore size of 200 μm and a porosity of 40%, and (D) the related cross-section SEM image.

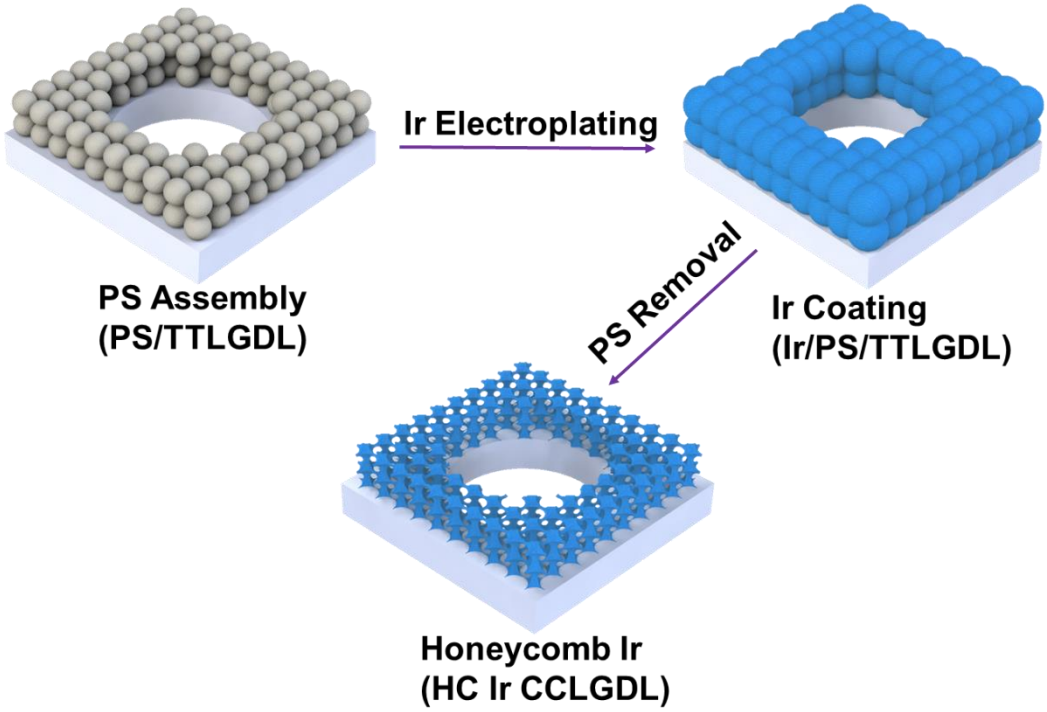


Figure 49. Schematic of the fabrication process of a honeycomb Ir CCLGDL.

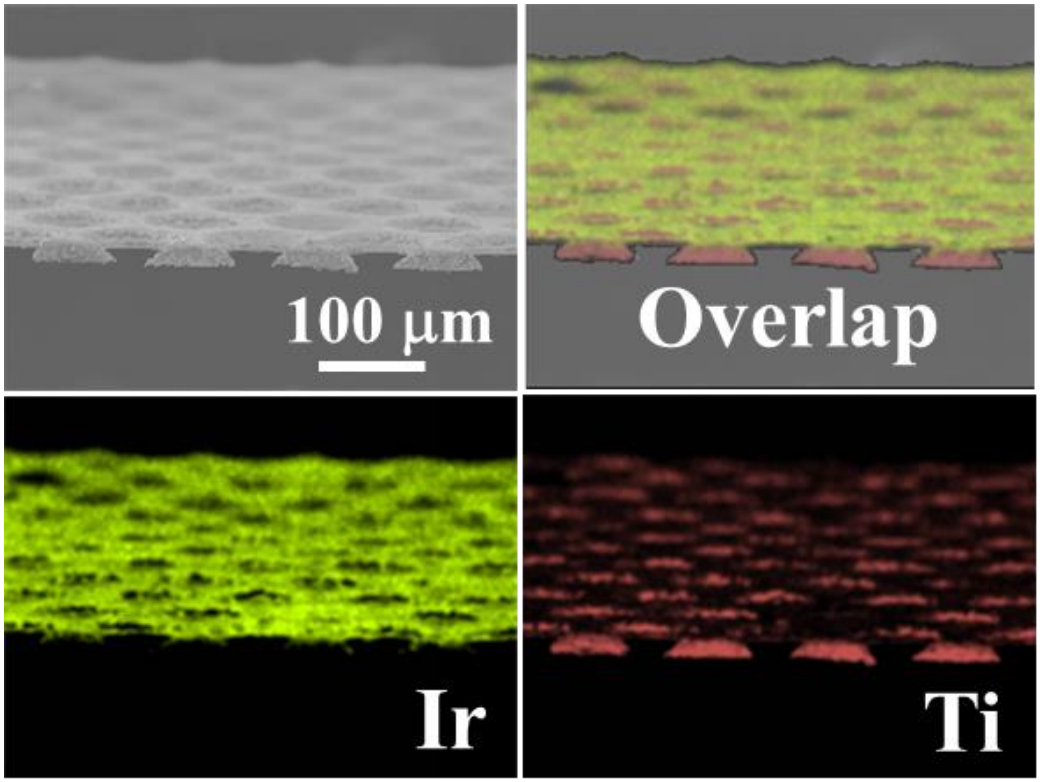


Figure 50. SEM-EDS mapping images of the HC Ir CCLGDL cross-section.

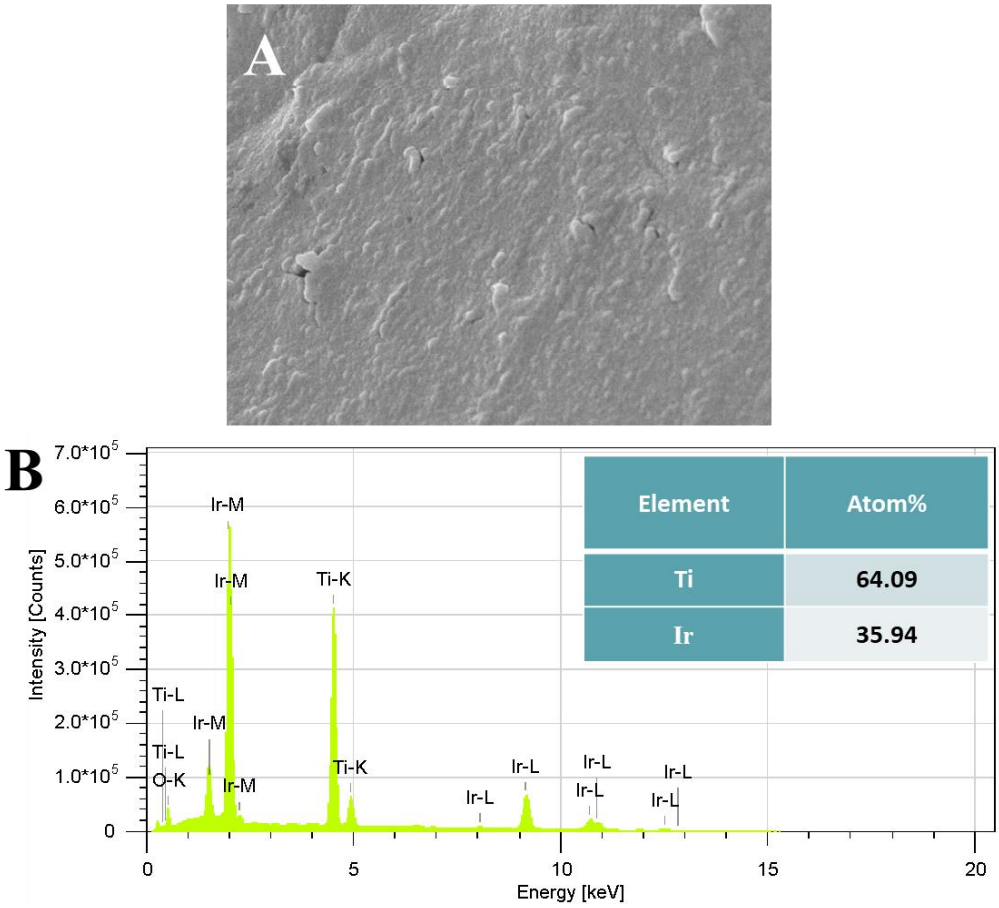


Figure 51. (A) SEM image of the dense Ir CCLGDL; (B) EDS analysis of the dense Ir CCLGDL.

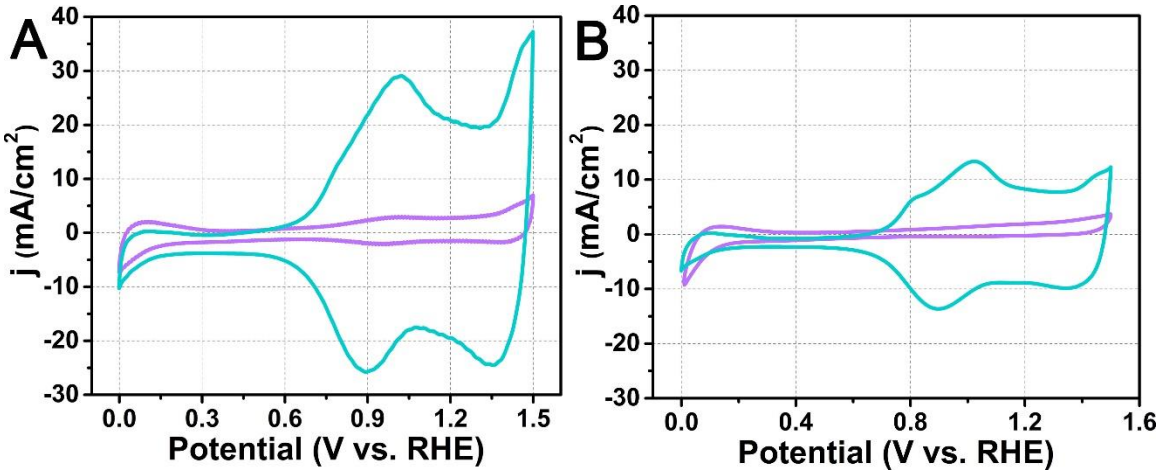


Figure 52. The initial CV scan cycle (purple line) and the CV scan cycle after full activation (green line) of the HC Ir (A) and the dense Ir (B).

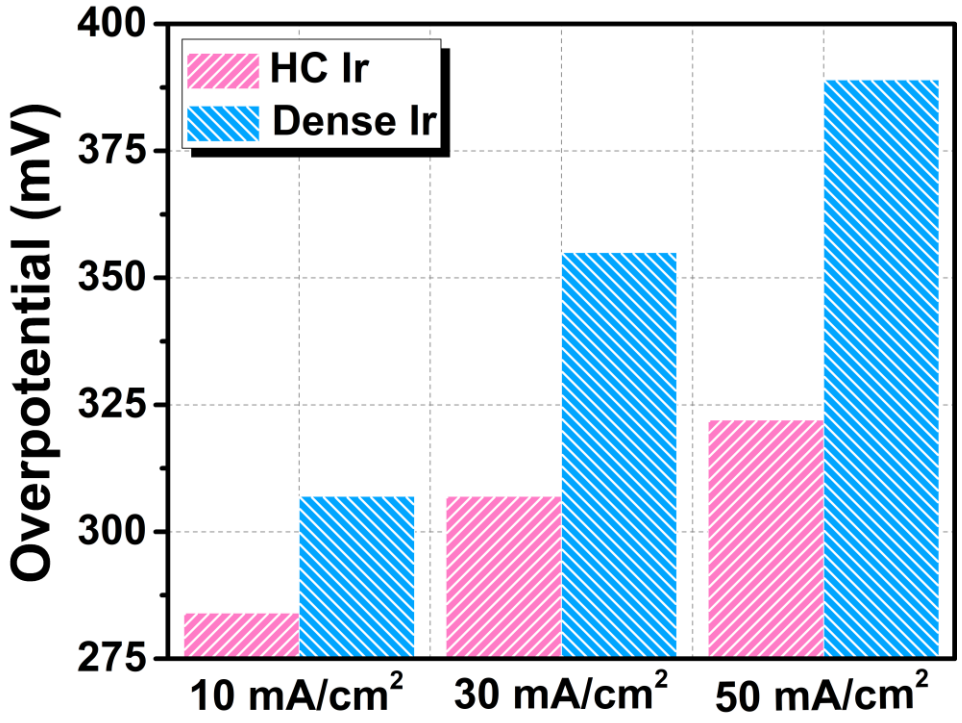


Figure 53. Overpotential comparison at different current densities.

Table 18. Details of the bubble size distribution.

Bubble size range (μm)	Pct. for HC Ir (%)	Pct. for dense Ir (%)
10 ~ 20	81.50	53.15
20 ~ 30	11.94	23.87
30 ~ 40	5.15	9.46
40 ~ 50	1.41	6.31
50 ~ 60	0	1.80
60 ~ 70	0	2.25
70 ~ 80	0	0.91
80 ~ 90	0	2.25

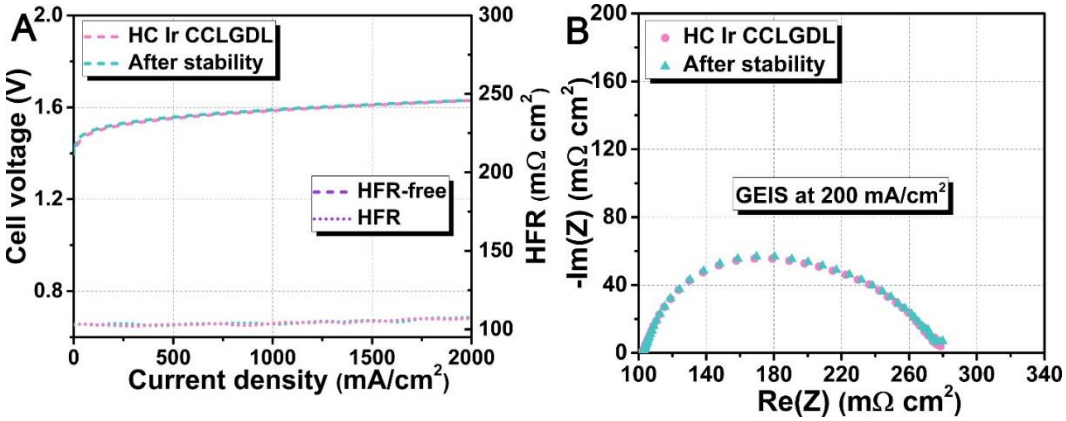


Figure 54. (A) The comparison of HFR-free performance and HFR, (B) Nyquist plot comparison at 200 mA/cm^2.

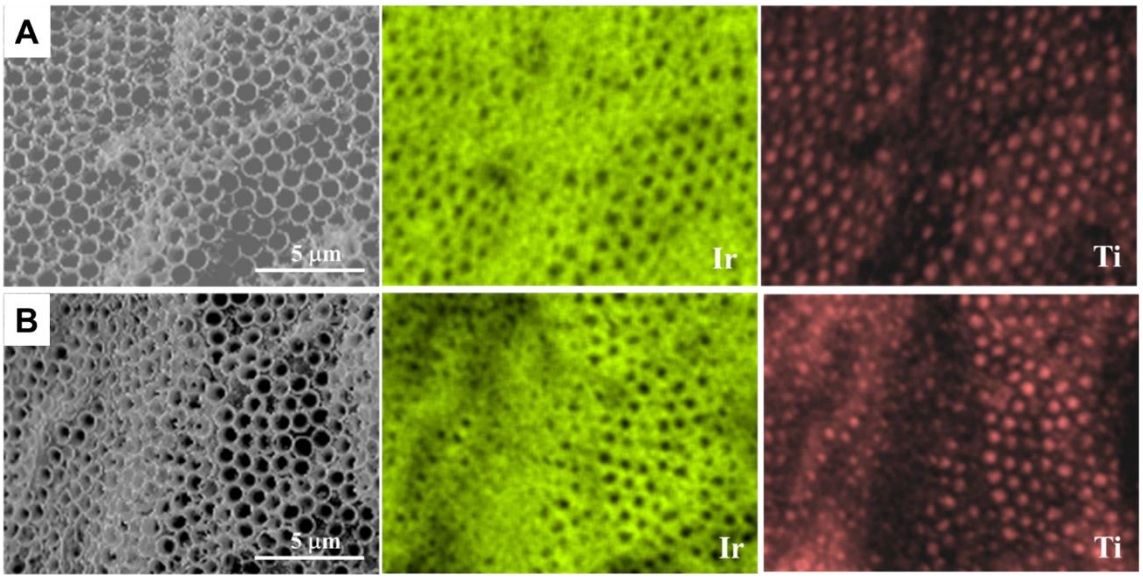


Figure 55. SEM-EDS mapping images of (A) the fresh HC Ir CCLGDL and (B) the tested HC Ir CCLGDL.

CHAPTER SIX

IONOMER-FREE NANOPOROUS IRIDIUM NANOSHEET ELECTRODES WITH BOOSTED PERFORMANCE AND CATALYST UTILIZATION FOR HIGH-EFFICIENCY WATER ELECTROLYZERS

A version of this chapter was originally published as:

Xie, Z.,† Ding, L.,† Yu, S.,† Wang, W., Capuano, C.B., Keane, A., Ayers, K., Cullen, D.A., Meyer III, H.M. and Zhang, F.Y., 2024. Ionomer-free nanoporous iridium nanosheet electrodes with boosted performance and catalyst utilization for high-efficiency water electrolyzers. Applied Catalysis B: Environmental 341 (2024): 123298.

† These authors contributed equally to this work.

CRediT authorship contribution statement

Z.X.: Conceptualization, Methodology, Data curation, Writing - original draft, review & editing, Investigation, Validation. L.D.: Methodology, Investigation, Validation, Writing - review & editing. S.Y.: Methodology, Investigation, Validation, Writing - review & editing. W.W.: Investigation, Validation, Writing - review & editing. C.B.C.: Investigation and Validation. A.K.: Investigation and Validation. K.A.: Investigation, Validation, Writing - review & editing. D.A.C.: Resources, Investigation, Validation, Writing - review & editing. M.H.M.: Investigation and Validation. F.-Y.Z.: Resources, Supervision, Project administration, Funding acquisition, Writing - review & editing.

I am fully responsible for the work submitted in these publications.

6.1 Abstract

Increasing the catalyst utilization efficiency and simplifying electrode fabrication processes are crucial to accelerate development of low-cost proton exchange membrane electrolyzer cells (PEMECs). Here, we develop a facile route to fabricate ionomer-free iridium nanosheet integrated electrodes, in which nanoporous iridium nanosheets (IrNS) with abundant exposed edges and nanopores are deposited on thin titanium liquid/gas diffusion layers (TT-LGDLs) via a low-temperature chemical synthesis strategy. Benefiting from high catalytic activity, good electrode conductivity and excellent liquid/gas transport properties, such nanoporous IrNS electrodes with low catalyst loadings require low cell voltages of 1.65 V and 1.78 V at 3000 and 6000 mA/cm^2, respectively. More impressively, a stable performance can be well maintained under extremely high current density tests of 5000 mA/cm^2, demonstrating the potential of low-loading nanoporous IrNS electrodes in solid-electrolyte based electrochemical conversion cells that require high current density operation.

6.2 Introduction

The climate change and global decarbonization is deriving the urgent demand for clean energy conversion and storage technologies[245-250]. The proton exchange membrane electrolyzer cell (PEMECs) has emerged as a very promising energy storage technology for hydrogen production from water electrolysis when integrated with solar, wind and other renewable energy sources[246, 247, 251-254]. Compared with conventional water electrolyzer systems, PEMECs have many unique advantages, including high efficiency, quick startup, compact design, low maintenance cost, and close-to-zero emissions. The membrane

electrode assembly (MEA) is very important to the overall cell performance and cost of the PEMEC. To achieve high efficiency and long durability of a PEMEC, high loadings of platinum-group metals (2~3.0 mg_{Ir}/cm^2) are generally required for the oxygen evolution reaction (OER) [249, 255-258].

Currently, the catalyst-coated membrane (CCM) and catalyst-coated porous transport layer as gas diffusion electrode (GDE) are two main electrode designs in PEMECs. Nafion ionomers are commonly applied in anode and cathode catalyst layers (CLs) for both CCM and GDE designs. The main roles of Nafion ionomer in CLs are as follows: 1) serving as proton conductors to facilitate proton transport from PEM to the catalyst surface and to extend the electrode/electrolyte reaction zone; 2) functioning as the binder to physically stabilize the catalysts on the PEM surface. For the CCM design, Bernt *et al.* studied the impact of ionomer content in anode CLs on cell performances and reported that 11.6 wt% Nafion ionomer in IrO_2/TiO_2 anode CLs showed the best cell performance among the tested anodes with an ionomer content from 2.2 to 28 wt%. [259] Kulkarni *et al.* fabricated ionomer-containing CCMs and GDEs, and compared their cell performances at different catalyst loadings. [260] They found that the ionomer in CLs hinders the catalyst utilization efficiency to some extent in both cases.

Recent studies have demonstrated advantages of ionomer-free electrode designs over conventional ionomer-containing electrodes, including improvement of catalyst utilization efficiency, energy efficiency enhancement, stability and remarkably simplified electrode fabrication steps [24, 25, 261-265]. For example, Sapountzi *et al.* fabricated CCMs with ionomer-free IrO_x and Pt catalyst layers at anode and cathode via a spark ablation process. [261] Such

ionomer-free CCMs with low catalyst loadings (0.8 mg_{Ir}/cm^2, 0.5 mg_{Pt}/cm^2) demonstrated significantly improved cell performance compared to conventional ionomer-containing CCMs (2 mg_{IrRuOx}/cm^2 at anode, 4 mg_{Pt}/cm^2 at cathode). More recently, Higashi *et al*. fabricated ionomer-free IrO_2 nanostructured textile based CCMs by the combination of electrospun PVP textiles and subsequent magnetron radiofrequency (RF) sputtering of IrO_2 catalysts and hot-pressing transfer to Nafion 212 membrane. [262] The cell performances at low loading levels of 0.1~0.3 mg_{Ir}/cm^2 are superior to ionomer-containing electrodes with the similar loadings. However, complicated CCM fabrication process and involvement of expensive electrospinning, sputtering and hot press equipment would limit the scale-up manufacturing, especially for large-size samples. Choe *et al.* reported an ionomer-free GDE design composed of electrodeposited IrO_2 catalysts on the Ti mesh substrate (0.4 mg/cm^2) and demonstrated a higher current density of 0.97 A/cm^2 at 1.6 V and improved stability compared to ionomer-containing IrO_2 GDE. [24] Lim *et al.* fabricated ionomer-free Pt@IrO_2 core-shell structured anodes by using sequential electrodeposition of 0.27 mg_{Pt}/cm^2 hemispherical Pt particles as support and 0.16 mg_{Ir}/cm^2 IrO_2 as catalysts on the Ti felt substrate. [34] This electrode with the total precious metal loading of 0.43 mg/cm^2 displayed enhanced cell performances than electrodeposited IrO_2 anode without Pt support.

To further enhance the catalyst utilization and performance of ionomer-free electrode designs, engineering nanostructures and tuning compositions of catalyst layers as well as electrode patterns have been explored [24, 171, 260, 262-264, 266-271]. Nevertheless, the cell performance and durability of most previously reported OER electrodes at high current densities are still far from satisfactory for real applications. Therefore, there is a continuing

need to optimize the electrolyzer electrode design with minimal catalyst use, and meanwhile to further improve energy efficiency and durability in harsh acidic and oxidizing conditions.

In this study, we report a simple process to prepare ionomer-free iridium nanosheet electrodes, in which nanoporous iridium nanosheets (IrNS) with abundant exposed edges and nanopores are deposited on thin titanium liquid/gas diffusion layers (LGDLs). Different from other reported electrolyzer electrodes in the literature, the nanoporous IrNS electrode has the following unique advantages: (1) Multifunctional TT-LGDLs can minimize ohmic and mass transport losses as compared to conventional 3D porous transport layers (PTLs); (2) The ionomer-free nanoporous iridium catalyst layer can provide abundant reaction sites for electrochemical reactions and significantly reduce the reaction overpotentials or activation losses in a PEMEC. (3) The required loading of catalysts can be greatly reduced from several mg/cm^2 down to 0.3 mg/cm^2 or lower, thus decreasing the catalyst material cost. (4) The whole electrode fabrication and assembly are simplified compared to conventional electrodes (CCM/LGDLs) with multi-step and complicated fabrication processes. Thanks to the above-mentioned benefits, nanoporous IrNS electrodes with low catalyst loadings can deliver the current densities of 2000 mA/cm^2 at a low cell voltage of 1.78 V when coupled with Nafion 117 (~ 175 μm), showing a about 10 times higher mass specific current than that of the conventional CCM baseline. More impressively, when coupled with Nafion 212 (~ 50 μm), a higher current density of 6000 mA/cm^2 can be achieved at the low cell voltage of 1.78 V. The stable cell performances are demonstrated for both Nafion 117 and Nafion 212 cases at high current

densities, indicating the great potential for the application of nanoporous IrNS electrodes in the practical PEMECs under the high current density operation. The whole electrode design in this work can also be generalized to other solid electrolyte-based electrochemical conversion cells that require high current density operation.

6.3 Experimental Section

6.3.1 Fabrication of ionomer-free IrNS integrated electrodes

TT-LGDLs with distributed circular pores were manufactured by chemical wet etching of titanium foils with the assistance of lithographically-pattered resist masks. [17] TT-LGDLs were cleaned thoroughly by sonication in acetone, ethanol and deionized (DI) water for 15 min in each step. Afterwards, oxalic acid (OA) treatment was performed to remove the native titanium oxide layer from LGDL substrates. The LGDL substrates were completely immersed into the reaction solution containing 1 mL 40 mM $IrCl_3$ solution (Sigma-Aldrich), 1 mL dimethylformamide (DMF) (Sigma-Aldrich), 1 mL DI water, 1 mL formic acid (Sigma-Aldrich), and 5 mg of poly(ethylene oxide)-b-polystyrene (PEO-b-PS, Polymer Source Inc). The reaction solution was heated at 80 ^{o}C for 5 h and cooled down to room temperature. Finally, the IrNS was deposited on the surface of LGDL substrates, forming the nanoporous IrNS electrode. After post-washing with acetone and ethanol at least three times, the nanoporous IrNS electrode was annealed at 150 ^{o}C for 15 min in vacuum for sample characterizations and cell performance testing. The catalyst loadings were achieved and determined by measuring the mass difference before and after the IrNS deposition on the employed LGDL substrate. Afterwards, based on the wetted surface area of the substrate, the catalyst loading is calculated.

6.3.2 Materials characterization

The surface morphology and chemical composition of nanoporous IrNS electrodes were characterized by a field emission scanning electron microscope (SEM) (JSM-IT700HR), which is equipped with energy-dispersive X-ray spectroscopy (EDS). The nanostructure of IrNS catalysts was characterized by aberration-corrected scanning transmission electron microscopy (STEM) on a JEOL JEM-ARM200F "NEOARM" operated at an acceleration voltage of 80 kV. A Rigaku SmartLab X-ray diffraction (XRD) system was used to investigate the crystalline structure of the sample. The surface chemistry of samples was identified by X-ray photoelectron spectroscopy (XPS) analysis on a Thermo Scientific K-Alpha spectrometer.

6.3.3 Electrochemical measurements

The as-synthesized IrNS catalysts on Ti substrate as the working electrode, a graphite rod as the counter electrode and an Ag/AgCl reference electrode were employed in a three-electrode system with 0.5 M H_2SO_4 as the liquid electrolyte. The linear sweep voltammetry (LSV) data were collected by a Potentiostat (VSP/VMP3B-100, Bio-Logic) at a scan rate of 5 mV/s at room temperature.

6.3.4 Cell assembly and performance evaluation of the PEMEC

A carbon paper (Toray 090) (280 μm in thickness, 78% porosity) was used as the cathode LGDL. The grade 2 Ti-made bipolar plate and graphite-made bipolar plate (AXF-5Q) with parallel flow channels were used at anode and cathode, respectively. The nanoporous IrNS electrode, single-sided CCM, and carbon paper, together with the gaskets and the bipolar plates were sandwiched by two stainless steel end-plates to assemble a PEMEC.

Afterwards, the PEMEC was compressed by eight evenly distributed ¼ 20 bolts, which were tightened to a torque of 40 lb-in. A schematic illustration of electrode assembly in a PEM water electrolyzer is shown in **Figure 62**. All the cell tests were performed in a PEM electrolyzer cell with a 5 cm^2 active area. A temperature of 80 °C, atmospheric pressure at both anode and cathode, and a water flow rate of 20 mL/min at anode side were used for all cell tests. The commercial cathode-only single-sided CCMs with the Pt black (1.0 mg_{Pt}/cm^2) at the cathode and Nafion 117 with a thickness of 175 µm serving as the electrolyte, and the commercial two-sided CCMs with 2.0 mg_{Ir}/cm^2 IrO_x at the anode, 1.0 mg_{Pt}/cm^2 Pt black at the cathode and N117 membrane as the baseline were supplied by Nel. The Pt/C (0.14 mg_{Pt}/cm^2) at cathode and Nafion 212 with a thickness of ~ 50 µm serving as the electrolyte were home-made by a direct spray coating process, based on the modified recipe in our previous publication. [180] The polarization curves were collected by a Potentiostat (VSP/VMP3B-100, Bio-Logic). The electrochemical impedance spectroscopy (EIS) plots were recorded from 10 kHz to 50 mHz at 1000 mA/cm^2. The high-frequency resistance (HFR) refers to the ohmic resistance value obtained at high frequencies, which is usually used to represent the total ohmic resistance of the PEM electrolyzer cell. The HFR plots were recorded under the high frequency of ~ 3 kHz by using the Staircase Galvano Electrochemical Impedance Spectroscopy (SGEIS) technique with Biologic EC-Lab software. HFR correction is conducted by using the mean HFR values and current density densities to calculate the HFR-free cell voltages according to the following equation: $V_{HFR\text{-}free} = V_{cell} - I*HFR$. With the help of HFR-correction, the activation losses between the IrNS electrode and CCM baseline in the PEMECs can be directly compared.

6.4 Results and Discussions

6.4.1 Morphology and crystal structure of nanoporous IrNS electrode

The schematic in **Figure 56** illustrates the cost-effective and facile fabrication of the nanoporous IrNS integrated electrode via a low-temperature chemical synthesis approach. The microstructures (e.g., pore size, porosity, etc.) of the TT-LGDL substrate have been systematically studied and optimized in our previous research. For instance, the TT-LGDL with the pore size of 100 μm and thickness of 25 μm exhibited over 9% energy efficiency enhancement at 2000 mA/cm^2 and enhanced mass transport properties compared to conventional 350-μm-thick Ti felt LGDLs. [17] Moreover, with the same porosity, the TT-LGDL with the pore size of 100 μm displayed smaller activation and mass transport losses than TT-LGDLs with larger pore sizes of 200 and 300 μm. [25] As a proof of concept, we selected the TT-LGDL with ~ 100 μm pore size and ~ 40% porosity as the substrate for deposition of the IrNS on TT-LGDLs in this study. The surface-treated TT-LGDL substrates were completely immersed into the reaction solution and kept at 80 ^{o}C for 5 h to obtain the nanoporous IrNS electrode, in which IrNS was deposited on the modified TT-LGDL substrates. During the synthesis process, the reducing agent of formic acid (HCOOH) undergoes decomposition and generates the carbon monoxide (CO) molecules. Previous studies have demonstrated that CO is capable of strongly binding to the specific crystal facets of diverse catalytic metals (e.g., Ir, Pd, etc.), facilitating the two-dimensional (2D) nanosheet formation [272, 273]. With the help of block polymer PEO-*b*-PS template, Ir nanocrystals nucleate and grow into 2D Ir nanosheets with numerous nanopores. In addition to the nanopore formation on the basal planes of Ir nanosheets, the secondary

porous structure with large pores is also constructed among individual nanosheets during the continuous growth process.

Different nanoporous IrNS catalyst loadings can be achieved by merely adjusting the iridium precursor concentrations under the same reaction time and temperature. Based on our experimental results, the minimum concentration of the Ir chemical precursor ($IrCl_3$) of at least 40 mM is required for successful and relatively uniform deposition of IrNS on the LGDL substrate. The amount of iridium loss during the deposition process is about 10%. Increasing the Ir concentration would result in the IrNS loading increase on the employed LGDL substrate without altering the nanostructures of IrNS catalysts. Conversely, when the $IrCl_3$ concentration is lower than 40 mM, the deposition of IrNS catalysts on the LGDL substrate becomes non-uniform. Our research work is still ongoing to better understand IrNS deposition mechanism on the LGDL substrate.

The morphology, nanostructure and elemental composition of the nanoporous IrNS integrated electrode were first characterized by SEM and EDS techniques. As shown in **Figure 57,** the applied TT-LGDL substrate in this study shows a relative smooth surface and well-defined circular pore morphology with the average pore size of ~ 100 μm, calculated porosity of ~ 40% and ~ 25 μm in thickness. The high-resolution SEM images in **Figure 57d-f** reveal that nanoporous IrNS catalysts with abundant exposed active edges were successfully deposited on a surface-treated TT-LGDL substrate with full surface coverage and good uniformity.

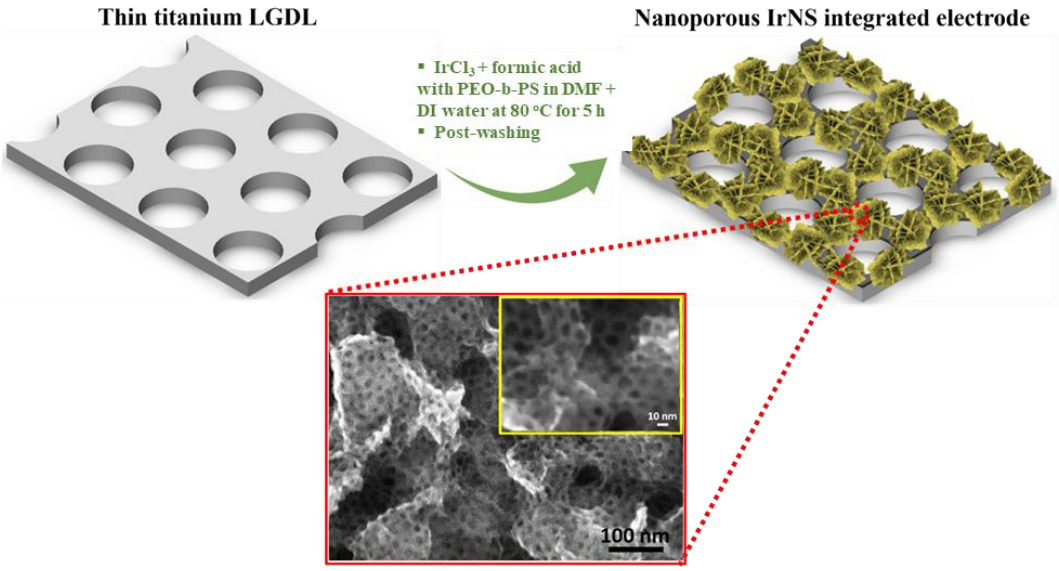


Figure 56. Schematic illustrating the design of the nanoporous IrNS integrated electrode composed of *in-situ* deposited ultrathin nanoporous iridium nanosheets on thin titanium LGDLs via a low-temperature chemical synthesis strategy.

The SEM images and corresponding EDS maps in **Figure 57g-i** and **Figure 63** show the relatively homogenous elemental distribution of Ir across the entire nanoporous IrNS integrated electrode, further confirming the uniform surface coverage of IrNS on the TT-LGDL substrate. To study the crystal structure of as-synthesized nanoporous IrNS catalysts, the catalysts and the underlying substrate were separated by sonication and then the catalysts were collected for the XRD measurement. The XRD pattern in **Figure 57j** indicates that as-synthesized nanoporous IrNS catalysts are polycrystalline and composed of metallic Ir with the fcc crystal structure, which matches well with the standard XRD pattern of Ir fcc (JCPDS No.: 06-0598). There are no detected secondary impurity phases or oxidized Ir phase in the sample. The metallic IrNS is expected to give rise to better conductivity of the entire catalyst layers than other iridium oxide-based catalysts. More importantly, the elimination of ionomer in the catalyst layer would also greatly reduce the ohmic resistance of the electrodes in practical PEMECs, especially compared to most commonly used ionomer-mixed catalyst layers. Collectively, the above SEM, EDS and XRD characterization results demonstrate the successful fabrication of ionomer-free nanoporous IrNS integrated electrodes with desirable nanostructure, good surface coverage and uniformity as well as the dominant metallic IrNS.

6.4.2 Nanostructure of nanoporous IrNS catalysts

To obtain more detailed structural information, high-angle annular dark-field (HAADF)-STEM images of as-synthesized IrNS catalysts were obtained. As seen from STEM images in **Figure 58a,** nanopores are formed within the individual nanosheets. The measured lattice fringes in **Figure 58b** are 0.19 and 0.22 nm, corresponding to (002) and (111) planes

of the metallic iridium with a fcc crystal structure. The inset in **Figure 58b** shows the fast Fourier transform (FFT) pattern calculated from the corresponding green box, further confirming the (111) crystal plane for the metallic iridium.

6.4.3 Full cell characterization of nanoporous IrNS in PEMECs with N117 membrane

Prior to the full cell characterization in PEMECs, the intrinsic activity of nanoporous IrNS catalysts for the OER was first evaluated in a half electrochemical cell via a three-electrode system in 0.5 M H_2SO_4 liquid electrolyte. As shown in **Figure 64**, the nanoporous IrNS electrode displays a low overpotential of 270 mV and small Tafel slope of 53 mV/dec, outperforming benchmarking IrO_2 nanoparticles and other Ir-based OER catalysts in the literatures. [274] The nanosheet structure and nanopores in the individual nanosheets can expose abundant active sites, leading to improved OER performance. When coupled with Nafion 117 (~ 175 μm), the polarization curves in **Figure 59a** show that the nanoporous IrNS integrated electrode with a low catalyst loading of 0.28 mg_{Ir}/cm^2 can deliver the current densities of 1000, 2000, 3000 and 4000 mA/cm^2 at low cell voltages of 1.65, 1.78, 1.90 and 2.02 V, respectively. On the contrary, the conventional CCM/TT-LGDL baseline with a high loading of 2.0 mg_{Ir}/cm^2 requires a higher cell voltage of 1.88 V at 2000 mA/cm^2, which is much larger than the nanoporous IrNS electrode by 100 mV. After high-frequency resistance (HFR) correction, nanoporous IrNS electrode displays about 10 mV activation loss reduction in comparison with the high-loaded CCM/TT-LGDL baseline, indicating boosted catalyst utilization with the newly developed nanoporous IrNS electrode design.

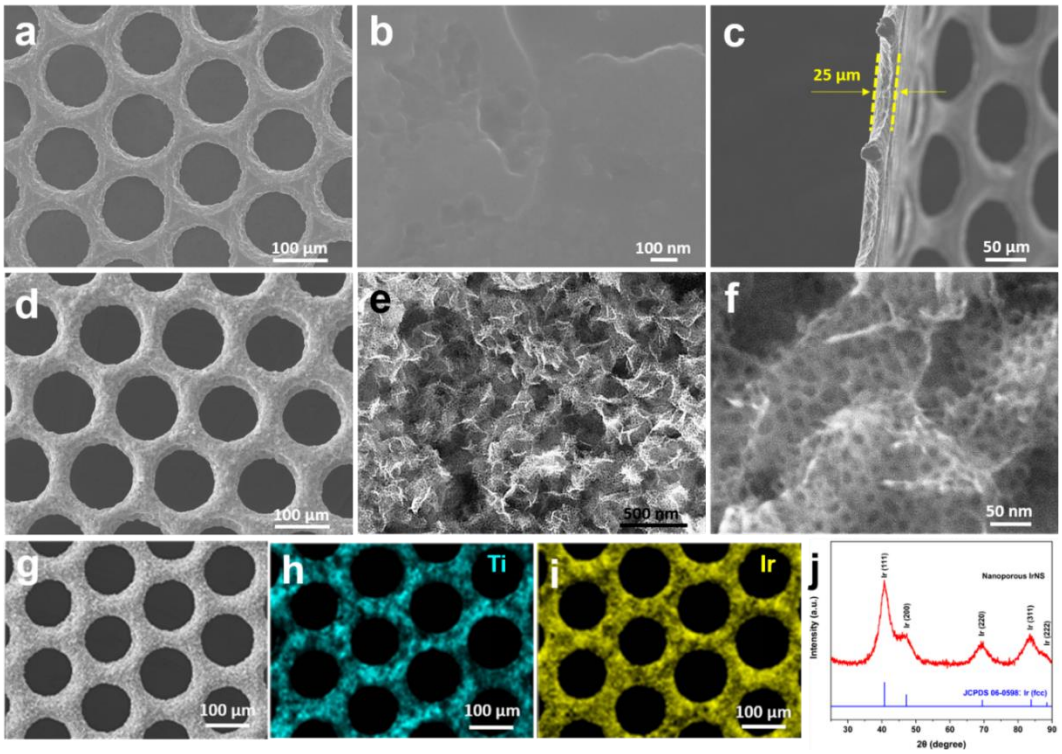


Figure 57. Morphological and compositional characterizations. (a-b) Top-view and (c) cross-section SEM images of the employed TT-LGDL substrate. (d-f) SEM images of the nanoporous IrNS integrated electrode. (g-i) SEM-EDS elemental mapping of the electrode. (j) XRD pattern of the nanoporous IrNS catalysts.

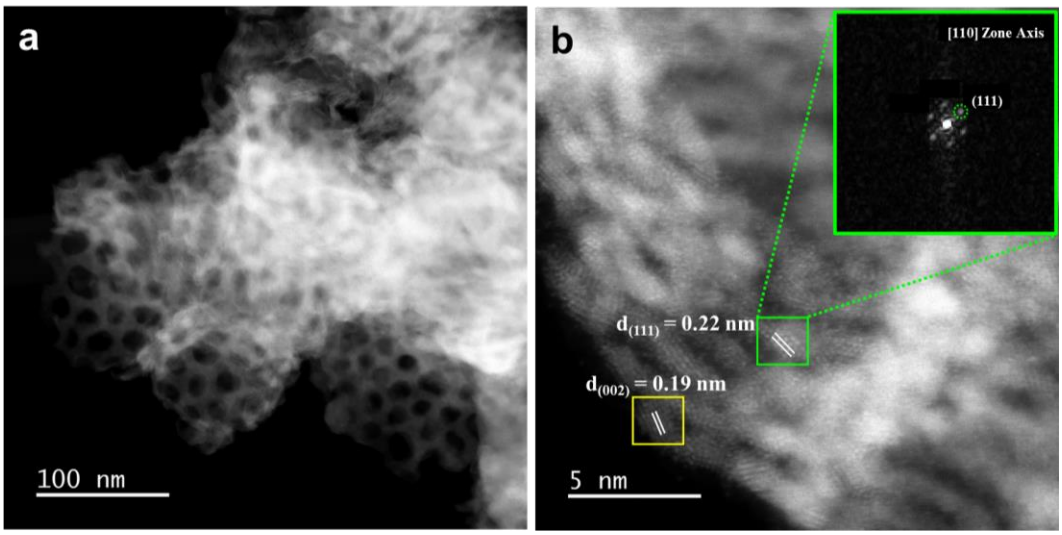


Figure 58. (a-b) HAADF-STEM images of as-synthesized IrNS catalysts prior to cell test in PEMECs.

Furthermore, large ohmic loss generally occurs in PEMECs with the conventional ionomer-mixed MEA, due to the poor conductivity of the entire catalyst layers. For instance, as shown in **Figure 59b**, the CCM/TT-LGDL baseline exhibits a high average HFR value of 143 $m\Omega*cm^2$ at 80 ^oC. However, benefiting from the ionomer-free IrNS catalyst layer, the nanoporous IrNS electrode shows an average HFR value of as small as 101 $m\Omega*cm^2$, which is about 42 $m\Omega*cm^2$ smaller than the baseline, which are consistent with the EIS results in **Figure 65**. Such a large HFR reduction results in about 84 mV improvement of the overall cell performance at 2000 mA/cm^2. The HFR-free EIS analysis at 1000 mA/cm^2 in **Figure 59c** shows that the PEMEC with nanoporous IrNS electrode has smaller activation and mass transport losses in total than the CCM/TT-LGDL baseline, as evidenced by the smaller size of semi-arch than the CCM/TT-LGDL baseline. This result implies that the ionomer-free nanoporous IrNS electrode could facilitate the electron transfer across the entire catalyst layer, superior to conventional ionomer-mixed catalyst layers in the CCM-based PEMECs.

To validate the electrode stability in PEMECs, the stability test of nanoporous IrNS electrodes under a high current density of 1800 mA/cm^2 was conducted. As seen from **Figure 59d**, after the initial 20-h test at 1000 mA/cm^2, the cell voltage slightly increases from ~ 1.762 V to 1.802 V during the subsequent 120-h test at 1800 mA/cm^2, displaying a small performance degradation rate of 0.33 mV/h. To compare the catalyst utilization levels, the mass-specific current plots are derived by normalizing the delivered current to mass for nanoporous IrNS integrated electrode (0.28 mg_{Ir}/cm^2) and conventional CCM/TT-LGDL baseline, as shown in **Figure 59e**.

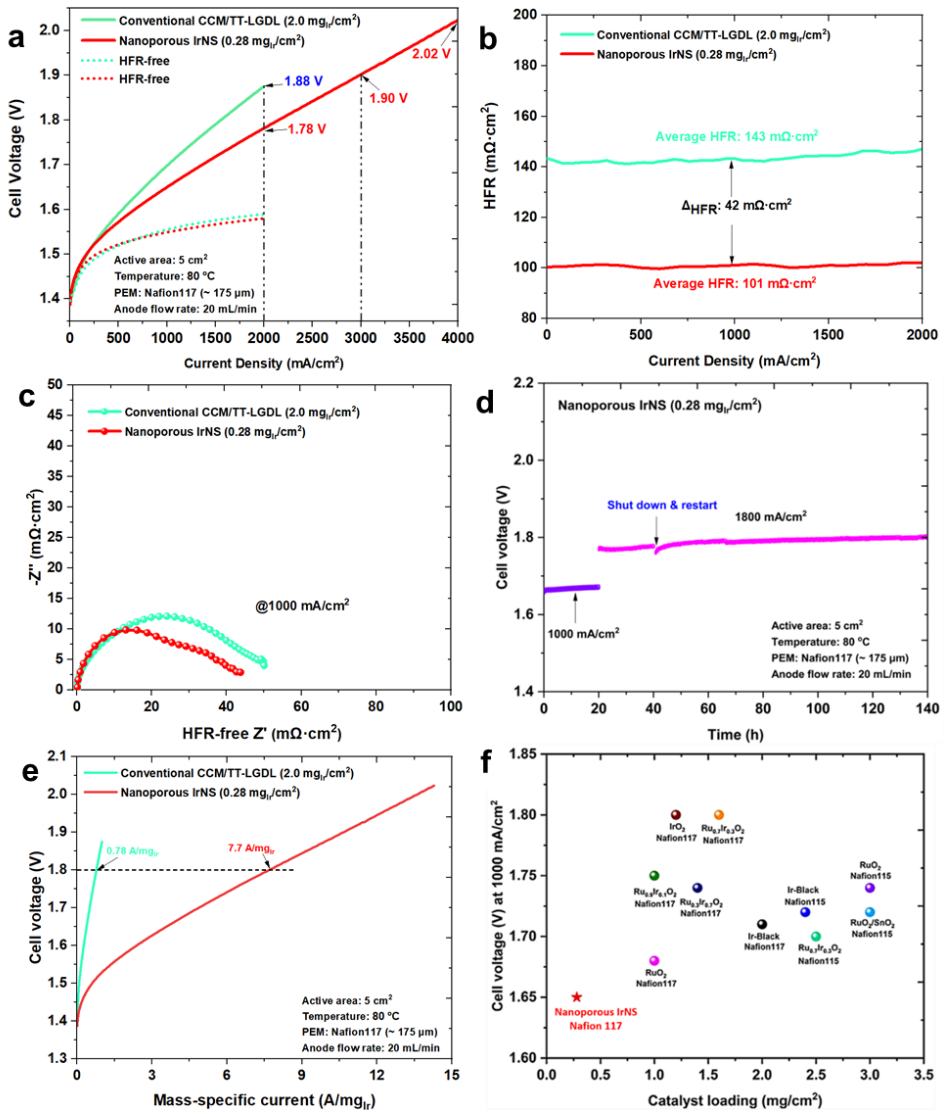


Figure 59. (a) Polarization curves of an IrNS integrated electrode coupled with N117 membrane and conventional CCM/TT-LGDL in PEMECs at 80 °C. (b) The HFR comparison between 0 and 2000 mA/cm^2. (c) The HFR-free EIS plots of nanoporous IrNS and conventional CCM/TT-LGDL at 1000 mA/cm^2. (d) Cell stability test at 1000 mA/cm^2 for initial 20 hours and subsequent test at 1800 mA/cm^2 for over 120 h. (e) Mass-specific current comparison. (f) Cell performance comparison.

By comparison, the mass-specific current of nanoporous IrNS integrated electrode is as high as 7.7 A/mg_{Ir} at the cell voltage of 1.8 V, which is about 10 times higher than the CCM/TT-LGDL baseline. This mass-specific current comparison demonstrates that boosted catalyst utilization and performance can be achieved by adopting ionomer-free nanoporous IrNS integrated electrode. Moreover, by comparison with the literature in **Figure 59f**, the cell performance of the PEMEC with nanoporous IrNS electrode in this study is superior to most previously reported noble metal-based OER electrodes in PEMECs up to date [274-283].

6.4.4 Full cell characterization of nanoporous IrNS in PEMECs with N212 membrane

To further explore the application of a nanoporous IrNS integrated electrode under high current densities of up to 6000 mA/cm^2, a thinner Nafion 212 membrane with the thickness of ~ 50 μm was applied for the cell test. The Pt/C (0.14 mg_{Pt}/cm^2) was spray coated onto the Nafion 212 membrane as cathode. As observed from the polarization curve in **Figure 60a**, low cell voltages of 1.60, 1.65 and 1.78 V were obtained at the current densities of 2000, 3000 and 6000 mA/cm^2, respectively, which exceeds the U.S. Department of Energy (DOE) 2026 technical performance target (1.8 V at 3000 mA/cm^2). [284] A stable HFR of 39 $m\Omega*cm^2$ was observed between 0 and 6000 mA/cm^2 in **Figure 66**. After HFR-correction, the corresponding HFR-free cell voltages are as low as 1.53 and 1.57 V at 2000 and 6000 mA/cm^2, respectively.

Currently, various accelerated stress test (AST) protocols are still under development, and the available AST protocols in the literatures are still not able to fully correlate AST results to prediction of real-life durability in commercial PEM water electrolyzer systems. This

challenge stems from the involvement of many stressors during the long-term operation conditions, such as high current density, dynamic load operation, on/off operation, temperature, water quality and differential gas pressure [285-287]. Unavoidable coupling effects between these stressors are complicated and have not been clearly understood yet. So far, stability tests of PEM water electrolyzers under constant current densities of 500~2000 mA/cm^2 have been widely reported in previous publications. In our work, we particularly chose 5000 mA/cm^2 as the main stressor to evaluate the stability of the nanoporous IrNS electrode. As seen from **Figure 60b**, our stability AST protocol includes a nominal current density operation at 1800 mA/cm^2 for 90 h and a subsequent high current density operation at 5000 mA/cm^2 for 130 h. At both current densities, the nanoporous IrNS electrode displays stable performances. Notably, the degradation rate is only about 3.32 μV/h during the continuous 70-h test within the period of 150-220 h at 5000 mA/cm^2. Therefore, the developed nanoporous IrNS integrated electrode at low loadings in this work shows the potential applications for the highly efficient and robust OER under high current density operation in practical PEMECs. Except the high current density operation stressor, other stressors such as dynamic load and differential gas pressure will be incorporated in our future studies.

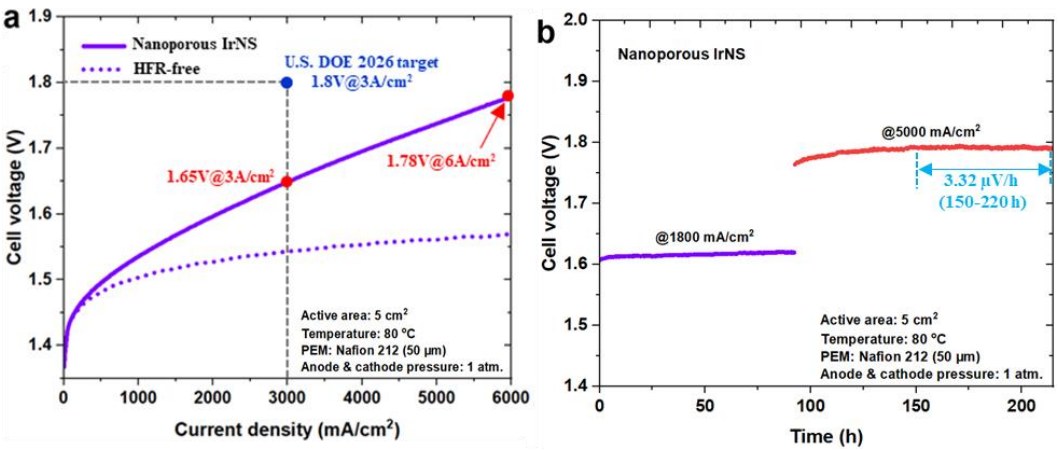


Figure 60. (a) Polarization curves of a nanoporous IrNS integrated electrode coupled with Nafion 212 membrane under high current densities of up to 6000 mA/cm^2. (b) Cell stability tests at 1800 mA/cm^2 for 90 h and 5000 mA/cm^2 for 130 h.

6.4.5 Post-analysis of IrNS catalysts after the electrolyzer test

The morphology/nanostructure, crystal structures and chemical compositions of IrNS catalysts after the cell durability test at 5000 mA/cm^2 were analyzed by using STEM and XPS techniques. The STEM image in **Figure 61a** verifies that most nanopores remain in IrNS catalysts but the partial loss of the nanosheet morphology appears after the cell durability test. The STEM image at a higher magnification in **Figure 61b** shows that the tested IrNS catalysts are composed of iridium oxide nanocrystals with the tetragonal crystal structure, as evidenced by the measured lattice fringes of 0.31 and 0.27 nm, corresponding to the (110) and (101) crystal planes of iridium oxide. The (110) crystal plane for iridium oxide is further confirmed by the diffraction spots in the FFT pattern calculated from the corresponding red box in the inset of **Figure 61b**. Therefore, the STEM results of as-synthesized IrNS catalysts in **Figure 58** and tested IrNS catalysts in **Figure 61** reveal that metallic IrNS catalysts before the cell test converted to iridium oxide after the stability test at 5000 mA/cm^2 in a PEM electrolzyer cell. The observed changes in morphology and nanostructure are probably attributed to the transformation from metallic iridium to iridium oxide.

The chemical composition of IrNS catalysts before and after the cell stability test was analyzed by using the XPS characterization. The high-resolution XPS spectra of Ir 4f are presented in **Figure 67**. To obtain an adequate curve-fitting, both spectra need three sets of $4f_{7/2}$ doublets (marked as Ir-1, Ir-2 and Ir-3), which are centered at ~62, ~63 and ~65 eV, respectively.

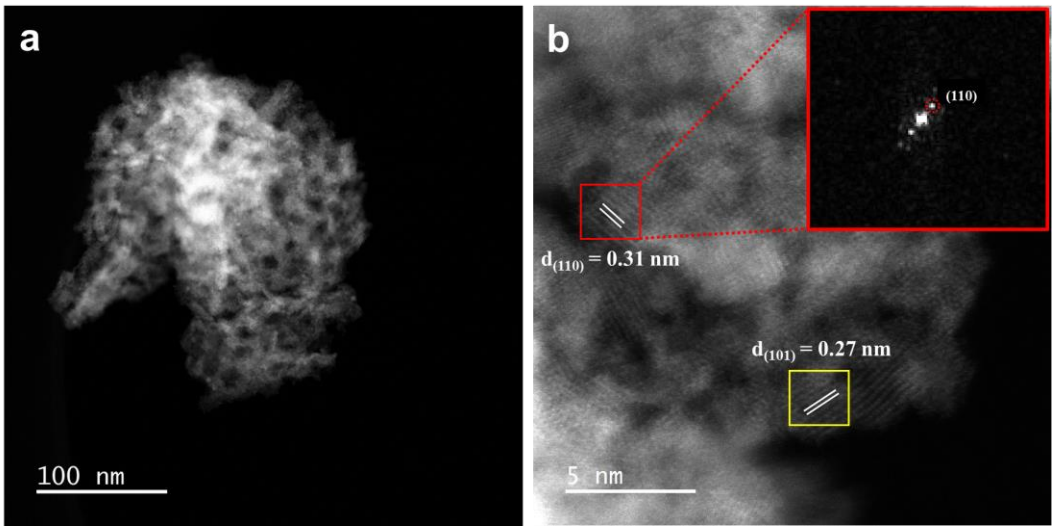


Figure 61. (a, b) HAADF-STEM images of IrNS catalysts after the cell stability test at 5000 mA/cm^2.

These are tentatively assigned to Ir^{3+}, Ir^{4+} and Ir^{X+} (X>4). For the as-synthesized IrNS catalysts, the iridium species with a mix of Ir^{3+}, Ir^{4+} and Ir^{X+} (X>4) coexist on the catalyst surface, which is likely due to natural oxidation by air exposure. However, metallic iridium is dominant in as-synthesized IrNS catalysts, as confirmed by the XRD analysis in **Figure 57j** and STEM characterization in **Figure 58**. This combination of metallic iridium with oxidized surface might improve the OER kinetics by providing good electronic conductivity and more active iridium species for the OER. [288] Compared to as-synthesized IrNS catalysts, it is found that the Ir $4f_{7/2}$ peak shifts towards higher binding energy after the cell stability test, which is probably attributed to the increased oxidation of catalysts during the long-term OER process. This phenomenon is consistent with previously reported studies on Ir-based OER catalysts [288-290].

6.5 Conclusions

In summary, we report a novel ionomer-free nanoporous iridium nanosheet electrode design, in which nanoporous iridium nanosheets with abundantly exposed edges and highly porous structures are successfully coated on TT-LGDLs by a low-temperature chemical synthesis method. The combination of high catalytic activity, good electrode electronic conductivity and excellent liquid/gas transport properties enables significantly boosted catalyst utilization and enhanced cell performance of nanoporous NS electrode. When coupled with Nafion 117 (~ 175 μm), nanoporous IrNS electrodes with low catalyst loadings can deliver the current densities of 2000 mA/cm^2 at a low cell voltage of 1.78 V, and a ~10 times higher mass specific current is achieved compared to the conventional CCM baseline at 1.8 V. Moreover, when coupled with Nafion 212 (~ 50 μm), the

nanoporous IrNS electrode manifests cell voltages as low as 1.65 V and 1.78 V at 3000 and 6000 mA/cm^2, respectively. The durability test provides additional confirmation that nanoporous IrNS is capable of maintaining stable performances at both 1.8 and 5 A/cm^2 for over 200 h. Therefore, our research has revealed the beneficial effects of ionomer-free nanostructured catalysts in enhancing catalyst utilization, cell performance, and durability in PEMECs, which offers new opportunities to minimize the usage and cost of Ir-based catalysts, while accelerating the commercialization of efficient, robust and scalable PEM water electrolysis in hydrogen production.

Appendix

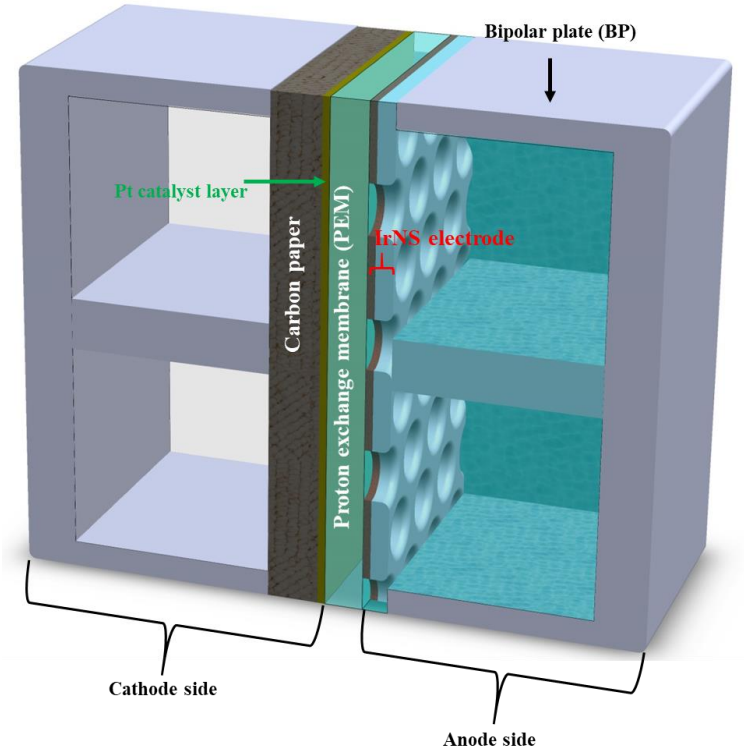


Figure 62. A schematic illustration of electrode assembly in a PEM water electrolyzer.

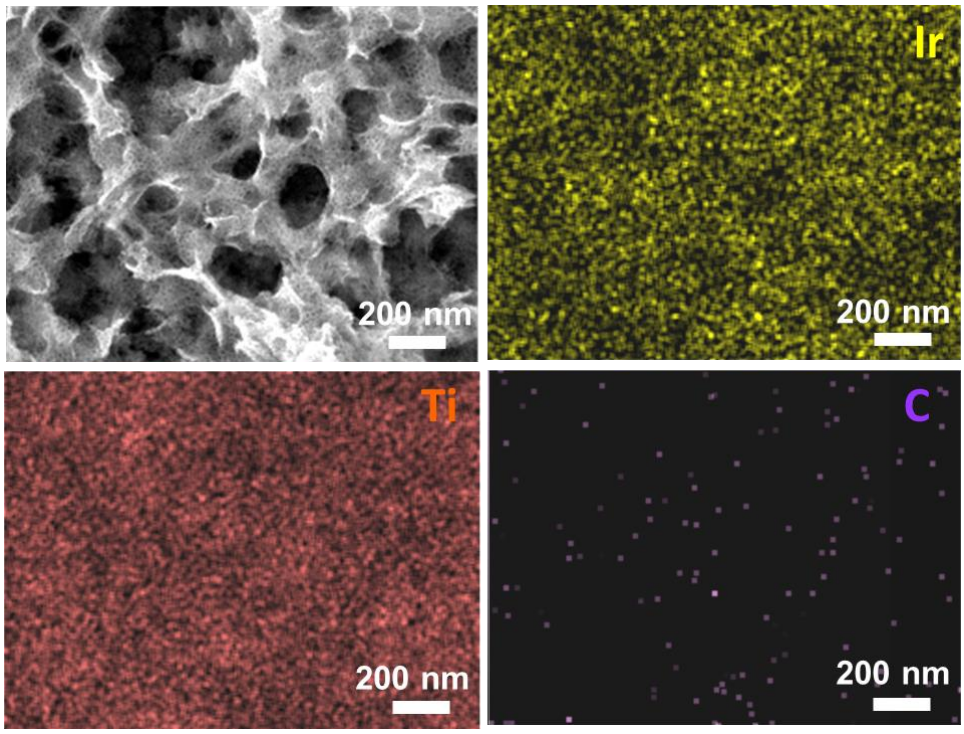


Figure 63. The SEM-EDS elemental mapping of the IrNS electrode at a higher magnification.

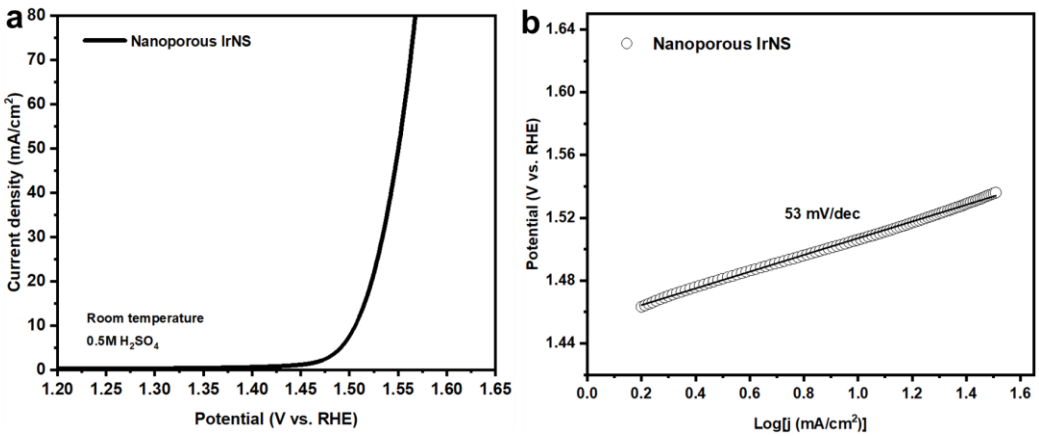


Figure 64. The polarization curve of nanoporous IrNS catalysts for the OER. (b) The corresponding Tafel plot.

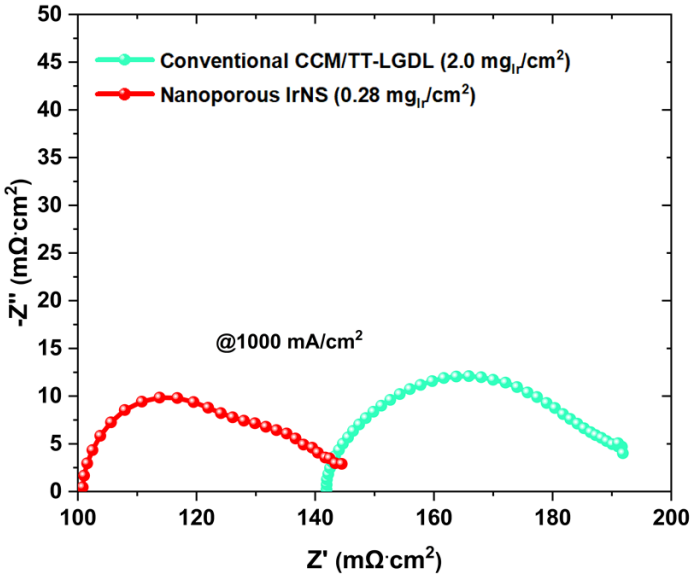


Figure 65. The EIS plots of nanoporous IrNS coupled with Nation 117 membrane and conventional CCM/TT-LGDL baseline at 1000 mA/cm^2.

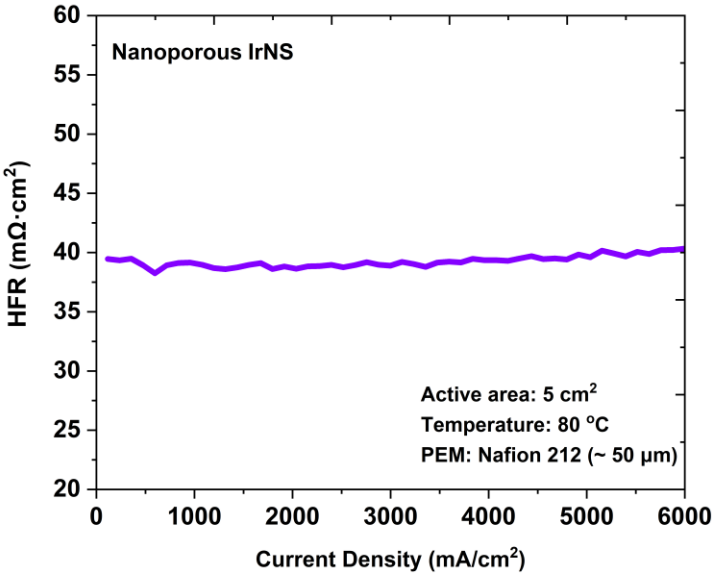


Figure 66. The high-frequency resistance (HFR) plot of a nanoporous IrNS integrated electrode coupled with Nafion 212 membrane between 0 and 6000 mA/cm^2.

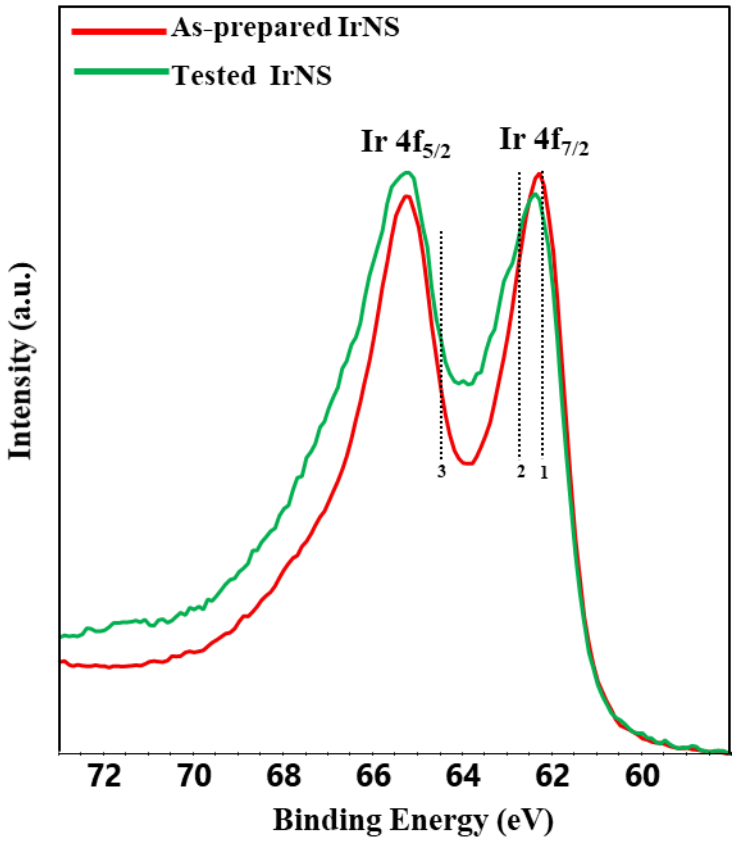


Figure 67. High-resolution XPS spectra of Ir 4f for nanoporous IrNS catalysts before and after the stability test in a PEM water electrolyzer.

CHAPTER SEVEN

ELECTROCHEMICALLY GROWN ULTRATHIN PLATINUM NANOSHEET ELECTRODES WITH ULTRALOW LOADINGS FOR ENERGY-SAVING AND INDUSTRIAL-LEVEL HYDROGEN EVOLUTION

A version of this chapter was originally published as:

Ding, L.,† Xie, Z., † Yu, S., † Wang, W., Terekhov, A.Y., Canfield, B.K., Capuano, C.B., Keane, A., Ayers, K., Cullen, D.A. and Zhang, F.Y., Electrochemically grown ultrathin platinum nanosheet electrodes with ultralow loadings for energy-saving and industrial-level hydrogen evolution. Nano-Micro Letters, 15(1), p.144.

† These authors contributed equally to this work.

CRediT authorship contribution statement

L.D.: Conceptualization, Methodology (Electrocatalyst/electrode fabrication, SEM, EDS, XRD characterization, performance evaluation), Data curation, Writing - original draft, review & editing, Investigation, Validation. Z.X.: Investigation, Methodology (SEM, EDS, XRD characterization, performance evaluation), Data curation, Validation, Writing – original draft. S.Y.: Investigation, Methodology (Electrocatalyst/electrode fabrication, SEM, EDS, XRD characterization, performance evaluation), Data curation, Writing – review & editing. W. W.: Methodology, Writing – review & editing. Terekhov, A.Y.: Methodology, Writing – review & editing. B.K.C.: Methodology, Writing – review & editing. C.B.C.: Validation, Writing - review & editing. A.K.: Methodology (CCM fabrication), Validation, Writing - review & editing. K.A.: Writing - review & editing.

D.A.C.: Methodology (STEM characterization), Validation, Writing - review & editing.

F.-Y.Z.: Conceptualization, Methodology, Project administration, Writing – review & editing, Supervision, Funding acquisition.

I am fully responsible for the work submitted in these publications.

7.1 Abstract

Nanostructured catalyst-integrated electrodes with remarkably reduced catalyst loadings, high catalyst utilization and facile fabrication are urgently needed to enable cost-effective, green hydrogen production *via* proton exchange membrane electrolyzer cells (PEMECs). Herein, benefitting from a thin seeding layer, bottom-up grown ultrathin Pt nanosheets (Pt-NSs) were first deposited on thin Ti substrates for PEMECs *via* a fast, template- and surfactant-free electrochemical growth process at room temperature, showing highly uniform Pt surface coverage with ultralow loadings and vertically well-aligned nanosheet morphologies. Combined with an anode-only Nafion 117 catalyst-coated membrane (CCM), the Pt-NS electrode with an ultralow loading of 0.015 mg_{Pt}/cm^2 demonstrates superior cell performance to the commercial CCM (3.0 mg_{Pt}/cm^2), achieving 99.5 % catalyst savings and more than 237-fold higher catalyst utilization. The remarkable performance with high catalyst utilization is mainly due to the vertically well-aligned ultrathin nanosheets with good surface coverage exposing abundant active sites for the electrochemical reaction. Overall, this study not only paves a new way for optimizing the catalyst uniformity and surface coverage with ultralow loadings but also provides new insights into nanostructured electrode design and facile fabrication for highly efficient and low-cost PEMECs and other energy storage/conversion devices.

7.2 Introduction

Currently, most hydrogen is produced from fossil fuels, leading to more than 2% of carbon dioxide emissions in the world [38, 214, 291-295]. An efficient method to reduce the carbon dioxide emission from hydrogen production is using water electrolysis with renewable energy as the electricity source. Due to their high energy efficiency, quick response, compact design, and gas crossover reduction, proton exchange membrane electrolyzer cells (PEMECs) are considered the most promising technology for green hydrogen production [43, 159, 169, 171, 296, 297]. Nevertheless, scarce and expensive platinum-based materials are typically used as catalysts for hydrogen evolution reactions (HERs) occurring at the cathode in PEMECs. Normally, high Pt loadings of 1~3 mg_{Pt}/cm^2 are required for the conventional catalyst-coated membrane (CCM) to ensure stable cell performance [180, 190, 220, 298-300], resulting in thick catalyst layers of more than 10 μm. However, Mo *et al.* [23] demonstrated that most of the catalysts in the conventional CCM are underutilized due to the involved ionomer with limited electron conductivity. In addition, the conventional CCM design normally involves multiple-step fabrication processes and elaborate equipment, which is time-consuming and high cost Therefore, there is an urgent need to develop high-performance electrodes with reduced Pt loadings, improved catalyst utilization and an efficient fabrication method.

To reduce the Pt loading, one efficient strategy is to directly deposit catalysts on the gas diffusion layer (GDL) to form gas diffusion electrodes (GDEs). So far, various Pt-based catalysts have been grown on the GDL and utilized as HER electrodes for the PEMEC. For example, Kang *et al.* [29] sputtered Pt films with low Pt loadings (0.032~0.193 mg_{Pt}/cm^2) on

thin and tunable liquid/gas diffusion layers (TTLGDLs) as the cathode electrodes, achieving 58 times higher mass activity than the commercial CCM with a Pt loading of 3 mg_{Pt}/cm^2 at 1.6 V. Laube *et al.* [301] used an atomic layer deposition method to deposit catalysts on the GDLs to reduce the catalyst loadings, achieving a Pt loading of 0.28 mg_{Pt}/cm^2 on the cathode. However, lower Pt loadings with fine nanostructures are desired to further decrease the catalyst cost with comparable or even improved performance since more active sites would be exposed with fine nanostructured catalyst layers. Moreover, compared to the flat or film-like catalyst layer, the nanostructured catalyst layer could not only offer larger surface areas, exposing more active sites but also achieve favorable bubble detachment due to the weaker bubble adhesive force. [302] Currently, some nanostructured Pt catalysts have been prepared for the PEMEC. For example, Li *et al.* [30] prepared electrodes with different Pt structures for the HER and revealed that a pine-shaped Pt nanostructured electrode with a loading of 0.215 mg_{Pt}/cm^2 showed superior performance to both a Pt nanosphere-based electrode and a flat Pt coating-based electrode. Meanwhile, smaller bubble detachment sizes are observed for the pine-shaped Pt nanostructured electrode. Xie *et al.* [33] developed fine Pt nanowires with an average diameter of about 5 nm *via* a wet-chemical method, achieving favorable bubble detachment and excellent performance in the PEMEC. A low Pt loading of 0.1 mg_{Pt}/cm^2, a low cell voltage of 1.643 V and a higher efficiency of 90.08% at 1 A/cm^2 were verified when combined with a Nafion 115 membrane, which are superior to those of the conventional CCM (1.846 V and 80.17%). Meanwhile, about 15 times catalyst savings are achieved with the fabricated Pt nanowire electrode. Additionally, Park *et al.* [303] fabricated flower-like Pt and polyhedral Pt particles with low loadings (0.020~0.071 mg_{Pt}/cm^2) on carbon papers *via* pulse

electrodeposition as cathode electrodes for the PEMEC. However, due to the poor catalyst surface coverage, high cell voltages were observed even with a thin (50 μm) Nafion 212 membrane. Overall, to accelerate the large-scale application of the PEMEC, highly efficient cathode electrodes with further decreased catalyst loadings, fine nanostructured catalyst layers, improved surface coverage under ultralow loadings, and efficient and easy scale-up fabrication are desired.

In this work, bottom-up grown Pt nanosheets (Pt-NSs) with ultralow loadings and good surface coverage were first deposited on thin tunable liquid/gas diffusion layers (TTLGDLs) (thickness: 25 μm, pore size: 100 μm, porosity: 40%) *via* a surfactant- and template-free and fast electrochemical growth process at room temperature, exhibiting ultrathin thickness of only about 4 nm and vertically well-aligned nanosheet morphologies. Compared to conventional Pt nanoparticle-based catalysts and CCM design, the catalyst and electrode fabrication processes would be greatly simplified. When combined with an anode-only Nafion 117 CCM, the Pt-NS integrated ultrathin electrode with an ultralow loading of 0.015 mg_{Pt}/cm^2 could achieve superior cell performance compared to the commercial CCM, saving 99.5% Pt catalyst and increasing catalyst utilization of more than 237-fold. Moreover, the highly efficient, facile, and cost-effective electrochemical growth process exhibits great potential for industrial application. Additionally, compared to conventional thick GDEs (several hundred μm), the ultrathin electrode shows a dramatically decreased thickness of about only 25 μm, which is material/weight/volume/cost-saving and would benefit a compact stack design in the future. Overall, the seed-assisted Pt-NS integrated electrode could not only guide the

preparation of a uniform catalyst surface coating but also accelerate the PEMEC industrial application, Meanwhile, it could be easily extended to fuel cells and other electrochemical energy storage/conversion systems.

7.3 Experimental Section

7.3.1 Platinum nanosheet integrated electrode fabrication

With a rapid and facile electrochemical growth process at room temperature, template-free and surfactant-free Pt nanosheets with ultralow loadings and fine surface coverage were deposited on titanium-based TTLGDLs. Before the electrochemical growth process, TTLGDLs were treated in oxalic acid to remove the surface oxide layer. Afterward, with a sputtering speed of ~ 0.34 nm/s and a sputtering time of 5 seconds, about a 2 nm-thick Pt nanoparticle layer was sputtered on TTLGDLs, serving as a seeding layer. The electrochemical growth process was performed in a three-electrode system, in which a Pt foil, a saturated calomel electrode (SCE) and the TTLGDL were used as the counter electrode, reference electrode and working electrode, respectively. With an electrolyte containing 5 mmol/L H_2PtCl_6 (Alfa Aesar) and 0.5 mol/L HCl (Alfa Aesar), fine Pt-NSs with ultralow loadings of 0.025 mg_{Pt}/cm^2 and 0.015 mg_{Pt}/cm^2 were quickly (< 25 s) and uniformly deposited on TTLGDLs at –1.0 V *vs.* SCE at room temperature. Meanwhile, higher Pt-NS loadings of 0.05 and 0.14 mg_{Pt}/cm^2 were also prepared to investigate the Pt-NS size and thickness variation along with the loading increase. Additionally, without the seeding layer, several samples with different Pt-NS loadings (0.025, 0.07 and 0.14 mg_{Pt}/cm^2) were also prepared for comparison. Moreover, sputtered Pt nanoparticles (PtNP)

and commercial Pt black (Fuel Cell Store) were also prepared on the Ti substrate for *ex-situ* hydrogen evolution reaction (HER) performance comparison.

7.3.2 Material characterization

A field emission JSM-IT700HR scanning electron microscope (SEM) with energy-dispersive X-ray spectroscopy (EDS) was used to characterize the morphology and composition of the samples. A Rigaku SmartLab X-ray diffraction (XRD) system was used to investigate the crystalline structure of the sample. The crystalline structure of Pt-NS catalysts was investigated by scanning transmission electron microscopy (STEM) on a probe-corrected JEOL NEOARM operated at an accelerating voltage of 80 kV.

7.3.3 Ex-situ electrochemical measurements

A typical three-electrode system with a saturated calomel electrode (SCE) as the reference electrode and a Pt foil as the counter electrode was used to evaluate the ex-situ HER performance of the prepared electrodes. All tests were performed on a potentiostat (SP300, Bio-Logic) in 0.5 M H_2SO_4 at room temperature. Based on the Nernst equation: $E_{RHE} = E_{SCE} + 0.26$ V, all the recorded potentials, E_{SCE}, were converted to a reversible hydrogen electrode (RHE). Before the tests, the electrolyte was saturated with Ar for 0.5 h to remove the oxygen. The linear sweep voltammetry (LSV) curves were recorded from 0 V to −0.5 V vs. RHE with a scan rate of 5 mV/s. The electrochemical impedance spectroscopy (EIS) plots were recorded within a frequency range of 400 kHz ~ 50 mHz. The "ZFit" impedance fitting tool within the EC-Lab software was utilized to analyze the EIS results with the Randomize + Simplex method. An equivalent circuit model with a resistance in series (R_Ω)

and two parallel *Q/R* components in high-frequency and low-frequency regions was chosen to fit the Nyquist plots. Based on the fitting, different parameters can be directly derived. The high-frequency resistance (HFR) plots during the PEMEC test were recorded under the high frequency of ~ 6 kHz by using the Staircase Galvano Electrochemical Impedance Spectroscopy (SGEIS) scan with the EC-Lab software. The current density range used for the scans was between 0 to 2 A/cm^2. Meanwhile, the visualization system setup consisting of a camera, lens and lighting can be found in our previous publications [168, 187, 221, 222, 304].

7.3.4 Cell performance evaluation of the PEMEC

All cell tests were carried out in a PEM electrolyzer cell with an active area of 5 cm^2 and a working temperature of 80 °C. The water flow rate at the anode side is 20 mL/min, and the pressure at both the anode and cathode is 1 atm. The prepared Pt-NS electrode was used as the cathode and an anode-only Nafion 117 membrane (175 μm thick, Nel Hydrogen) with 2.0 mg_{Ir}/cm^2 IrO_x was used as the anode. A commercial CCM with 3.0 mg_{Ir}/cm^2 IrO_x as the anode and 3.0 mg_{Pt}/cm^2 Pt black as the cathode was used as a baseline. All the test plots were recorded on a potentiostat (VSP/VMP3B-100, Bio-Logic).

7.4 Results and Discussions

7.4.1 Morphology and composition of the Pt-NS electrode

As illustrated in **Figure 68**, Pt-NSs can be easily grown on the thin Ti substrate (~25 μm) *via* a highly efficient, cost-effective, template-free, and surfactant-free electrochemical growth process at room temperature. With or without a thin Pt seeding layer, different

nanosheet structures with different sizes and coverages are observed on the thin substrate. Specifically, in the absence of the seeding layer, a nonuniform Pt-NS coating with nanoparticles and large nanosheet sizes is observed on the substrate surface; while with the thin Pt seeding layer, a highly uniform Pt-NS coating with small nanosheet sizes is formed. As shown in **Figure 69A**, without the Pt seeding layer, large Pt nanosheet assemblies along with some small Pt nanoparticles are nonuniformly deposited on the substrate surface at a Pt-NS loading of 0.025 mg_{Pt}/cm^2. When increasing the catalyst loading to 0.07 mg_{Pt}/cm^2, Pt nanosheet assemblies grow larger (**Figure 77**). Meanwhile, larger nanosheets with sizes of 100 ~ 170 nm and an average thickness of about 12 nm are observed. When further increasing the loading to 0.14 mg_{Pt}/cm^2, the Pt-NSs still do not fully cover the Ti substrate. As shown in **Figure 78**, some nanoparticles and bare Ti surfaces can be still seen. However, benefiting from the thin seeding layer of Pt nanoparticles with an average size of about 5 nm (**Figures 79A and B**), vertically aligned Pt-NSs with uniform surface coverage are observed with an ultralow loading of 0.025 mg_{Pt}/cm^2 (**Figure 69B**). Moreover, the resultant fine Pt-NSs show much smaller sizes of 28 ~ 55 nm and thinner nanosheets of about 4 nm compared to those without the thin seeding layer. By merely shortening the electrochemical growth time, a further decreased Pt-NS loading of only 0.015 mg_{Pt}/cm^2 was also prepared. As shown in **Figure 69C,** at the loading of 0.015 mg_{Pt}/cm^2, fine and vertically aligned nanosheets with uniform surface coatings are still formed on the substrate, showing a smaller thickness of about 3 nm and similar sizes to the 0.025 mg_{Pt}/cm^2-based nanosheets. Hence, a thin seeding layer is a prerequisite for highly uniform Pt-NS coatings on the Ti substrate with ultralow loadings. In addition, with the help of the seeding layer, the nanosheet size and thickness can be well-modulated by merely tuning the electrochemical

growth time. As shown in **Figures 79C and D**, when the Pt-NS loading increases to 0.05 mg_{Pt}/cm^2 and 0.14 mg_{Pt}/cm^2, the Pt-NS sizes increase to 50 ~ 100 nm and 100 ~ 120 nm, showing thicknesses of about 10 nm and 15 nm, respectively. Notably, along with the loading increase, the Pt nanosheets maintain the fine, vertically aligned nanosheet morphologies, growing into larger sizes and providing a large surface area.

SEM images of the Pt-NS catalyst layer (0.025 mg_{Pt}/cm^2) from the top view (**Figure 69D**) and tilted view (**Figure 69E**) further reveal the fine and vertically well-aligned Pt nanosheets. In addition, as demonstrated in **Figure 69E**, a relatively uniform thickness of about 43 nm for the Pt-NS catalyst layer is presented, successfully achieving a nanoscale catalyst layer with fine nanosheet structures. Notably, the exposed bottom surface of the Pt-NS catalyst layer shows nanosheet arrays with some porous structures, demonstrating a bottom-up Pt nanosheet growth process (**Figure 69F**). The bottom-up Pt-NS growth should be due to the thin seeding layer, which could provide homogeneous nucleation sites and assist the Pt nanosheet to grow from the bottom. The seed-assist bottom-up Pt-NS growth allows high surface uniformity of the fine Pt-NSs with ultralow loadings showing nanoscale catalyst layer, small nanosheet sizes, and thin nanosheet thicknesses, which could offer large surface areas and benefit the electrochemical reaction. These results differ from other publications [30, 303, 305-309], in which nonuniform Pt coatings are observed on substrate surfaces. For example, bare areas are observed for the pine-shaped Pt nanostructured electrode even with a Pt loading up to 0.215 mg_{Pt}/cm^2. [30] In addition, low Pt surface coverage is also observed for the porous Pt nanoflowers with a loading of 0.200 mg_{Pt}/cm^2 prepared by a template-free electrodeposition process. [307] Liu, *et al.* [309]

electrodeposited different Pt nanostructures (spherical, nanocube, or willow-like) on glassy carbon substrates by tuning the deposition potentials of a square-wave potential electrodeposition process. However, low surface coverages were observed for all those nanostructured Pt catalysts. Hence, the seed-assisted Pt-NS electrochemical growth with high surface coverage, fine nanosheet morphology, and ultralow loadings shows great advantages to develop highly efficient catalysts at low cost.

The top view and cross-section view SEM-EDS mapping images (**Figure 69G and H**) confirm the full surface coverage of the Pt-NS catalyst layer on the TTLGDL substrate and only about 25 μm thickness for the whole electrode. Unlike conventional thick electrodes with several hundred-μm thicknesses, the Pt-NS integrated ultrathin electrode with ultralow catalyst loadings would be beneficial for a more compact and low-cost cell and stack design in the future. As shown in the EDS results (**Figure 69I**), about 4.37% Pt catalysts are deposited on the Ti substrate surface with an ultralow loading of 0.025 mg_{Pt}/cm^2. Meanwhile, as seen from the XRD pattern (**Figure 69J**), apart from the peaks of the Ti substrate, five 2θ peaks assigned to Pt are observed at about 39.8°, 46.4°, 67.9°, 81.5° and 86.2°, which are ascribed to Pt(111), Pt(200), Pt(220), Pt(311), and Pt(222), respectively. [310 311 312] These results match well with the face-centered cubic (fcc) structure of crystalline Pt.

7.4.2 Growth mechanisms of the Pt-NSs

To study the growth mechanism of Pt-NS on the Ti substrate, we prepared two types of Pt-NS samples with and without the seeding layer. For the seeding layer case, by adjusting

the electrodeposition times, Pt-NS samples with different loadings of 0.015, 0.025, 0.05 and 0.15 mg_{Pt}/cm^2 were prepared. For the case of without the seeding layer, three samples with different Pt-NS loadings (0.025, 0.07 and 0.14 mg_{Pt}/cm^2) were also prepared for comparison. With an increase in electrodeposition time, there is a concurrent increase in the loading of Pt-NS, which is accompanied by a noticeable change in morphology. Based on SEM characterizations of each type of sample at different loadings (corresponding to different electrodeposition times), we proposed the possible Pt-NS growth mechanism. Two processes are involved during the electrodeposition procedure. One is a diffusion process, in which Pt ions are transported from the bulk solution through the diffusive layer toward the electrode; the other is an activation process, in which the Pt ions are reduced on the electrode surface. [313] The possible mechanisms of the Pt nanosheet formation with or without the Pt seeding layer are shown in **Figure 70** and discussed as follows. As reported in the previous studies, [314] [315] the nanosheet formation could be attributed to the applied large electrodeposition overpotential. Under a large electrochemical growth overpotential of –1.0 V *vs.* SCE, the Pt species in the electrolyte are quickly reduced into Pt crystal nuclei in the initial stage. During this stage, Pt species are consumed because of the fast reduction process, while the Pt ion diffusion to the electrode could compensate for the consumption. However, due to the high reduction rate under the large overpotential, the consumed Pt ions cannot be quickly compensated, leading to a diffusion-controlled process. In this case, the edges of Pt crystal nuclei preferentially grow faster than the other parts, resulting in nanosheet morphology formation for the subsequent growth stage.

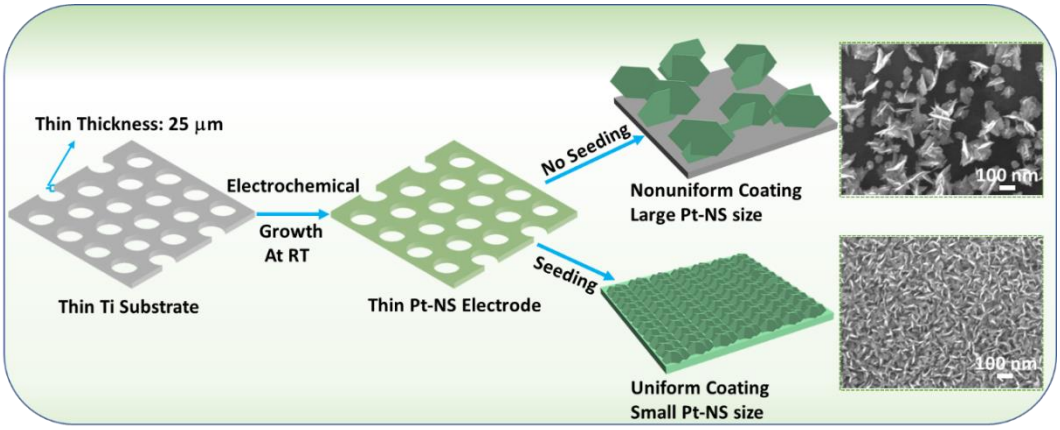


Figure 68. Schematic of the Pt-NS fabrication on the thin Ti substrate (with seeding and no seeding, respectively) *via* a highly efficient and facile electrochemical growth process at room temperature.

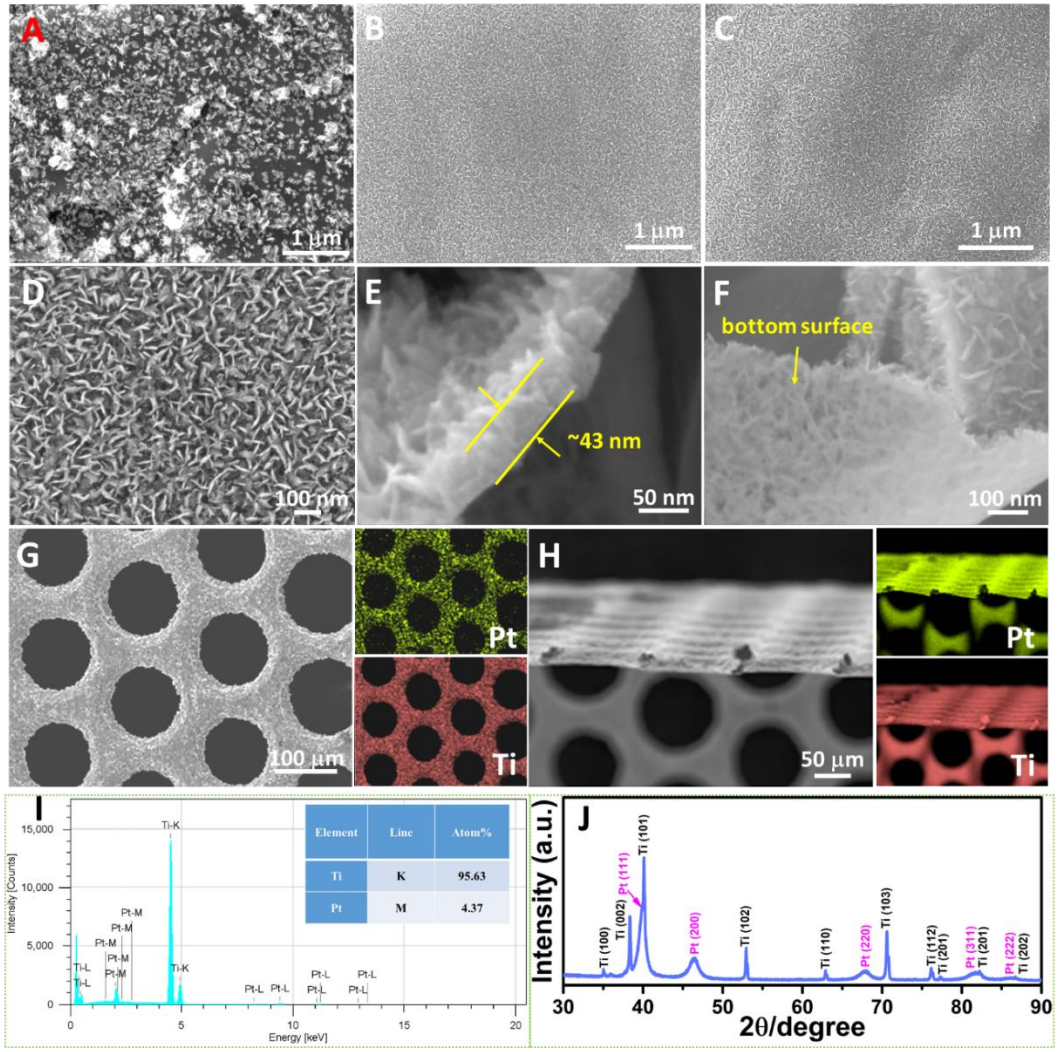


Figure 69. (A-C) Low magnification SEM images of Pt-NSs with different loadings: (A) 0.025 mg_{Pt}/cm^2 (without the seeding layer), (B) 0.025 mg_{Pt}/cm^2 (with the seeding layer), (C) 0.015 mg_{Pt}/cm^2 (with the seeding layer); (D-F) High magnification SEM images of Pt-NSs based on 0.025 mg_{Pt}/cm^2; (G) Top-view and (H) cross-section view SEM-EDS mapping images of the Pt-NS electrode based on 0.025 mg_{Pt}/cm^2; The related (I) EDS spectra; (J) XRD pattern of the Pt-NSs.

However, the Pt crystal nuclei are distributed nonuniformly on the non-seeded Ti substrate, probably due to different energy barriers for nucleation in different locations across the whole substrate surface and differences in the local surface roughness.

Favorable nucleation usually initiates at the rougher surface with higher binding energy sites for Pt species. The nonuniform nucleation on a non-seeded substrate may lead to different nanosheet growth rates in different locations. Hence, without a thin Pt seeding layer, large Pt-NSs with nonuniform surface coverage and thick nanosheets are formed on the substrate. Meanwhile, some small nanoparticles are also observed on the substrate. However, a thin Pt seeding layer could provide more uniform and denser nucleation sites, which can effectively regulate the nucleation rate to successfully achieve bottom-up growth. As a result, with the seeding layer, highly uniform nanosheet growth with ultrathin nanosheet thickness, small nanosheet sizes, and fine vertically aligned nanosheet morphologies are obtained across the entire substrate surface, unlike a seed-free electrochemical growth process. Our research work is still ongoing to better understand the Pt-NS growth mechanism on titanium substrate by employing potential *in-situ* characterization techniques to monitor the real-time Pt-NS growth process.

To evaluate the HER performance of the Pt-NS, electrochemical measurements in 0.5 M H_2SO_4 in a typical three-electrode system were performed at room temperature. For comparison, sputtered Pt nanoparticles (PtNP) and commercial Pt black with the same Pt loading were also tested under the same conditions. All potentials from the three-electrode system are iR-corrected and normalized to RHE. As shown in **Figure 71A**, the Pt-NS electrode shows a low overpotential of −30 mV at −10 mA/cm^2, close to that of the

commercial Pt black (−26 mV) and lower than that of the PtNP (−44 mV). Notably, larger than about −16 mA/cm^2, the Pt-NS shows superior HER performance to the commercial Pt black. At a current density of −80 mA/cm^2, the Pt-NS shows a low overpotential of only −52 mV (Pt black: −102 mV), implying that the Pt-NS with fine nanosheet morphologies could offer rich active sites to decrease the overpotential within the high current density range. To investigate the hydrogen adsorption kinetics of ionomer-free Pt catalysts with different morphologies, the EIS plots of Pt-NS and PtNP were recorded at −40 mV.

As revealed from the Nyquist plots (**Figure 71B**), two arcs in the high-frequency (HF) and low-frequency (LF) ranges are observed, indicating a two-time-constant process. [168 230 316] To fit Nyquist plots, a model with a resistance in series (R_Ω) and two parallel connections of resistance and constant phase elements assigned to the HF (R_{hf} and Q_{hf}) and LF (R_{lf} and Q_{lf}) ranges, respectively, was used, as shown in **Figure 71C**. The fitted data is presented in **Table 20**, in which similar ohmic resistances are observed for both Pt-NS and PtNP, and this is reasonable since the two electrodes were both tested in 0.5 M H_2SO_4 at room temperature. The resistance summaries of R_{hf} and R_{lf} of the Pt-NS are lower than those of the PtNP, indicating a faster HER faradaic process. Meanwhile, the double-layer capacitances for HF ($C_{dl,\,hf}$) and LF ($C_{dl,\,lf}$) of the two electrodes were also derived from the plot fitting, which can be used to represent the active site number of the catalysts [139, 317-319]. As mentioned above, the Nyquist plots show a two-time-constant process, in which the $C_{dl,\,hf}$ at HF with a smaller time constant belongs to a "fast process", while the $C_{dl,\,lf}$ at LF is a "slow process," since a larger time constant is needed for the reaction sites. [168 320 321] Hence, a higher $C_{dl,\,hf}$ value indicates more active sites are exposed for the "fast process" and a

lower $C_{dl,\ lf}$ value implies that fewer active sites are assigned to the "slow process." As shown in **Figure 71D**, the Pt-NS exhibits a higher $C_{dl,\ hf}$ value of 23.5 mF/cm^2, which is about 7.2-fold higher than that of the PtNP (3.26 mF/cm^2), indicating that abundant electrochemical reaction active sites are exposed for the Pt-NS electrode. Meanwhile, compared to the PtNP, a lower $C_{dl,\ lf}$ value is obtained for the Pt-NS. Overall, the Pt-NS with ultrathin, vertically well-aligned nanosheets yields abundant active sites for HERs, resulting in an excellent performance.

To further validate the rich active sites of the Pt-NS electrode, *in-situ* visualization was performed with a high-speed and microscale visualization system to investigate the bubble dynamics at a current density of 200 mA/cm^2 (**Movie S1**). For comparison, the bubble dynamics on the PtNP electrode were also captured at the same current density (**Movie S2**). It is clearly shown that compared to the PtNP electrode, much more bubble detachment sites are observed on the Pt-NS electrode (**Figure 71E and F**). Notably, the more numerous bubble detachment sites on the Pt-NS electrode mean that enhanced total reaction zones are achieved on the electrode surface, reflecting the abundant reaction sites to some extent. In addition, much smaller bubbles are observed on the Pt-NS electrode surface, indicating weaker bubble adhesive force on the electrode, which could achieve favorable bubble detachment. As reported in previous references [30 33], compared to the catalyst layer with flat surfaces, the nanostructured catalyst layer could decrease the bubble contact area on the electrode surface, successfully achieving weaker bubble adhesive force and quicker bubble removal with smaller sizes.

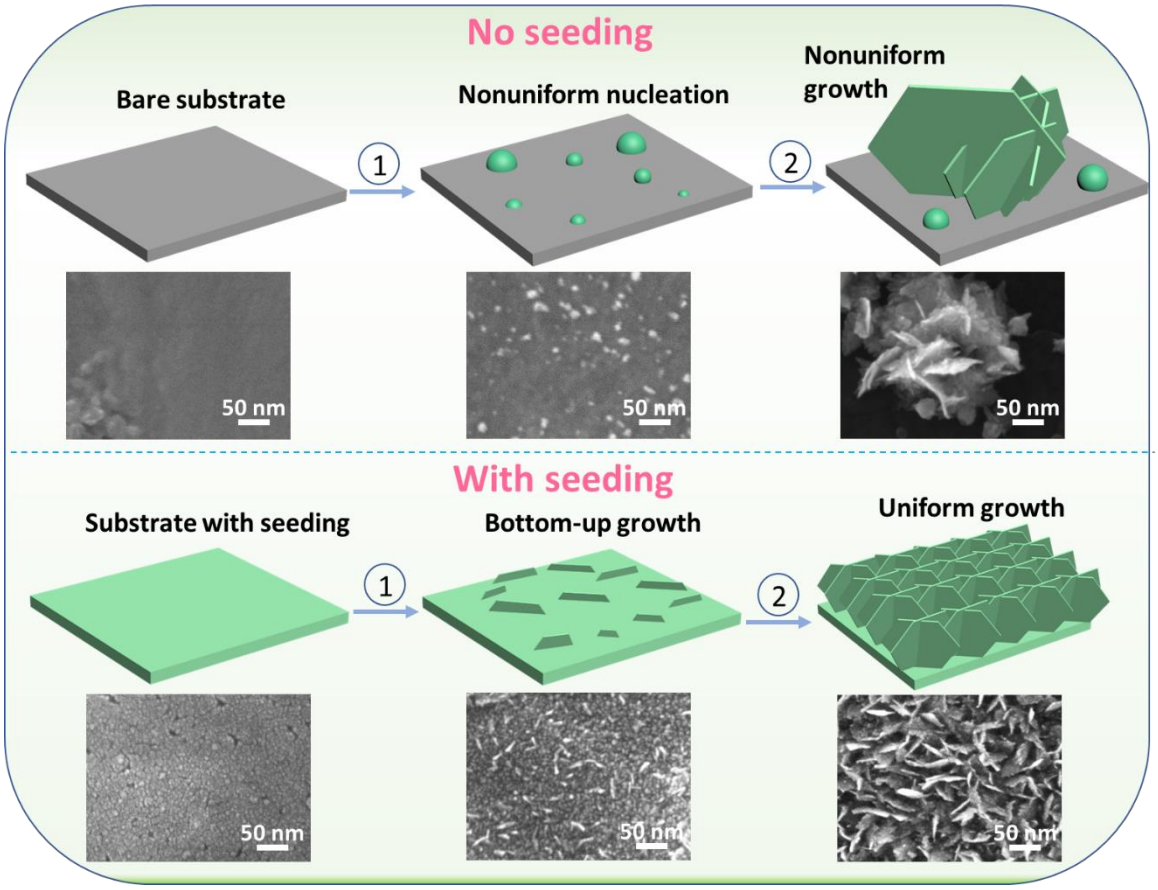


Figure 70. Pt-NS growth mechanisms without (top part) and with (bottom part) the seeding layer.

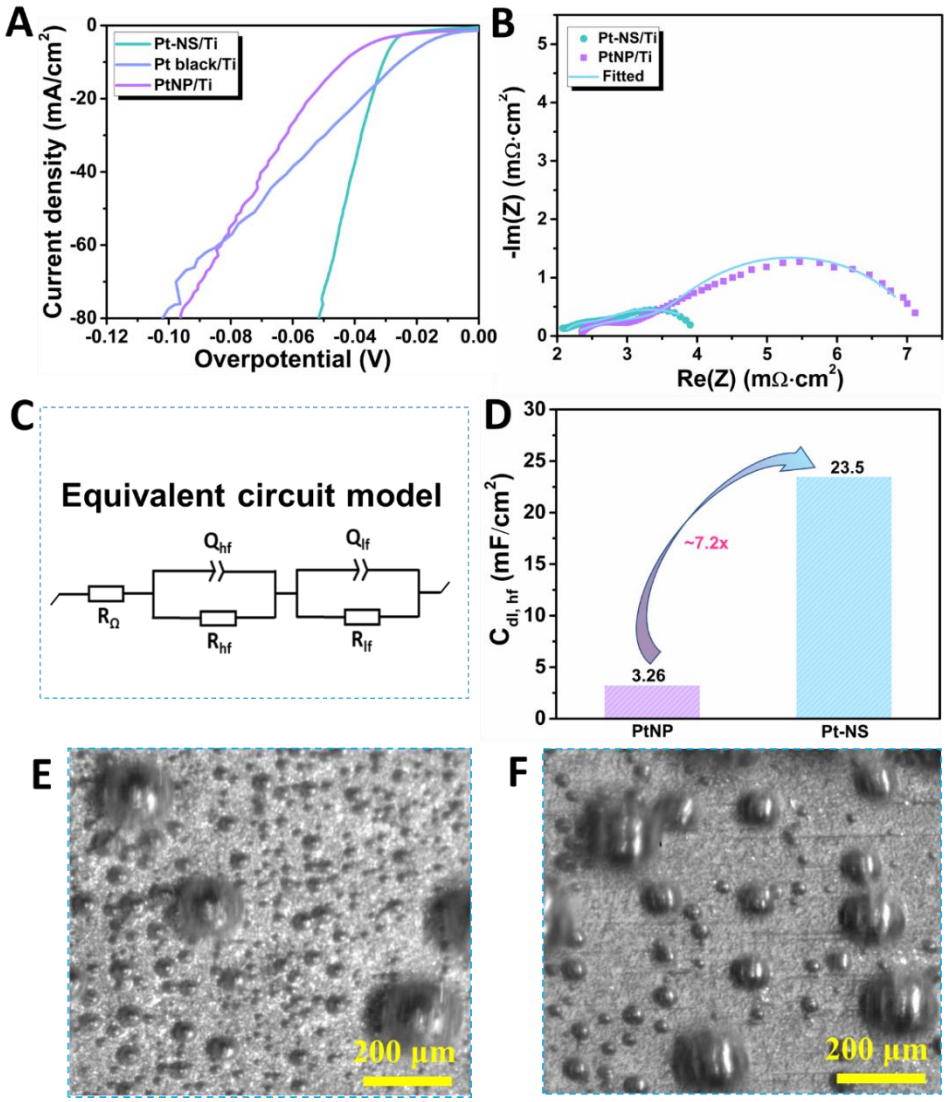


Figure 71 Electrochemical characterizations of the Pt-NS/Ti *via* a three-electrode system in 0.5 M H_2SO_4. at room temperature. (A) IR-corrected HER polarization curves with a scan rate of 5.0 mV/s; (B) EIS plots recorded at −40 mV; (C) The fitting equivalent circuit model; (D) Double-layer capacitance comparison; High-speed visualization of hydrogen bubble dynamics on (E) the Pt-NS electrode and (F) the PtNP electrode, respectively, at 200 mA/cm^2 (Movies S1 and S2).

To compare the cell performances of electrodes with and without the seeding layer, the identical anode-only Nafion 117 membranes were used for practical PEMEC tests at 80 °C. The test results were collected and presented in **Figure 72**. Impressively, with or without the seeding layer, the Pt-NS electrodes show remarkably different performances. As illustrated in **Figure 72A**, with the same catalyst loading of 0.025 A/cm^2, the seed-assisted electrode delivers a low cell voltage of 1.86 V at 2 A/cm^2, which is 90 mV lower than that of the seed-free electrode (1.95 V) (**Figure 72B**). In addition, when the current density is higher than 1.25 A/cm^2, a curve-up phenomenon is observed in the polarization curve for the seed-free electrode, suggesting insufficient active sites for the high-current density cell operation. Moreover, as shown in **Figure 72C**, an obviously increased HFR plot is also observed for the seed-free electrode within the test current density range of 0 to 2 A/cm^2, increasing from 123 mΩ·cm^2 to 147 mΩ·cm^2. While almost stable HFR plot is presented for the seed-assisted electrode. For the HFR-free polarization curves, an obvious curve-up phenomenon is also observed for the seed-free electrode. Meanwhile, a higher HFR-free voltage of 1.65 V is presented, which is 40 mV higher than the seed-assisted electrode (**Figure 72D**). Overall, the inferior performance and increased HFR plot of the seed-free electrode are mainly due to the poor Pt surface coverage, as shown in **Figure 69A**, which cannot provide sufficient active sites for the electrochemical reaction, especially at the high current density regions.

7.4.3 Pt-NS characterization in PEMECs

Based on the above results, the seeding layer plays a crucial role in the catalyst surface coverage and also cell performance. Hence, with the seeding layer, a lower Pt loading of

0.015 mg_{Pt}/cm^2 is also prepared for the cell tests. Meanwhile, a commercial CCM with a Pt loading of 3.0 mg_{Pt}/cm^2 was also evaluated as the baseline under identical operating conditions. Notably, with less than 0.9% catalyst loading could achieve a similar onset voltage of 1.40 V to the commercial CCM baseline (1.39 V). This could be because abundant active sites are exposed for the Pt-NS electrode, which is ascribed to the fine, vertically aligned Pt nanosheets with an ultrathin thickness of only 4 nm and small nanosheet sizes. Moreover, the Pt-NS electrodes show lower cell voltages of 1.86 V (0.025 mg_{Pt}/cm^2) and 1.91 V (0.015 mg_{Pt}/cm^2) at 2 A/cm^2, respectively, which are superior to that of the commercial CCM (1.93 V) (**Figure 73A**). As seen in **Figure 73B**, the ionomer-free Pt-NS electrodes show low average HFR values of 117 $m\Omega \cdot cm^2$ for the 0.025-based electrode and 107 $m\Omega \cdot cm^2$ for the 0.015-based electrode, respectively, which are much lower than that of the commercial CCM (180 $m\Omega \cdot cm^2$). The low HFR values indicate the good conductivity of the Pt-NS electrodes, which could improve catalyst utilization, while the commercial CCM with a thick ionomer-involved catalyst layer shows high HFR values and limited conductivity, in which most of the catalysts are underutilized. To compare their activation loss differences, HFR-free polarization curves of Pt-NS electrodes and the baseline CCM are derived. As shown in **Figures 80**, the HFR-free cell voltages of Pt-NS electrodes with 0.015 mg_{Pt}/cm^2 and 0.025 mg_{Pt}/cm^2 and the baseline CCM are 1.69 V, 1.61 V, and 1.58 V, respectively at 2 A/cm^2. The activation loss of the 0.025-based electrode is slightly worse than the baseline CCM but better than the 0.015-based electrode. Such activation loss differences among the three electrodes are mainly due to the catalyst loading difference. Based on the HFR-free cell voltages, Tafel plots of different whole cells with different electrodes are derived. Since the anode setups for all cells are the same, the HER

kinetics for the three cells are considered identical under the same HFR-free voltage; hence, the Tafel slope difference in the three cells should be only ascribed to the cathodes. As shown in **Figure 73C**, similar Tafel slope values (0.025-based electrode: 61 mV/dec; 0.015-based electrode: 68 mV/dec; commercial CCM: 63 mV/dec) are observed for all cells, indicating similar intrinsic catalyst activity of all electrodes in cell tests. Moreover, the similar Tafel slopes indicate that compared to the commercial CCM with an ionomer-mixed catalyst layer, there is no ion-conductivity issue for the Pt-NS electrodes with ionomer-free catalyst layer fabrication.

The cell efficiency and catalyst savings are compared as well in **Figure 73D**. At the same current density of 1 A/cm^2, both 0.025-based and 0.015-based Pt-NS electrodes display higher cell efficiencies of 87.16% and 87.78% than the baseline CCM (85.55%), achieving more than 99% catalyst savings over the CCM. To further evaluate the Pt catalyst utilization of different electrodes, mass-specific current, namely, current density normalized by the Pt mass, was introduced. As shown in **Figure 73E**, with the identical test conditions, the mass-specific currents of the Pt-NS electrodes with different loadings can reach up to about 80 A/mg (0.025 mg$_{Pt}$/cm^2) and 133 A/mg (0.015 mg$_{Pt}$/cm^2), which are much higher than that of the commercial CCM (0.666 A/mg). The big differences demonstrate that compared to the commercial CCM, the ionomer-free Pt-NS electrode with ultrathin, fine, vertically aligned Pt nanosheets exposes abundant active reaction sites for the electrochemical reaction and achieves high catalyst utilization.

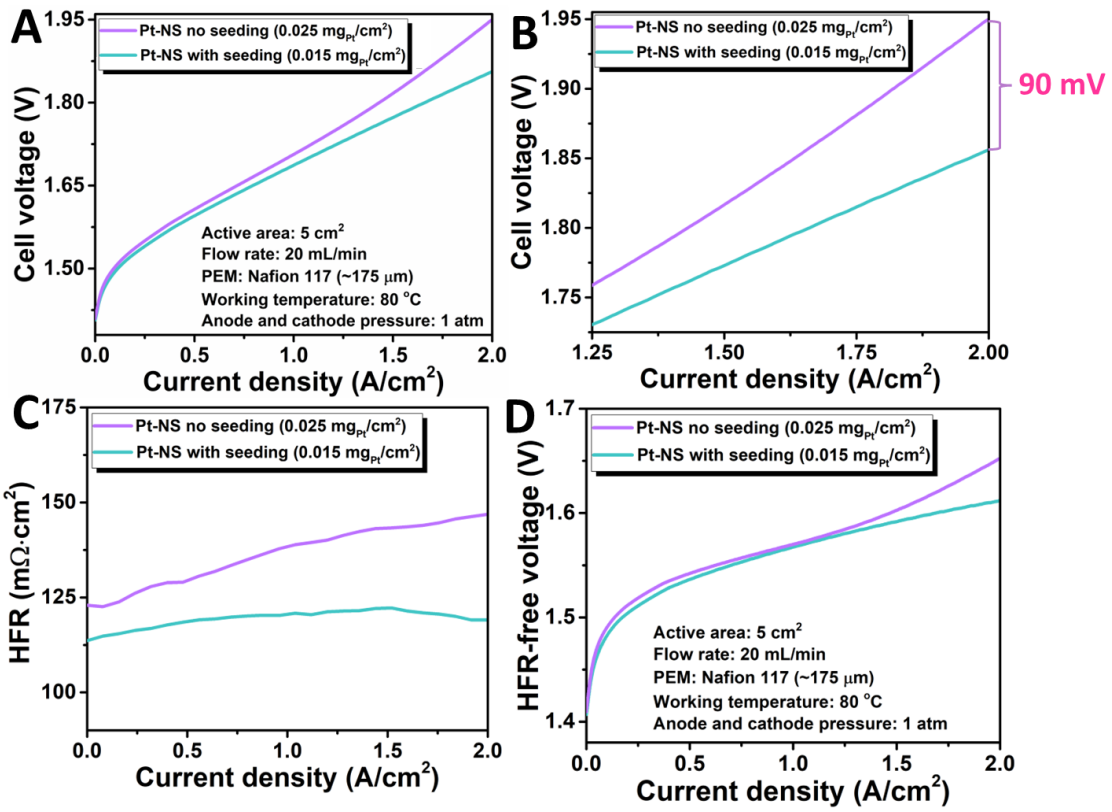


Figure 72. ***In-situ*** **cell performance comparison of Pt-NS with and without the seeding layer in a PEMEC at 80 °C. (A) Cell polarization curves of the Pt-NS electrodes with and without the seeding layer; (B) Enlarge cell polarization curves of the Pt-NS electrodes with and without the seeding layer within the current density range of 1.25 to 2 A/cm^2; (C) The related high-frequency resistance (HFR) plots; (D) The HFR-free cell polarization curves.**

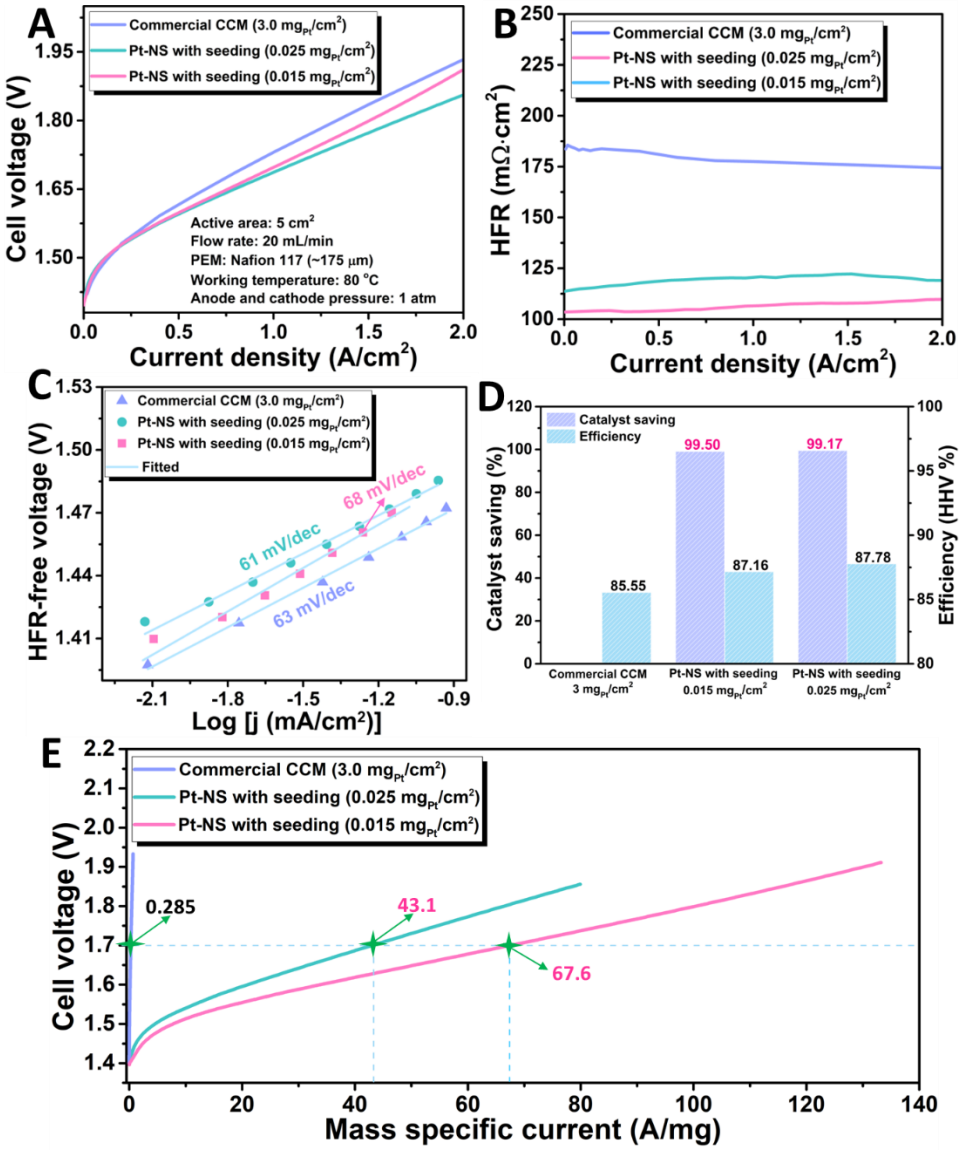


Figure 73. Cell performance comparison of the Pt-NS electrodes and the commercial CCM in a PEMEC at 80 °C. (A) Cell polarization curves; (B) The related HFR plots; (C) The corresponding Tafel plots; (D) Catalyst saving (Baseline: the CCM) and efficiency comparison at 1 A/cm^2 of the Pt-NS electrodes and the commercial CCM; (E) The related Pt mass-normalized cell polarization curves.

At a specific cell voltage of 1.7 V, the 0.025-based and 0.015-based Pt-NS electrodes show high mass-specific currents of 43.1 A/mg and 67.6 A/mg, respectively, impressively achieving about 151-fold and 237-fold higher than the commercial CCM (0.285 A/mg). With the high catalyst utilization, the Pt loading can be significantly reduced with comparable performance, cutting down the PEMEC cost.

In addition, the stability of the 0.025-based Pt-NS electrode was evaluated at a high current density of 1.8 A/cm^2 for 48 h. As shown in **Figure 74A**, the cell voltage of about 1.85 V is well maintained after the 48-h stability test. In addition, the polarization curves before and after the stability test overlap with each other in the current density range of 0 ~ 2 A/cm^2, further demonstrating the excellent stability of the Pt-NS electrode in a practical PEMEC (**Figure 74B**). It is noted that the performance of the Pt-NS electrode becomes slightly better during the initial 24-hour stability test at 1.8 A/cm^2, which is probably due to the gradual stabilization of the PEMEC at a high current density. A similar phenomenon is also presented in other studies. [286, 322, 323] However, after shutdown and restart, the performance gradually decreases in the second 24-hour stability test. This opposite trend is probably attributed to the potential shielding effect of the generated hydrogen bubbles at the reaction interface between the Pt-NS electrode and solid electrolyte PEM, causing the slight decrease of reaction sites during the HER. After the 48-hour stability test, as seen in **Figure 74B**, the overlapping polarization curves before and after the stability test suggest that the observed slight performance loss in the second 24-hour stability test is reversible. This phenomenon has been reported in previous studies. [202] [203] For example, Honsho *et al*. reported that the reversible performance loss is most likely related to gas stagnation within

the pores of the catalyst layers. [202] Batalla *et al*. reported that reversible voltage increase can be recovered when the cell current is interrupted. [203] In addition, in the long-term perspective, coupling PEM water electrolysis with sustainable and renewable energy sources is highly appealing due to its high efficiency, close-to-zero emissions, and widespread applications. However, some renewable energy sources such as solar and wind power can be intermittent during practical applications. Thus, the main purpose of the shutdown and restart of the Pt-NS electrode integrated PEM electrolyzer cell during the stability test is to evaluate its response to an intermittent load. To further demonstrate the remarkable performance of the ultrathin Pt nanosheet-integrated thin electrodes, a cell performance comparison with the previously reported cathode catalysts for PEMECs was performed. As seen from **Figure 74C**, even with a thicker Nafion 117 membrane (175 μm), the Pt-NS electrodes with ultralow Pt loadings in our work exhibit superior cell performance, achieving low cell voltages of 1.86 V for the 0.025-based and 1.91 V for the 0.015-based at 2 A/cm^2. Additionally, significantly boosted catalyst utilization is also demonstrated, as evidenced by much higher mass-specific currents, of 43.13 A/mg for the 0.025-based and 67.60 A/mg for the 0.015-based at 1.7 V, than most of the recently reported cathode catalysts for the PEMEC (**Figure 74D**) [29, 180, 205, 220, 276, 303, 324-326].

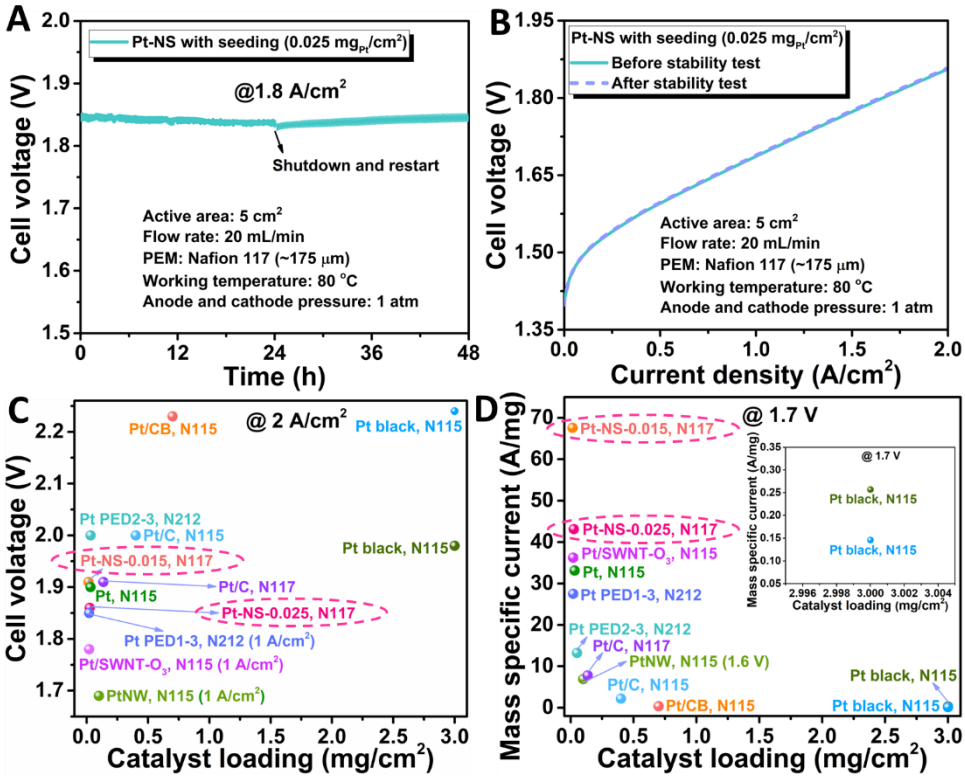


Figure 74. (A) Cell stability test at 1.8 A/cm^2; (B) Cell performance comparison before and after the stability test; (C) Cell voltage comparison at 2 A/cm^2 with previously reported cathode catalysts; (D) The corresponding mass-specific current comparison at 1.7 V; inset: enlarged area (the lower right) of the mass-specific current comparison at 1.7 V.

The details about different electrode fabrications are listed and compared in **Table 19**. Compared to complex fabrication methods involving multiple steps and expensive equipment in most recently reported studies, in this work a facile electrochemical growth process with high efficiency (≤ 25 s) was adopted to fabricate the electrodes at room temperature with ultralow loadings (≤ 0.025 mg_{Pt}/cm^2) and ultrathin vertically aligned Pt nanosheets, without the use of any surfactants, templates, pH adjusters, and elaborate equipment. This electrochemical growth process offers an ionomer-free catalyst layer with good conductivity and is much more efficient and facile than most studies. For example, Rajala *et al.* [325] prepared platinum nanowires on ozonized single-walled carbon nanotubes (SWNT-O_3) for the PEMEC, employing multiple fabrication procedures with high cost. Specifically, expensive SWNTs were functionalized *via* an ozone generator as the supporters, and then Pt catalysts were modified on the SWNT-O_3 to obtain Pt/SWNT-O_3 at a high temperature of 300 ℃ under a 5% H_2/Ar atmosphere. Afterward, the obtained Pt/SWNT-O_3 catalysts were prepared into catalyst ink and then sprayed onto a carbon paper, which involved ionomers in the catalyst layer offering limited conductivity. Moreover, a high annealing temperature of 300 ℃ and expensive equipment such as a spray coater was needed for the electrode fabrication. Even with a one-step fabrication method such as pulse electrodeposition or sputtering, the catalyst morphology and performance of the prepared electrode are limited. For example, Park *et al.* [303] adopted a pulse electrodeposition method to prepare the electrode, which exhibited poor catalyst surface coverage and resulted in an inferior performance of ≥ 1.85 V at 1 A/cm^2 even with a much thinner membrane of Nafion 212 (~50 μm). Overall, the highly efficient and

sustainable electrode fabrication with high performance and low cost demonstrated in our work, which enables easy electrode fabrication scale-up, could efficiently accelerate PEMEC large-scale applications.

7.4.4 Post-analysis of the Pt-NS electrode after the cell test

Post-test characterizations of the Pt-NS electrode (0.025 mg_{Pt}/cm^2), including SEM and SEM-EDS mapping and analysis, were performed to check Pt nanosheet morphology and composition changes. As seen from the SEM images in **Figure 75A-D**, the fine nanosheet morphologies are well-maintained after the 48-h stability test at the high current density of 1.8 A/cm^2. In addition, the SEM-EDS mapping results show that uniform Pt surface coverage is still observed on the Ti substrate (**Figure 75E**). Meanwhile, based on the EDS result, the test Pt-NS electrode exhibits a similar Pt content (4.31%) with the fresh one (**Figures 81**), indicating that there is no significant catalyst loss from the substrate after the cell test. Overall, the above results demonstrate the good stability of the prepared Pt-NS electrode in a practical PEMEC.

Meanwhile, to further investigate any potential structural and crystal changes of Pt nanosheets that may occur before and after the stability test, we prepared samples by scraping the Pt nanosheets from the electrode surface and characterized both fresh and tested samples using HAADF-STEM imaging. **Figure 76A** confirms the well-defined structure of the nanosheets of the fresh sample and indicates that the thickness of individual platinum nanosheets is approximately 4 nm.

Table 19. Details of different electrode fabrications.

Ref./ Cathode (mg_{Pt}/cm^2)	Cathode fabrication	Catalyst structure/ catalyst surface coating	Fabrication steps / time	Elaborate or additional equipment	With or without ionomer
This work/ Pt-NS (0.025)	Electrochemical growth	Ultrathin nanosheets/ Uniform coating	One-step / < 25 s	No	Ionomer-free
This work/ Pt-NS (0.015)	Electrochemical growth	Ultrathin nanosheets/ Uniform coating	One-step / < 25 s	No	Ionomer-free
[180]/ Pt black (3)	Commercial Pt black + spray	Nanoparticles/-	Multiple complex steps	Spray coater	With ionomer
[180]/ Pt black (3)	Commercial Pt black + spray + decal	Nanoparticles/-	Multiple complex steps	Spray coater, hot press	With ionomer
29/ Pt (0.032)	Sputtering	Nanoparticles/ Uniform coating	One-step / 45 s	Sputter coater	Ionomer-free
324/ PtNW (0.1)	Wet chemical reduction	Nanowires/ Uniform coating	One-step / 16 h	No	Ionomer-free
303/ Pt PED1-3 (0.020)	Pulse electrodeposition	Flower-like structures/ Nonuniform coating	One-step / 300 s	No	Ionomer-free
303/ Pt PES2-3 (0.051)	Pulse electrodeposition	Polyhedral particles/ Nonuniform coating	One-step / 300 s	No	Ionomer-free
325/ Pt/SWNT-O3 (0.02)	Ozonized SWNT preparation + annealing in H_2/N_2 at 300 °C + spray	Nanowires/-	Multiple complex steps	Ozone generator, tube furnace, spray coater	With ionomer
205/ Pt/C (0.4)	Commercial Pt/C + spray	Nanoparticles/-	Multiple complex steps	Spray coater	With ionomer
326/ Pt/C (0.136)	Commercial Pt/C + spray	Nanoparticles/-	Multiple complex steps	Spray coater	With ionomer
276/ Pt/CB (0.7)	Modified Adams fusion method (annealing at 500 °C) + spray	Nanoparticles/-	Multiple complex steps	Muffle furnace, spray coater	With ionomer

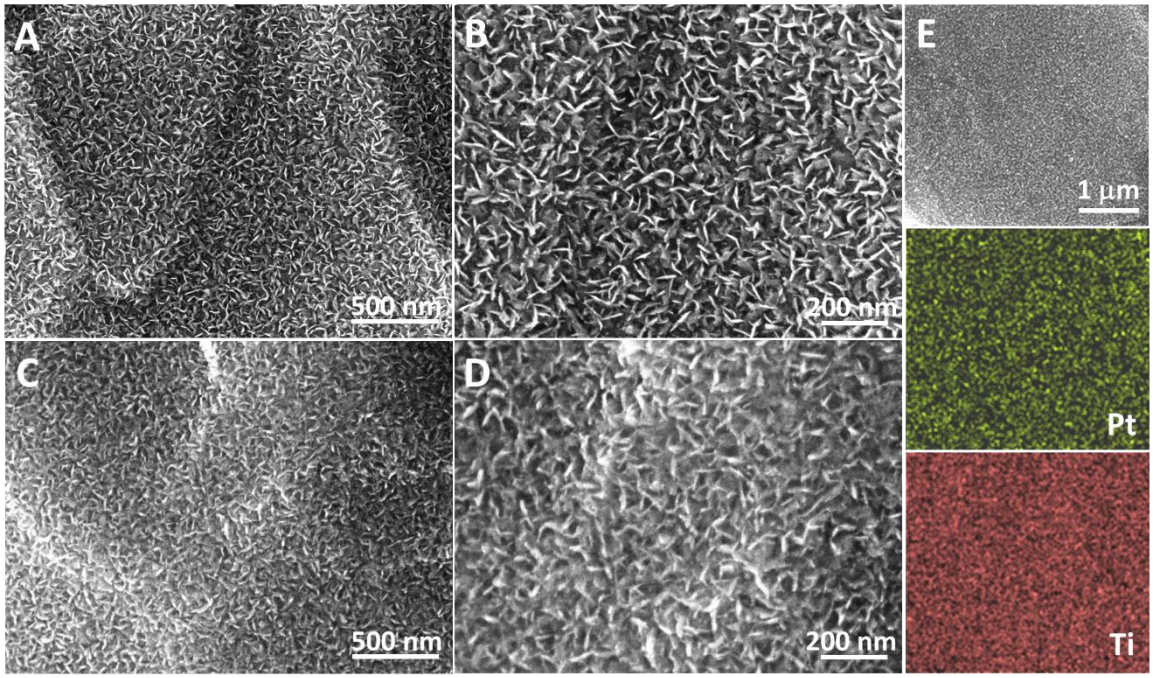


Figure 75. Morphology comparison before and after the *in-situ* cell stability test. SEM images of the (A, B) fresh and (C, D) tested Pt-NS electrode; (E) SEM-EDS mapping images of the tested Pt-NS electrode.

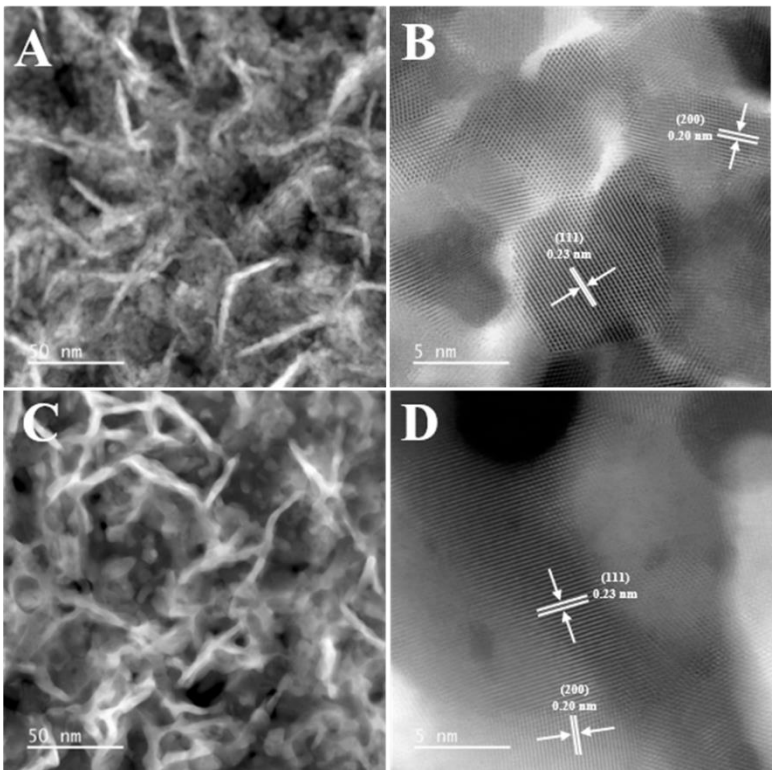


Figure 76. High-angle annular dark-field (HAADF) STEM images of (A, B) the fresh and (C, D) tested Pt-NS electrode.

As shown in **Figure 76B**, the lattice spacings of 0.23 and 0.20 nm are determined, corresponding to the crystal planes of Pt(111) and Pt(200), respectively. Furthermore, the HAADF-STEM images of the tested sample in **Figure 76C and D** reveal that the nanosheet structure and crystal structure have been preserved even after the stability test at a high current density of 1.8 A/cm^2. These findings are in good accordance with the results from **Figure 75**, which offer compelling evidence for the good structural stability of the as-obtained Pt nanosheets.

7.5 Conclusions

In summary, we developed vertically well-aligned Pt nanosheets (Pt-NSs) with bottom-up growth on thin Ti substrates, showing nanoscale catalyst layers (≤ 50 nm) and full surface coverage even at ultralow catalyst loadings *via* a facile electrochemical growth process at room temperature. The fabricated ultralow-loaded Pt-NSs exhibit ultrathin thicknesses of only about 4 nm, small nanosheet sizes, and vertically well-aligned nanosheet morphologies. Moreover, the entire electrode fabrication process is very rapid, environmentally friendly, and easily scalable, and occurs without the use of any surfactants, templates, pH adjusters, and elaborate equipment. When coupled with an anode-only catalyst-coated Nafion 117 membrane, the Pt-NS electrode with an ultralow Pt loading of 0.015 mg$_{Pt}$/cm^2 shows superior cell performance to the commercial CCM (mg$_{Pt}$/cm^2), achieving 99.5% catalyst savings and more than 237-fold higher catalyst utilization. Overall, this study could not only guide uniform catalyst coating on substrates at ultralow loadings but also pave a new way for developing nanostructured electrodes with nanoscale catalyst layers for energy-saving PEMECs and other energy storage/conversion devices.

Appendix

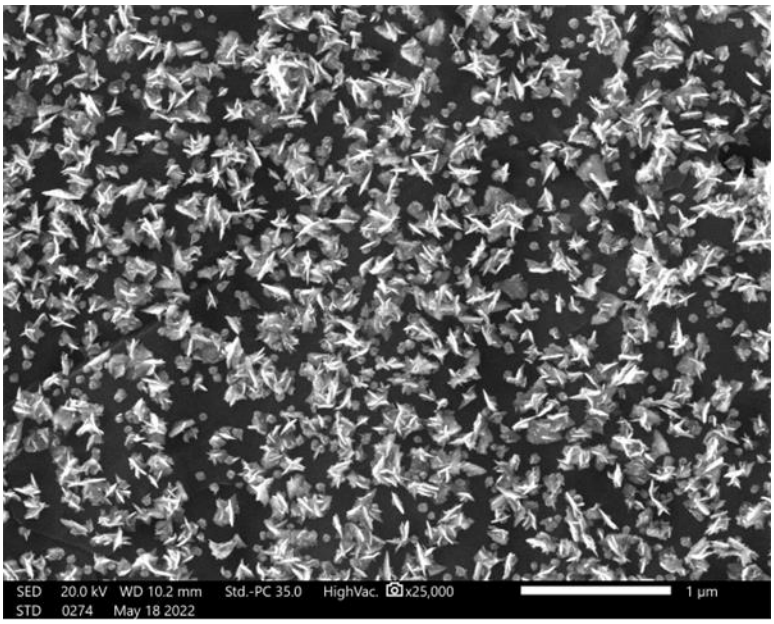


Figure 77. SEM image of Pt-NSs without the seeding layer: 0.07 mg_{Pt}/cm^2 Pt-NSs.

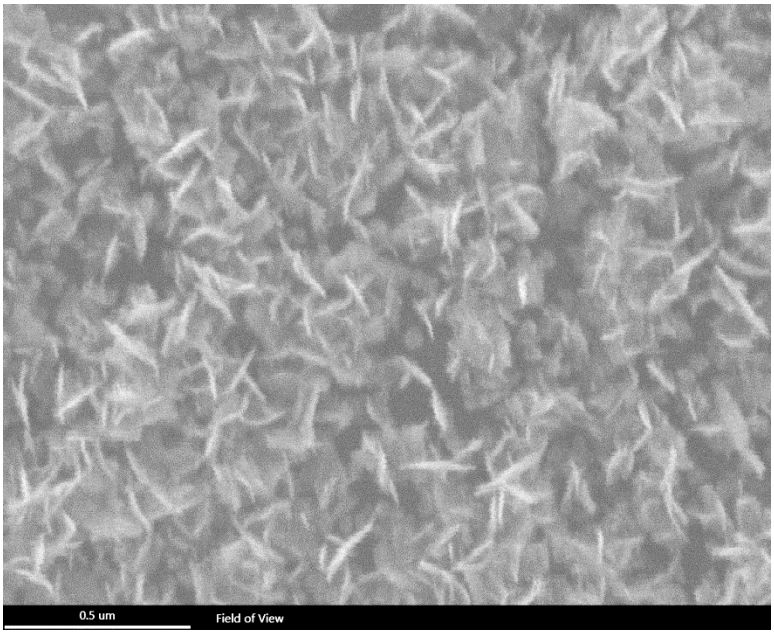


Figure 78. SEM image of Pt-NSs without the seeding layer: 0.14 mg_{Pt}/cm^2 Pt-NSs.

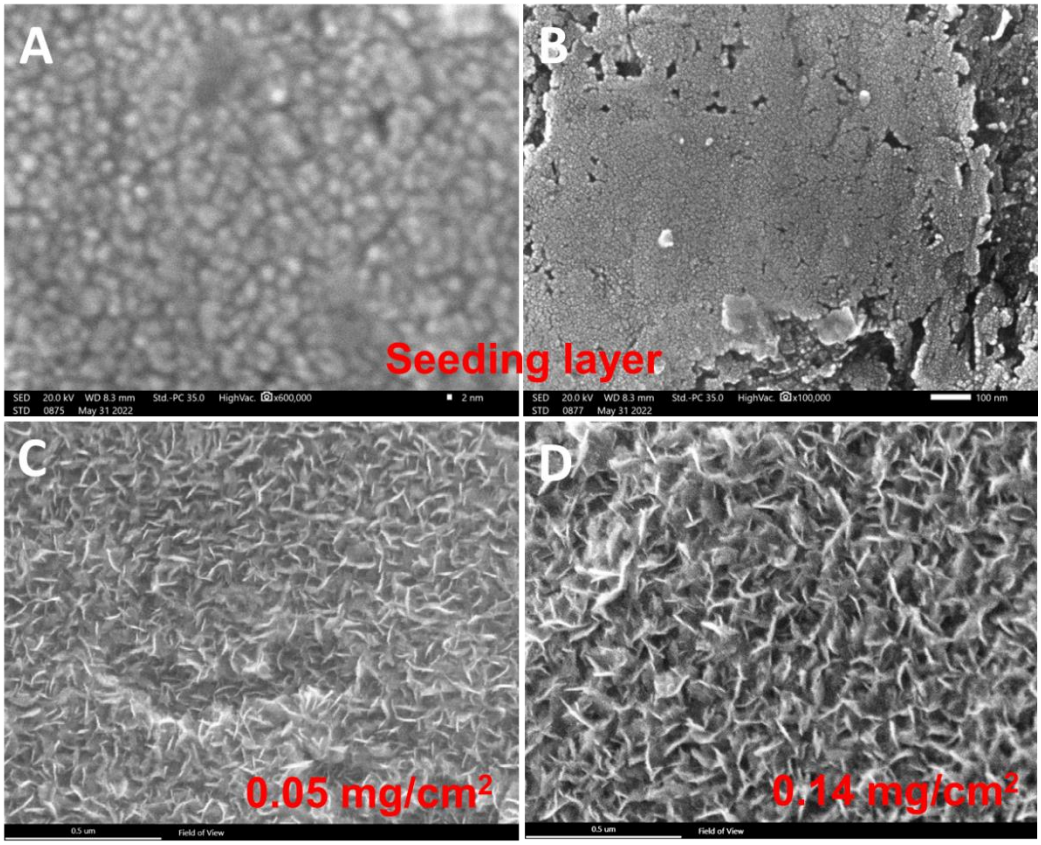


Figure 79. SEM images of Pt nanoparticle seeding layers (A and B); SEM images of Pt-NSs with the seeding layer, (C) 0.050 mg_{Pt}/cm^2 Pt-NSs, (D) 0.140 mg_{Pt}/cm^2 Pt-NSs.

Table 20. EIS fitting parameters derived from the Nyquist plots in Figure 71C.

Electrode	R_{Ω} [mΩ·cm^2]	R_{hf} [mΩ·cm^2]	Q_{hf} [mF·s^{n-1}/cm^2]	n_{hf}	R_{lf} [mΩ·cm^2]	Q_{lf} [mF·s^{n-1}/cm^2]	n_{lf}	$C_{dl,hf}$ [mF/cm^2]	$C_{dl,lf}$ [mF/cm^2]	Error (%)
Pt-NS	2.06	1.75	85.46	0.600	0.416	5.39	0.766	23.5	0.833	0.012
Pt-NP	2.14	3.26	63.7	0.345	1.87	138	0.819	3.26	115	0.023

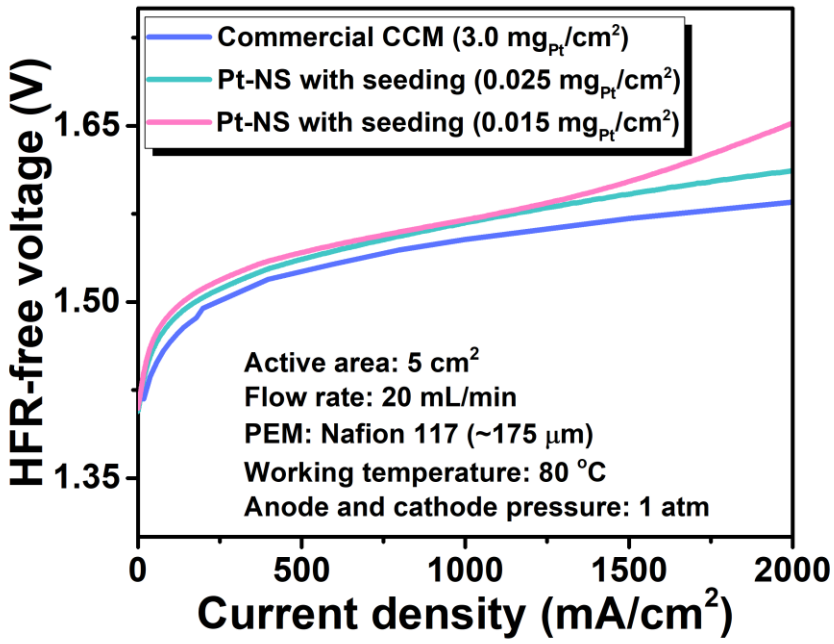


Figure 80. The HFR-free cell polarization curves of commercial CCM and Pt-NS with seeding layer: 0.025 mg$_{Pt}$/cm^2 and 0.015 mg$_{Pt}$/cm^2.

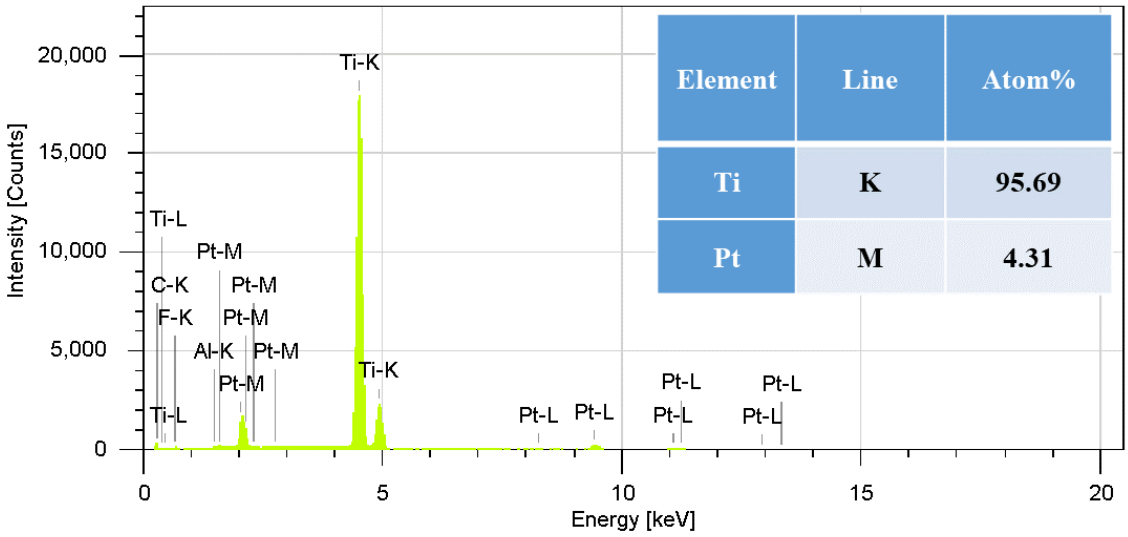


Figure 81. EDS analysis of the tested Pt-NS CCLGDL (0.025 mg_{Pt}/cm^2).

CHAPTER EIGHT

CONCLUSIONS AND SUGGESTIONS FOR FUTURE WORKS

This dissertation contributes to the development of tunable electrocatalysts/electrodes with high material utilization and durability for high-efficiency and low-cost water electrolyzers to produce green hydrogen. The main achievements are concluded by summarizing the content of each chapter as follows:

In Chapter two, W-doped NiFe (NiFeW) layered double hydroxides were prepared via an easy and fast one-step electrodeposition process at room temperature and ambient pressure, showing ultrathin nanosheet features and serving as bifunctional catalysts for water splitting. As a result, excellent performance is achieved with low overpotentials of only 239 mV and 115 mV for the oxygen evolution reaction (OER) and hydrogen evolution reaction (HER), respectively, at a current density of 10 mA/cm^2 in alkaline condition. Additionally, the bifunctional NiFeW electrocatalysts were served as both anode and cathode catalysts and further evaluated in a full electrolyzer configuration, achieving a low cell voltage of 1.59 V at 10 mA/cm^2, 110 mV lower than that of the commercial IrO_2 (anode) and Pt (cathode) catalysts. Notably, the NiFeW nanosheets show better performance than a series of reported bifunctional electrocatalysts. The outstanding performances are mainly ascribed to the W doping in the NiFe matrix, which efficiently engineered the electrocatalyst morphology to achieve vertically well-aligned ultrathin nanosheets with a thin thickness of only about 5 nm. The fine nanosheet structures could offer a large surface area and expose abundant reaction active sites. Moreover, the W doping also engineered the electronic structure of NiFe hydroxides to boost charge transfer kinetics for both the OER and HER. Furthermore, the NiFeW electrocatalysts show mixed phases of amorphous-looking phase and crystalline phase, which could ensure both activity

and stability of the catalysts. Overall, the ultrathin NiFeW nanosheets with an efficient fabrication strategy are promising as bifunctional electrodes for alkaline water electrolyzers.

In Chapter three, the impact of different W doping concentrations on the NiFe electrocatalysts was investigated with an electrodeposition process. With the different W doping, the morphologies of the fabricated NiFeW electrocatalysts show different nanostructures. Different W precursor concentrations of 0 mM, 2.5 mM, 5 mM, 7.5 mM, and 10 mM were used, without W doping, the NiFe shows a smooth film-like structure. With a low-level addition of W precursor (2.5 mM), some nanosheet-like grains are observed. As the W precursor concentration increased to 5 mM, well-aligned nanosheets were observed. However, as the W precursor doping concentration further increased (7.5 mM and 10 mM), the formed nanosheets became dense and smaller. Hence, the W doping amount significantly influences the NiFeW electrocatalysts. Meanwhile, it also influences the OER and HER of the catalysts. As a result, compared to NiFe hydroxides, the optimized NiFeW catalysts achieve improved overpotentials of 31 mV and 114 mV for the OERs and HERs at 10 mA/cm^2, respectively, in 1 M KOH. Moreover, the electrochemically surface area (ECSA) of different electrocatalysts was derived. The optimized NiFeW shows the highest ECSA value of 235.5 cm^2_{ECSA}/ cm^2, which is more than 4 times larger than that of the pristine NiFe hydroxides (57.5 cm^2_{ECSA}/ cm^2). This could be the main reason for the improved performance. Overall, due to the significantly enhanced performances and a fast electrodeposition method, the well-aligned NiFeW-LDHs exhibit great potential to boost the large-scale application of practical water splitting.

In Chapter four, high-performance Ir-integrated electrodes were fabricated via a fast and facile electrodeposition process to serve efficient anodes for PEMECs, successfully demonstrating high-current operation of up to 6 A/cm^2. Additionally, excellent stability was demonstrated under an ultrahigh current density of 5 A/cm^2 with a low degradation rate of 0.223 mV/h, which is recoverable, and no performance loss was observed after the stability test. Additionally, a platinum layer on the Ti substrates plays a significant role in the crack-free catalyst layer and superior performances of the electrode. The Pt layer could protect the substrate and also enhance the conductivity of the catalyst layer thus improving the catalyst utilization. Additionally, the Pt coating shows rough surfaces, which might decrease the internal stress of the catalyst, resulting in a crack-free catalyst layer and increasing the catalysts' adhesion on the substrate. As a result, the catalyst layer also serves as a protection layer for the substrate and prevents substrate oxidation. Overall, the cell voltage can be improved by 33, 59, and 87 mV at current densities of 2, 4, and 6 A/cm^2, respectively, with the Pt coating on the substrate.

In Chapter five, highly porous Ir catalyst-coated thin/tunable liquid/gas diffusion layers with fine honeycomb-structured catalyst layers (HC Ir CCLGDL) were developed via an efficient integration of fast electrodeposition and template use. The fabricated HC Ir CCLGDL was applied to the anode for the PEMEC, achieving improved reaction kinetics. Notably, the fine honeycomb catalyst layer (CL), not only could expose more active sites but also improve multiphase transport properties. As a result, with a low Ir loading of 0.27 mg/cm^2, a low cell voltage of 1.842 V at 2000 mA/cm^2, and a high mass activity of 4.16 A/mg_{Ir} at 1.7 V were achieved when combined with a Nafion 117 membrane. Operando

high-speed visualizations in the practical PEMEC were also performed to first investigate the catalyst layer structure impact on real-time electrochemical reactions and mass transport phenomena. With the visualization results, increased active sites and improved multiphase transport properties with favorable bubble detachment and water diffusion were demonstrated. The excellent performance is superior to most of the recently reported anode catalysts. Moreover, outstanding stability at a high current density of 1800 mA/cm^2 in the practical PEMEC is also demonstrated.

In Chapter six, ionomer-free iridium nanosheet electrodes were deposited on thin titanium liquid/gas diffusion layers (LGDLs) via a facile and low-temperature wet chemical method, in which nanoporous iridium nanosheets (IrNS) with abundantly exposed edges and nanopores are revealed. Benefiting from the novel and unique nanostructures of the nanoporous IrNSs, high catalytic activity, good electrode conductivity and excellent liquid/gas transport properties were achieved. The nanoporous IrNS electrodes with a low Ir loading of 0.28 mg/cm^2 can deliver low cell voltages within the test current range from 0 ~ 6 A/cm^2. Impressively, small cell voltages of 1.65 and 1.78 V were delivered at 3 and 6 A/cm^2, which far exceeded the 2026 DOE target of 1.8 A at 3 A/cm^2 with an Ir loading less than 0.4 mg/cm^2. Meanwhile, remarkable stability was demonstrated at an ultrahigh current density of 5 A/cm^2 with a pretty low degradation rate of only 3.32 μV/h, which is close to the 2026 DOE target (2.3 μV/h).

In Chapter seven, ultrathin Pt nanosheets (Pt-NSs) were electrochemically grown on thin Ti substrates as cathodes for PEMECs with a template- and surfactant-free electrolyte. Benefiting from a thin seeding layer, the Pt-NSs show bottom-up growth and vertically

well-aligned nanosheets with an average ultrathin thickness of only about 4 nm. Compared to the commercial catalyst-coated membrane (CCM) design with Pt nanoparticles as the cathode catalysts, the Pt-NSs show a significantly simplified fabrication process. With an ultralow loading of 0.015 mg_{Pt}/cm^2, compared to the commercial CCM (3 mg_{Pt}/cm^2), more than 99% catalyst saving, and 237-fold catalyst utilization were achieved when combined with an anode-only Nafion 117 CCM. The remarkable performance of the Pt-NSs with significantly simplified electrode fabrication is also better than reported cathode catalysts/electrodes. The highly efficient, sustainable, low cost and scalable electrodeposition process shows great potential for industrial application. Moreover, the ultrathin electrode shows material/weight/volume/cost-saving and would benefit a compact stack design in the future. Overall, due to the efficient and scalable electrode fabrication, excellent performance and high catalyst utilization, the Pt-NSs could be easily extended to other electrochemical energy storage/conversion systems such as fuel cells.

This dissertation elaborates on the development of tunable electrocatalysts/electrodes with high material utilization and stability in water electrolyzers for green hydrogen production. Significantly simplified fabrication methods with easy scalability and low cost such as facile electrodeposition, and low-temperature wet chemical strategy were used in this research for novel and advanced GDE development with tunable CLs of nanostructure, composition, and phase control. The developed low-cost, simplified, and easily scalable fabrication processes could accelerate the large-scale application and commercialization of the PEMEC. With the developed efficient fabrication methods, novel and advanced

electrocatalysts/electrodes with tunable nanostructures, morphologies, and composition were designed, fabricated, and evaluated in this research.

For future research, it is feasible to further optimize the electrocatalysts/electrodes by engineering composition and phase. With well-designed fabrication strategies, it is possible to integrate nanostructures, compositions, and phases in one electrocatalyst/electrode. For catalyst phase engineering, some strategies such as tuning electrolytes, changing electrodeposition parameters, using a post-annealing process could be used. For example, it is possible to prepare amorphous IrO_x-based electrodes by tuning the electrodeposition conditions such as electrodeposition modes and electrolytes. For composition engineering, foreign element introduction would be a good strategy. For example, introducing Ru into the Ir catalysts to improve the intrinsic activity of the catalysts. Normally, to balance the activity and stability of the IrRu-based electrocatalysts/electrodes, it is crucial to control the atomic ratio of the Ir and Ru, which is normally larger than 7 to 3 for Ir to Ru. [327, 328] In addition, some acid-stable elements could be dropped into the Ir-based catalysts, such as Sn, Re, Nb, and Pt to improve the activity and stability of the Ir or Ru. [329-332] Studies have reported that doping with some elements with high valence states could efficiently tune the electronic structure of Ir and Ru, lowering down the energy barrier of the potential determine step thus achieving improved catalytic activity. Moreover, the doped element could eliminate the Ir or Ru overoxidation by donating electrons during the reaction process. Hence, introducing foreign acid-stable elements is a promising approach to improve both the activity and stability of the Ir-based electrocatalysts/electrodes.

Furthermore, the element doping could reduce the Ir use and decrease the PGM catalyst loading thus cutting down the capital cost of the PEMEC.

LIST OF REFERENCES

1. Shiva Kumar, S.; Himabindu, V., Hydrogen production by PEM water electrolysis – A review. *Materials Science for Energy Technologies* **2019,** *2* (3), 442-454.
2. Stähler, M., Stähler, A., Scheepers, F., Carmo, M., Lehnert, W. and Stolten, D., Impact of porous transport layer compression on hydrogen permeation in PEM water electrolysis. International journal of hydrogen energy, **2020,** 45 (7), 4008-4014.
3. Villagra, A., and P. Millet. An analysis of PEM water electrolysis cells operating at elevated current densities. *International Journal of Hydrogen Energy* **2019,** 44 (20) 9708-9717.
4. Nguyen, T.; Abdin, Z.; Holm, T.; Mérida, W., Grid-connected hydrogen production via large-scale water electrolysis. *Energ Convers Manage* **2019,** *200*, 112108.
5. Han, B.; Steen, S. M.; Mo, J.; Zhang, F.-Y., Electrochemical performance modeling of a proton exchange membrane electrolyzer cell for hydrogen energy. *International Journal of Hydrogen Energy* **2015,** *40* (22), 7006-7016.
6. Pushkarev, A. S.; Pushkareva, I. V.; Akelkina, S. V.; Kozlova, M. V.; Grigoriev, S. A.; Kuleshov, N. V.; Bessarabov, D. G., Electrocatalytic materials for solid polymer electrolyte water electrolyzers. *J. Phys: Conf. Ser.* **2020,** *1683* (5), 052022.
7. Wang, M.; Wang, Z.; Gong, X.; Guo, Z., The intensification technologies to water electrolysis for hydrogen production–A review. *Renewable Sustainable Energy Rev.* **2014,** *29*, 573-588.
8. Mo, J.; Kang, Z.; Yang, G.; Li, Y.; Retterer, S. T.; Cullen, D. A.; Toops, T. J.; Bender, G.; Pivovar, B. S.; Green Jr, J. B.; Zhang, F.-Y., In situ investigation on ultrafast oxygen evolution reactions of water splitting in proton exchange membrane electrolyzer cells. *Journal of Materials Chemistry A* **2017,** *5* (35), 18469-18475.
9. Millet, P.; Ngameni, R.; Grigoriev, S. A.; Mbemba, N.; Brisset, F.; Ranjbari, A.; Etiévant, C., PEM water electrolyzers: From electrocatalysis to stack development. *International Journal of Hydrogen Energy* **2010,** *35* (10), 5043-5052.
10. Anwar, S.; Khan, F.; Zhang, Y.; Djire, A., Recent development in electrocatalysts for hydrogen production through water electrolysis. *International Journal of Hydrogen Energy* **2021,** *46* (63), 32284-32317.
11. Millet, P.; Andolfatto, F.; Durand, R., Design and performance of a solid polymer electrolyte water electrolyzer. *International Journal of Hydrogen Energy* **1996,** *21* (2), 87-93.
12. Takenaka, H.; Torikai, E.; Kawami, Y.; Wakabayashi, N., Solid polymer electrolyte water electrolysis. *International Journal of Hydrogen Energy* **1982,** *7* (5), 397-403.
13. Li, D.; Motz, A. R.; Bae, C.; Fujimoto, C.; Yang, G.; Zhang, F.-Y.; Ayers, K. E.; Kim, Y. S., Durability of anion exchange membrane water electrolyzers. *Energy Environ. Sci.* **2021,** *14* (6), 3393-3419.
14. Vincent, I.; Bessarabov, D., Low cost hydrogen production by anion exchange membrane electrolysis: A review. *Renewable Sustainable Energy Rev.* **2018,** *81*, 1690-1704.
15. Miller, H. A.; Bouzek, K.; Hnat, J.; Loos, S.; Bernäcker, C. I.; Weißgärber, T.; Röntzsch, L.; Meier-Haack, J., Green hydrogen from anion exchange membrane water

electrolysis: a review of recent developments in critical materials and operating conditions. *Sustainable Energy & Fuels* **2020,** *4* (5), 2114-2133.
16. Millet, P.; Mbemba, N.; Grigoriev, S. A.; Fateev, V. N.; Aukauloo, A.; Etiévant, C., Electrochemical performances of PEM water electrolysis cells and perspectives. *International Journal of Hydrogen Energy* **2011,** *36* (6), 4134-4142.
17. Mo, J.; Kang, Z.; Yang, G.; Retterer, S. T.; Cullen, D. A.; Toops, T. J.; Green, J. B.; Zhang, F.-Y., Thin liquid/gas diffusion layers for high-efficiency hydrogen production from water splitting. *Appl Energ* **2016,** *177*, 817-822.
18. Han, B.; Mo, J.; Kang, Z.; Zhang, F.-Y., Effects of membrane electrode assembly properties on two-phase transport and performance in proton exchange membrane electrolyzer cells. *Electrochim Acta* **2016,** *188*, 317-326.
19. Ayers, K.; Danilovic, N.; Harrison, K.; Xu, H., PEM Electrolysis, a Forerunner for Clean Hydrogen. *Electrochem. Soc. Interface.* **2021,** *30* (4), 67-72.
20. Fornaciari, J. C.; Gerhardt, M. R.; Zhou, J.; Regmi, Y. N.; Danilovic, N.; Bell, A. T.; Weber, A. Z., The Role of Water in Vapor-fed Proton-Exchange-Membrane Electrolysis. *J Electrochem Soc* **2020,** *167* (10), 104508.
21. Ayers, K. E.; Anderson, E. B.; Capuano, C.; Carter, B.; Dalton, L.; Hanlon, G.; Manco, J.; Niedzwiecki, M., Research Advances towards Low Cost, High Efficiency PEM Electrolysis. *ECS Trans.* **2010,** *33* (1), 3.
22. Zhang, W.; Liu, M.; Gu, X.; Shi, Y.; Deng, Z.; Cai, N., Water Electrolysis toward Elevated Temperature: Advances, Challenges and Frontiers. *Chem Rev* **2023,** *123* (11), 7119-7192.
23. Mo, J.; Kang, Z.; Retterer, S. T.; Cullen, D. A.; Toops, T. J.; Green, J. B.; Mench, M. M.; Zhang, F.-Y., Discovery of true electrochemical reactions for ultrahigh catalyst mass activity in water splitting. *Sci. Adv.* **2016,** *2* (11), e1600690.
24. Choe, S.; Lee, B.-S.; Cho, M. K.; Kim, H.-J.; Henkensmeier, D.; Yoo, S. J.; Kim, J. Y.; Lee, S. Y.; Park, H. S.; Jang, J. H., Electrodeposited IrO2/Ti electrodes as durable and cost-effective anodes in high-temperature polymer-membrane-electrolyte water electrolyzers. *Applied Catalysis B: Environmental* **2018,** *226*, 289-294.
25. Yu, S.; Li, K.; Wang, W.; Xie, Z.; Ding, L.; Kang, Z.; Wrubel, J.; Ma, Z.; Bender, G.; Yu, H.; Baxter, J.; Cullen, D. A.; Keane, A.; Ayers, K.; Capuano, C. B.; Zhang, F.-Y., Tuning Catalyst Activation and Utilization Via Controlled Electrode Patterning for Low-Loading and High-Efficiency Water Electrolyzers. *Small* **2022,** *18* (14), 2107745.
26. Oh, J. H.; Han, G. H.; Kim, H.; Jang, H. W.; Park, H. S.; Kim, S. Y.; Ahn, S. H., Activity and stability of Ir-based gas diffusion electrode for proton exchange membrane water electrolyzer. *Chem. Eng. J.* **2021,** *420*, 127696.
27. Slavcheva, E.; Radev, I.; Bliznakov, S.; Topalov, G.; Andreev, P.; Budevski, E., Sputtered iridium oxide films as electrocatalysts for water splitting via PEM electrolysis. *Electrochim Acta* **2007,** *52* (12), 3889-3894.
28. Liu, C.; Wippermann, K.; Rasinski, M.; Suo, Y.; Shviro, M.; Carmo, M.; Lehnert, W., Constructing a Multifunctional Interface between Membrane and Porous Transport Layer for Water Electrolyzers. *ACS Appl. Mater. Interfaces* **2021,** *13* (14), 16182-16196.
29. Kang, Z.; Yang, G.; Mo, J.; Li, Y.; Yu, S.; Cullen, D. A.; Retterer, S. T.; Toops, T. J.; Bender, G.; Pivovar, B. S.; Green, J. B.; Zhang, F.-Y., Novel thin/tunable gas

diffusion electrodes with ultra-low catalyst loading for hydrogen evolution reactions in proton exchange membrane electrolyzer cells. *Nano Energy* **2018,** *47*, 434-441.
30. Li, Y.; Zhang, H.; Xu, T.; Lu, Z.; Wu, X.; Wan, P.; Sun, X.; Jiang, L., Under-Water Superaerophobic Pine-Shaped Pt Nanoarray Electrode for Ultrahigh-Performance Hydrogen Evolution. **2015,** *25* (11), 1737-1744.
31. Kamei, J.; Saito, Y.; Yabu, H., Biomimetic Ultra-Bubble-Repellent Surfaces Based on a Self-Organized Honeycomb Film. *Langmuir* **2014,** *30* (47), 14118-14122.
32. Lu, Z.; Zhu, W.; Yu, X.; Zhang, H.; Li, Y.; Sun, X.; Wang, X.; Wang, H.; Wang, J.; Luo, J.; Lei, X.; Jiang, L., Ultrahigh Hydrogen Evolution Performance of Under-Water "Superaerophobic" MoS2 Nanostructured Electrodes. **2014,** *26* (17), 2683-2687.
33. Xie, Z.; Yu, S.; Yang, G.; Li, K.; Ding, L.; Wang, W.; Cullen, D. A.; Meyer, H. M.; Retterer, S. T.; Wu, Z.; Sun, J.; Gao, P.-X.; Zhang, F.-Y., Ultrathin Platinum Nanowire Based Electrodes for High-Efficiency Hydrogen Generation in Practical Electrolyzer Cells. *Chem. Eng. J.* **2021**, 128333.
34. Lim, A.; Kim, J.; Lee, H. J.; Kim, H.-J.; Yoo, S. J.; Jang, J. H.; Park, H. Y.; Sung, Y.-E.; Park, H. S., Low-loading IrO2 supported on Pt for catalysis of PEM water electrolysis and regenerative fuel cells. *Appl. Catal. B: Environ.* **2020,** *272*, 118955.
35. Kim, H.; Kim, J.; Kim, J.; Han, G. H.; Guo, W.; Hong, S.; Park, H. S.; Jang, H. W.; Kim, S. Y.; Ahn, S. H., Dendritic gold-supported iridium/iridium oxide ultra-low loading electrodes for high-performance proton exchange membrane water electrolyzer. *Appl. Catal. B* **2021,** *283*, 119596.
36. Yasutake, M.; Noda, Z.; Matsuda, J.; Lyth, S. M.; Nishihara, M.; Ito, K.; Hayashi, A.; Sasaki, K., Ru-core Ir-shell electrocatalysts deposited on a surface-modified Ti-based porous transport layer for polymer electrolyte membrane water electrolysis. *International Journal of Hydrogen Energy* **2024,** *49*, 169-183.
37. McCrory, C. C. L.; Jung, S.; Ferrer, I. M.; Chatman, S. M.; Peters, J. C.; Jaramillo, T. F., Benchmarking Hydrogen Evolving Reaction and Oxygen Evolving Reaction Electrocatalysts for Solar Water Splitting Devices. *J Am Chem Soc* **2015,** *137* (13), 4347-4357.
38. Sheng, W.; Myint, M.; Chen, J. G.; Yan, Y., Correlating the hydrogen evolution reaction activity in alkaline electrolytes with the hydrogen binding energy on monometallic surfaces. *Energy Environ. Sci.* **2013,** *6* (5), 1509.
39. Li, K.; Li, Y.; Wang, Y.; Ge, J.; Liu, C.; Xing, W., Enhanced electrocatalytic performance for the hydrogen evolution reaction through surface enrichment of platinum nanoclusters alloying with ruthenium in situ embedded in carbon. *Energy Environ. Sci.* **2018,** *11* (5), 1232-1239.
40. Yang, G.; Yu, S.; Kang, Z.; Li, Y.; Bender, G.; Pivovar, B. S.; Green, J. B.; Cullen, D. A.; Zhang, F. Y., Electrocatalysts: Building electron/proton nanohighways for full utilization of water splitting catalysts. *Adv. Energ. Mater.* **2020,** *10* (16), 2070075.
41. Lei, L.; Huang, D.; Zhou, C.; Chen, S.; Yan, X.; Li, Z.; Wang, W., Demystifying the active roles of NiFe-based oxides/(oxy)hydroxides for electrochemical water splitting under alkaline conditions. *Coord. Chem. Rev.* **2020,** *408*, 213177.
42. Kang, Z.; Mo, J.; Yang, G.; Retterer, S. T.; Cullen, D. A.; Toops, T. J.; Green Jr, J. B.; Mench, M. M.; Zhang, F.-Y., Investigation of thin/well-tunable liquid/gas

diffusion layers exhibiting superior multifunctional performance in low-temperature electrolytic water splitting. *Energy Environ. Sci.* **2017,** *10* (1), 166-175.
43. Pivovar, B.; Rustagi, N.; Satyapal, S., Hydrogen at scale (H2@scale): Key to a clean, economic, and sustainable energy system. *Electrochem. Soc. Interface* **2018,** *27* (1), 47-52.
44. Yang, G.; Yu, S.; Mo, J.; Kang, Z.; Dohrmann, Y.; List, F. A.; Green, J. B.; Babu, S. S.; Zhang, F.-Y., Bipolar plate development with additive manufacturing and protective coating for durable and high-efficiency hydrogen production. *J. Power Sources* **2018,** *396*, 590-598.
45. Tao, H. B.; Zhang, J.; Chen, J.; Zhang, L.; Xu, Y.; Chen, J. G.; Liu, B., Revealing Energetics of Surface Oxygen Redox from Kinetic Fingerprint in Oxygen Electrocatalysis. *J Am Chem Soc* **2019,** *141* (35), 13803-13811.
46. Xie, Z.; Wang, Y., Facile synthesis of MOF-Derived Co@CoNx/bamboo-like carbon tubes for efficient electrocatalytic water oxidation. *Electrochim. Acta* **2019,** *296*, 372-378.
47. Li, K.; Jin, Z.; Ge, J.; Liu, C.; Xing, W., Platinum nanoparticles partially-embedded into carbon sphere surfaces: a low metal-loading anode catalyst with superior performance for direct methanol fuel cells. *J. Mater. Chem. A* **2017,** *5* (37), 19857-19865.
48. Trotochaud, L.; Young, S. L.; Ranney, J. K.; Boettcher, S. W., Nickel–Iron Oxyhydroxide Oxygen-Evolution Electrocatalysts: The Role of Intentional and Incidental Iron Incorporation. *J Am Chem Soc* **2014,** *136* (18), 6744-6753.
49. Batchellor, A. S.; Boettcher, S. W., Pulse-Electrodeposited Ni–Fe (Oxy)hydroxide Oxygen Evolution Electrocatalysts with High Geometric and Intrinsic Activities at Large Mass Loadings. *ACS Catal.* **2015,** *5* (11), 6680-6689.
50. Qiu, Z.; Tai, C.-W.; Niklasson, G. A.; Edvinsson, T., Direct observation of active catalyst surface phases and the effect of dynamic self-optimization in NiFe-layered double hydroxides for alkaline water splitting. *Energy Environ. Sci.* **2019,** *12* (2), 572-581.
51. Wei, C.; Sun, S.; Mandler, D.; Wang, X.; Qiao, S. Z.; Xu, Z. J., Approaches for measuring the surface areas of metal oxide electrocatalysts for determining their intrinsic electrocatalytic activity. *Chem Soc Rev* **2019,** *48* (9), 2518-2534.
52. Ding, L.; Zhang, M.; Zhang, Y.; Yang, J.; Zheng, J.; Xu, J., A type of raspberry-like silica composite with tunable nickel nanoparticles coverage towards nanocatalysis and protein adsorption. *Green Chem.* **2016,** *18* (23), 6282-6290.
53. Ding, L.; Zhang, M.; Ren, Y.; Xu, J.; Zheng, J.; Alsulami, H.; Kutbi, M. A.; Zhang, F.-Y., Carbon-supported nickel nanoparticles on SiO2 cores for protein adsorption and nitroaromatics reduction. *ACS Appl. Nano Mater.* **2020,** *3* (5), 4623-4634.
54. Luo, Y.; Wu, Y.; Wu, D.; Huang, C.; Xiao, D.; Chen, H.; Zheng, S.; Chu, P. K., NiFe-Layered Double Hydroxide Synchronously Activated by Heterojunctions and Vacancies for the Oxygen Evolution Reaction. *ACS Appl. Mat. Interfaces* **2020,** *12* (38), 42850-42858.
55. Liu, R.; Lin, Y.; Chou, L.-Y.; Sheehan, S. W.; He, W.; Zhang, F.; Hou, H. J. M.; Wang, D., Water splitting by tungsten oxide prepared by atomic layer deposition and decorated with an oxygen-evolving catalyst. *Angew. Chem. Int.* **2011,** *50* (2), 499-502.

56. Han, N.; Yang, K. R.; Lu, Z.; Li, Y.; Xu, W.; Gao, T.; Cai, Z.; Zhang, Y.; Batista, V. S.; Liu, W.; Sun, X., Nitrogen-doped tungsten carbide nanoarray as an efficient bifunctional electrocatalyst for water splitting in acid. *Nat. Comm.* **2018,** *9* (1).
57. Zhang, B.; Zheng, X.; Voznyy, O.; Comin, R.; Bajdich, M.; García-Melchor, M.; Han, L.; Xu, J.; Liu, M.; Zheng, L., Homogeneously dispersed multimetal oxygen-evolving catalysts. *Science* **2016,** *352* (6283), 333-337.
58. Zhu, Y.; Chen, G.; Zhong, Y.; Zhou, W.; Shao, Z., Rationally designed hierarchically structured tungsten nitride and nitrogen-rich graphene-like carbon nanocomposite as efficient hydrogen evolution electrocatalyst. *Adv. Sci.* **2018,** *5* (2), 1700603.
59. Dong, J.; Zhang, F.-Q.; Yang, Y.; Zhang, Y.-B.; He, H.; Huang, X.; Fan, X.; Zhang, X.-M., (003)-Facet-exposed Ni3S2 nanoporous thin films on nickel foil for efficient water splitting. *Appl. Catal. B* **2019,** *243*, 693-702.
60. Li, Z.; Shao, M.; An, H.; Wang, Z.; Xu, S.; Wei, M.; Evans, D. G.; Duan, X., Fast electrosynthesis of Fe-containing layered double hydroxide arrays toward highly efficient electrocatalytic oxidation reactions. *Chem. Sci.* **2015,** *6* (11), 6624-6631.
61. Xie, Z.; Tang, H.; Wang, Y., MOF‐derived Ni‐doped CoS2 grown on carbon fiber paper for efficient oxygen evolution reaction. *ChemElectroChem* **2019,** *6* (4), 1206-1212.
62. Amiinu, I. S.; Pu, Z.; He, D.; Monestel, H. G. R.; Mu, S., Scalable cellulose-sponsored functionalized carbon nanorods induced by cobalt for efficient overall water splitting. *Carbon* **2018,** *137*, 274-281.
63. Liang, H.; Li, L.; Meng, F.; Dang, L.; Zhuo, J.; Forticaux, A.; Wang, Z.; Jin, S., Porous Two-Dimensional Nanosheets Converted from Layered Double Hydroxides and Their Applications in Electrocatalytic Water Splitting. *Chemistry of Materials* **2015,** *27* (16), 5702-5711.
64. Niu, Q.; Zhang, M.; Liu, L.; Zheng, J.; Fang, Q.; Xu, J., A facile template method to fabricate strongly coupled 1D sandwich-like C@Fe3O4@C/Ni coaxial microtubes with enhanced catalytic performance. *CrystEngComm* **2020,** *22* (32), 5302-5309.
65. Ding, L.; Zhang, M.; Zheng, J.; Xu, J.; Alharbi, N. S.; Wakeel, M., Fabrication of ultrafine nickel nanoparticles anchoring carbon fabric composites and their High catalytic performance. *Colloids Surfaces A* **2019,** *562*, 146-153.
66. Zhang, M.; Ding, L.; Zheng, J.; Liu, L.; Alsulami, H.; Kutbi, M. A.; Xu, J., Surface modification of carbon fibers with hydrophilic Fe3O4 nanoparticles for nickel-based multifunctional composites. *Appl. Surf. Sci.* **2020,** *509*, 145348.
67. Friebel, D.; Louie, M. W.; Bajdich, M.; Sanwald, K. E.; Cai, Y.; Wise, A. M.; Cheng, M.-J.; Sokaras, D.; Weng, T.-C.; Alonso-Mori, R.; Davis, R. C.; Bargar, J. R.; Nørskov, J. K.; Nilsson, A.; Bell, A. T., Identification of Highly Active Fe Sites in (Ni,Fe)OOH for Electrocatalytic Water Splitting. *J Am Chem Soc* **2015,** *137* (3), 1305-1313.
68. Xing, J.; Li, Y.; Guo, S.; Jin, T.; Li, H.; Wang, Y.; Jiao, L., Molybdenum carbide in-situ embedded into carbon nanosheets as efficient bifunctional electrocatalysts for overall water splitting. *Electrochim Acta* **2019,** *298*, 305-312.

69. Shin, H.; Xiao, H.; Goddard, W. A., III, In Silico Discovery of New Dopants for Fe-Doped Ni Oxyhydroxide (Ni1–xFexOOH) Catalysts for Oxygen Evolution Reaction. *J Am Chem Soc* **2018,** *140* (22), 6745-6748.
70. Chen, J.; Ren, B.; Cui, H.; Wang, C. J. S., Constructing Pure Phase Tungsten‐Based Bimetallic Carbide Nanosheet as an Efficient Bifunctional Electrocatalyst for Overall Water Splitting. **2020**, 1907556.
71. Yang, Y.; Zhang, K.; Lin, H.; Li, X.; Chan, H. C.; Yang, L.; Gao, Q., MoS2-Ni3S2 heteronanorods as efficient and stable bifunctional electrocatalysts for overall water splitting. *ACS Catal.* **2017,** *7* (4), 2357-2366.
72. Kang, Z.; Guo, H.; Wu, J.; Sun, X.; Zhang, Z.; Liao, Q.; Zhang, S.; Si, H.; Wu, P.; Wang, L.; Zhang, Y., Engineering an earth-abundant element-based bifunctional electrocatalyst for highly efficient and durable overall water splitting. *Adv. Funct. Mater.* **2019,** *29* (9), 1807031.
73. Guo, P.; Wang, Z.; Zhang, T.; Chen, C.; Chen, Y.; Liu, H.; Hua, M.; Wei, S.; Lu, X., Initiating an efficient electrocatalyst for water splitting via valence configuration of cobalt-iron oxide. *Appl. Catal. B* **2019,** *258*, 117968.
74. Tian, J.; Chen, J.; Liu, J.; Tian, Q.; Chen, P., Graphene quantum dot engineered nickel-cobalt phosphide as highly efficient bifunctional catalyst for overall water splitting. *Nano Energy* **2018,** *48*, 284-291.
75. Jin, R.; Huang, J.; Chen, G.; Chen, W.; Ouyang, B.; Chen, D.; Kan, E.; Zhu, H.; Li, C.; Yang, D., Water-sprouted, plasma-enhanced Ni-Co phospho-nitride nanosheets boost electrocatalytic hydrogen and oxygen evolution. *Chem. Eng. J.* **2020,** *402*, 126257.
76. Fei, H.; Dong, J.; Feng, Y.; Allen, C. S.; Wan, C.; Volosskiy, B.; Li, M.; Zhao, Z.; Wang, Y.; Sun, H.; An, P.; Chen, W.; Guo, Z.; Lee, C.; Chen, D.; Shakir, I.; Liu, M.; Hu, T.; Li, Y.; Kirkland, A. I.; Duan, X.; Huang, Y., General synthesis and definitive structural identification of MN4C4 single-atom catalysts with tunable electrocatalytic activities. *Nat. Catal.* **2018,** *1* (1), 63-72.
77. Wang, Q.; Shang, L.; Shi, R.; Zhang, X.; Zhao, Y.; Waterhouse, G. I. N.; Wu, L.-Z.; Tung, C.-H.; Zhang, T., NiFe layered double hydroxide nanoparticles on Co,N-codoped carbon nanoframes as efficient bifunctional catalysts for rechargeable zinc-air batteries. *Adv. Energ. Mater.* **2017,** *7* (21), 1700467.
78. Zhou, T.; Xu, W.; Zhang, N.; Du, Z.; Zhong, C.; Yan, W.; Ju, H.; Chu, W.; Jiang, H.; Wu, C.; Xie, Y., Ultrathin cobalt oxide layers as electrocatalysts for high‐performance flexible Zn-air batteries. *Adv. Mater.* **2019,** *31* (15), 1807468.
79. Li, Y.; Huang, B.; Sun, Y.; Luo, M.; Yang, Y.; Qin, Y.; Wang, L.; Li, C.; Lv, F.; Zhang, W.; Guo, S., Multimetal borides nanochains as efficient electrocatalysts for overall water splitting. *Small* **2019,** *15* (1), 1804212.
80. Yu, Z.-Y.; Duan, Y.; Gao, M.-R.; Lang, C.-C.; Zheng, Y.-R.; Yu, S.-H., A one-dimensional porous carbon-supported Ni/Mo2C dual catalyst for efficient water splitting. *Chem. Sci.* **2017,** *8* (2), 968-973.
81. Dinh, K. N.; Zheng, P.; Dai, Z.; Zhang, Y.; Dangol, R.; Zheng, Y.; Li, B.; Zong, Y.; Yan, Q., Ultrathin porous NiFeV ternary layer hydroxide nanosheets as a highly efficient bifunctional electrocatalyst for overall water splitting. *Small* **2018,** *14* (8), 1703257.

82. Hu, K.; Wu, M.; Hinokuma, S.; Ohto, T.; Wakisaka, M.; Fujita, J.-I.; Ito, Y., Boosting electrochemical water splitting via ternary NiMoCo hybrid nanowire arrays. *J. Mater. Chem. A* **2019,** *7* (5), 2156-2164.
83. Li, X.; Shang, X.; Zhang, X.-Y.; Dong, B.; Yan, K.-L.; Liu, Y.-R.; Han, G.-Q.; Chi, J.-Q.; Chai, Y.-M.; Liu, C.-G., Ni-Se nanostructrures dependent on different solvent as efficient electrocatalysts for hydrogen evolution reaction in alkaline media. *Mater. Chem. Phys.* **2018,** *207*, 389-395.
84. Xiao, K.; Zhou, L.; Shao, M.; Wei, M., Fabrication of (Ni,Co)0.85Se nanosheet arrays derived from layered double hydroxides toward largely enhanced overall water splitting. *J. Mater. Chem. A* **2018,** *6* (17), 7585-7591.
85. Sun, Y.-Y.; Jiang, M.-Y.; Wu, L.-K.; Hou, G.-Y.; Tang, Y.-P.; Liu, M., Ultra-thin NiFeSe nanosheets as a highly efficient bifunctional electrocatalyst for overall water splitting. *Sustain. Energ. Fuels* **2020**.
86. Chen, Y.; Dong, C.; Zhang, J.; Zhang, C.; Zhang, Z., Hierarchically porous Mo-doped Ni–Fe oxide nanowires efficiently catalyzing oxygen/hydrogen evolution reactions. *J. Mater. Chem. A* **2018,** *6* (18), 8430-8440.
87. Das, D.; Santra, S.; Nanda, K. K., In situ fabrication of a nickel/molybdenum carbide-anchored n-doped graphene/cnt hybrid: An efficient (pre)catalyst for oer and her. *ACS Appl. Mat. Interfaces* **2018,** *10* (41), 35025-35038.
88. Yan, G.; Zhang, X.; Xiao, L., Prussian blue analogues-derived bimetallic phosphide hollow nanocubes grown on Ni foam as water splitting electrocatalyst. *J Mater Sci* **2019,** *54* (9), 7087-7095.
89. Zhong, C.; Han, Z.; Wang, T.; Wang, Q.; Shen, Z.; Zhou, Q.; Wang, J.; Zhang, S.; Jin, X.; Li, S.; Wang, P.; Gao, D.; Zhou, Y.; Zhang, H., Aliovalent fluorine doping and anodization-induced amorphization enable bifunctional catalysts for efficient water splitting. *J. Mater. Chem. A* **2020,** *8* (21), 10831-10838.
90. Hu, E.; Feng, Y.; Nai, J.; Zhao, D.; Hu, Y.; Lou, X. W., Construction of hierarchical Ni-Co-P hollow nanobricks with oriented nanosheets for efficient overall water splitting. *Energy Environ. Sci.* **2018,** *11* (4), 872-880.
91. Babar, P.; Lokhande, A.; Shin, H. H.; Pawar, B.; Gang, M. G.; Pawar, S.; Kim, J. H., Cobalt iron hydroxide as a precious metal-free bifunctional electrocatalyst for efficient overall water splitting. *Small* **2018,** *14* (7), 1702568.
92. Zhu, Y. P.; Ma, T. Y.; Jaroniec, M.; Qiao, S. Z., Self-templating synthesis of hollow Co3O4 microtube arrays for highly efficient water electrolysis. *Angew. Chem. Int.* **2017,** *56* (5), 1324-1328.
93. Shi, H.; Liang, H.; Ming, F.; Wang, Z., Efficient overall water-splitting electrocatalysis using lepidocrocite VOOH hollow nanospheres. *Angew. Chem.* **2017,** *129* (2), 588-592.
94. Tang, T.; Jiang, W.-J.; Niu, S.; Liu, N.; Luo, H.; Chen, Y.-Y.; Jin, S.-F.; Gao, F.; Wan, L.-J.; Hu, J.-S., Electronic and morphological dual modulation of cobalt carbonate hydroxides by mn doping toward highly efficient and stable bifunctional electrocatalysts for overall water splitting. *J. Am. Chem. Soc.* **2017,** *139* (24), 8320-8328.
95. Tang, C.; Cheng, N.; Pu, Z.; Xing, W.; Sun, X. J. A. C., NiSe nanowire film supported on nickel foam: an efficient and stable 3D bifunctional electrode for full water splitting. **2015,** *127* (32), 9483-9487.

96. Zhu, Y.; Zhou, W.; Zhong, Y.; Bu, Y.; Chen, X.; Zhong, Q.; Liu, M.; Shao, Z., A perovskite nanorod as bifunctional electrocatalyst for overall water splitting. *Adv. Energy Mater.* **2017,** *7* (8), 1602122.
97. Yin, J.; Li, Y.; Lv, F.; Lu, M.; Sun, K.; Wang, W.; Wang, L.; Cheng, F.; Li, Y.; Xi, P.; Guo, S., Oxygen vacancies dominated Nis2/CoS2 interface porous nanowires for portable zn-air batteries driven water splitting devices. *Adv. Mater.* **2017,** *29* (47), 1704681.
98. Balogun, M.-S.; Qiu, W.; Huang, Y.; Yang, H.; Xu, R.; Zhao, W.; Li, G.-R.; Ji, H.; Tong, Y., Cost-effective alkaline water electrolysis based on nitrogen- and phosphorus-doped self-supportive electrocatalysts. *Adv. Mater.* **2017,** *29* (34), 1702095.
99. Shao, M., Palladium-based electrocatalysts for hydrogen oxidation and oxygen reduction reactions. *J. Power Sources* **2011,** *196* (5), 2433-2444.
100. Minke, C., Suermann, M., Bensmann, B. and Hanke-Rauschenbach, R., Is iridium demand a potential bottleneck in the realization of large-scale PEM water electrolysis? *International Journal of Hydrogen Energy*, **2021,** *46*(46), 23581-23590.
101. Li, W.; Gao, X.; Xiong, D.; Wei, F.; Song, W.-G.; Xu, J.; Liu, L., Hydrothermal synthesis of monolithic Co3Se4 nanowire electrodes for oxygen evolution and overall water splitting with high efficiency and extraordinary catalytic stability. *Adv. Energ. Mater.* **2017,** *7* (17), 1602579.
102. Suermann, M., Bensmann, B. and Hanke-Rauschenbach, R., Degradation of proton exchange membrane (PEM) water electrolysis cells: looking beyond the cell voltage increase. *Journal of The Electrochemical Society*, **2019,** *166*(10), p.F645.
103. Kang, Z.; Mo, J.; Yang, G.; Li, Y.; Talley, D. A.; Han, B.; Zhang, F.-Y., Performance Modeling and Current Mapping of Proton Exchange Membrane Electrolyzer Cells with Novel Thin/Tunable Liquid/Gas Diffusion Layers. *Electrochim Acta* **2017,** *255*, 405-416.
104. Solmaz, R.; Kardaş, G., Electrochemical deposition and characterization of NiFe coatings as electrocatalytic materials for alkaline water electrolysis. *Electrochim Acta* **2009,** *54* (14), 3726-3734.
105. Yang, G.; Yu, S.; Li, Y.; Li, K.; Ding, L.; Xie, Z.; Wang, W.; Dohrmann, Y.; Zhang, F.-Y., A simple convertible electrolyzer in membraneless and membrane-based modes for understanding water splitting mechanism. *J. Power Sources* **2021,** *487*, 229353.
106. Yang, G.; Yu, S.; Mo, J.; Li, Y.; Kang, Z.; Bender, G.; Pivovar, B. S.; Green, J. B.; Cullen, D. A.; Zhang, F.-Y., Impacts of catalyst nanolayers on water permeation and swelling of polymer electrolyte membranes. *J. Power Sources* **2020,** *448*, 227582.
107. Shao, M.; Merzougui, B.; Shoemaker, K.; Stolar, L.; Protsailo, L.; Mellinger, Z. J.; Hsu, I. J.; Chen, J. G., Tungsten carbide modified high surface area carbon as fuel cell catalyst support. *J. Power Sources* **2011,** *196* (18), 7426-7434.
108. Ren, J.; Antonietti, M.; Fellinger, T.-P., Efficient Water Splitting Using a Simple Ni/N/C Paper Electrocatalyst. *Adv. Energy Mater.* **2015,** *5* (6), 1401660.
109. Suen, N.-T.; Hung, S.-F.; Quan, Q.; Zhang, N.; Xu, Y.-J.; Chen, H. M., Electrocatalysis for the oxygen evolution reaction: recent development and future perspectives. *Chem Soc Rev* **2017,** *46* (2), 337-365.

110. Wei, W.; Cui, X.; Chen, W.; Ivey, D. G., Improved electrochemical impedance response induced by morphological and structural evolution in nanocrystalline MnO2 electrodes. *Electrochim Acta* **2009,** *54* (8), 2271-2275.
111. Tao, L. M.; Huang, M.; Guo, S. J.; Wang, Q. L.; Li, M.; Xiao, X.; Cao, G. Y.; Shao, Y.; Shen, Y.; Fu, Y. Q.; Wang, M. K., Surface modification of NiCo2Te4 nanoclusters: a highly efficient electrocatalyst for overall water-splitting in neutral solution. *Appl. Catal. B* **2019,** *254*, 424-431.
112. Li, P.; Duan, X.; Kuang, Y.; Li, Y.; Zhang, G.; Liu, W.; Sun, X., Tuning electronic structure of NiFe layered double hydroxides with vanadium doping toward high efficient electrocatalytic water oxidation. *Adv. Energ. Mater.* **2018,** *8* (15), 1703341.
113. Chen, G.; Wang, T.; Zhang, J.; Liu, P.; Sun, H.; Zhuang, X.; Chen, M.; Feng, X., Accelerated Hydrogen Evolution Kinetics on NiFe-Layered Double Hydroxide Electrocatalysts by Tailoring Water Dissociation Active Sites. *Adv Mater* **2018,** *30* (10), 1706279.
114. Bo, X.; Li, Y.; Hocking, R. K.; Zhao, C., NiFeCr Hydroxide Holey Nanosheet as Advanced Electrocatalyst for Water Oxidation. *ACS Appl. Mat. Interfaces* **2017,** *9* (47), 41239-41245.
115. Wang, A.-L.; Xu, H.; Li, G.-R., NiCoFe Layered Triple Hydroxides with Porous Structures as High-Performance Electrocatalysts for Overall Water Splitting. *ACS Energy Letters* **2016,** *1* (2), 445-453.
116. Qu, M.; Jiang, Y.; Yang, M.; Liu, S.; Guo, Q.; Shen, W.; Li, M.; He, R., Regulating electron density of NiFe-P nanosheets electrocatalysts by a trifle of Ru for high-efficient overall water splitting. *Appl. Catal. B* **2020,** *263*, 118324.
117. Liu, C.; Han, Y.; Yao, L.; Liang, L.; He, J.; Hao, Q.; Zhang, J.; Li, Y.; Liu, H., Engineering Bimetallic NiFe‐Based Hydroxides/Selenides Heterostructure Nanosheet Arrays for Highly‐Efficient Oxygen Evolution Reaction. *Small* **2021,** *17* (7), 2007334.
118. Jia, X.; Zhao, Y.; Chen, G.; Shang, L.; Shi, R.; Kang, X.; Waterhouse, G. I. N.; Wu, L.-Z.; Tung, C.-H.; Zhang, T., Ni3FeN Nanoparticles Derived from Ultrathin NiFe-Layered Double Hydroxide Nanosheets: An Efficient Overall Water Splitting Electrocatalyst. *Adv. Energy Mater.* **2016,** *6* (10), 1502585.
119. Demir, D. D.; Salcı, A.; Solmaz, R., Fabrication of Mo-modified carbon felt as candidate substrate for electrolysis: Optimization of pH, current and metal amount. *International Journal of Hydrogen Energy* **2018,** *43* (23), 10540-10548.
120. Demir, D. D.; Salcı, A.; Solmaz, R., Preparation, characterization and hydrogen production performance of MoPd deposited carbon felt/Mo electrodes. *International Journal of Hydrogen Energy* **2018,** *43* (23), 10530-10539.
121. Yang, R.; Zhou, Y.; Xing, Y.; Li, D.; Jiang, D.; Chen, M.; Shi, W.; Yuan, S., Synergistic coupling of CoFe-LDH arrays with NiFe-LDH nanosheet for highly efficient overall water splitting in alkaline media. *Appl. Catal. B* **2019,** *253*, 131-139.
122. Si, S.; Hu, H.-S.; Liu, R.-J.; Xu, Z.-X.; Wang, C.-B.; Feng, Y.-Y., Co-NiFe layered double hydroxide nanosheets as an efficient electrocatalyst for the electrochemical evolution of oxygen. *Internat. J. Hydrogen Energ.* **2020,** *45* (16), 9368-9379.

123. Xu, D.; Stevens, M. B.; Rui, Y.; Deluca, G.; Boettcher, S. W.; Reichmanis, E.; Li, Y.; Zhang, Q.; Wang, H., The role of Cr doping in NiFe oxide/(oxy)hydroxide electrocatalysts for oxygen evolution. *Electrochim. Acta* **2018,** *265*, 10-18.
124. Park, H. K.; Ahn, H.; Lee, T. H.; Lee, J. Y.; Lee, M. G.; Lee, S. A.; Yang, J. W.; Kim, S. J.; Ahn, S. H.; Kim, S. Y.; Lee, C. H.; Park, E. S.; Jang, H. W., Grain boundaries boost oxygen evolution reaction in NiFe electrocatalysts. *Small Methods* **2020**, 2000755.
125. Hsieh, C. T.; Chuah, X. F.; Huang, C. L.; Lin, H. W.; Chen, Y. A.; Lu, S. Y., NiFe/(Ni,Fe)3S2 core/shell nanowire arrays as outstanding catalysts for electrolytic water splitting at high current densities. *Small Methods* **2019,** *3* (10), 1900234.
126. Lu, X.; Zhao, C., Electrodeposition of hierarchically structured three-dimensional nickel-iron electrodes for efficient oxygen evolution at high current densities. *Nature Comm.* **2015,** *6* (1), 6616.
127. Hoang, T. T. H.; Gewirth, A. A., High activity oxygen evolution reaction catalysts from additive-controlled electrodeposited Ni and NiFe films. *ACS Catal.* **2016,** *6* (2), 1159-1164.
128. Nia, N. S.; Creus, J.; Feaugas, X.; Savall, C. J. J. o. a.; compounds, The effect of tungsten addition on metallurgical state and solute content in nanocrystalline electrodeposited nickel. **2014,** *609*, 296-301.
129. Nia, N. S.; Creus, J.; Feaugas, X.; Savall, C. J. A. S. S., Influence of metallurgical parameters on the electrochemical behavior of electrodeposited Ni and Ni–W nanocrystalline alloys. **2016,** *370*, 149-159.
130. Nia, N. S.; Savall, C.; Creus, J.; Bourgon, J.; Girault, P.; Metsue, A.; Cohendoz, S.; Feaugas, X. J. M. S.; A, E., On the implication of solute contents and grain boundaries on the Hall-Petch relationship of nanocrystalline Ni-W alloys. **2016,** *678*, 204-214.
131. Bo, X.; Li, Y.; Chen, X.; Zhao, C., Operando raman spectroscopy reveals Cr-induced-phase reconstruction of NiFe and CoFe oxyhydroxides for enhanced electrocatalytic water oxidation. *Chem. Mater.* **2020,** *32* (10), 4303-4311.
132. Li, Y.; Dastafkan, K.; Sun, Q.; Ma, Y.; Wang, X.; Yang, X.; Wang, Z.; Zhao, C., Ni-based 3D hierarchical heterostructures achieved by selective electrodeposition as a bifunctional electrocatalyst for overall water splitting. *Electrochim Acta* **2021,** *379*, 138042.
133. Hsieh, C.-T.; Huang, C.-L.; Chen, Y.-A.; Lu, S.-Y., NiFeMo alloy inverse-opals on Ni foam as outstanding bifunctional catalysts for electrolytic water splitting of ultra-low cell voltages at high current densities. *Appl. Catal. B* **2020,** *267*, 118376.
134. Kim, S. H.; Sohn, H. J.; Joo, Y. C.; Kim, Y. W.; Yim, T. H.; Lee, H. Y.; Kang, T., Effect of saccharin addition on the microstructure of electrodeposited Fe-36 wt.% Ni alloy. *Surf. Coat. Technol.* **2005,** *199* (1), 43-48.
135. Qian, G.; Yu, G.; Lu, J.; Luo, L.; Wang, T.; Zhang, C.; Ku, R.; Yin, S.; Chen, W.; Mu, S., Ultra-thin N-doped-graphene encapsulated Ni nanoparticles coupled with MoO2 nanosheets for highly efficient water splitting at large current density. *Journal of Materials Chemistry A* **2020,** *8* (29), 14545-14554.
136. Xiao, X.; He, C.-T.; Zhao, S.; Li, J.; Lin, W.; Yuan, Z.; Zhang, Q.; Wang, S.; Dai, L.; Yu, D., A general approach to cobalt-based homobimetallic phosphide ultrathin

nanosheets for highly efficient oxygen evolution in alkaline media. *Energy Environ. Sci.* **2017,** *10* (4), 893-899.
137. Huang, L.; Chen, D.; Luo, G.; Lu, Y. R.; Chen, C.; Zou, Y.; Dong, C. L.; Li, Y.; Wang, S., Zirconium‐regulation‐induced bifunctionality in 3D cobalt–iron oxide nanosheets for overall water splitting. *Adv. Mater.* **2019,** *31* (28), 1901439.
138. Chu, K.; Cheng, Y.-H.; Li, Q.-Q.; Liu, Y.-P.; Tian, Y., Fe-doping induced morphological changes, oxygen vacancies and Ce3+-Ce3+ pairs in CeO2 for promoting electrocatalytic nitrogen fixation. *J. Mater. Chem. A* **2020,** *8* (12), 5865-5873.
139. Ding, L.; Li, K.; Xie, Z.; Yang, G.; Yu, S.; Wang, W.; Yu, H.; Baxter, J.; Meyer, H. M.; Cullen, D. A.; Zhang, F.-Y., Constructing Ultrathin W-Doped NiFe Nanosheets via Facile Electrosynthesis as Bifunctional Electrocatalysts for Efficient Water Splitting. *ACS Appl. Mater. Interfaces* **2021**.
140. Shakibi Nia, N.; Hauser, D.; Schlicker, L.; Gili, A.; Doran, A.; Gurlo, A.; Penner, S.; Kunze‐Liebhäuser, J., Zirconium Oxycarbide: A Highly Stable Catalyst Material for Electrochemical Energy Conversion. *Chemphyschem* **2019,** *20* (22), 3067-3073.
141. Chen, G.-F.; Ma, T. Y.; Liu, Z.-Q.; Li, N.; Su, Y.-Z.; Davey, K.; Qiao, S.-Z., Efficient and stable bifunctional electrocatalysts Ni/NixMy (M=p, s) for overall water splitting. *Adv. Funct. Mater.* **2016,** *26* (19), 3314-3323.
142. Anjum, M. A. R.; Lee, J. S., Sulfur and Nitrogen Dual-Doped Molybdenum Phosphide Nanocrystallites as an Active and Stable Hydrogen Evolution Reaction Electrocatalyst in Acidic and Alkaline Media. *ACS Catal.* **2017,** *7* (4), 3030-3038.
143. Rasten, E.; Hagen, G.; Tunold, R., Electrocatalysis in water electrolysis with solid polymer electrolyte. *Electrochim Acta* **2003,** *48* (25-26), 3945-3952.
144. Ge, J.; Zheng, J. Y.; Zhang, J.; Jiang, S.; Zhang, L.; Wan, H.; Wang, L.; Ma, W.; Zhou, Z.; Ma, R., Controllable atomic defect engineering in layered NixFe1−x(OH)2 nanosheets for electrochemical overall water splitting. *Journal of Materials Chemistry A* **2021,** *9* (25), 14432-14443.
145. Yang, Y.; Lin, Z.; Gao, S.; Su, J.; Lun, Z.; Xia, G.; Chen, J.; Zhang, R.; Chen, Q., Tuning Electronic Structures of Nonprecious Ternary Alloys Encapsulated in Graphene Layers for Optimizing Overall Water Splitting Activity. *ACS Catal.* **2017,** *7* (1), 469-479.
146. Tang, Y.; Fang, X.; Zhang, X.; Fernandes, G.; Yan, Y.; Yan, D.; Xiang, X.; He, J., Space-Confined Earth-Abundant Bifunctional Electrocatalyst for High-Efficiency Water Splitting. *ACS Appl. Mat. Interfaces* **2017,** *9* (42), 36762-36771.
147. Liu, Y.; Jiang, S.; Li, S.; Zhou, L.; Li, Z.; Li, J.; Shao, M., Interface engineering of (Ni, Fe)S2@MoS2 heterostructures for synergetic electrochemical water splitting. *Appl. Catal. B* **2019,** *247*, 107-114.
148. Jiang, Y.; Lu, Y.; Lin, J.; Wang, X.; Shen, Z., A Hierarchical MoP Nanoflake Array Supported on Ni Foam: A Bifunctional Electrocatalyst for Overall Water Splitting. *Small Methods* **2018,** *2* (5), 1700369.
149. Li, H.; Wen, P.; Li, Q.; Dun, C.; Xing, J.; Lu, C.; Adhikari, S.; Jiang, L.; Carroll, D. L.; Geyer, S. M., Earth-Abundant Iron Diboride (FeB2) Nanoparticles as Highly Active Bifunctional Electrocatalysts for Overall Water Splitting. *Adv. Energy Mater.* **2017,** *7* (17), 1700513.

150. Song, F.; Hu, X., Exfoliation of layered double hydroxides for enhanced oxygen evolution catalysis. *Nature Comm.* **2014,** *5* (1).
151. Cai, G.; Zhang, W.; Jiao, L.; Yu, S.-H.; Jiang, H.-L., Template-Directed Growth of Well-Aligned MOF Arrays and Derived Self-Supporting Electrodes for Water Splitting. *Chem* **2017,** *2* (6), 791-802.
152. Chen, Z.; Waje, M.; Li, W.; Yan, Y., Supportless Pt and PtPd Nanotubes as Electrocatalysts for Oxygen-Reduction Reactions. *Angew. Chem., Int. Ed. Engl.* **2007,** *46* (22), 4060-4063.
153. Lu, Q.; Hutchings, G. S.; Yu, W.; Zhou, Y.; Forest, R. V.; Tao, R.; Rosen, J.; Yonemoto, B. T.; Cao, Z.; Zheng, H.; Xiao, J. Q.; Jiao, F.; Chen, J. G., Highly porous non-precious bimetallic electrocatalysts for efficient hydrogen evolution. *Nat. Commun* **2015,** *6* (1), 6567.
154. Xu, X.; Chen, Y.; Zhou, W.; Zhu, Z.; Su, C.; Liu, M.; Shao, Z., A perovskite electrocatalyst for efficient hydrogen evolution reaction. *Adv. Mater.* **2016,** *28* (30), 6442-6448.
155. Wang, W.; Xie, Z.; Li, K.; Yu, S.; Ding, L.; Zhang, F.-Y., Recent progress in in-situ visualization of electrochemical reactions in electrochemical energy devices. *Curr. Opin. Electrochem.* **2022**, 101088.
156. Garcia-Navarro, J.; Schulze, M.; Friedrich, K. A., Understanding the Role of Water Flow and the Porous Transport Layer on the Performance of Proton Exchange Membrane Water Electrolyzers. *ACS Sustain. Chem. Eng.* **2019,** *7* (1), 1600-1610.
157. Acar, C.; Dincer, I., The potential role of hydrogen as a sustainable transportation fuel to combat global warming. *Int J Hydrogen Energ* **2020,** *45* (5), 3396-3406.
158. Garcia, G.; Arriola, E.; Chen, W.-H.; De Luna, M. D., A comprehensive review of hydrogen production from methanol thermochemical conversion for sustainability. *Energy* **2021,** *217*, 119384.
159. Chen, Z.; Yun, S.; Wu, L.; Zhang, J.; Shi, X.; Wei, W.; Liu, Y.; Zheng, R.; Han, N.; Ni, B.-J., Waste-Derived Catalysts for Water Electrolysis: Circular Economy-Driven Sustainable Green Hydrogen Energy. *Nano-Micro Lett.* **2023,** *15* (1).
160. Ding, L.; Wang, W.; Xie, Z.; Li, K.; Yu, S.; Capuano, C. B.; Keane, A.; Ayers, K.; Zhang, F.-Y., Highly Porous Iridium Thin Electrodes with Low Loading and Improved Reaction Kinetics for Hydrogen Generation in PEM Electrolyzer Cells. *ACS Applied Materials & Interfaces* **2023,** *15* (20), 24284-24295.
161. Carmo, M.; Fritz, D. L.; Merge, J.; Stolten, D., A comprehensive review on PEM water electrolysis. *Int J Hydrogen Energ* **2013,** *38* (12), 4901-4934.
162. Rashid, M.; Al Mesfer, M. K.; Naseem, H.; Danish, M., Hydrogen production by water electrolysis: a review of alkaline water electrolysis, PEM water electrolysis and high temperature water electrolysis. *Int. j. eng. adv. technol.* **2015,** *4* (3), 2249 – 8958.
163. Li, K.; Yu, S.; Li, D.; Ding, L.; Wang, W.; Xie, Z.; Park, E. J.; Fujimoto, C.; Cullen, D. A.; Kim, Y. S., Engineered Thin Diffusion Layers for Anion-Exchange Membrane Electrolyzer Cells with Outstanding Performance. *ACS Appl. Mater. Interfaces* **2021,** *13* (43), 50957-50964.
164. Ju, W.; Heinz, M. V. F.; Pusterla, L.; Hofer, M.; Fumey, B.; Castiglioni, R.; Pagani, M.; Battaglia, C.; Vogt, U. F., Lab-Scale Alkaline Water Electrolyzer for Bridging

Material Fundamentals with Realistic Operation. *ACS Sustain. Chem. Eng.* **2018,** *6* (4), 4829-4837.
165. Sankar, S.; Roby, S.; Kuroki, H.; Miyanishi, S.; Tamaki, T.; Anilkumar, G. M.; Yamaguchi, T., High-Performing Anion Exchange Membrane Water Electrolysis Using Self-Supported Metal Phosphide Anode Catalysts and an Ether-Free Aromatic Polyelectrolyte. *ACS Sustain. Chem. Eng.* **2023,** *11* (3), 854-865.
166. Yan, Y.; Chen, Y.; Shao, M.; Chen, X.; Yang, Z.; Wang, J.; Chen, H.; Ni, L.; Diao, G.; Chen, M., Construction of Ultrathin Cobalt-Based Nanosheet Arrays on Titanium Mesh as Asymmetric Electrodes for Overall Water Splitting. *ACS Sustain. Chem. Eng.* **2023,** *11* (6), 2499-2510.
167. Grigoriev, S.; Fateev, V.; Bessarabov, D.; Millet, P., Current status, research trends, and challenges in water electrolysis science and technology. *Int. J. Hydrog. Energy.* **2020,** *45* (49), 26036-26058.
168. Ursua, A., Gandia, L.M. and Sanchis, P., Hydrogen production from water electrolysis: current status and future trends. Proceedings of the IEEE, **2011,** 100 (2), 410-426.
169. Xie, Z.; Yu, S.; Ma, X.; Li, K.; Ding, L.; Wang, W.; Cullen, D. A.; Meyer III, H. M.; Yu, H.; Tong, J., MoS2 nanosheet integrated electrodes with engineered 1T-2H phases and defects for efficient hydrogen production in practical PEM electrolysis. *Appl. Catal. B: Environ.* **2022,** *313*, 121458.
170. Ettingshausen, F.; Kleemann, J.; Marcu, A.; Toth, G.; Fuess, H.; Roth, C., Dissolution and migration of platinum in PEMFCs investigated for start/stop cycling and high potential degradation. *Fuel Cells* **2011,** *11* (2), 238-245.
171. Yang, G.; Xie, Z.; Yu, S.; Li, K.; Li, Y.; Ding, L.; Wang, W.; Zhang, F.-Y., All-In-One Bipolar Electrode: A New Concept For Compact And Efficient Water Electrolyzers. *Nano Energy* **2021,** *90*, 106551.
172. Stiber, S.; Balzer, H.; Wierhake, A.; Wirkert, F. J.; Roth, J.; Rost, U.; Brodmann, M.; Lee, J. K.; Bazylak, A.; Waiblinger, W., Porous transport layers for proton exchange membrane electrolysis under extreme conditions of current density, temperature, and pressure. *Advanced Energy Materials* **2021,** *11* (33), 2100630.
173. Siracusano, S.; Trocino, S.; Briguglio, N.; Pantò, F.; Aricò, A. S., Analysis of performance degradation during steady-state and load-thermal cycles of proton exchange membrane water electrolysis cells. *Journal of Power Sources* **2020,** *468*, 228390.
174. Bernt, M.; Siebel, A.; Gasteiger, H. A., Analysis of voltage losses in PEM water electrolyzers with low platinum group metal loadings. *J Electrochem Soc* **2018,** *165* (5), F305.
175. Lickert, T.; Kiermaier, M. L.; Bromberger, K.; Ghinaiya, J.; Metz, S.; Fallisch, A.; Smolinka, T., On the influence of the anodic porous transport layer on PEM electrolysis performance at high current densities. *Int J Hydrogen Energ* **2020,** *45* (11), 6047-6058.
176. Alia, S. M.; Reeves, K. S.; Baxter, J. S.; Cullen, D. A., The impact of ink and spray variables on catalyst layer properties, electrolyzer performance, and electrolyzer durability. *J Electrochem Soc* **2020,** *167* (14), 144512.
177. Park, J.; Kang, Z.; Bender, G.; Ulsh, M.; Mauger, S. A., Roll-to-roll production of catalyst coated membranes for low-temperature electrolyzers. *Journal of Power Sources* **2020,** *479*, 228819.

178. Pham, C. V.; Escalera‐López, D.; Mayrhofer, K.; Cherevko, S.; Thiele, S., Essentials of High Performance Water Electrolyzers–From Catalyst Layer Materials to Electrode Engineering. *Advanced Energy Materials* **2021,** *11* (44), 2101998.
179. Ding, L.; Xie, Z.; Yu, S.; Wang, W.; Terekhov, A. Y.; Canfield, B. K.; Capuano, C. B.; Keane, A.; Ayers, K.; Cullen, D. A.; Zhang, F.-Y., Electrochemically Grown Ultrathin Platinum Nanosheet Electrodes with Ultralow Loadings for Energy-Saving and Industrial-Level Hydrogen Evolution. *Nano-Micro Letters* **2023,** *15* (1).
180. Xie, Z.; Yu, S.; Yang, G.; Li, K.; Ding, L.; Wang, W.; Zhang, F.-Y., Optimization of catalyst-coated membranes for enhancing performance in proton exchange membrane electrolyzer cells. *Internat. J. Hydrogen Energ.* **2020**.
181. Mo, J.; Yang, G.; Li, Y.; Kang, Z.; Bender, G.; Pivovar, B. S.; Green Jr, J. B.; Zhang, F.-Y., Experimental studies on the effects of sheet resistance and wettability of catalyst layer on electro-catalytic activities for oxygen evolution reaction in proton exchange membrane electrolysis cells. *International Journal of Hydrogen Energy* **2020,** *45* (51), 26595-26603.
182. Lamy, C.; Millet, P., A critical review on the definitions used to calculate the energy efficiency coefficients of water electrolysis cells working under near ambient temperature conditions. *Journal of Power Sources* **2020,** *447*, 227350.
183. Ioroi, T.; Kitazawa, N.; Yasuda, K.; Yamamoto, Y.; Takenaka, H., IrO2-deposited Pt electrocatalysts for unitized regenerative polymer electrolytefuel cells. *J Solid State Electrochem.* **2001,** *31* (11), 1179-1183.
184. Ioroi, T.; Kitazawa, N.; Yasuda, K.; Yamamoto, Y.; Takenaka, H., Iridium oxide/platinum electrocatalysts for unitized regenerative polymer electrolyte fuel cells. *J. Electrochem. Soc.* **2000,** *147* (6), 2018.
185. Kang, Z.; Yu, S.; Yang, G.; Li, Y.; Bender, G.; Pivovar, B. S.; Green, J. B.; Zhang, F.-Y., Performance improvement of proton exchange membrane electrolyzer cells by introducing in-plane transport enhancement layers. *Electrochim. Acta* **2019,** *316*, 43-51.
186. Yang, G.; Mo, J.; Kang, Z.; Dohrmann, Y.; List III, F. A.; Green Jr, J. B.; Babu, S. S.; Zhang, F.-Y., Fully printed and integrated electrolyzer cells with additive manufacturing for high-efficiency water splitting. *Appl. Energy* **2018,** *215*, 202-210.
187. Wang, W.; Yu, S.; Li, K.; Ding, L.; Xie, Z.; Li, Y.; Yang, G.; Cullen, D. A.; Yu, H.; Kang, Z., Insights into the rapid two-phase transport dynamics in different structured porous transport layers of water electrolyzers through high-speed visualization. *J. Power Sources* **2021,** *516*, 230641.
188. Kang, Z.; Alia, S. M.; Young, J. L.; Bender, G., Effects of various parameters of different porous transport layers in proton exchange membrane water electrolysis. *Electrochim. Acta* **2020,** *354*, 136641.
189. Gonçalves, J.M., Martins, P.R., Araki, K. and Angnes, L., Recent progress in water splitting and hybrid supercapacitors based on nickel-vanadium layered double hydroxides. *Journal of Energy Chemistry*, **2021,** *57*, 496-515.
190. Ding, L.; Li, K.; Xie, Z.; Yang, G.; Yu, S.; Wang, W.; Cullen, D. A.; Yu, H.; Zhang, F.-Y., W-induced morphological modification of NiFe layered double hydroxides as efficient electrocatalysts for overall water splitting. *Electrochim. Acta* **2021**, 139199.

191. Wu, X.; Chen, J.; Wen, Z., Promotion for Full Water Splitting toward Vanadium-Incorporated MoO2–MoNi4 Hybrid Nanoarrays. *ACS Sustain. Chem. Eng.* **2021,** *9* (39), 13225-13232.
192. Li, H.; Wu, X.; Wang, P.; Song, S.; He, M.; Li, C.; Wang, W.; Fang, Z.; Yuan, X.; Song, W.; Li, Z., Interface Engineering of Hollow CoO/Co4S3@CoO/Co4S3 Heterojunction for Highly Stable and Efficient Electrocatalytic Overall Water Splitting. *ACS Sustain. Chem. Eng.* **2022,** *10* (39), 13112-13124.
193. Li, K.; Ding, L.; Xie, Z.; Yang, G.; Yu, S.; Wang, W.; Cullen, D. A.; Meyer, H. M.; Hu, G.; Ganesh, P.; Watkins, T. R.; Zhang, F.-Y., Robust Copper-Based Nanosponge Architecture Decorated by Ruthenium with Enhanced Electrocatalytic Performance for Ambient Nitrogen Reduction to Ammonia. *ACS Sustain. Chem. Eng.* **2023**.
194. Macdonald, J. R.; Barsoukov, E., Impedance spectroscopy: theory, experiment, and applications. John Wiley & Sons: 2018.
195. Van Pham, C.; Bühler, M.; Knöppel, J.; Bierling, M.; Seeberger, D.; Escalera-López, D.; Mayrhofer, K. J.; Cherevko, S.; Thiele, S., IrO2 coated TiO2 core-shell microparticles advance performance of low loading proton exchange membrane water electrolyzers. *Appl. Catal. B: Environ.* **2020,** *269*, 118762.
196. Wang, L.; Saveleva, V. A.; Zafeiratos, S.; Savinova, E. R.; Lettenmeier, P.; Gazdzicki, P.; Gago, A. S.; Friedrich, K. A., Highly active anode electrocatalysts derived from electrochemical leaching of Ru from metallic Ir 0.7 Ru 0.3 for proton exchange membrane electrolyzers. *Nano Energy* **2017,** *34*, 385-391.
197. Böhm, D.; Beetz, M.; Gebauer, C.; Bernt, M.; Schroeter, J.; Kornherr, M.; Zoller, F.; Bein, T.; Fattakhova-Rohlfing, D., Highly conductive titania supported iridium oxide nanoparticles with low overall iridium density as OER catalyst for large-scale PEM electrolysis. *Appl. Mater. Today* **2021,** *24*, 101134.
198. Kang, Y.; Jiang, B.; Malgras, V.; Guo, Y.; Cretu, O.; Kimoto, K.; Ashok, A.; Wan, Z.; Li, H.; Sugahara, Y., Heterostructuring mesoporous 2D iridium nanosheets with amorphous nickel boron oxide layers to improve electrolytic water splitting. *Small Methods* **2021,** *5* (10), 2100679.
199. Retuerto, M.; Pascual, L.; Torrero, J.; Salam, M. A.; Tolosana-Moranchel, Á.; Gianolio, D.; Ferrer, P.; Kayser, P.; Wilke, V.; Stiber, S., Highly active and stable OER electrocatalysts derived from Sr2MIrO6 for proton exchange membrane water electrolyzers. *Nat. Commun* **2022,** *13* (1), 7935.
200. Lim, J.; Kang, G.; Lee, J. W.; Jeon, S. S.; Jeon, H.; Kang, P. W.; Lee, H., Amorphous Ir atomic clusters anchored on crystalline IrO2 nanoneedles for proton exchange membrane water oxidation. *J. Power Sources* **2022,** *524*, 231069.
201. Oh, H.-S.; Nong, H. N.; Reier, T.; Gliech, M.; Strasser, P., Oxide-supported Ir nanodendrites with high activity and durability for the oxygen evolution reaction in acid PEM water electrolyzers. *Chem. Sci.* **2015,** *6* (6), 3321-3328.
202. Honsho, Y.; Nagayama, M.; Matsuda, J.; Ito, K.; Sasaki, K.; Hayashi, A. J. J. o. P. S., Durability of PEM water electrolyzer against wind power voltage fluctuation. **2023,** *564*, 232826.
203. Sánchez Batalla, B.; Laube, A.; Hofer, A.; Struckmann, T.; Bachmann, J.; Weidlich, C., Degradation studies of proton exchange membrane water electrolysis cells

with low platinum group metals – Catalyst coating achieved by atomic layer deposition. *International Journal of Hydrogen Energy* **2022,** *47* (94), 39719-39730.
204. Feng, Q.; Xiong, Y.; Xie, L.; Zhang, Z.; Lu, X.; Wang, Y.; Yuan, X.-Z.; Fan, J.; Li, H.; Wang, H., Tungsten Carbide Encapsulated in Grape-Like N-Doped Carbon Nanospheres: One-Step Facile Synthesis for Low-Cost and Highly Active Electrocatalysts in Proton Exchange Membrane Water Electrolyzers. *ACS Appl. Mater. Interfaces* **2019,** *11* (28), 25123-25132.
205. Jiang, G.; Yu, H.; Li, Y.; Yao, D.; Chi, J.; Sun, S.; Shao, Z., Low-Loading and Highly Stable Membrane Electrode Based on an Ir@WOxNR Ordered Array for PEM Water Electrolysis. *ACS Appl. Mater. Interfaces* **2021,** *13* (13), 15073-15082.
206. Ao, X.; Zhang, W.; Zhao, B.; Ding, Y.; Nam, G.; Soule, L.; Abdelhafiz, A.; Wang, C.; Liu, M., Atomically dispersed Fe–N–C decorated with Pt-alloy core–shell nanoparticles for improved activity and durability towards oxygen reduction. *Energy Environ. Sci.* **2020,** *13* (9), 3032-3040.
207. Han, M.; Wang, N.; Zhang, B.; Xia, Y.; Li, J.; Han, J.; Yao, K.; Gao, C.; He, C.; Liu, Y.; Wang, Z.; Seifitokaldani, A.; Sun, X.; Liang, H., High-Valent Nickel Promoted by Atomically Embedded Copper for Efficient Water Oxidation. *ACS Catal.* **2020,** *10* (17), 9725-9734.
208. Mandal, M.; Moore, M.; Secanell, M., Measurement of the Protonic and Electronic Conductivities of PEM Water Electrolyzer Electrodes. *ACS Appl. Mater. Interfaces* **2020,** *12* (44), 49549-49562.
209. Nørskov, J. K.; Bligaard, T.; Logadottir, A.; Kitchin, J. R.; Chen, J. G.; Pandelov, S.; Stimming, U., Trends in the Exchange Current for Hydrogen Evolution. *J. Electrochem. Soc.* **2005,** *152* (3), J23.
210. Ahn, W.; Park, M. G.; Lee, D. U.; Seo, M. H.; Jiang, G.; Cano, Z. P.; Hassan, F. M.; Chen, Z., Hollow multivoid nanocuboids derived from ternary Ni–Co–Fe Prussian blue analog for dual‐electrocatalysis of oxygen and hydrogen evolution reactions. *Adv. Funct. Mater.* **2018,** *28* (28), 1802129.
211. Wang, X.; Zhang, Y.; Li, J.; Liu, G.; Gao, M.; Ren, S.; Liu, B.; Zhang, L.; Han, G.; Yu, J., Platinum Cluster/Carbon Quantum Dots Derived Graphene Heterostructured Carbon Nanofibers for Efficient and Durable Solar‐Driven Electrochemical Hydrogen Evolution. *Small Methods* **2022,** *6* (4), 2101470.
212. Lee, J. K.; Lee, C.; Fahy, K. F.; Kim, P. J.; Krause, K.; Lamanna, J. M.; Baltic, E.; Jacobson, D. L.; Hussey, D. S.; Bazylak, A., Accelerating Bubble Detachment in Porous Transport Layers with Patterned Through-Pores. *ACS Appl. Mater. Interfaces* **2020,** *3* (10), 9676-9684.
213. Yu, S.; Xie, Z.; Li, K.; Ding, L.; Wang, W.; Yang, G.; Zhang, F.-Y., Morphology Engineering of Iridium Electrodes via Modifying Titanium Substrates with Controllable Pillar Structures for Highly Efficient Oxygen Evolution Reaction. *Electrochim. Acta* **2021**, 139797.
214. Cao, L.; Scheiba, F.; Roth, C.; Schweiger, F.; Cremers, C.; Stimming, U.; Fuess, H.; Chen, L.; Zhu, W.; Qiu, X., Novel nanocomposite Pt/RuO2· x H2O/carbon nanotube catalysts for direct methanol fuel cells. *Angew. Chem. Int. Ed.* **2006,** *45* (32), 5315-5319.

215. Ferrero, D. and Santarelli, M., Investigation of a novel concept for hydrogen production by PEM water electrolysis integrated with multi-junction solar cells. *Energy conversion and management*, **2017,** *148*, 16-29.
216. Thomassen, M. S.; Reksten, A. H.; Barnett, A. O.; Khoza, T.; Ayers, K., PEM water electrolysis. In Electrochemical Power Sources: Fundamentals, Systems, and Applications, Elsevier: 2022; pp 199-228.
217. Ayers, K., The potential of proton exchange membrane–based electrolysis technology. *Curr. Opin. Electrochem.* **2019,** *18*, 9-15.
218. Liu, Y.; Huang, S.; Wang, D.; Zhang, H.; Shan, D.; Peng, S.; Shen, G.; Wang, L.; Wang, X.; Interfaces, Modifying Ti-Based Gas Diffusion Layer Passivation for Polymer Electrolyte Membrane Water Electrolysis via Electrochemical Nitridation. *ACS Appl. Mat. Interfaces* **2022,** *14* (13), 15728-15735.
219. Lim, B. H.; Majlan, E. H.; Tajuddin, A.; Husaini, T.; Daud, W. R. W.; Radzuan, N. A. M.; Haque, M. A., Comparison of catalyst-coated membranes and catalyst-coated substrate for PEMFC membrane electrode assembly: A review. *Chin. J. Chem. Eng.* **2021,** *33*, 1-16.
220. Maier, M., Smith, K., Dodwell, J., Hinds, G., Shearing, P.R. and Brett, D.J.L., Mass transport in PEM water electrolysers: A review. *International Journal of Hydrogen Energy*, **2022,** *47* (1), 30-56.
221. Li, Y.; Yang, G.; Yu, S.; Mo, J.; Li, K.; Xie, Z.; Ding, L.; Wang, W.; Zhang, F.-Y., High-speed characterization of two-phase flow and bubble dynamics in titanium felt porous media for hydrogen production. *Electrochim Acta* **2021,** *370*, 137751.
222. Li, Y.; Yang, G.; Yu, S.; Kang, Z.; Mo, J.; Han, B.; Talley, D. A.; Zhang, F.-Y., In-situ investigation and modeling of electrochemical reactions with simultaneous oxygen and hydrogen microbubble evolutions in water electrolysis. *International Journal of Hydrogen Energy* **2019,** *44* (52), 28283-28293.
223. Wang, W.; Li, K.; Ding, L.; Yu, S.; Xie, Z.; Cullen, D. A.; Yu, H.; Bender, G.; Kang, Z.; Wrubel, J. A.; Ma, Z.; Capuano, C. B.; Keane, A.; Ayers, K.; Zhang, F.-Y., Exploring the Impacts of Conditioning on Proton Exchange Membrane Electrolyzers by In Situ Visualization and Electrochemistry Characterization. *ACS Applied Materials & Interfaces* **2022,** *14* (7), 9002-9012.
224. Li, G.; Li, K.; Yang, L.; Chang, J.; Ma, R.; Wu, Z.; Ge, J.; Liu, C.; Xing, W.; Boosted performance of Ir species by employing TiN as the support toward oxygen evolution reaction. *ACS Appl. Mat. Interfaces* **2018,** *10* (44), 38117-38124.
225. Spöri, C.; Briois, P.; Nong, H. N.; Reier, T.; Billard, A.; Kühl, S.; Teschner, D.; Strasser, P., Experimental activity descriptors for iridium-based catalysts for the electrochemical oxygen evolution reaction (OER). *ACS Catal.* **2019,** *9* (8), 6653-6663.
226. Yang, L.; Zhang, K.; Chen, H.; Shi, L.; Liang, X.; Wang, X.; Liu, Y.; Feng, Q.; Liu, M.; Zou, X., An ultrathin two-dimensional iridium-based perovskite oxide electrocatalyst with highly efficient {001} facets for acidic water oxidation. *J. Energy Chem.* **2022,** *66*, 619-627.
227. Zhang, S.; Zhang, X.; Shi, X.; Zhou, F.; Wang, R.; Li, X., Facile fabrication of ultrafine nickel-iridium alloy nanoparticles/graphene hybrid with enhanced mass activity and stability for overall water splitting. *J. Energy Chem.* **2020,** *49*, 166-173.

228. Tan, X.; Shen, J.; Semagina, N.; Secanell, M., Decoupling structure-sensitive deactivation mechanisms of Ir/IrOx electrocatalysts toward oxygen evolution reaction. *J. Catal.* **2019,** *371*, 57-70.
229. Yang, L.; Yu, G.; Ai, X.; Yan, W.; Duan, H.; Chen, W.; Li, X.; Wang, T.; Zhang, C.; Huang, X.; Chen, J.-S.; Zou, X., Efficient oxygen evolution electrocatalysis in acid by a perovskite with face-sharing IrO6 octahedral dimers. *Nature Comm.* **2018,** *9* (1).
230. Siracusano, S.; Trocino, S.; Briguglio, N.; Baglio, V.; Aricò, A., Electrochemical Impedance Spectroscopy as a Diagnostic Tool in Polymer Electrolyte Membrane Electrolysis. *Materials* **2018,** *11* (8), 1368.
231. Kang, Z.; Yang, G.; Mo, J.; Yu, S.; Cullen, D. A.; Retterer, S. T.; Toops, T. J.; Brady, M. P.; Bender, G.; Pivovar, B. S., Developing titanium micro/nano porous layers on planar thin/tunable LGDLs for high-efficiency hydrogen production. *Int. J. Hydrog. Energy.* **2018,** *43* (31), 14618-14628.
232. Hirschorn, B.; Orazem, M. E.; Tribollet, B.; Vivier, V.; Frateur, I.; Musiani, M. J. E. a., Determination of effective capacitance and film thickness from constant-phase-element parameters. **2010,** *55* (21), 6218-6227.
233. Bessarabov, D.; Wang, H.; Li, H.; Zhao, N., PEM electrolysis for hydrogen production: principles and applications. CRC press: 2016.
234. Lv, H.; Wang, S.; Li, J.; Shao, C.; Zhou, W.; Shen, X.; Xue, M.; Zhang, C., Self-assembled RuO2@IrOx core-shell nanocomposite as high efficient anode catalyst for PEM water electrolyzer. *Appl. Surf. Sci* **2020,** *514*, 145943.
235. Lv, H.; Wang, S.; Hao, C.; Zhou, W.; Li, J.; Xue, M.; Zhang, C., Oxygen‐Deficient Ti0. 9Nb0. 1O2‐x as an Efficient Anodic Catalyst Support for PEM Water Electrolyzer. *ChemCatChem* **2019,** *11* (10), 2511-2519.
236. Wang, S.; Lv, H.; Tang, F.; Sun, Y.; Ji, W.; Zhou, W.; Shen, X.; Zhang, C., Defect engineering assisted support effect:IrO2/N defective g-C3N4 composite as highly efficient anode catalyst in PEM water electrolysis. *Chem. Eng. Sci.* **2021,** *419*, 129455.
237. Baik, C.; Lee, S. W.; Pak, C., Glycine-induced ultrahigh-surface-area IrO2@ IrOx catalyst with balanced activity and stability for efficient water splitting. *Electrochim. Acta* **2021,** *390*, 138885.
238. Jiang, G.; Yu, H.; Hao, J.; Chi, J.; Fan, Z.; Yao, D.; Qin, B.; Shao, Z., An effective oxygen electrode based on Ir0. 6Sn0. 4O2 for PEM water electrolyzers. *J. Energy Chem.* **2019,** *39*, 23-28.
239. Taie, Z.; Peng, X.; Kulkarni, D.; Zenyuk, I. V.; Weber, A. Z.; Hagen, C.; Danilovic, N., Pathway to Complete Energy Sector Decarbonization with Available Iridium Resources using Ultralow Loaded Water Electrolyzers. *ACS Appl. Mater. Interfaces* **2020,** *12* (47), 52701-52712.
240. Alia, S. M.; Stariha, S.; Borup, R. L., Electrolyzer durability at low catalyst loading and with dynamic operation. *J. Electrochem. Soc.* **2019,** *166* (15), F1164.
241. Yu, H.; Danilovic, N.; Wang, Y.; Willis, W.; Poozhikunnath, A.; Bonville, L.; Capuano, C.; Ayers, K.; Maric, R., Nano-size IrOx catalyst of high activity and stability in PEM water electrolyzer with ultra-low iridium loading. *Appl. Catal. B: Environ.* **2018,** *239*, 133-146.

242. Grigoriev, S.A., Fateev, V.N., Bessarabov, D.G. and Millet, P., Current status, research trends, and challenges in water electrolysis science and technology. *International Journal of Hydrogen Energy*, **2020,** *45* (49), 26036-26058.
243. Kang, Z.; Chen, Y.; Wang, H.; Alia, S. M.; Pivovar, B. S.; Bender, G., Discovering and Demonstrating a Novel High-Performing 2D-Patterned Electrode for Proton-Exchange Membrane Water Electrolysis Devices. *ACS Appl. Mater. Interfaces* **2022**.
244. George, J. E.; Chidangil, S.; George, S. D., Recent progress in fabricating superaerophobic and superaerophilic surfaces. *Advanced Materials Interfaces* **2017,** *4* (9), 1601088.
245. Nie, N.; Zhang, D.; Wang, Z.; Ge, S.; Gu, Y.; Yang, B.; Lai, J.; Wang, L., Stable p-block metals electronic perturbation in PtM@CNT (M=Ga, In, Pb and Bi) for acidic seawater hydrogen production at commercial current densities. *Applied Catalysis B: Environmental* **2023,** *322*, 122100.
246. Grigoriev, S.A., Fateev, V.N., Bessarabov, D.G. and Millet, P., Current status, research trends, and challenges in water electrolysis science and technology. International Journal of Hydrogen Energy, **2020,** 45 (49), 26036-26058.
247. Chi, J. and Yu, H., Water electrolysis based on renewable energy for hydrogen production. Chinese Journal of Catalysis, **2018,** 39 (3), 390-394.
248. Yu, J., Li, Q., Li, Y., Xu, C.Y., Zhen, L., Dravid, V.P. and Wu, J., Ternary metal phosphide with triple-layered structure as a low-cost and efficient electrocatalyst for bifunctional water splitting. *Advanced Functional Materials*, **2016,** *26* (42), 7644-7651.
249. Yu, H.; Bonville, L.; Jankovic, J.; Maric, R., Microscopic insights on the degradation of a PEM water electrolyzer with ultra-low catalyst loading. *Applied Catalysis B: Environmental* **2020,** *260*, 118194.
250. Wang, Y.; Qian, G.; Xu, Q.; Zhang, H.; Shen, F.; Luo, L.; Yin, S., Industrially promising IrNi-FeNi3 hybrid nanosheets for overall water splitting catalysis at large current density. *Applied Catalysis B: Environmental* **2021,** *286*, 119881.
251. Chandesris, M., Médeau, V., Guillet, N., Chelghoum, S., Thoby, D. and Fouda-Onana, F., Membrane degradation in PEM water electrolyzer: Numerical modeling and experimental evidence of the influence of temperature and current density. International Journal of Hydrogen Energy, **2015,** 40 (3), 1353-1366.
252. Carmo, M., Keeley, G.P., Holtz, D., Grube, T., Robinius, M., Müller, M. and Stolten, D., PEM water electrolysis: Innovative approaches towards catalyst separation, recovery and recycling. *International Journal of Hydrogen Energy*, **2019,** *44* (7), 3450-3455.
253. Bernt, M., Schröter, J., Möckl, M. and Gasteiger, H.A., Analysis of gas permeation phenomena in a PEM water electrolyzer operated at high pressure and high current density. Journal of The Electrochemical Society, **2020,** 167 (12), 124502.
254. Bernt, M. and Gasteiger, H.A., Influence of ionomer content in IrO2/TiO2 electrodes on PEM water electrolyzer performance. Journal of The Electrochemical Society, **2016,** 163 (11), F3179.
255. Shirvanian, P.; van Berkel, F., Novel components in Proton Exchange Membrane (PEM) Water Electrolyzers (PEMWE): Status, challenges and future needs. A mini review. *Electrochemistry Communications* **2020,** *114*, 106704.

256. Bernt, M.; Schramm, C.; Schröter, J.; Gebauer, C.; Byrknes, J.; Eickes, C.; Gasteiger, H. A., Effect of the IrO_x Conductivity on the Anode Electrode/Porous Transport Layer Interfacial Resistance in PEM Water Electrolyzers. *Journal of The Electrochemical Society* **2021,** *168* (8), 084513.
257. Ayers, K., High efficiency PEM water electrolysis: enabled by advanced catalysts, membranes, and processes. *Current Opinion in Chemical Engineering* **2021,** *33*, 100719.
258. Liu, C.; Carmo, M.; Bender, G.; Everwand, A.; Lickert, T.; Young, J. L.; Smolinka, T.; Stolten, D.; Lehnert, W., Performance enhancement of PEM electrolyzers through iridium-coated titanium porous transport layers. *Electrochemistry Communications* **2018,** *97*, 96-99.
259. Bernt, M.; Gasteiger, H. A., Influence of Ionomer Content in IrO2/TiO2 Electrodes on PEM Water Electrolyzer Performance. *Journal of The Electrochemical Society* **2016,** *163* (11), F3179.
260.Medina, P. and Santarelli, M., Analysis of water transport in a high pressure PEM electrolyzer. *International Journal of Hydrogen Energy*, **2010,** *35*(11), 5173-5186.
261. Sapountzi, F. M.; Lavorenti, M.; Vrijburg, W.; Dimitriadou, S.; Tyburska-Pueschel, B.; Thüne, P.; Niemantsverdriet, H.; Pfeiffer, T. V.; Tsampas, M. N. Spark Ablation for the Fabrication of PEM Water Electrolysis Catalyst-Coated Membranes *Catalysts* [Online], 2022.
262. Higashi, S.; Beniya, A., Ultralight conductive IrO2 nanostructured textile enables highly efficient hydrogen and oxygen evolution reaction: Importance of catalyst layer sheet resistance. *Applied Catalysis B: Environmental* **2023,** *321*, 122030.
263. Ni, A., Upadhyay, M., Kumar, S.S., Uwitonze, H. and Lim, H., Anode analysis and modelling hydrodynamic behaviour of the multiphase flow field in circular PEM water electrolyzer. *International Journal of Hydrogen Energy*, **2023,** *48* (43), 16176-16183.
264. Weiß, A., Siebel, A., Bernt, M., Shen, T.H., Tileli, V. and Gasteiger, H.A., Impact of intermittent operation on lifetime and performance of a PEM water electrolyzer. *Journal of the electrochemical society*, **2019,** *166* (8), F487-F497.
265. Ding, L.; Wang, W.; Xie, Z.; Aaron, D. S.; Paxson, A.; Hamdan, M.; Mench, M. M.; Zhang, F.-Y., Efficient Integrated Electrode Enables High-Current Operation and Excellent Stability for Green Hydrogen Production. *ACS Sustainable Chemistry & Engineering* **2023**.
266. Qiu, C., Xu, Z., Chen, F.Y. and Wang, H., Anode Engineering for Proton Exchange Membrane Water Electrolyzers. *ACS Catalysis*, **2024,** *14* (2), 921-954.
267. Kulkarni, D.; Huynh, A.; Satjaritanun, P.; O'Brien, M.; Shimpalee, S.; Parkinson, D.; Shevchenko, P.; DeCarlo, F.; Danilovic, N.; Ayers, K. E.; Capuano, C.; Zenyuk, I. V., Elucidating effects of catalyst loadings and porous transport layer morphologies on operation of proton exchange membrane water electrolyzers. *Applied Catalysis B: Environmental* **2022,** *308*, 121213.
268. Kıstı, M.; Uysal, S.; Kaya, M. F., Development of Pt coated SS316 mesh gas diffusion electrodes for a PEM water electrolyzer anode. *Fuel* **2022,** *324*, 124775.
269. Zhang, K., Liang, X., Wang, L., Sun, K., Wang, Y., Xie, Z., Wu, Q., Bai, X., Hamdy, M.S., Chen, H. and Zou, X., Status and perspectives of key materials for PEM electrolyzer. Nano Research Energy, **2022,** 1 (3),e9120032.

270. Chatterjee, S.; Peng, X.; Intikhab, S.; Zeng, G.; Kariuki, N. N.; Myers, D. J.; Danilovic, N.; Snyder, J., Nanoporous Iridium Nanosheets for Polymer Electrolyte Membrane Electrolysis. *Advanced Energy Materials* **2021,** *11* (34), 2101438.
271. Wang, W.; Ding, L.; Xie, Z.; Yu, S.; Canfield, B.; Bender, G.; Wrubel, J. A.; Pivovar, B. S.; Zhang, F.-Y., Discovering Reactant Supply Pathways at Electrode/PEM Reaction Interfaces Via a Tailored Interface-Visible Characterization Cell. *Small* **2023,** *19* (28), 2207809.
272. Huang, X.; Tang, S.; Mu, X.; Dai, Y.; Chen, G.; Zhou, Z.; Ruan, F.; Yang, Z.; Zheng, N., Freestanding palladium nanosheets with plasmonic and catalytic properties. *Nature Nanotechnology* **2011,** *6* (1), 28-32.
273. Jiang, B.; Guo, Y.; Kim, J.; Whitten, A. E.; Wood, K.; Kani, K.; Rowan, A. E.; Henzie, J.; Yamauchi, Y., Mesoporous Metallic Iridium Nanosheets. *Journal of the American Chemical Society* **2018,** *140* (39), 12434-12441.
274. Kim, M. Y.; Ban, H.-J.; Song, Y.-W.; Lim, J.; Park, S.-J.; Kim, W. J.; Hong, Y.; Kang, B.-S.; Kim, H.-S., Synthesis and electrochemical properties of nano-composite IrO2/TiO2 anode catalyst for SPE electrolysis cell. *International Journal of Hydrogen Energy* **2022,** *47* (73), 31098-31108.
275. Lim, J. Y.; Rahman, G.; Chae, S. Y.; Lee, K.-Y.; Kim, C.-S.; Joo, O.-S., Highly stable RuO2/SnO2 nanocomposites as anode electrocatalysts in a PEM water electrolysis cell. *International Journal of Energy Research* **2014,** *38* (7), 875-883.
276. Shiva Kumar, S.; Ramakrishna, S. U. B.; Bhagawan, D.; Himabindu, V., Preparation of RuxPd1-xO2 electrocatalysts for the oxygen evolution reaction (OER) in PEM water electrolysis. *Ionics* **2018,** *24* (8), 2411-2419.
277. Ramakrishna, S. U. B.; Srinivasulu Reddy, D.; Shiva Kumar, S.; Himabindu, V., Nitrogen doped CNTs supported Palladium electrocatalyst for hydrogen evolution reaction in PEM water electrolyser. *International Journal of Hydrogen Energy* **2016,** *41* (45), 20447-20454.
278. Shiva Kumar, S.; Ramakrishna, S. U. B.; Rama Devi, B.; Himabindu, V., Phosphorus-doped carbon nanoparticles supported palladium electrocatalyst for the hydrogen evolution reaction (HER) in PEM water electrolysis. *Ionics* **2018,** *24* (10), 3113-3121.
279. Shiva Kumar, S.; Ramakrishna, S. U. B.; Naga Mahesh, K.; Rama Devi, B.; Himabindu, V., Palladium supported on phosphorus–nitrogen dual-doped carbon nanoparticles as cathode for hydrogen evolution in PEM water electrolyser. *Ionics* **2019,** *25* (6), 2615-2625.
280. Audichon, T.; Mayousse, E.; Morisset, S.; Morais, C.; Comminges, C.; Napporn, T. W.; Kokoh, K. B., Electroactivity of RuO2–IrO2 mixed nanocatalysts toward the oxygen evolution reaction in a water electrolyzer supplied by a solar profile. *International Journal of Hydrogen Energy* **2014,** *39* (30), 16785-16796.
281. Hegge, F.; Lombeck, F.; Cruz Ortiz, E.; Bohn, L.; von Holst, M.; Kroschel, M.; Hübner, J.; Breitwieser, M.; Strasser, P.; Vierrath, S., Efficient and Stable Low Iridium Loaded Anodes for PEM Water Electrolysis Made Possible by Nanofiber Interlayers. *ACS Applied Energy Materials* **2020,** *3* (9), 8276-8284.

282. Jiang, G.; Yu, H.; Hao, J.; Chi, J.; Fan, Z.; Yao, D.; Qin, B.; Shao, Z., An effective oxygen electrode based on Ir0.6Sn0.4O2 for PEM water electrolyzers. *Journal of Energy Chemistry* **2019,** *39*, 23-28.
283. Slavcheva, E.; Borisov, G.; Lefterova, E.; Petkucheva, E.; Boshnakova, I., Ebonex supported iridium as anode catalyst for PEM water electrolysis. *International Journal of Hydrogen Energy* **2015,** *40* (35), 11356-11361.
284. DOE, U. S., Technical Targets for Proton Exchange Membrane Electrolysis. https://www.energy.gov/eere/fuelcells/technical-targets-proton-exchange-membrane-electrolysis, 2003 (accessed 1 May 2023).
285. Aßmann, P.; Gago, A. S.; Gazdzicki, P.; Friedrich, K. A.; Wark, M., Toward developing accelerated stress tests for proton exchange membrane electrolyzers. *Current Opinion in Electrochemistry* **2020,** *21*, 225-233.
286. Rakousky, C.; Reimer, U.; Wippermann, K.; Carmo, M.; Lueke, W.; Stolten, D., An analysis of degradation phenomena in polymer electrolyte membrane water electrolysis. *Journal of Power Sources* **2016,** *326*, 120-128.
287. Alia, S.M., Reeves, K.S., Baxter, J.S. and Cullen, D.A., The impact of ink and spray variables on catalyst layer properties, electrolyzer performance, and electrolyzer durability. *Journal of The Electrochemical Society*, **2020,** *167* (14), 144512.
288. Zaccarine, S. F.; Shviro, M.; Weker, J. N.; Dzara, M. J.; Foster, J.; Carmo, M.; Pylypenko, S., Multi-Scale Multi-Technique Characterization Approach for Analysis of PEM Electrolyzer Catalyst Layer Degradation. *J Electrochem Soc* **2022,** *169* (6), 064502.
289. Claudel, F.; Dubau, L.; Berthomé, G.; Sola-Hernandez, L.; Beauger, C.; Piccolo, L.; Maillard, F., Degradation Mechanisms of Oxygen Evolution Reaction Electrocatalysts: A Combined Identical-Location Transmission Electron Microscopy and X-ray Photoelectron Spectroscopy Study. *ACS Catalysis* **2019,** *9* (5), 4688-4698.
290. Feng, J.; Lv, F.; Zhang, W.; Li, P.; Wang, K.; Yang, C.; Wang, B.; Yang, Y.; Zhou, J.; Lin, F.; Wang, G.-C.; Guo, S., Iridium-Based Multimetallic Porous Hollow Nanocrystals for Efficient Overall-Water-Splitting Catalysis. *Advanced Materials* **2017,** *29* (47), 1703798.
291. Chabot, V.; Higgins, D.; Yu, A.; Xiao, X.; Chen, Z.; Zhang, J., A review of graphene and graphene oxide sponge: material synthesis and applications to energy and the environment. *Energy Environ. Sci.* **2014,** *7* (5), 1564.
292. Li, X.; Zhao, L.; Yu, J.; Liu, X.; Zhang, X.; Liu, H.; Zhou, W., Water Splitting: From Electrode to Green Energy System. *Nano-Micro Lett.* **2020,** *12* (1).
293. Chen, X.; Zhang, Z.; Chi, L.; Nair, A. K.; Shangguan, W.; Jiang, Z., Recent Advances in Visible-Light-Driven Photoelectrochemical Water Splitting: Catalyst Nanostructures and Reaction Systems. *Nano-Micro Lett.* **2016,** *8* (1), 1-12.
294. Hossain, A.; Sakthipandi, K.; Atique Ullah, A. K. M.; Roy, S., Recent Progress and Approaches on Carbon-Free Energy from Water Splitting. *Nano-Micro Lett.* **2019,** *11* (1).
295. Liu, Y.; Vijayakumar, P.; Liu, Q.; Sakthivel, T.; Chen, F.; Dai, Z., Shining Light on Anion-Mixed Nanocatalysts for Efficient Water Electrolysis: Fundamentals, Progress, and Perspectives. *Nano-Micro Lett.* **2022,** *14* (1).
296. Pu, Z.; Amiinu, I. S.; Cheng, R.; Wang, P.; Zhang, C.; Mu, S.; Zhao, W.; Su, F.; Zhang, G.; Liao, S.; Sun, S., Single-Atom Catalysts for Electrochemical Hydrogen

Evolution Reaction: Recent Advances and Future Perspectives. *Nano-Micro Lett.* **2020,** *12* (1).
297. Yang, G.; Wang, W.; Xie, Z.; Yu, S.; Li, Y.; Ding, L.; Li, K.; Zhang, F.-Y., Favorable morphology and electronic conductivity of functional sublayers for highly efficient water splitting electrodes. *J Energy Storage* **2021,** *36*, 102342.
298. Qian, G.; Chen, J.; Yu, T.; Luo, L.; Yin, S., N-Doped Graphene-Decorated NiCo Alloy Coupled with Mesoporous NiCoMoO Nano-sheet Heterojunction for Enhanced Water Electrolysis Activity at High Current Density. *Nano-Micro Lett.* **2021,** *13* (1).
299. Cao, J.; Wang, K.; Chen, J.; Lei, C.; Yang, B.; Li, Z.; Lei, L.; Hou, Y.; Ostrikov, K., Nitrogen-Doped Carbon-Encased Bimetallic Selenide for High-Performance Water Electrolysis. *Nano-Micro Lett.* **2019,** *11* (1).
300. Du, C.-F.; Liang, Q.; Dangol, R.; Zhao, J.; Ren, H.; Madhavi, S.; Yan, Q., Layered Trichalcogenidophosphate: A New Catalyst Family for Water Splitting. *Nano-Micro Lett.* **2018,** *10* (4).
301. Laube, A.; Hofer, A.; Ressel, S.; Chica, A.; Bachmann, J.; Struckmann, T., PEM water electrolysis cells with catalyst coating by atomic layer deposition. *International Journal of Hydrogen Energy* **2021,** *46* (79), 38972-38982.
302. Wang, D.; Zhu, Z.; Yang, B.; Yin, W.; Drelich, J., Nano-scaled roughness effect on air bubble-hydrophilic surface adhesive strength. *Colloids Surf. A Physicochem. Eng. Asp.* **2020,** *603*, 125228.
303. Park, H.; Choe, S.; Kim, H.; Kim, D.-K.; Cho, G.; Park, Y.; Jang, J. H.; Ha, D.-H.; Ahn, S. H.; Kim, S.-K., Direct fabrication of gas diffusion cathode by pulse electrodeposition for proton exchange membrane water electrolysis. *Appl Surf Sci* **2018,** *444*, 303-311.
304. Li, Y.; Kang, Z.; Deng, X.; Yang, G.; Yu, S.; Mo, J.; Talley, D. A.; Jennings, G. K.; Zhang, F.-Y., Wettability effects of thin titanium liquid/gas diffusion layers in proton exchange membrane electrolyzer cells. *Electrochim. Acta* **2019,** *298*, 704-708.
305. Wei, L.; Fan, Y.-J.; Wang, H.-H.; Tian, N.; Zhou, Z.-Y.; Sun, S.-G. J. E. A., Electrochemically shape-controlled synthesis in deep eutectic solvents of Pt nanoflowers with enhanced activity for ethanol oxidation. **2012,** *76*, 468-474.
306. Guo, M.; Hong, H.; Tang, X.; Fang, H.; Xu, X. J. E. a., Ultrasonic electrodeposition of platinum nanoflowers and their application in nonenzymatic glucose sensors. **2012,** *63*, 1-8.
307. Zhang, H.; Zhou, W.; Du, Y.; Yang, P.; Wang, C., One-step electrodeposition of platinum nanoflowers and their high efficient catalytic activity for methanol electro-oxidation. *Electrochem. Commun.* **2010,** *12* (7), 882-885.
308. Song, J., Kim, Y., Lee, J., Kim, H.J., Sung, Y.E., Lim, T. and Kwon, O.J., Implementation of Proton Exchange Membrane Water Electrolyzer with Ultralow Pt Loading Cathode through Pt Particle Size Control. *ACS Sustainable Chemistry & Engineering*, **2023,** *11* (45), 16258-16266.
309. Liu, X.; Wang, K.; Zhou, L.; Pu, H.; Zhang, T.; Jia, J.; Deng, Y., Shape-Controlled Synthesis of Concave Pt and Willow-Like Pt Nanocatalysts via Electrodeposition with Hydrogen Adsorption/Desorption and Investigation of Their Electrocatalytic Performances toward Ethanol Oxidation Reaction. *ACS Sustainable Chemistry & Engineering* **2020,** *8* (16), 6449-6457.

310. Xie, Z.; Yu, S.; Cui, C.; Yu, H.; Li, K.; Ding, L.; Wang, W.; Cullen, D. A.; Meyer, H. M.; Baxter, J. S.; Gao, P.-X.; Zhang, F.-Y., Unveiling mechanism of surface-guided platinum nanowire growth. *J Mater Sci* **2022,** *57* (27), 12875-12885.
311. Li, C.; Clament Sagaya Selvam, N.; Fang, J., Shape-Controlled Synthesis of Platinum-Based Nanocrystals and Their Electrocatalytic Applications in Fuel Cells. *Nano-Micro Letters* **2023,** *15* (1), 83.
312. Cai, X.-L.; Liu, C.-H.; Liu, J.; Lu, Y.; Zhong, Y.-N.; Nie, K.-Q.; Xu, J.-L.; Gao, X.; Sun, X.-H.; Wang, S.-D., Synergistic Effects in CNTs-PdAu/Pt Trimetallic Nanoparticles with High Electrocatalytic Activity and Stability. *Nano-Micro Lett.* **2017,** *9* (4).
313. Liu, J.; Zhong, C.; Du, X.; Wu, Y.; Xu, P.; Liu, J.; Hu, W. J. E. A., Pulsed electrodeposition of Pt particles on indium tin oxide substrates and their electrocatalytic properties for methanol oxidation. **2013,** *100*, 164-170.
314. Du, X. T.; Yang, Y.; Liu, J.; Liu, B.; Liu, J. B.; Zhong, C.; Hu, W. B., Surfactant-free and template-free electrochemical approach to prepare well-dispersed Pt nanosheets and their high electrocatalytic activities for ammonia oxidation. *Electrochimica Acta* **2013,** *111*, 562-566.
315. Zhang, L.; Liu, T.; Ren, R.; Zhang, J.; He, D.; Zhao, C.; Suo, H., In situ synthesis of hierarchical platinum nanosheets-polyaniline array on carbon cloth for electrochemical detection of ammonia. *J Hazard Mater* **2020,** *392*, 122342.
316. Li, B.; Si, Y.; Fang, Q.; Shi, Y.; Huang, W.-Q.; Hu, W.; Pan, A.; Fan, X.; Huang, G.-F., Hierarchical Self-assembly of Well-Defined Louver-Like P-Doped Carbon Nitride Nanowire Arrays with Highly Efficient Hydrogen Evolution. *Nano-Micro Letters* **2020,** *12* (1).
317. Wu, H.; Lu, Q.; Zhang, J.; Wang, J.; Han, X.; Zhao, N.; Hu, W.; Li, J.; Chen, Y.; Deng, Y., Thermal Shock-Activated Spontaneous Growing of Nanosheets for Overall Water Splitting. *Nano-Micro Lett.* **2020,** *12* (1).
318. Li, J.; Li, J.; Ren, J.; Hong, H.; Liu, D.; Liu, L.; Wang, D., Electric-Field-Treated Ni/Co3O4 Film as High-Performance Bifunctional Electrocatalysts for Efficient Overall Water Splitting. *Nano-Micro Lett.* **2022,** *14* (1).
319. Lin, J.; Yan, Y.; Li, C.; Si, X.; Wang, H.; Qi, J.; Cao, J.; Zhong, Z.; Fei, W.; Feng, J., Bifunctional Electrocatalysts Based on Mo-Doped NiCoP Nanosheet Arrays for Overall Water Splitting. *Nano-Micro Lett.* **2019,** *11* (1).
320. Chen, J.; Ha, Y.; Wang, R.; Liu, Y.; Xu, H.; Shang, B.; Wu, R.; Pan, H., Inner Co Synergizing Outer Ru Supported on Carbon Nanotubes for Efficient pH-Universal Hydrogen Evolution Catalysis. *Nano-Micro Letters* **2022,** *14* (1), 186.
321. Wang, P.; Luo, Y.; Zhang, G.; Chen, Z.; Ranganathan, H.; Sun, S.; Shi, Z., Interface Engineering of NixSy@MnOxHy Nanorods to Efficiently Enhance Overall-Water-Splitting Activity and Stability. *Nano-Micro Letters* **2022,** *14* (1), 120.
322. Rakousky, C.; Keeley, G. P.; Wippermann, K.; Carmo, M.; Stolten, D., The stability challenge on the pathway to high-current-density polymer electrolyte membrane water electrolyzers. *Electrochim Acta* **2018,** *278*, 324-331.
323. Qian, G.; Chen, J.; Yu, T.; Liu, J.; Luo, L.; Yin, S., Three-Phase Heterojunction NiMo-Based Nano-Needle for Water Splitting at Industrial Alkaline Condition. *Nano-Micro Letters* **2022,** *14* (1).

324. Xie, Z.; Yu, S.; Yang, G.; Li, K.; Ding, L.; Wang, W.; Cullen, D. A.; Meyer III, H. M.; Retterer, S. T.; Wu, Z.; Sun, J.; Gao, P.-X.; Zhang, F.-Y., Ultrathin platinum nanowire based electrodes for high-efficiency hydrogen generation in practical electrolyzer cells. *Chem. Eng. J.* **2021,** *410*, 128333.
325. Rajala, T.; Kronberg, R.; Backhouse, R.; Buan, M. E. M.; Tripathi, M.; Zitolo, A.; Jiang, H.; Laasonen, K.; Susi, T.; Jaouen, F., A platinum nanowire electrocatalyst on single-walled carbon nanotubes to drive hydrogen evolution. *Appl. Catal. B.* **2020,** *265*, 118582.
326. Kang, Z.; Wang, M.; Yang, Y.; Wang, H.; Liu, Y.; Mo, J.; Li, J.; Deng, P.; Jia, C.; Tian, X., Performance improvement induced by membrane treatment in proton exchange membrane water electrolysis cells. *Int. J. Hydrog. Energy.* **2022,** *47* (9), 5807-5816.
327. Siracusano, S.; Van Dijk, N.; Payne-Johnson, E.; Baglio, V.; Aricò, A. S., Nanosized IrOx and IrRuOx electrocatalysts for the O2 evolution reaction in PEM water electrolysers. *Appl. Catal. B* **2015,** *164*, 488-495.
328. Pantò, F.; Siracusano, S.; Briguglio, N.; Aricò, A. S., Durability of a recombination catalyst-based membrane-electrode assembly for electrolysis operation at high current density. *Appl Energ* **2020,** *279*, 115809.
329. Choi, S.; Park, J.; Kabiraz, M. K.; Hong, Y.; Kwon, T.; Kim, T.; Oh, A.; Baik, H.; Lee, M.; Paek, S. M.; Choi, S. I.; Lee, K., Pt Dopant: Controlling the Ir Oxidation States toward Efficient and Durable Oxygen Evolution Reaction in Acidic Media. *Adv. Funct. Mater.* **2020,** *30* (38), 2003935.
330. Huo, W.; Zhou, X.; Jin, Y.; Xie, C.; Yang, S.; Qian, J.; Cai, D.; Ge, Y.; Qu, Y.; Nie, H.; Yang, Z., Rhenium Suppresses Iridium (IV) Oxide Crystallization and Enables Efficient, Stable Electrochemical Water Oxidation. *Small* **2023,** *19* (19), 2207847.
331. Wang, J.; Yang, H.; Li, F.; Li, L.; Wu, J.; Liu, S.; Cheng, T.; Xu, Y.; Shao, Q.; Huang, X., Single-site Pt-doped RuO2 hollow nanospheres with interstitial C for high-performance acidic overall water splitting. *Sci. Adv.* **2022,** *8* (9), eabl9271.
332. Liu, H.; Zhang, Z.; Fang, J.; Li, M.; Sendeku, M. G.; Wang, X.; Wu, H.; Li, Y.; Ge, J.; Zhuang, Z., Eliminating over-oxidation of ruthenium oxides by niobium for highly stable electrocatalytic oxygen evolution in acidic media. *Joule* **2023,** *7* (3), 558-573.

VITA

Lei Ding was born in Qianxi, GuiZhou Province, P. R. China. She studied at Shanghai University of Engineering Science from 2010 to 2014 for B. S. degree in the major of Chemical Engineering and Technology. Afterward, she pursued her M. S. study and received M. S. degree at Shanghai University of Engineering Science in 2018 in the major of Materials Physics and Chemistry. She started to pursue her Ph.D. at the University of Tennessee, Knoxville (UTK) from August 2019 in the Department of Mechanical, Aerospace and Biomedical Engineering under the supervision of Dr. Feng-Yuan Zhang.